Aikaterini Mandaltsi

Wadham College

Supervisors

Paul N. Watton
Mark S. Thompson

MODELLING THE MECHANOBIOLOGICAL EVOLUTION OF ANEURYSMS: **An integrative in vivo, in vitro and in silico approach**

A thesis submitted for the degree of Doctor of Philosophy

2016

Για την μαμά, τον μπαμπά, τον Γρηγόρη και την Λέλα

A thesis submitted for the degree of Doctor of Philosophy.

Modelling the mechanobiological evolution of aneurysms

By Aikaterini Mandaltsi, Wadham College.

Submitted 2016.

Abstract

In silico models of intracranial aneurysm (IA) evolution aim to reliably represent the mechanical blood flow environment, the biology of the arterial wall and, crucially, the complex link between the two, namely the mechanobiology of healthy and diseased arteries. The ultimate goal is to create diagnostic tools for personalised management and treatment of aneurysm disease. Towards that target, the work presented in this thesis aims to establish a directly interactive link between experimental (*in vivo* and *in vitro*) and computational work for biologically and clinically relevant research on aneurysm disease. Mechanobiological hypotheses were firstly investigated in a novel 1D mathematical conceptual model of aneurysm evolution: for the first time these included representations of endothelial heterogeneity and smooth muscle cell (SMC) active stress response and apoptosis. The 1D investigations analysed and assessed the role of wall shear stress (WSS) homeostasis in elastin degradation, and the evolving role of the adventitia as a protective sheath in health and primary load-bearer in disease. The 1D framework was applied to a specific patient's aneurysm using both imaging and histological data to parameterise the model, calculating a material parameter for the adventitital collagen. The predicted evolution captured aspects of tissue changes measured with time focusing on the remodelled tissue wall thickness consistent with the experimental measurements, and physiological cyclic deformation in order to propose an approach to modelling adventitia's adaptive role to load bearing. Furthermore, an existing Fluid-Solid-Growth (FSG) computational framework was adapted and calibrated for the same patient-specific case with the help from the experimental data and the analysis from the 1D framework. This FSG model quantifies the arterial mechanical environment and captures the mechanical response of the fibrous arterial constituents. Comparing 1D and 3D investigations to establish consistency for our models, the 3D model tested the hypothesis of WSS homeostasis, additionally introducing the element of spatial heterogeneity in the definition, and a new hypothesis

linking cyclic deformation with collagen growth that ensures a physiological mechanical environment in stabilised aneurysms. Moreover, the FSG framework was applied in a specific rabbit aneurysm case and extended to link growth and remodelling to the detailed representation of the pulsatile blood flow mechanical environment. This research illustrates the power of computational modelling when coupled with rich data sets on the physiology, histology and geometry of healthy and diseased vascular tissue. In particular, the integrative modelling framework provides the foundation for establishing mechanobiological links crucial to aneurysm progression, and a basis for further research towards creating reliable aneurysm clinical tools.

Statement of Originality

I hereby declare that this submission is my own work and to the best of my knowledge it contains no materials previously published or written by another person, or substantial proportions of material which have been accepted for the award of any other degree or diploma at the University of Oxford or any other educational institution, except where due acknowledgement is made in the thesis.

Any contribution made to the research by others, with whom I have worked at the University of Oxford or elsewhere, is explicitly acknowledged in the thesis.

I also declare that the intellectual content of this thesis is the product of my own work, except to the extent that assistance from others in the project's design and conception or in style, presentation and linguistic expression is acknowledged.

Aikaterini Mandaltsi.
17^{th} June 2016

Acknowledgements

I would like to sincerely thank Dr Paul Watton for his unwavering support throughout my doctorate degree and the amazing opportunities (national and international) he has given me. I would also like to express my gratitude to Dr Mark Thompson for his continuous encouragement and guidance. I would like to thank Prof. Anne Robertson for her help and hospitality in Pittsburgh, and her nurturing attitude towards other women in science. I would also like to thank Dr Alberto Marzo for his expert advice on CFD. Many thanks go to everyone in the Mechanobiology group, but especially to Catherine, I-Tung and Yuqian for their cooperation and for making me feel very welcome in Sheffield. Finally, I would like to thank my family and friends, who have been devoted in their support for me, from near and afar.

I acknowledge the support of the RCUK Digital Economy Programme (Oxford Centre for Doctoral Training in Healthcare Innovation) for funding a unique academic opportunity in Oxford.

This thesis template was created by Brett Tully (2010) *'Allostasis of Cerebral Water: Modelling the Transport of Cerebrospinal Fluid'*, PhD Thesis, University of Oxford.

Dissemination

Peer-Reviewed Journal Papers and Conference Proceedings

1. Mandaltsi A., Wong W., Robertson AM., Watton PN., *Modelling the mechanobiological evolution of intracranial aneurysms: An integrative in vivo, in vitro and in silico approach for a clinical case*, Journal of Royal Society, 2016 (in preparation).

2. Aparicio P., Mandatlsi A., Boamah J., Chen H., Selimovic A., Bratby M., Uberoi R., Ventikos Y., Watton PN., *Modelling the influence of endothelial heterogeneity on the progression of arterial disease: application to abdominal aortic aneurysm evolution*, International Journal for Numerical Methods in Biomedical Engineering, 30(5):563-86, 2014.

3. Mandaltsi A., Wong W., Mei Y., Robertson AM., Gundiah N., Watton PN., *Modelling the mechanobiological evolution of intracranial aneurysms: An integrative in vivo, in vitro and in silico approach*, European Congress on Computational Methods in Applied Sciences and Engineering, Crete Island, Greece, 5-10 June, 2016.

4. Mandaltsi A., Robertson AM., Watton PN., *Modelling the evolution of rabbit elastase aneurysms: An integrative in vivo, in vitro and in silico approach*, 9^{th} European Solid Mechanics Conference, Madrid, Spain, 6-10 July 2015.

5. Mandaltsi A., Robertson AM., Watton PN., *Modelling the evolution of rabbit elastase aneurysms: An integrative in vivo, in vitro and in silico approach*, 2^{nd} Workshop on Soft Tissue Mechanics, Glasgow, UK, 10-12 June 2015.

6. Aparicio P., Mandatlsi A., Thompson MS., Watton PN., *Investigating the role of Cell Signalling on Intracranial Aneurysm Evolution: A novel chemo-mechanobiological mathematical model*, 7^{th} World Congress of Biomechanics, Boston, US, 6-11 July 2014.

7. Aparicio P., Mandatlsi A., Boamah J., Ventikos Y., Watton PN., *Modelling the influence of endothelial cell heterogeneity on abdominal aor-*

tica aneurysm evolution: a patient-specific simulation using a novel fluid-solid-growth (FSG) framework, XXIV Congress of the International Society of Biomechanics, Natal, Brazil, 4-9 August, 2013.

8. Mandaltsi A., Ventikos Y., Watton PN., *Modelling the influence of endothelial cell heterogeneity on aneurysm evolution: a novel mathematical model*, 8^{th} International Symposium on Biomechanics in Vascular Biology and Cardiovascular Disease, Rotterdam, Netherlands, 18-19 April 2013.

9. Mandaltsi A., Ventikos Y., Watton PN., *Modelling the influence of endothelial cell heterogeneity on aneurysm evolution: a novel mathematical model*, 1^{st} UK Conference on Patient Specific Modelling (PSM) and Translational Research, Cardiff, UK, 9-10 January 2013.

CONTENTS

List of Figures

LIST OF TABLES

ACRONYMS

AAA	Abdominal aortic aneurysm
AFI	Aneurysm formation index
CFD	Computational fluid dynamics
CT	Computed tomography
EC	Endothelial cell
ECM	Extra-cellular matrix
FE	Finite element
FSG	Fluid-Solid-Growth
GL	Green-Lagrange
GON	Gradient oscillatory number
G&R	Growth & Remodelling
IA	Intracranial aneurysm
LCCA	Left common carotid artery
MMP	Matrix metalloproteinase
MRI	Magnetic resonance imaging
OSI	Oscillatory shear index
PK	Piola-Kirchhoff
RCCA	Right common carotid artery
SEF	Strain energy function
SMC	Smooth muscle cell
TAA	Thoracic aortic aneurysm
WSS	Wall shear stress
RA	Rotational angiography

KEY MATHEMATICAL NOTATION

Variables	
t	Time
h	Loaded thickness
H	Unloaded thickness
λ	Stretch
l	Loaded length
L	Unloaded length
r	Loaded radius
R	Unloaded radius
p	Pressure
$\bar{m}$	Density (for arterial fibres and cells)
m	Normalised density (for arterial fibres and cells)
$\hat{\sigma}$	Azimuthal Cauchy stress
ψ	Strain energy of fibres and cells per unit volume
K	Material parameter (for arterial fibres and cells)
E	Green-Lagrangian strain (for arterial fibres and cells)
τ	Wall shear stress
A	Areal stretch
Subscripts and superscripts	
z	Axial
0	At $t = 0$
E	Elastin
C	Collagen
SMC	Smooth muscle cells
M	Media
A	Adventitial
γ	Angle to the circumferential axis
R	Recruitment
AT	Attachment
CS	Cyclic stretch

CHAPTER 1

INTRODUCTION

1.1 ANEURYSM DISEASE

Aneurysms are excessive, permanent and localised dilatations of the arterial wall. The three most common types of aneurysms, in terms of location, are: cerebral (or intracranial) aneurysms (IAs); abdominal aortic aneurysms (AAAs) and thoracic aortic aneurysms (TAAs). The majority of research focuses on IAs and AAAs and this thesis investigates IAs. Even though there are differences in the disease for the two aneurysm types, they also share important characteristics and thus aneurysm research for IAs can shed light on AAAs, and vice versa (Humphrey and Taylor, 2008).

There are two main types of IAs in terms of form (illustrated in Figure 1.1): saccular (Figure 1.1(i)) and fusiform (Figure 1.1(ii)). 90% of IA cases are of the saccular type with the characteristic berry-like, spherical shape, which is connected to the vessel by a neck (Lasheras, 2007). IAs form in the cerebral arteries surrounding the circle of Willis and specific occurrence in the internal carotid artery is frequently observed (Foutrakis et al., 1999); the wall's outpouching of a proximal intracranial artery is commonly observed at a bifurcation (Krings et al., 2011), or, if it's not detected in a bifurcation, it oftens points in the direction of the flow (Atlas, 1997).

The disease affects approximately 5% of adults of all ages, and general population statistics of unruptured IAs show a range of occurence between 0.4% and 6%

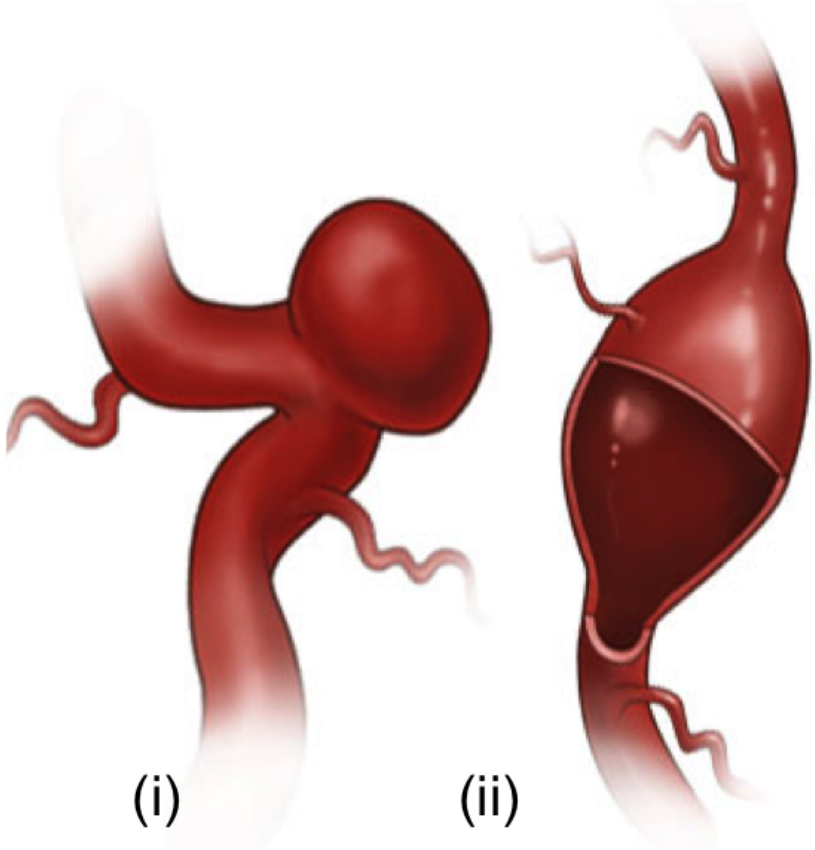

Figure 1.1: Types of intracranial aneurysms (based on their form): (i) saccular and (ii) fusiform. Image adapted from the Neurological Institute of New York (`http://columbianeurology.org/about-us/neurological-institute-new-york`).

(Rinkel et al. (1998), Winn et al. (1977), Higashida et al. (2007), Lasheras (2007)). IAs are potentially lethal if they rupture, as this might lead to a stroke (5 to 15% of stroke cases are related to ruptured IAs (Bederson et al., 2000)). The fraction of detected IAs that do rupture each year is in fact very small (0.1-1%) (Ujiie et al. (1993), Thompson et al. (2015), Juvela et al. (2000), Wiebers et al. (2003), Winn et al. (1977)); however, mortality and morbidity rates in the case of rupture can be high (30-50% (Juvela et al., 2000)), with the likely outcomes (up to 80%) being severe brain damage or death (Weir, 2002). In the US, subarachnoid haemorrhage (a form of haemorrhagic stroke) from a ruptured IA is observed in 1 in 10,000 persons and has a particularly high mortality rate (45%) for the first 30 days following the incident as well as a high risk of rebleeding (Brisman et al., 2006).

The precise aetiology of IA formation, and potential rupture, is unknown and the nature of the disease is certainly multifactorial (Caranci et al., 2013). Physiologic

influences, such as hypertension, have been found to relate to enlargement and rupture (Tateshima et al. (2007), Resnick et al. (2003)). Environmental factors, such as smoking, pose a risk to vascular integrity ((Schievink, 1997), (McGloughlin and Doyle, 2010)). Additional risk factors include age, as older age relates to increased risk, (Inagawa and Hirano, 1990); gender (female) and geographical region (Japan and Finland) (de Rooij et al., 2007) and carotid artery stenosis (Keedy, 2006). Such risk factors might also differ depending on the anatomical location (Casimiro et al., 2004); the site of the aneurysm might also be related to the risk of rupture, for example, in the middle cerebral artery (Asari and Ohmoto, 1994). Certain aneurysms have been also found to have a familial form (Schievink, 1997). This suggests that those who have suffered an aneurysm are more likely to suffer subsequent ones than those who have not suffered any at all (Casimiro et al., 2004). Even though genetic factors related to aneurysm disease have been examined (Krex et al., 2001) and possibly associative genes related to IA formation have been investigated (Krischek and Inoue (2006) Rinkel (2008)), there is still no clear understanding of the genetics of the disease (Ruigrok et al., 2005). There have been many conditions associated with IA: polycystic kidney disease, fibromuscular dysplasia, Marfan's syndrome, arteriovenous malformations of the brain (Brisman et al., 2006). However, it should be noted that atherosclerosis has been found to be a result, rather than a cause or coexisting condition, in IA development (Kosierkiewicz et al., 1994).

Besides the highly complex pathophysiology of IA disease, IAs are also mostly asymptomatic (Brisman et al., 2006); detecting an IA is either coincidental (for example, during cerebral imaging after traumatic injury) or due to subarachnoid haemorrhage, namely when it's too late to assess the risk of rupture. Consequently, IA detection and clinical decision-making on treatment becomes very difficult. Fortunately, the improved sensitivity of medical imaging techniques (computed tomography angiography, magnetic resonance angiography or angiography by direct intra-arterial catheterisation), a lot of which are non-invasive, allow for better detection in hospitals, and provide more accurate depictions of aneurysm geometries (Keedy (2006), Wolfe et al. (2006)). IA treatment, in most cases, involves intervention with endovascular or open surgery as a default option for detected IAs (Brisman et al. (2006), Wong et al. (2011)). Figure 1.2 summarises these options. Clipping of the aneurysmal neck, is seen in Figure 1.2(i): craniotomy is followed by clip ligation with MRI (magnetic resonance imaging) compatible alloys that are placed across the neck of the aneurysm. Clipping has been one of the established options for

clinical intervention for many years (Keedy, 2006), although it can be a non-viable option if there are problems of access due to the specific location of the aneurysm. Figure 1.2(ii) shows the option of endovascular occlusion; a microcatheter is advanced into the aneurysm and detachable coils are placed to decrease the amount of blood or to stop blood from filling the aneurysm (Alshekhlee et al., 2010). Effective coiling of unruptured IAs has been associated with higher survival, lower mortality rate during the procedure and incidence of vasospasm (sudden constriction of the blood vessel), as well as better cost-effectiveness (Van Rooij and Sluzewski (2006), Hohlrieder et al. (2002), Greving et al. (2009)). A long-term follow up study (Molyneux et al., 2009) also showed lower long-term risk of death following coiling. However, it is not necessarily suited to all types of aneurysms: for example, coiling would not be effective for wide-necked aneurysms. For smaller and distal aneurysms, parent artery occlusion with detachable coils and aneurysmal resection to prevent blood flow from reaching the site of the aneurysm is a similar surgical therapy option (Cloft et al., 1999).

Figure 1.2(iii) and Figure 1.2(iv) show two more recent surgical interventional methods, both of which make use of stents. Figure 1.2(iii) displays the stent remodelling technique - coils are delivered to aneurysms using stents as scaffolds (Pierot, 2011), so the coils are able to be delivered and placed within the aneurysm more effectively. Balloon-assisted coiling (Cottier et al., 2001) is a similar technique for the same purpose. Figure 1.2(iv) presents the most recent of the interventional methods. A flow diverting stent has a twofold purpose: haemodynamic and biological (Pierot, 2011). By redirecting flow from the aneurysm sac, flow stasis and gradual thrombosis is able to take place within the aneurysm, while tissue overgrowth is allowed across the aneurysm neck. The material used and the specific design (in terms of porosity, for example) that will allow the best trade off between efficacy (radial stiffness) and device (longitudinal) flexibility (Ma et al., 2015) are particularly important for this method and animal models have been developed to support it (Kallmes et al., 2007). Wong et al. (2011) suggests that this method is suited better to larger, wide necked and possibly fusiform unruptured IAs. Unfortunately, long-term anti-platelet therapy after stenting is essential to inhibit thrombus formation but can also pose potential bleeding complications.

This overview of surgical options illustrates that there is no single best interventional method for all aneurysms. Incidental findings of IAs need to be assessed

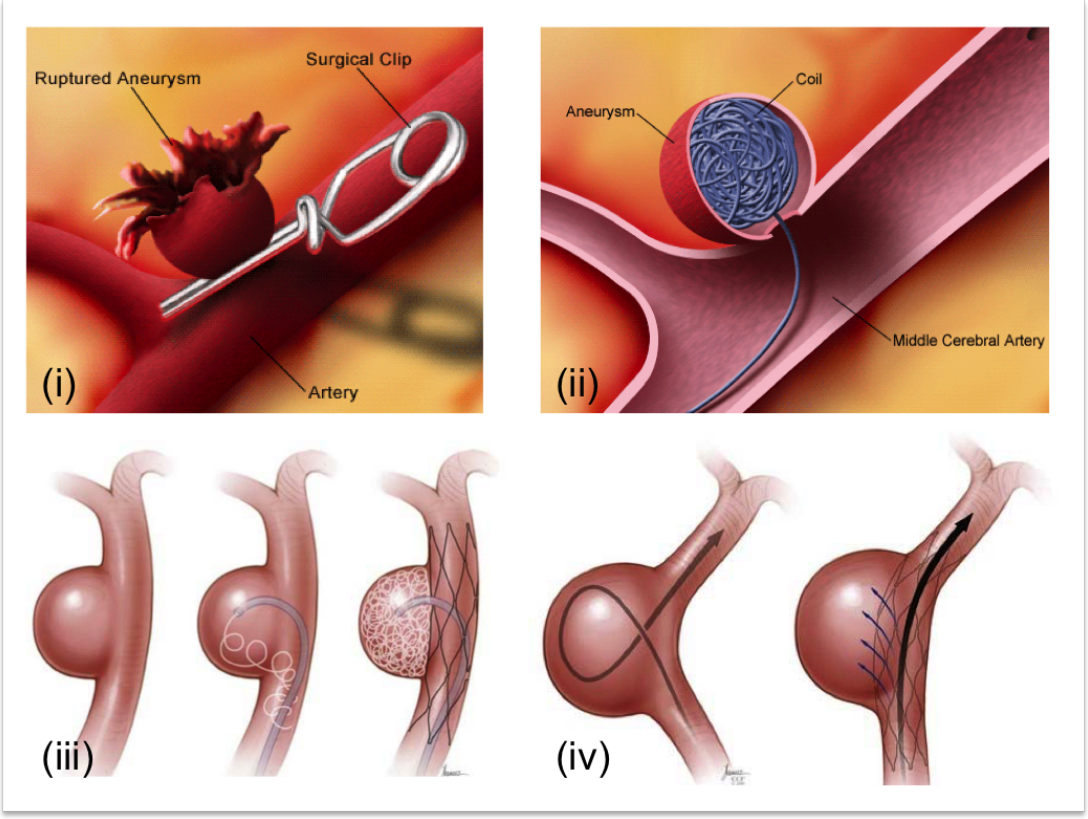

Figure 1.2: Options for intracranial aneurysm intervention: (i) clipping of aneurysmal neck (here an already ruptured aneurysm is depicted); (ii) coiling of the aneurysmal sac; (iii) the remodelling technique, combining stent deployment for the correct catherisation of coils and (iv) flow diverting stent deployment. Combined image adapted from the Neurological Institute of New York (`http://columbianeurology.org/about-us/neurological-institute-new-york`) and Winn (2011).

for risk of rupture against the risks of treatment, and decision on treatment needs to take into account the patient (and their preference), the specific aneurysm (type, shape, location), and the availability or expertise of the clinicians (Keedy, 2006). Despite the plethora of research on the complex aetiology of the disease, size is still used as the main indicator of rupture risk in clinical decision making (Juvela et al., 2000), based on observations such as the fact that IAs larger than 10mm (Wiebers et al., 2003) have a greater statistical risk of rupturing. This is clearly insufficient information for the characterisation of such a complex disease. We need to especially consider that, due to insufficient clinical criteria, the majority of patients with detected IAs who receive surgical intervention might be faced with unnecessary risks

from interventions (6% morbidity, Park et al. (2005), Molyneux et al. (2009)) as well as great costs; the cost is approximately £30K per procedure (NHS, 2012), contributing to the total overall disease cost of £0.5Bn/year in the UK (Rivero-Arias et al., 2010), which is only increasing, especially with the availability of imaging techniques.

There is undeniably an urgent need to revolutionise IA management and treatment, especially when we compare the estimated risk from intervention (6%) with that from risk of rupture (0.1-1%). Healthcare innovation for IAs requires developing diagnostic tools to distinguish stable IAs from those likely to rupture, therapeutic approaches to stabilise IAs, and clinical tools to personalise, evaluate and optimise treatment strategies. Computational modelling is key to achieving these goals. It is envisaged that models of aneurysm evolution will lead to a greater understanding of the disease and, in the longer term, assist aneurysm management, by offering more sophisticated criteria for predicting rupture.

1.2 ARTERIAL BIOLOGY AND PATHOBIOLOGY

Looking into the biology of healthy and diseased arterial tissue helps us understand more about the disease and enables us to investigate the ways in which aneurysms might develop and rupture. Investigations on pathogenesis of aneurysms are particularly difficult due to the limited availability of relevant clinical data, but close observations on biological changes allow us to make postulations about events contributing to the presence of the disease. Biology is important, since arterial tissue is living, namely, it is constantly produced and degraded, changing and being affected by its immediate environment. In this section the healthy architecture and biological function of the arterial wall will be firstly outlined and subsequently experimental evidence on the pathological biology of the aneurysmal arterial wall will be summarised.

Figure 1.3 illustrates the biological architecture of the healthy arterial wall, described in terms of the layers from the lumen towards the external layers. The innermost layer (tunica intima) consists of a monolayer of endothelial cells (ECs) and subendothelial connective tissue (a basement membrane composed of type IV collagen and laminin (Humphrey and Taylor, 2008)). The internal elastic lamina, which contributes greatly to the mechanical strength of the healthy artery (Ste-

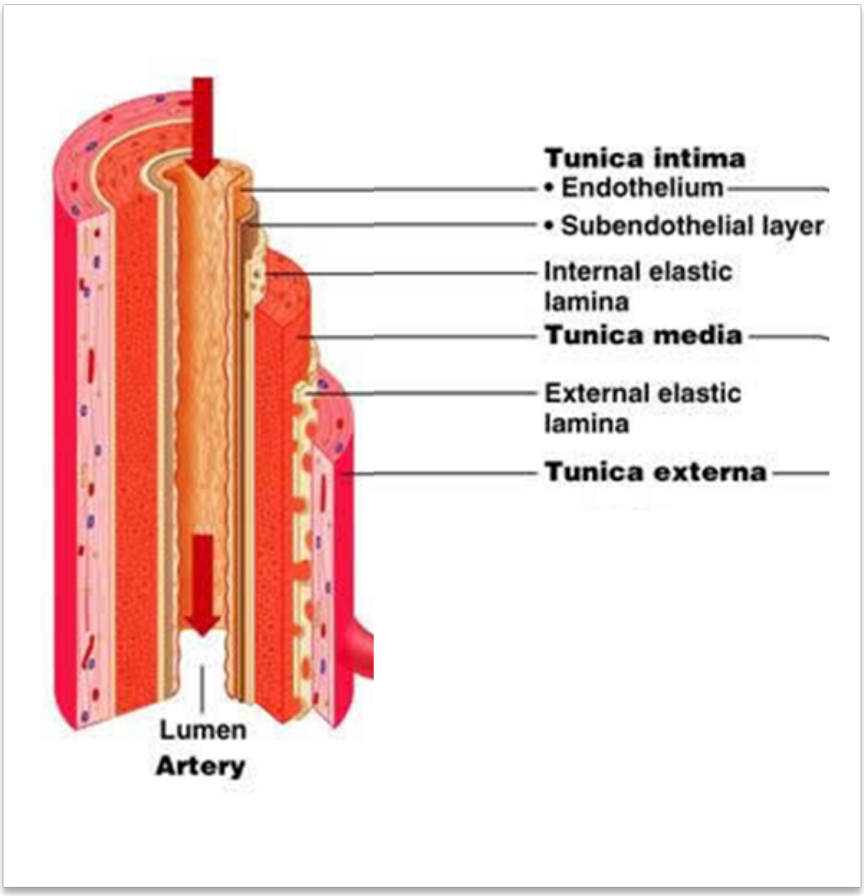

Figure 1.3: Structure of the healthy arterial wall. Image adapted from 'Anatomy & Physiology: a learning initiative' (`http://anatomyandphysiologyi.com/`). The cerebral arterial wall consists of: tunica intima (endothelium and subendothelial connective tissue), internal elastin lamina, tunica media (elastin and collagen fibres, smooth muscle cells and proteoglycans) and tunica externa (fibroblasts and collagen fibres).

hbens, 1989), separates the intima from the media (middle layer). Tunica media consists of closely packed layers of smooth muscle cells (SMCs) surrounded by the extra-cellular matrix (ECM); this is comprised of multiple types of collagen, elastin fibres and proteoglycans. Adventitia is the outermost layer (tunica externa) and consists of fibroblasts embedded in an extensive plexus of type I collagen with admixed elastin (Humphrey and Taylor, 2008). Adventitia in cerebral arteries is very thin compared to arteries in other parts of the body (Krings et al., 2011). It should be noted that, contrary to the illustration in Figure 1.3 which is generalised for all human arteries, for cerebral arteries, there is no external elastic lamina between the media and adventitia.

ECs are responsible for the control of material passage between the circulating blood and the artery wall, as well as for actively maintaining vascular homeostasis (biomechanical and biochemical state of equilibrium) and the regulation of vascular tone. Vascular homeostasis and tone regulation are accomplished by maintaining the balance between vasodilators and vasoconstrictors, and preventing platelet aggregation and anticoagulant effects (Traub and Berk, 1998). The communication between ECs and SMCs play a significant role in this regulation of arterial tone. Elastin and collagen fibres, as part of the ECM, are proteins and load-bearing arterial constituents, contributing to the known non-linear elasticity of the arterial tissue (Shadwick, 1999). Elastin fibres cease to be renewed early on in a person's life (Wagenseil and Mecham, 2007), whereas collagen fibres have a very high turnover, but their mechanical stiffness can increase with age (Avery and Bailey, 2006).

SMCs and fibroblasts within the arterial wall continually maintain the structure of the artery (Chiquet (1999), Chiquet et al. (2003)). SMCs regulate the diameter of the artery and maintain the structure of the ECM by controlling the production and degradation of the ECM proteins; this is the synthetic state of the cell (Robertson and Watton, 2013). Moreover SMCs, apart from contributing to the production of important fibres in the medial layer, also exert some of the forces that balance the blood flow forces on the arterial wall, aiming to maintain vascular mechanical homeostasis; this is the contractile state of the cell. By being partially contracted, the cells are able to either relax or contract as a response to the changes of the blood vessel's diameter (Robertson and Watton, 2013). Similarly, fibroblasts affect arterial mechanics by regulating the production of collagen fibres and other ECM components found in the adventitial layer (Meran and Steadman, 2011), through the production of matrix metalloproteinases (MMPs), which are ECM protein-degrading enzymes, and their inhibitors.

Ex vivo imaging and histological tissue studies have allowed investigation of the changes in the structure of the arterial wall during IA evolution (Robertson et al. (2015), Killer-Oberpfalzer et al. (2012), Frösen et al. (2004)). The histopathological characteristics of the pathogenesis, enlargement and rupture of IAs are researched as a combination of postnatal changes in the arterial wall against congenital and environmental factors (Stehbens, 1963).

A general observation in cerebral aneurysmal tissue is the fragmentation of the tunica media (Toth et al. (1998), Zhang et al. (2003)) or even the loss of tunica media

(Brisman et al., 2006) with a disruption of the internal elastin lamina (Rajesh et al., 2004). No elastic lamina, sparse medial elastin and lack of supporting perivascular tissue together with structural irregularities are particularly observed in aneurysms at the apex of bifurcations (Finlay et al., 1998). SMCs in some cases migrate to the intima, between the endothelium and the elastic lamina, and proliferate; this event is called myointimal hyperplasia (Frösen et al. (2004), Okamoto et al. (2001), Intengan and Schiffrin (2001)). In the media, SMCs might show different patterns: a normal, organised group of SMCs and ECs, or, their near absence (Rajesh et al. (2004), Frösen et al. (2004)). It is suggested that perhaps the flexible role of SMC as both synthetic and contractile might be related to dysfunction and disease progression (Lacolley et al., 2012).

A significant increase in MMP activity (inflammation) leads to degradation of medial collagen and can lead to continued enlargement (Kassam et al. (2004), Mimata et al. (1997), Bruno et al. (1998), Gaetani et al. (1998)). The collagen turnover rate is an important factor for the temporality of rupture risk of aneurysms (Langille, 1993): newly formed aneurysms might be more likely to rupture, since old collagen might be destroyed without new collagen being yet attached to the arterial ECM (Mitchell and Jakubowski, 2000). The collagen fibres in the adventitia appear mostly intact, but might be stretched (Stehbens, 1963). Due to the disruption of the media and the presence of diffused macrophages and leukocytes in ruptured samples (Katakoa et al., 1999), it is believed that inflammatory and immunological relations are important in the assessment of rupture risk (Takagi et al., 2002) and need to also be genetically investigated (Shi et al., 2009).

An important study on pathobiologies of IAs by Frösen et al. (2004) indicated that identifying the histopathological profile might be key to distinguishing between greater or lesser risk of rupture. Presented in an order of increasing identified risk of rupture, some aneurysms were found with orderly layers of SMCs and intact endothelium; others showed a more disorganised network of SMCs; another category presented decreased SMC numbers, myointimal dysplasia or thrombus, while a final group displayed a thin hypocellular wall with EC apoptosis. It should be noted that the IA pathobiologies mentioned here refer to the stereotypical saccular aneurysm. In fact, IAs are a manifestation of a wide range of diseases (Krings et al., 2011) and there are many other vessel wall pathologies associated with aneurysm disease (dissection, intramural haemorrhage, immunodeficiency, trauma), which

are investigated in parallel, but, due to their distinct biological differences, might require different therapeutic approaches.

1.3 MECHANOBIOLOGY AND HOMEOSTASIS

In common with most biological structures, arteries are self-repairing, adaptive vessels that are at risk of compromise through disease. Damage from ageing, from cellular malfunctions, and from atypical tissue responses to changing mechanical demands, can have severe consequences. However, arteries generally have a remarkable capacity, through genetics and biochemical processes, for growth, repair and continual renewal (Robertson and Watton, 2013), in order to sustain or return to vascular homeostasis, a state of dynamic equilibrium.

Vascular homeostasis requires that cells sense their local chemical environment (pH, oxygenation, growth factors, cytokines, chemokines, hormones and lipoproteins (Aird, 2006)) and mechanical environment and establish, maintain, remodel, or repair the ECM to provide suitable compliance and yet sufficient strength (Humphrey et al., 2015). Naturally, receptors connecting ECM with cells and signalling molecules to transmit information to the nucleus are required in order for processes of homeostasis to take place. Emphasis should be given to the observation that cells are able to sense their immediate mechanical environment. In fact, mechanical forces are regulators of life's form and function, as cells are sensitive to varying magnitudes and time scales and mechanical stimuli can be translated into a chemical response (Kolahi and Mofrad, 2010) affecting cell functionality (proliferation, apoptosis, differentiation, morphology, alignment, migration or synthesis (Kakisis et al., 2004)): this is the process of mechanotransduction. Mechanobiology is therefore the study of the interaction between mechanics and biology.

We refer to growth and remodelling (G&R) as the arterial processes, which chemo-mechanically trigger intramural cell functions that result in the deposition and degradation of tissue components. Figure 1.4 overviews arterial states during which G&R takes place (Humphrey, 2008). G&R occurs both for the normal processes of development, maintenance and ageing and in response to altered conditions due to disease (for example, atherosclerosis and inflammation), injury (for example, wound healing and vasospasm) or environmental adaptations (for example, exercise and vein grafts). Most of these examples are related to changes in arte-

rial loads and therefore imply a corresponding mechanical homeostasis. Exploring the underlying mechanobiology in health and aneurysm disease is key to understanding its aetiology and building on more reliable diagnostic criteria. As haemodynamic and biological triggers disturb the local vascular homeostasis and vascular remodelling attempts to return to the homeostatic conditions (Humphrey, 2009), the inability of the artery to reach a new mechanical homeostatic state might play a role in the progression of aneurysm.

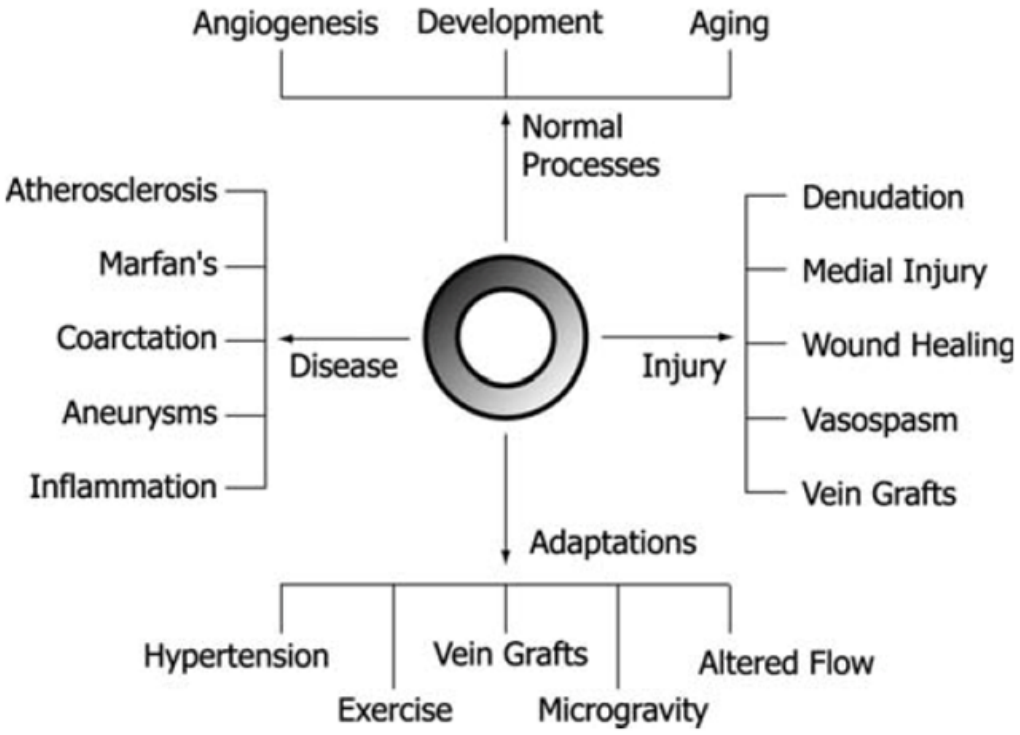

Figure 1.4: Growth and remodelling mechanisms are found in normal arterial processes, as well as in responses to disease, injury and environmental adaptations (adapted from Humphrey (2008)).

The endothelium, being the first layer exposed to haemodynamic forces due to blood flow, dynamically responds to them, thus contributing to vascular physiology and pathophysiology (Nerem, 1993). Wall shear stress (WSS, namely the frictional force per unit area on the inner layer of the arterial wall) and cyclic deformation (due to pulsations over the cardiac cycle) are important mechanical stimuli affecting EC morphology and functionality. In particular, there are interesting indications that different characteristics of the WSS relative to its direction, magnitude and spatial

or temporal variations might have an effect on EC form and function, even though the underlying mechanisms of their sensing capability for such characteristics is not exactly clear. The morphology of the cells is affected by both the direction of WSS and cyclic stretch. Unidirectional WSS results in long, narrow and flat cells (Aird, 2007) elongated in the direction of the flow and perpendicular to the direction of the cyclic stretch, while biaxial cyclic stretch leads to a polygonal shape (Wang et al., 2000): morphology of this kind is present in bifurcations where flow patterns are more complex. Morphology can have an effect on the permeability of the endothelium: this is particularly important as we know that the endothelium controls the transport of substances from the blood flow (Cummins et al., 2007). Disturbed flow might have an inflammatory effect on the arterial wall where the endothelium's changed permeability allows macromolecules (Chiu and Chien, 2011). Changes in molecular homeostasis have been associated with aneurysm disease (Kassam et al., 2004).

Furthermore, endothelial dysfunction associated with aneurysm disease has been linked to increased average WSS (Kyriacou and Humphrey, 1996), large temporal WSS variations (Chatziprodromou et al. (2007a), Chien (2007a)) and combinations of high WSS and high positive spatial WSS gradient (Meng et al., 2007). It is important to note that when we are referring to elevated values, it is in terms of a well-defined homeostatic level. In fact, those homeostatic states might differ for the endothelium at different arterial locations, from subject to subject and from one point in time to another. These homeostatic heterogeneities have been proposed as the combined result of the endothelium's capacity to both retain a memory of previous homeostatic states (argument on nature) and adapt to changing local conditions (argument on nurture) (Aird, 2006). This biological suggestion of homeostatic heterogeneity and adaption is supported, for example, by *in vivo* calculations of WSS in homeostatic conditions (Cebral et al. (2005), Acevedo-Bolton et al. (2006)) that might significantly differ from what might be perceived as a normal physiological WSS range (Kamiya and Togawa, 1980).

Mechanobiological links and homeostatic states have been also identified for other intramural cells and load-bearing arterial constituents. Mechanical homeostasis for SMCs can be described in terms of physiological levels of cyclic stretch (10% with a 25-50% mean strain (Matsumoto and Nagayama, 2012)) when SMCs are in their contractile state. Fibroblasts are able to regulate biochemical signals as a re-

sponse to their mechanical environment (Hanein and Horwitz, 2012) and can transduce mechanical into chemical information and, combining it with growth factor related stimuli, change gene expressions and ECM synthesis (Chiquet et al., 2009). Collagen can be degraded by active collagenases (Bruno et al., 1998) and synthesised by mural cells (Frösen et al., 2006), but may also be derived directly from the circulation (Todor et al., 1998) and it has been suggested that WSS heterogeneities might locally alter collagen production (Rodriguez-Feo et al., 2005).

Combining the aneurysm pathobiology presented in §1.2 and the discussed mechanobiological links from this section, we can study the proposed framework by Frösen et al. (2012), illustrated with Figure 1.5, which aims to summarise the interactions between mechanical, biological (of the artery) and geometrical (morphological) factors for the progression of saccular IA disease by investigating different tissue samples from ruptured and unruptured aneurysms. Local weakening of the artery (internal elastin lamina degeneration) under the persistent action of haemodynamic loads (potentially exarcerbated by hypertension (Inci and Spetzler, 2000)) might result in an initial perturbation of the arterial geometry. Further enlargement is then due to mechano-related G&R (David and Humphrey (2003), Shah and Humphrey (1999), Humphrey (2002)), affected by changes of the flow conditions from homeostatic states. Endothelial dysfunction lies in the centre of aneurysm disease progression. Affected by abnormal shear stresses, a dysfunctional endothelium, combined with high oxidative stress (cumulative damage to cell structures due to the increase of reactive oxygen species, not to be confused with mechanical stress), might allow for macrophage infiltration. In the Frösen et al. (2012) study, both ruptured and unruptured aneurysms were observed: the macrophage infiltration in an unruptured aneurysm would only lead to myointimal hyperplasia and an organising thrombus, but in a subsequently ruptured aneurysm it might lead to an accumulation of cytotoxic and pro-inflammatory substances inside the wall. Resulting mechanical damage and proteolytic activity will, in turn, result in a degenerated matrix and a poorly organised luminal thrombus. Such a mechanobiological process of disease will result in an aneurysm that is very likely to rupture.

This section presents a suggested framework for the disease progression of the specific type of saccular aneurysm, on the basis of histological studies of ruptured and unruptured aneurysm tissue. The framework certainly cannot fully explain all mechanobiological processes involved, a lot of which we have limited biological

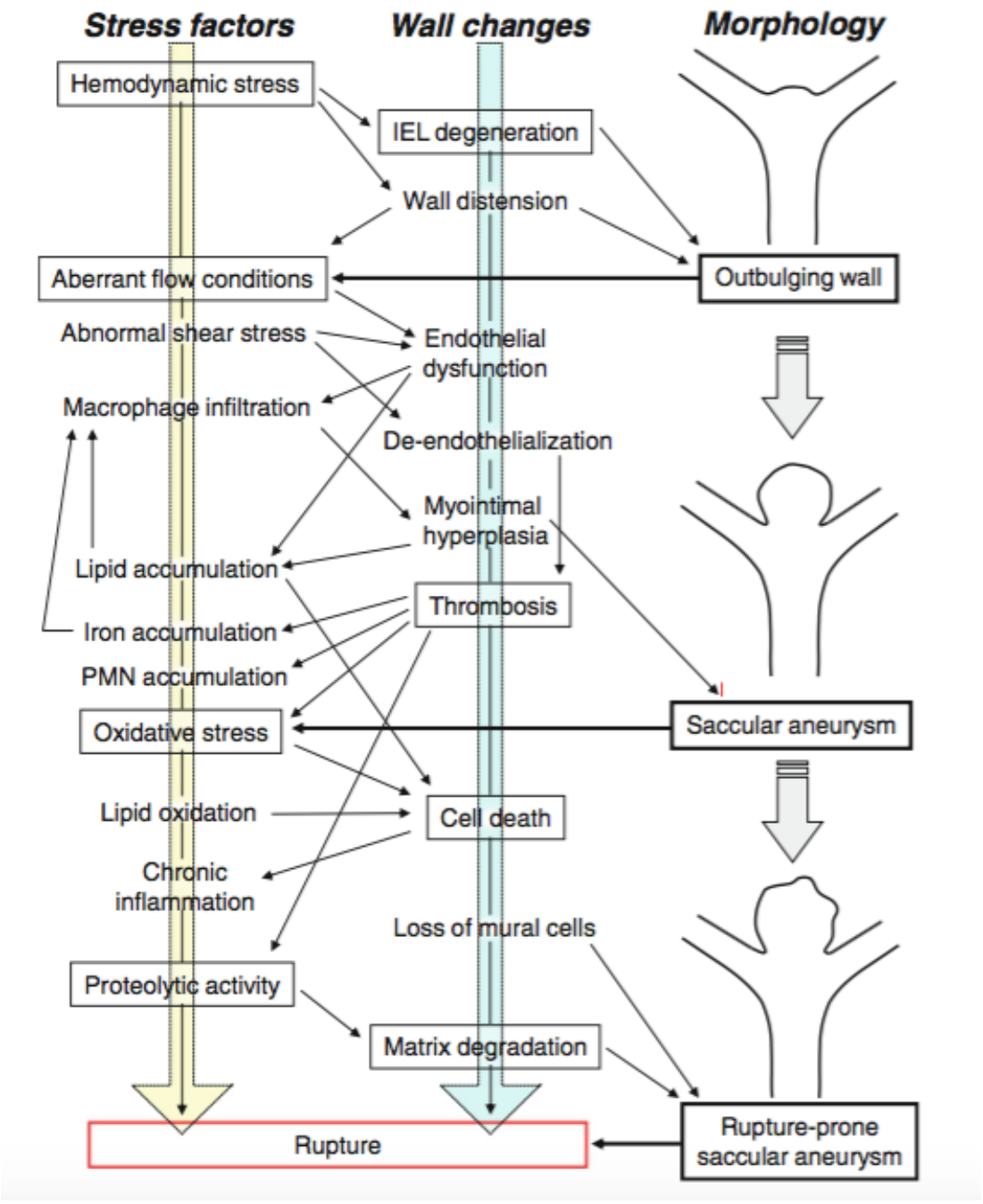

Figure 1.5: Suggested mechanisms of saccular cerebral aneurysm evolution. It is proposed that the interplay among stress factors, biological changes of the arterial wall and an evolving aneurysmal morphology can progressively lead to growth of intracranial aneurysms and potentially result in aneurysm rupture (image adapted from (Frösen et al., 2012)).

knowledge about, or all types of IA evolutions. However, it assists in thinking about disease progression as a process of interrelated mechanobiological events and risk of rupture in terms of disruption of mechanical homeostasis and arterial ability to adapt to new homeostatic states. We can, for example, have a better understanding of the reasons why the position in the cerebral arterial network might be important in the assessment of rupture risk or why maximum biaxial stresses might be related to rupture(Shah et al. (1997), Ma et al. (2004)). We understand that the location of a lesion relative to the inlet flow is crucial for its rupture potential because it influences haemodynamics within the aneurysm and thus the mechanobiological responses associated with them. Investigations in mechanobiology certainly direct criteria for clinical decision-making away from size alone. For example, shape and thickness might be better determinants of potential rupture, since they are more closely related to the mechanics of the arterial wall (Ma et al., 2004). Moreover, morphological features, such as aneurysm to vessel size ratio and the aneurysm angle to incoming flow, are better indicators of potential rupture, since they take into account the interactive effect of biology and mechanics (Dhar et al., 2008).

1.4 *In vivo, in vitro* AND *in silico* MODELLING

Clinical statistical information on aneurysm patient profiles is important in the context of evidence-based medicine for creating a database of risk factors that could be used to identify and offer preventative measures to groups of people susceptible to aneurysm and rupture risk, as outlined in §1.1. However, as it was described in §1.2 and §1.3, aneurysm disease is biologically complicated and made only more intricate by the impact of mechanobiology in the comparisons between health and disease. On account of that complexity, there is an urgent need to revolutionise research with complex new models. Computational, theoretical and experimental modelling are key to achieving this goal. Experimental research is divided into *in vivo* and *in vitro* modelling and computational and theoretical research is called in this thesis *in silico* modelling.

1.4.1 *In vivo* imaging

In vivo acquired vasculature and aneurysm imaging includes computed tomography angiography, magnetic resonance angiography or angiography by direct intra-arterial catheterisation. They are the imaging techniques most often used today for

the depiction of both clinical and animal aneurysms and, with the help from methods of image reconstruction, we are able to recreate 3D aneurysm images of high quality. It is important to note that some of those imaging techniques are minimally invasive and can thus also help increase the frequency of clinical monitoring, while always considering the limitations in frequency when exposure to radiation is required (e.g. with computed tomography angiography). *In vivo* acquired imaging helps us to identify geometrical characteristics important for the description of the aneurysm that are not limited to mere size (Ma et al., 2004), and can also be crucial at guiding interventional methods such as stent deployment with, for example, MR-compatible MRI stents (Buecker et al., 2002). Additionally, *in vivo* calculated blood flow boundary conditions have been made possible with methods such as magnetic resonance and Doppler velocimetry (note that transcranial velocimetry is required for brain aneurysms). These measurements greatly assist in computationally recreating vascular haemodynamics more realistically and thus accurately for specific cases investigated, as well as in creating databases for representative calculations in different types of arteries (Reymond et al., 2011). This thesis utilises *in vivo* acquired images of a patient specific and a rabbit aneurysm case, and *in vivo* calculated blood flow boundary conditions for the same rabbit aneurysm case.

1.4.2 CFD and *in vivo*/*in vitro* models

CFD (computational fluid dynamics) is the branch of *in silico* modelling used widely in aneurysm research for the computational representation of the blood flow environment. An illustration of a CFD simulation can be seen in Figure 1.6: the instantaneous streamlines are depicted to show the flow pattern during peak systole within an arterial geometry with an IA. It is also used for investigating the correlations between flow and aneurysm disease (formation, development and rupture risk). This helps us to understand that geometry can affect flow patterns (Hoi et al., 2004). A range of CFD studies have been implemented with specific *in vivo* medical imaging data (Cebral et al. (2003), Cebral et al. (2005), Cebral et al. (2004), Shojima et al. (2004), Jou et al. (2005), Moore et al. (1999)) and large human aneurysm databases have been used for patient-specific CFD studies into the impact of geometry on flow characteristics (Cebral et al., 2011). These in turn can imply the influence of flow mechanics on mechanobiological paths of disease progression (Chen et al., 2013). Computational fluid studies have investigated the possible links between aneurysm inception and haemodynamic indices such OSI (oscillatory shear index, for the de-

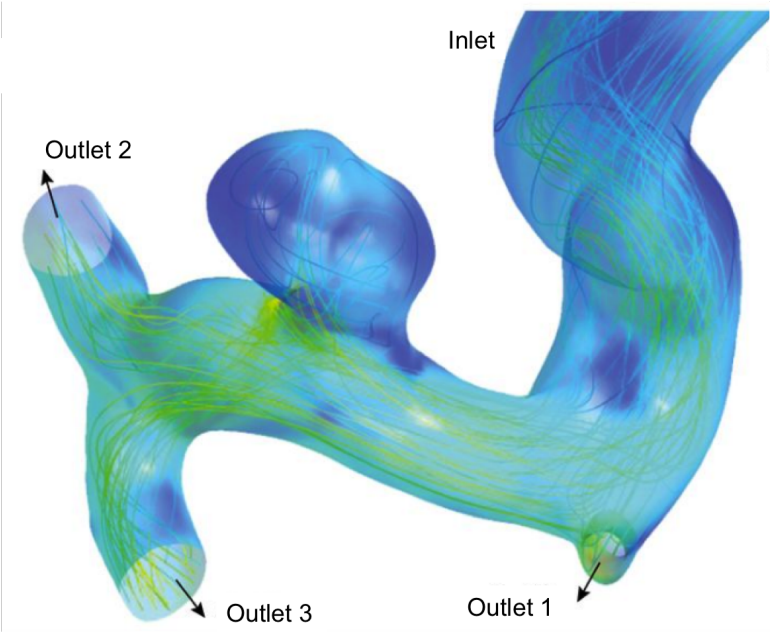

Figure 1.6: Illustrative computational fluid dynamics simulation, depicting the instantaneous streamlines for the flow pattern in an IA arterial geometry during peak systole (image adapted from Poelma et al. (2015)).

scription of pulsatile flow; Hoi et al. (2004)) and GON (gradient oscillatory number; Shimogonya et al. (2012)). Such flow derivatives during the cardiac cycle have been further examined in relation to aneurysm formation, creating specific indices such as aneurysm formation index (AFI) for the purposes of CFD (Mantha et al., 2006). Indicative results are that complex and unstable flows have been related to inception (Cebral et al., 2005), while low WSS has been related to continued enlargement (Acevedo-Bolton et al., 2006). It has also been suggested that real-time 3D image reconstruction and CFD analysis can be a valuable virtual real-time application tool for interventional device placement, guiding preinterventional rehearsals of stent deployment (Spranger and Ventikos, 2014). The limitations of available data, the need for careful consideration of assumptions, and the use of databases for reflections on correlations between flow features and aneurysm growth and their clinical importance have been pointed out (Robertson and Watton (2012), Cebral and Meng (2012)) especially in response to criticism on the use of CFD applications (Kalmes, 2012). With the aim of testing computational methods and consistencies in haemodynamical simulations, international initiatives have been taken for the CFD analysis of stent deployment flow modelling (Radaelli et al., 2008). This thesis utilises CFD analysis for an integrative fluid-solid-growth (FSG) computational

framework of aneurysm evolution and is implemented on both a clinical and an animal aneurysm geometry.

In order for the CFD studies to become more biologically and clinically relevant, the close interaction between CFD studies and *in vitro*/ *in vivo* models, in addition to clinical geometry databases and boundary flow conditions, must be sought. The combination of CFD case specific studies with *in vitro* modelling of corresponding tissue from those cases allows an interactive process of haemodynamics, imaging and histology for the identification of vascular changes in the arterial wall that are related to the *in silico* calculated blood flow mechanics (Meng et al. (2006), Tremmel et al. (2010)). For example, animal aneurysm models have been conducted for the purposes of linking CFD at arterial bifurcations with arterial remodelling at those frequently afflicted areas: such applications have been implemented for a dog aneurysm model (Meng et al., 2007) and for a rabbit one (Metaxa et al., 2010), by carrying out CFD on the *in vivo* acquired animal aneurysm images and executing histological tests on the specific animal aneurysmal tissue. High WSS and high WSS gradient were identified as potentially risky haemodynamic conditions in both cases. This thesis incorporates *in vitro* testing (tissue thickness measurements, mechanical tissue stretching) of a patient's aneurysmal tissue for the parameterisation of the proposed *in silico* models.

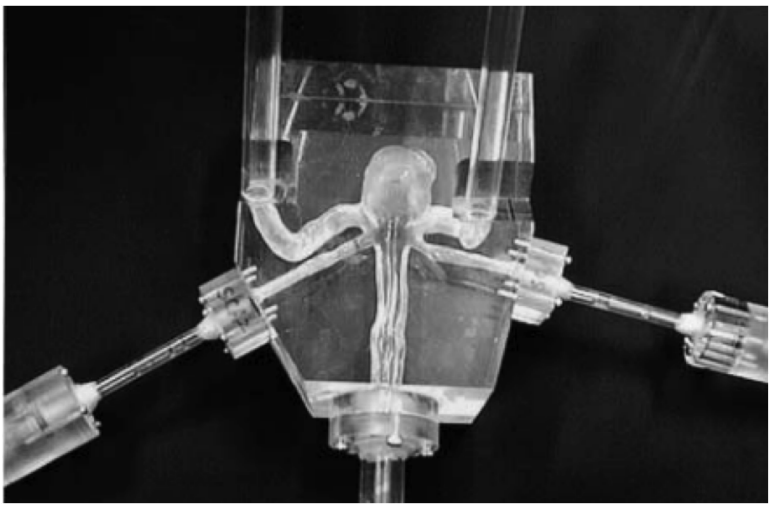

Figure 1.7: Aneurysm model made of clear acrylic plastic for the *in vitro* testing of intra-aneurysmal flow dynamics (image adapted from Tateshima et al. (2001)).

Vascular constructs have often been used to recreate the blood flow environment *in vitro*. Tateshima et al. (2003) built clear acrylic aneurysm models man-

ufactured by 3D computerised tomography angiograms for the analysis of intra aneurysm blood and with laser Doppler velocimetry and particle imaging velocimetry (an example of such construct is illustrated in Figure 1.7) and Tateshima (2002) focused on the calculations of WSS and indications of non-uniform and high intra-aneurysmal WSS correlated with the natural history of cerebral aneurysms. Aneurysm constructs (with ECs lining the *in vitro* model) have been created for the testing of stents (Lieber et al., 1997), with an emphasis on calculating areas of elevated WSS and the probability of thrombus formation. When *in vitro* constructs are used, there is a need to identify any similarities with and differences from real *in vivo* geometries. Benndorf et al. (2010) compared *in vitro* constructs (from computed tomography (CT) imaging) with *ex vivo* canine arteries for the testing of flow modelling after stent deployment. Vascular constructs have also been used as an additional point of comparison with CFD analysis from *in vivo* geometrical data: software phantoms and *in vitro* flow phantoms were used in conjuction with the aid of MRI for the quantification of WSS. This methodology aims to inform and test both *in silico* and *in vitro* techniques. Vascular constructs have even been placed *in vivo* in canine carotid arteries to test the extent of arterial adaptation to changes in WSS (Kamiya and Togawa, 1980).

1.4.3 *In vitro* cell testing

Other *in vitro* models focus on the effect of mechanical forces on single cells, cell cultures and cellularised phantoms for closer investigations into arterial mechanobiology (gene expression, cell and fibre form and function, Qiu et al. (2014), Nerem (1993)). Bovine ECs in flow chambers have been exposed to steady fluid forces as part of an *in vitro* study that investigated the link between endothelium functionality and the combination of low WSS and high WSS gradient (Depaola et al., 1992). A similar study examined bovine EC proliferation in response to sustained high flow (Metaxa et al., 2008). Silicone membranes with human aortic ECs were tested under cyclic stretching to illustrate the effect of reactive oxygen species on fibre remodelling and the reorientation of ECs in response to cyclic deformation (Wang et al., 2000). *In vitro* SMC cultures in biomimetic hydrogels (3D matrix made of collagen to imitate the ECM) have been tested for the links between interstitial flow and SMC function (Wang and Tarbell, 2000). SMC cultures were tested under stress for the examination of differentiation, proliferation and migration (Opitz et al., 2007). Single SMC tests have been carried out to investigate shear stress and

cyclic stretch (Pang et al., 2011) or mechanical stretch and SMC function and proliferation (Cheng et al., 2007).

1.4.4 Animal aneurysm models

A wide range of clinical and animal models used in support of *in vitro* and *in silico* modelling have already been mentioned. As human clinical follow up data is very rare (Boussel et al., 2008), animal aneurysm models can be crucial to our understanding of vascular homeostasis and mechanobiology, and for the biological motivation and validation of our *in silico* models. The experimental methodology often used includes inducing cerebral aneurysms to animals by ligating the common carotid artery, creating experimental (renal) hypertension and treating with lathyrogenics following the intervention. Follow up angiography images were acquired after this procedure in monkeys (Hashimoto et al., 1987), histopathological analysis was carried out for primates (Kim et al. (1989a), Kim et al. (1989b)), histological observations of the internal elastic lamina and the density of SMCs were also performed for rats (Hazama et al., 1986). Hashimoto et al. (1980) focused on the flow modelling around the induced aneurysms in rats for the correlations of haemodynamics with aneurysm occurence around the Circle of Willis in humans. Some of the information collected (geometry, boundary flow conditions) is acquired noninvasively; however, tissue samples often require the sacrifice of the animal. Animal aneurysm tissue samples can provide valuable data on tissue architecture, cell form and function, density of arterial fibres and cells, and the mechanical behaviour of arterial load-bearing constituents (Hill et al., 2012a). The particular advantage of animal aneurysm models is the availability of temporal data, which can help us explore potential mechanisms of aneurysm inception and of disease progression. Naturally, in order for these models to offer transferable information to human aneurysm research, animal aneurysms need to show similarities with human ones, in terms of the arterial geometry, the haemodynamics, and the arterial structure: based on these criteria, primates and rabbits are suitable candidates for aneurysm *in vivo* and *in vitro* research (Zeng et al., 2011). This thesis utilises the aneurysm geometry and boundary flow conditions measured for a rabbit aneurysm model.

1.4.5 *In silico* modelling

A plethora of complex *in vivo* and *in vitro* experimental information has been presented for arterial physiological and pathophysiological mechanobiology, the mechanisms behind which are only finitely understood. In addition, mathematical and computational (*in silico*) representations of the mechanical response of the arterial wall, and its adaption and evolution in architecture and function as a response to the blood flow mechanical environment, are of great significance, especially in order to model aneurysm inception and growth. In the short-term, they can help with a better understanding of the underlying biology and, in the long-term, accurately recreate experimental settings in order to suggest diagnostic tools for the assessment of aneurysm rupture risk.

Relevant mathematical research started with the non-linear elastic analysis that represented the biomechanical instability of tissue (Akkas, 1990). Strain energy functions (SEFs) (such as Fung-exponentials) to illustrate the mechanical behaviour of the arterial wall (a 1D setting presented in Scott et al. (1972)) were implemented, only to be updated by using subdomain inverse finite element code (Seshaiyer et al., 2001) in order to study the local properties of the arterial tissue's anisotropy. Such mathematical analyses were fitted to experimental data that measured local strains and curvature from axisymmetrically inflated biomembranes at various pressures (Hsu et al., 1995). Investigating aneurysm enlargement in terms of static and dynamic instabilities utilised both analytic methods (Fung stress-strain relations, Haslach and Humphrey (2004), Humphrey and Kyriacou (1996)) and numerical methods (Runge-Kutta solutions of nonlinear differential equations of elastodynamics, Shah and Humphrey (1999)) for displaying dynamic stability of spherical lesions. For the more realistic representations of cerebral aneurysm, nonlinear anisotropic stress analysis was required for geometrically and materially accurate finite element models of WSS (Ma et al., 2007) and the concept of remodelling and spatially varying material parameters was proposed so that a physiological biaxial state of stress is recovered in inflated lesions (Ryan and Humphrey, 1999).

Paul Watton developed the first mathematical model of aneurysm evolution (Watton, 2002), introducing micro-structural variables into a realistic tissue model so that the evolving structure and composition of the arterial wall could be simulated. The model has been adapted to consider IA evolution (Watton and Ventikos (2009), Watton et al. (2009b)) extended to link G&R (process of regulation of

the density and orientation of arterial fibres by intramural cells) for the different layers of the vascular wall in response to the local haemodynamic stimuli (Watton et al., 2009a), integrated into physiological geometries with G&R additionally linked to the cyclic stretch stimuli (Watton et al. (2011), Aparício et al. (2014) Selimovic et al. (2014)) and to account for volumetric changes (Eriksson et al., 2014). The research in this thesis further explores the possibilities of mechanobiological modelling within the framework initially developed by Watton et al, while additionally introduces the biomechanical effect of SMC active stress response in 1D models of aneurysm evolution, which has been previously overlooked by previous models. Mathematical algorithms for G&R have been further implemented in several models (referring back to Figure 1.4) for the enlargement of cerebral fusiform aneurysms (Baek et al., 2006), cerebral vasospasm (Baek et al., 2007), arterial adaptations to altered blood flow and pressure (Valentín and Humphrey, 2009b), and theoretical models of aneurysm growth by collagen fibre remodeling ((Kroon and Holzapfel, 2007)). Soft tissue modelling is represented by a constrained mixture theory for various arterial constituents with different and evolving properties, turnover and configurations (Humphrey and Rajagopal, 2002), with adaptation on G&R and representing aneurysm growth (Gleason and Humphrey, 2005).

Fluid-solid interactions combining haemodynamics with arterial wall mechanical properties (Feng et al. (2005), Shimogonya et al. (2009)), and haemodynamics with G&R models of the evolving wall (over the cardiac cycle) (Chatziprodromou et al. (2007b), Figueroa et al. (2009)) have been further investigated. Constitutive behaviours of tissues and cells, and stress analyses of tissues and cells (Fung (1993), Humphrey (2002)) and their temporal evolution as a response to perturbed loads (kinematic growth, Taber (1998), Rachev (2000)) can be found in a number of models. The need for wall distensibility in numerical studies of pulsatile flow, both for increasing model precision and in order to represent deformation related effects on wall biology, is identified as an essential update from the current rigid wall models (Low et al., 1993).

On a molecular level, research has been focused on modelling biologically significant cell signalling pathways that can reveal more quantitative information about the translation of mechanical stimuli to the expression of molecules, crucial to endothelial functions. Plank et al. (2006) has worked on mathematically analysing calcium and nitric oxide pathways in relation to atherosclerosis; Dale

et al. (1996) investigated pathways which describe collagen fibre formation during wound healing. However, similar steps have not been explicitly made towards understanding and describing the pathways that relate mechanical stimuli to endothelial features (such as permeability) and functions (regulation of vascular tone), which can be related to the development of aneurysms. Although computational models can accurately simulate the mechanics of IAs (blood flow patterns, IA deformation due to pulsatile blood pressure), to date they still do not accurately represent IA mechanobiology. This is because clinical and experimental observations have provided limited insights into the arguably complex mechanobiology that occurs at the cellular scale. Consequently, even state-of-the-art computational models of IA evolution are limited in what they can represent, and therefore in what they can predict. This thesis introduces novel mechanobiological links between WSS homeostasis and endothelial heterogeneity, cyclic deformation and collagen growth, and pulsatile flow and elastin degradation, within a mathematical and computational framework in place for IA evolution, which are currently missing from the models and thus aim to bridge this gap in mechanobiological representation.

The multi-physics nature of the problem requires an integrative experimental and computational modelling approach to drive forward understanding. It is necessary for an integrative *in silico-in vitro-in vivo* approach to develop more sophisticated (nonlinear elastic) models of arterial tissue that are constantly updated by quantitative and qualitative observations on aneurysm growth. In turn, *in silico* models of aneurysm evolution can inform and suggest *in vitro* and *in vivo* experiments (Figure 1.8). As a result, both modelling hypotheses and experiments can be constantly updated to advance our understanding of arterial physiological and pathophysiological mechanobiology.

A computational framework with interaction from experiments is expected to have two main effects. The shorter term effect is providing important insight into the biology, mechanobiology and, consequently, aetiology of the disease. The longer term effect is its clinical application as a diagnostic tool. Ultimately, a substantial proportion of aneurysms that currently receive intervention would instead be treated in a non-invasive manner, with follow-up monitoring alone. This would lead to greater comfort for patients, and reduced healthcare costs. Additionally, a small proportion of aneurysms for which intervention is not deemed necessary in current practice would be recommended for immediate treatment, with a resultant

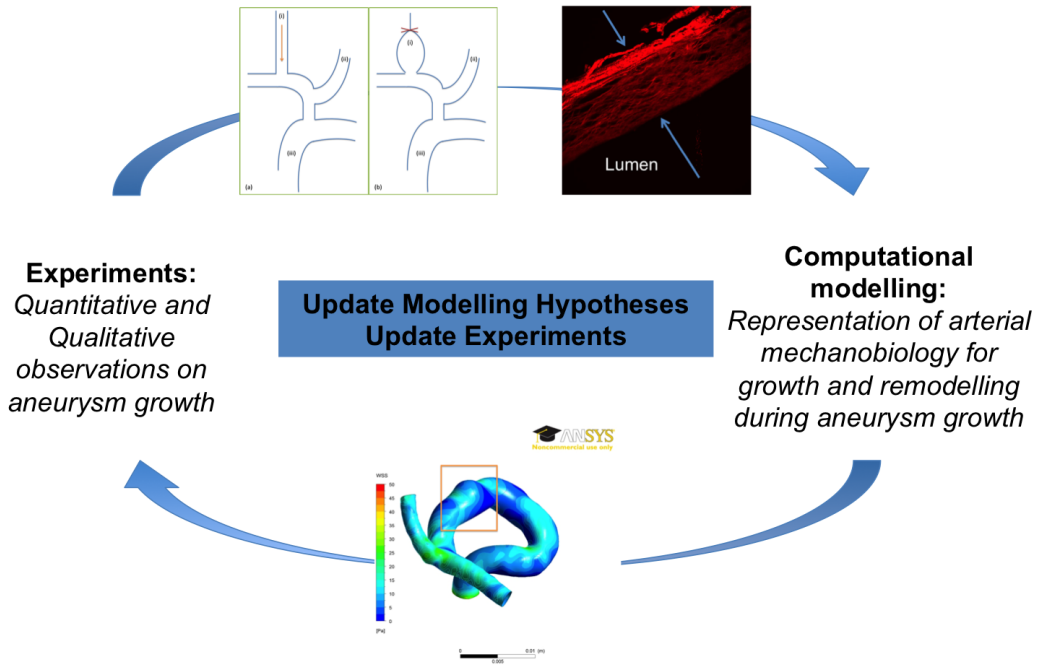

Figure 1.8: Illustration for cycle of modelling framework between *in silico* and *in vivo*/*in vitro* experimental information. Quantitative and qualitative observations on aneurysm growth need to provide valuable insight into the suggested computational representations of arterial mechanobiology for the growth and remodelling algorithms during aneurysm growth. Equivalently, computational modelling results, conclusions and limitations should further inform future experimental studies.

increase in survival rates for those in potentially high risk groups. This thesis creates a novel modelling basis for the interaction between *in vivo*, *in vitro* and *in silico* modelling: the following section outlines the key aims and investigations of the presented research.

1.5 THESIS AIMS AND OVERVIEW

Vascular mechanobiology and mechanical homeostasis for the progression of aneurysm disease are central to the research presented in this thesis. The main aims of this thesis are:

- to identify from experimental evidence important mechanobiological links in

the description of aneurysm disease that are missing from current models of aneurysm evolution, incorporate them for the first time into conceptual and computational models, and test their effect on aneurysm stabilisation: WSS homeostasis and endothelial heterogeneity, cyclic deformation and collagen growth, and pulsatile flow and elastin degradation;

- to incorporate a novel representation of the biomechanical behaviour of smooth muscle cells' active stress response in 1D models of aneurysm evolution;
- to test within the mechanobiologically updated 1D and 3D models of aneurysm evolution the adaptive mechanical role of the adventitia in health and disease;
- to suggest a comprehensive workflow for the effective interaction between *in vivo*, *in vitro* and *in silico* models.

This thesis presents a novel analysis of two experimental datasets, enabling the utility of the developed models and workflow to be evaluated in two different ways:

- clinical data which is utilised as a case study for the application of the proposed interaction workflow, due to the availability of geometrical and tissue information;
- rabbit aneurysm model geometry, used for its controlled experimental environment, in order to apply the vessel reconstruction procedure and investigate a hypothesis of secondary (further) aneurysm enlargement.

Both 1D and 3D conceptual models of aneurysm evolution were implemented in the presented work. Despite its simplified configuration, 1D modelling presents several advantages:

- it provides rapid preliminary understanding of complex biological concepts and their mathematical descriptions;
- detailed sensitivity and parameter analyses are possible to test the suggested hypotheses;

- it is utilised in the mathematical fit of 1D experimental mechanical testing data.

On the other hand, 3D modelling is important because:

- it utilises realistic geometries, which is important for both aneurysm solid mechanics and flow parameters;
- it allows direct comparisons with *in vivo* and *in vitro* data from clinical and animal models;
- it allows us to examine spatial variations, which is not possible in 1D configurations; thus the heterogeneities expected in real vasculature can help us explore further the significance of mechanobiology.

What is crucial in this work is how these two modes of *in silico* modelling interact with each other and, in turn, inform and are informed by the *in silico* and *in vitro* data for parameterisation, calibration and validation of mathematical and computational hypotheses. Chapter 2 presents a new 1D conceptual model of aneurysm evolution that incorporates endothelial heterogeneity, using the basic structural model for the artery (Watton et al. (2004), Holzapfel et al. (2002)), which represents elastin and collagen fibres, their reference configurations and G&R. The 'nature versus nurture' argument for the heterogeneity of the endothelium is illustrated by presenting both temporally adaptive and non-adaptive definitions of mechanical (WSS) homeostasis. The arterial dysfunction is then modelled by linking elastin degradation to the deviations of WSS from homeostatic levels. As a result a novel way of exploring the little-understood connection between mechanics and biology in current conceptual models of aneurysm evolution is suggested. Chapter 2 additionally examines the effect of active SMC activity on the mechanical response of the artery, illustrating its contribution to a 1D two-layer (media, adventitia) aneurysm model. The loss of the medial arterial layer (elastin and collagen fibre degradation, SMC apoptosis) is modelled and therefore the short term effect of active SMC mechanical response and the long term effect of the adventitial collagen fibres as the main load-bearing arterial constituents in an aneurysmal geometry are investigated.

The 1D modelling hypotheses in Chapter 3 are advanced by proposing their inclusion in a framework of interaction between *in vivo*, *in vitro* and *in silico* modelling, presented for a specific clinical aneurysm case study. The 1D model configuration is utilised and updated to include the gradual recruitment of collagen fibres to load bearing, fibre orientation, and a temporally adaptive distribution of homeostatic stretches for the adventitial collagen fibres, the protective sheath to the degrading media. Geometrical (*in vivo* 3D clinical aneurysm geometry with neighbouring vasculature, *ex vivo* aneurysm thickness) and mechanical data (stress-stretch) are used to approximate a material parameter for the adventitial collagen, tailored to the specific study, the dimensions of the initially healthy artery, and a range of loaded thickness with correspondingly estimated ranges of cyclic and homeostatic stretches for the aneurysmal tissue. This information is transferred to the 1D aneurysm evolution model in order to investigate the effect of adventitial collagen homeostatic stretch evolution on G&R in the patient-specific presented case.

The interaction between experimental and mathematical modelling is further explored by introducing 3D computational methods in Chapter 4. The FSG computational framework (Watton et al., 2011) is presented, which links the structural analysis of the equilibrium deformation of the arterial wall with computational fluid dynamics of 3D complex geometries and implemented G&R algorithms, in order to represent aneurysm evolution in 3D. The G&R algorithms follow the updates on the modelling hypotheses as investigated in Chapter 2 and Chapter 3: gradual collagen fibre recruitment, fibre orientation, elastin degradation and flow and temporally adaptive homeostatic stretch distributions for the adventitial collagen. In order for the framework to model aneurysm evolution, a geometry is required to represent the initial healthy state. Chapter 4 overviews a vessel reconstruction methodology, which restores the geometry around the aneurysm in a way that is informed by the neighbouring vasculature, and aims to keep most of it intact. This methodology is applied on the clinical aneurysm case introduced as a case study for the interaction workflow in Chapter 3, and on a rabbit aneurysm geometry, a result of an elastase-induced animal aneurysm model, for the FSG study presented in Chapter 6.

Chapter 5 and Chapter 6 present the results of 3D simulations of aneurysm evolution on the clinical and rabbit aneurysm cases respectively. In Chapter 5, the calibrating measures from the 1D investigations of Chapter 3 (geometrical information for the healthy configuration, adventitial collagen material parameter, final home-

ostatic adventitial stretch distribution) are transferred to the application of the 3D modelling (Chapter 4) for the clinical case. The structural code of the FSG framework is applied in order to study the approximations on the aneurysm remodelled thickness in 3D compared to those in 1D (Chapter 3), while also observing the G&R of the collagen fibres during the phases of aneurysm evolution (media degradation, aneurysm development and geometry stabilisation). Within this modelling context, a link between collagen growth and cyclic stretch is additionally proposed and examined. Furthermore, the fully integrated FSG framework on the clinical case is applied for the representation of endothelial heterogeneity (motivated in Chapter 2) in 3D. The transfer of this hypothesis from a 1D conceptual configuration to a realistic 3D geometry allows not only the investigation for temporal adaption, but also for spatial heterogeneity in mechanical homeostasis and its illustrative link to elastin degradation. These 3D investigations close the cycle of *in silico* modelling as part of the integrative workflow introduced in Chapter 3 and it consequently allows suggestions on directions for future *in vivo* and *in silico* investigations. Chapter 6 similarly applies the FSG framework for the rabbit aneurysm geometry. However, for this particular animal model case, *in vivo* calculated boundary flow conditions over the cardiac cycle are available. Due to the availability of such data, the distribution of a pulsatile flow metric (OSI) is chosen for examination in the reconstructed geometry so that the hypothesis on the possibility of a link between pulsatile flow heterogeneities and an observed secondary aneurysm growth along the prescribed rabbit aneurysmal area is examined. The reconstructed rabbit aneurysm geometry is used with a general primary distortion (to represent the initial weakening of the artery) and implement a preliminary illustrative link between OSI and elastin degradation on a localised area of the rabbit aneurysm geometry in order to observe the evolution of elastin degradation, secondary aneurysm growth and OSI.

Finally, Chapter 7 revisits the main results and points of the research presented in this thesis, while addressing its limitations. The direction and outlook of this research on the continual interaction of theoretical *in silico* modelling with relevant *in vivo* and *in vitro* research conclude this dissertation..

CHAPTER 2

1D MATHEMATICAL INVESTIGATIONS ON THE MECHANOBIOLOGY OF INTRACRANIAL ANEURYSMS

This chapter presents an updated and modified 1D mathematical model to test two mechanobiologically significant concepts in arterial modelling and remodelling hypotheses: (a) endothelial heterogeneity and mechanical homeostasis and (b) smooth muscle cell active mechanical response and apoptosis. Watton et al. (2004) formed the first comprehensive mathematical model for abdominal aortic aneurysm. It was based on formulations on the mechanical response of the individual layers of the arterial wall, each modelled as a fibre-reinforced composite ((Holzapfel et al., 2000), Gasser et al. (2006)), and on the remodelling of collagen tissue at (altered) fixed lengths (Humphrey, 1999). The model from Watton et al. (2004) was updated to then incorporate variables relating to the normalised mass density of the elastinous and collagenous constituents (proportional to the cells that control their production) and the reference configurations in which the collagenous constituents are recruited to load bearing. It was further updated for the modelling of saccular cerebral aneurysm (Watton and Ventikos (2009), Watton et al. (2009b)) and these are the models used as a basis for the conceptual framework presented in this chapter.

2.1 1D CYLINDRICAL MODEL OF CEREBRAL ANEURYSM EVOLUTION - STUDY ON HOMEOSTATIC WSS

The endothelium, being the first layer exposed to haemodynamic forces, dynamically responds to them (Chien, 2007b); thus contributing to vascular physiology and pathophysiology (Nerem, 1993). The evolution of arterial diseases, such as aneurysms, is generally accepted to be closely linked to the mechanical environment of the arterial wall (McGloughlin, 2011). The wall shear stress (WSS) that acts on the endothelial layer is hypothesised to play an influential role on disease progression (Spring et al. (2006), Sheard (2009)); in particular it has been linked to the degradation of the elastin fibres in the medial layer (Frösen et al., 2004). In this chapter I test the hypothesis that deviations of the magnitudes of WSS from homeostatic levels can drive elastin degradation. Previous work assumes that the biological mechanisms responsible for elastin degradation have a hard-wired threshold value for a specific mechanical stimuli (such as wall shear stress, WSS) below which those mechanisms become active or appreciable. Information on this threshold could be contained within the genetic code, known to be conserved during the lifespan of an individual (Snustad and Simmons, 2006). However, endothelial cells (ECs) are in a continual state of turnover, display regional heterogeneity (Regan and Aird, 2012) and therefore the proposed model suggests that they calibrate themselves to the local mechanical environment. This chapter presents models that include temporally non-adaptive and adaptive definitions for WSS, to represent the endothelium's heterogeneity being the result of both nature and nurture, that is, a consequence of both epigenetics and environment. These models radically update and sophisticate the existing 1D aneurysm evolution model. The disturbance of the mechanical equilibrium of the artery (initially modelled as a prescribed degradation of elastin fibres) drives growth and remodelling (G&R) processes that enable the artery to restore homeostasis, or alternatively may influence degenerative processes that lead to disease progression. In my model presented here G&R refers to the process of regulation of the density and reference configuration of the arterial fibres by the intramural cells. This first study investigates the effect of the homeostatic definition on the degradation of elastin, the aneurysm growth and the growth and remodelling evolution of the collagen fibres during aneurysm evolution.

2.1.1 Methodology for conceptual model of cerebral aneurysm evolution

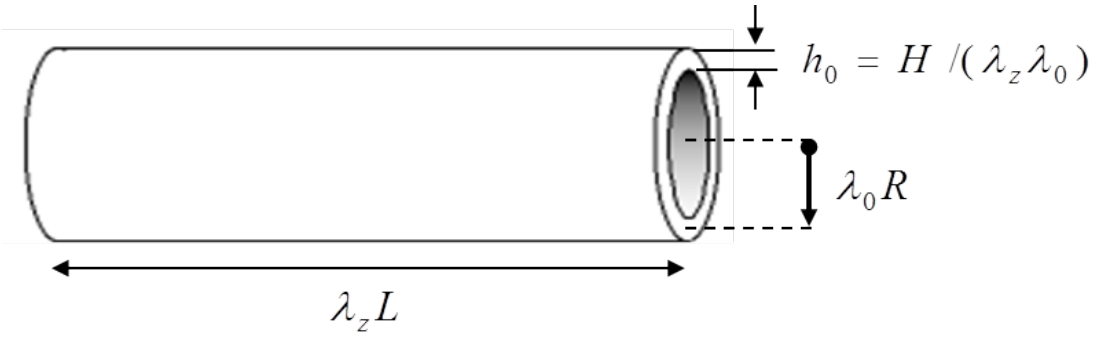

Figure 2.1: Thin cylindrical membrane at loaded configuration at $t = 0$, of loaded radius $\lambda_0 R$, thickness $\frac{H}{\lambda_z\lambda_0}$ and length $\lambda_z L$, representing the artery for a 1D conceptual model of aneurysm evolution.

Following Watton et al. (2011), a conceptual 1D model of aneurysm evolution is employed (Figure 2.1), whereby the artery is represented as a non-linearly elastic cylindrical membrane (radius R and thickness H of the midplane in the unloaded configuration). For the purposes of this preliminary 1D study, the artery is comprised of one layer, consisting of elastin and collagen fibres (this will be updated in §2.2). The cylindrical membrane is subjected to a constant axial stretch λ_z, circumferential stretch λ and a physiological (systolic) pressure p; for the studies in this chapter the systolic arterial configuration will be examined (later chapters will introduce diastole as well) .

The principle of virtual displacements (Watton et al., 2004) governs the steady deformation field for mechanical equilibrium of the cylindrical membrane and the governing force balance in Eqn. (2.1) describes the gross mechanical response of the artery as the result of the additive contributions from each constituent within the arterial wall:

$$p = \frac{H}{R\lambda^2\lambda_z}\left(m_E\hat{\sigma}_E + m_C\hat{\sigma}_C\right), \tag{2.1}$$

where $\hat{\sigma}$ is the azimuthal Cauchy stress of the corresponding arterial constituent; in this setting from elastin $\hat{\sigma}_E$ and collagen $\hat{\sigma}_C$ fibres. m_E and m_C are the normalised densities of elastin and collagen fibres respectively. Normalised density is defined as the ratio of the current density of the fibres to their density at $t = 0$ (Eqn. (2.2)). From the definition we can infer that the values at $t = 0$ are $m_E = m_C = 1$).

$$m_E = \frac{\bar{m}_E(t)}{\bar{m}_E(t=0)} \quad and \quad m_C = \frac{\bar{m}_C(t)}{\bar{m}_C(t=0)} \tag{2.2}$$

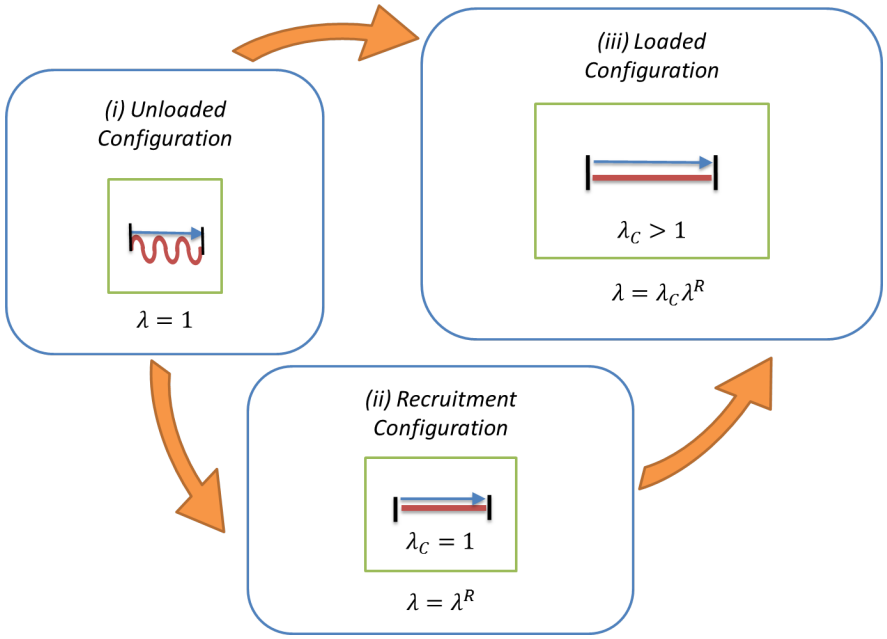

Figure 2.2: Illustration for reference configurations of collagen fibres. (i) At the unloaded configuration, circumferential (elastin) stretch ($\lambda_E = \lambda$) is equal to 1. (ii) At the recruitment configurations (at an elastin stretch named λ^R) of the collagen fibres, the stretch of the fibres λ_C is 1. (iii) At a loaded configuration a mathematical relationship between recruitment, collagen and elastin stetches can be defined.

It is important to make a distinction on the reference configurations of the arterial constituents. Stretches for elastin and collagen fibres are separately defined according to their respective reference configurations. The reference configuration for each arterial constituent relative to the tissue stretch at which they start bearing load is set. Elastin is the constituent that begins to bear load relative to the unloaded configuration (it can be experimentally seen that most elastin fibres are straight, and therefore bearing load, in an unloaded artery (Shadwick, 1999)). Therefore, elastin stretch is mathematically identical to the defined circumferential stretch λ. Figure 2.2 illustrates the reference configuration for collagen fibres. Collagen fibres in an unloaded artery present a crimpled structure and they only begin to be recruited to load bearing at physiological pressures. Collagen fibre stretch λ_C is then defined with respect to their recruitment configurations, namely the stretched configuration at which the onset of the load bearing by the collagen fibres begins; this stretch

is called the recruitment stretch λ^R, which enables a mapping between elastin and collagen stretches:

$$\lambda_C = \frac{\lambda}{\lambda^R} \tag{2.3}$$

Collagen fibres are continually maintained by fibroblast and smooth muscle cells, which deposit them to the extra-cellular matrix (ECM) in a state of stretch (Alberts et al., 2008) and it is hypothesised that this stretch, which will be called attachment stretch λ_C^{AT}, is independent of the current configuration (Humphrey, 1999). This concept has been explored previously (Humphrey and Rajagopal (2002),Eriksson et al. (2009),Watton et al. (2004)), but this framework is used to update it with the introduction of the mechanical homeostasis concept.

Bearing those definitions for reference configurations and the attachment stretch in mind, the Cauchy stresses is determined for the arterial constituents. For elastin fibres:

$$\hat{\sigma}_E = \lambda \frac{\partial \psi_E}{\partial \lambda} = K_E \lambda^2 \left(1 - \frac{1}{\lambda_z^2 \lambda^4}\right), \tag{2.4}$$

where ψ_E is the strain energy stored in the elastin fibres per unit volume; an isotropic neo-Hookean SEF is employed (Holzapfel et al., 2000), defined in terms of the circumferential stretch λ. K_E is a material parameter related to elastin fibres.

Additionally, it is assumed that collagen fibres in the model are circumferentially orientated on the arterial cylinder and they present non-linear behaviour at higher stretches (Shadwick, 1999) and thus a simple non-linear polynomial function is used to describe the collagen stress contribution per unit volume:

$$\hat{\sigma}_C = \lambda_C \frac{\partial \psi_C}{\partial \lambda_C} = K_C \lambda_C^2 \left(\frac{E_C}{E_C^{AT}}\right)^5 \tag{2.5}$$

where E_C, E_C^{AT} are the Green-Lagrangian strains (for collagen and attachment stretches respectively) defined as:

$$E_C = \frac{\lambda_C^2 - 1}{2} \tag{2.6}$$

In order to initiate the representation of aneurysm evolution, the experimental observation that aneurysm growth is linked to the degradation and elimination of elastin fibres within the aneurysmal wall (Frösen et al. (2004),Shimizu et al. (2006)) is used. For the purposes of this study, I want to introduce in addition the effect of arterial WSS on elastin degradation (Hennig et al., 2011), by driving elastin degradation on the basis of deviations of WSS from homeostatic values. In order to simulate this, the degradation of elastin is initially prescribed, by exponentially decreasing the normalised density of the elastin fibres m_E to a value of m_E^{min} during the first $t_{prescribe}$ years of the simulation;

$$m_E(t) = (m_E^{min})^{\frac{t}{t_{prescribe}}}, \quad 0 < t < t_{prescribe} \tag{2.7}$$

As the elastin degrades, it is expected that, in order for the mechanical equilibrium represented by Eqn. (2.1) to be sustained, the circumferential stretch $\lambda(t)$ will temporally increase; the change in the membrane's geometry also changes the WSS τ on the cylinder, which is calculated by (Cheng et al., 2002):

$$\tau(t) = \frac{4Q\mu}{\pi(\lambda(t)R)^3}, \tag{2.8}$$

where Q is the blood flow volumetric flow rate, assumed temporally constant, and μ stands for the viscosity of blood. Following the period $t_{prescribe}$ of prescribed elastin degradation, the change in elastin is linked to deviations of WSS from homeostatic values, defined as:

$$\frac{dm_E}{dt}(t) = \gamma(w(\tau(t) - \tau_{hom_1}) + (1-w)(\tau(t) - \tau_{hom_2})), \tag{2.9}$$

where parameter γ is prescribed to determine the speed of degradation and w is a weighting factor between two definitions for homeostatic levels. The two cases of homeostatic WSS are presented (τ_{hom_1} and τ_{hom_2}), motivated by the biological concept of adaptive versus non-adaptive homeostasis. For the first one τ_{hom_1}, WSS homeostasis equals WSS at $t = 0$, i.e.

$$\tau_{hom_1} = \tau(t = 0) \tag{2.10}$$

The initial WSS represents the mechanical environment of the blood vessel up to the point of the initiation of the elastin degradation; this homeostatic WSS defini-

tion therefore represents the non-adaptive case. For the second definition of τ_{hom_2}, the average of the WSS values over the past period of time T is calculated as the homeostatic WSS:

$$\tau_{hom_2} = \frac{1}{T} \int_{t-T}^{t} \tau(t) dt \tag{2.11}$$

Because the value of τ_{hom_2} changes in time with the evolution of WSS, this definition of WSS homeostasis represents the adaptive case. In order to investigate the occurrence of both events at different extents, the weighting factor w in Eqn. (2.9) can take values between 0 and 1:

- Case 1: $w = 0$ (adaptive)
- Case 2: $w = 0.1$
- Case 3: $w = 0.3$
- Case 4: $w = 0.5$
- Case 5: $w = 1$ (non-adaptive)

Continual deposition and degradation of collagen fibres coupled with new fibres attaching in the state of attachment stretch (Nissen et al., 1978) (independent of the current configuration of the tissue) implies that the natural reference configuration of the collagen should evolve. This evolution of collagen's configuration, in terms of its recruitment stretch, is calculated by:

$$\frac{d\lambda^R}{dt} = \alpha(\frac{\lambda_C - \lambda_C^{AT}}{\lambda_C^{AT}}), \tag{2.12}$$

where α is a rate parameter controlling the speed of reconfiguration and λ_C^{AT} is the attachment stretch for collagen. This describes the reconfiguration of collagen fibres that is aimed to achieve the return of collagen stretches at attachment levels. To compensate for the loss of elastin, the deposition of more collagen fibres (Gupta and Grande-Allen (2006), McAnulty (2007)) is also expected. This is calculated with an evolution equation that is driven by deviations of collagen stretches from attachment values:

$$\frac{dm_C}{dt} = \beta m_C(\frac{\lambda_C - \lambda_C^{AT}}{\lambda_C^{AT}}), \tag{2.13}$$

where β is a rate parameter controlling the speed of collagen growth. These evolution equations of the collagen mass densities (Eqn. (2.13)) and recruitment configurations (Eqn. (2.12)), as a response to the degrading elastin fibres, represent the growth and remodelling (G&R) hypotheses for aneurysm development respectively.

Table 2.1 summarises the modelling variables for this 1D conceptual cylindrical model of aneurysm simulation. The unloaded dimensions, and systolic physiological pressure p are representative for a cerebral artery and have been used in previous models (Hansen et al. (1995), Watton and Hill (2009)). The choice on the constant axial stretch λ_z and initial circumferential stretch $\lambda(0)$ are also driven by relevant literature (Monson et al. (2003), Kroon and Holzapfel (2009)). It is assumed that collagen fibres are in homeostastis at the beginning of the simulation and therefore initial collagen stretch $\lambda_C(0)$ equals λ_C^{AT} and a value of 1.1 is set for the duration of the simulation (further analysis on the attachment stretch in the following chapter). Constant blood flow volumetric flow rate Q and viscosity μ are indicated in the table. The choice of material parameters for elastin and collagen were calculated from the $t = 0$ mechanical equilibrium equation (Eqn. (2.1)) by assuming that the majority of load under physiological conditions is borne by elastin fibres (Armentano et al., 1995); the exact stress contribution might be dependent on various factors, including the health condition of the specific artery (Wuyts et al., 1995). Specifically, it is assumed that the proportion of load by elastin, defined as F_E is borne by elastin fibres and therefore it is expected (based on Eqn. (2.1)) that:

$$F_E \cdot p = \frac{H}{R\lambda(0)^2\lambda_z} m_E(0)\hat{\sigma}_E(0) \tag{2.14}$$

The value of F_E and the resulting material parameters are determined in Table 2.1. For elastin degradation, the initial prescribed degradation is set to take place during the first year of the simulation, exponentially leading to a normalised density of 0.7. Rate parameters for G&R were calibrated for a circumferential increase within the duration of the simulation that will allow the investigation of the change in WSS and the effect of the WSS homeostasis definitions.

For each time increment (equivalent of ten days), the calculations for the updated changes in elastin degradation, collagen recruitment stretch and collagen

Table 2.1: Overview for the geometrical data, physiological data and parameters for the 1D cylindrical conceptual model of aneurysm evolution (study of WSS homeostasis).

Modelling variables for 1D cylindrical model	
Geometry and pressure (Watton and Hill, 2009)	
R	2mm
H	0.4mm
p	16kPa
Stretches (Kroon and Holzapfel, 2009)	
$\lambda(0) = \lambda_E(0)$	1.3
λ_C^{AT}	1.1
λ_z	1.3
$\lambda_C(0) = \lambda_C^{AT}$	1.1
Degradation	
m_E^{min}	0.7
$t_{prescribe}$	1 (years)
Q	$1.9635 \cdot 10^{-5} \frac{m^3}{s}$ (Cheng et al., 2002)
μ	$0.003 Pa \cdot s$ (Cheng et al., 2002)
T	0.5 (years)
Material Parameters	
F_E	0.8
K_E	10.5MPa
K_C	29kPa
Growth and Remodelling	
α	1 $(years^{-1})$
β	1 $(years^{-1})$
γ	0.04 $(years^{-1})$

mass lead to a re-evaluation of the collagen stretch λ_C by numerically solving the force balance equation in Eqn. (2.1) on MATLAB (the *fzero* function is implemented using a combination of bisection, secant, and inverse quadratic interpolation methods). The simulation was run for a period of 30 years. For illustration purposes the case where elastin degradation equals to 0 past the first year of prescribed degradation has been included.

2.1.2 Simulation results

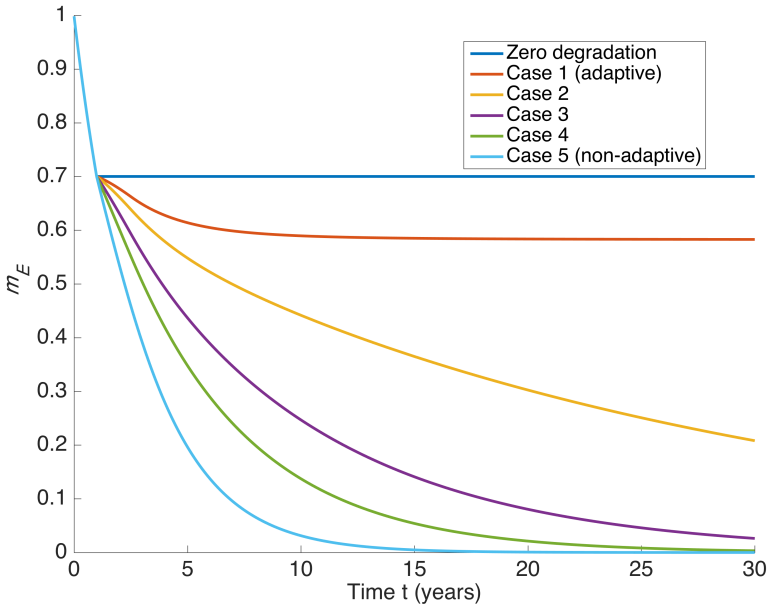

Figure 2.3: Evolution of normalised mass density of elastin fibres (m_E) in a 1D conceptual model of aneurysm evolution (study of WSS homeostasis).

The results of this 1D conceptual study on aneurysm evolution with a focus on WSS homeostasis are, expectedly, identical for the first year of simulations, since the same initial conditions and prescribed elastin degradation were assigned. By the end of the first year, normalised elastin density m_E reduces to 0.7, as presented in Figure 2.3. Following the first year of prescribed elastin degradation, the degradation for each case differs. For Case 1 (adaptive), elastin degradation is the smallest, reducing to a steady value of only 0.6 by the end of the simulations and therefore it is closest to the illustrative threshold of zero further degradation. The fully non-adaptive Case 5 shows the greatest degradation, for which m_E reaches 0, by Year 15. For inbetween Cases 3 and 4 most elastin fibres are lost by the end of the simulation,

and Case 2 has reached a value of around 0.2 for m_E by the end of the simulation; however, it has not reached a steady state value (incremental elastin degradation is non-zero by the end of the simulation).

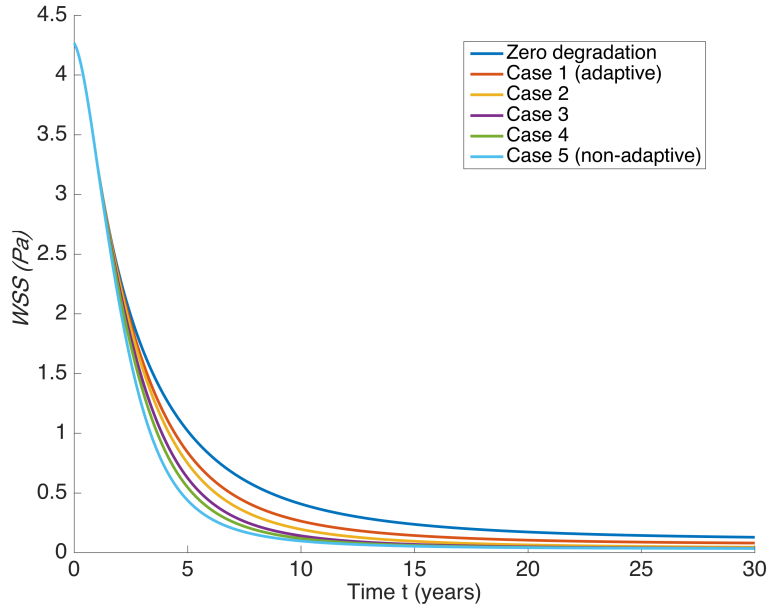

Figure 2.4: Evolution of WSS (τ) in a 1D conceptual model of aneurysm evolution (study of WSS homeostasis).

Figure 2.4 and Figure 2.5 show the evolution of WSS and circumferential stretch λ. As the elastin degrades, increases in λ lead to a decrease in WSS. Past the period of prescribed degradation, the perturbation of WSS from homeostatic values affects the rate of elastin degradation (based on Eqn. (2.9)). It is observed in Figure 2.4 that, for all cases, WSS decreases within a small range of 0.03 Pa for Case 5 to 0.08Pa for Case 1, while λ steadily increases for all cases to a final range of 4.9 for Case 1 to 6.5 for Case 5. It can be noted that even though the case of zero degradation and Case 1 appear to be tending towards a steady value, Cases 2 to 5 appear to be tending towards the same asymptote, representing a group of non-stabilised aneurysms.

Increases in λ result in increases of collagen stretches: Figure 2.6 illustrates the evolution of collagen stretches λ_C. Deviation of the λ_C from its homeostatic value (attachment stretch) leads to the evolution in the reference configuration of collagen fibres, based on the remodelling hypothesis of Eqn. (2.12), which aims to return collagen fibre stretch back to homeostatic levels. It is noted that, as remodelling

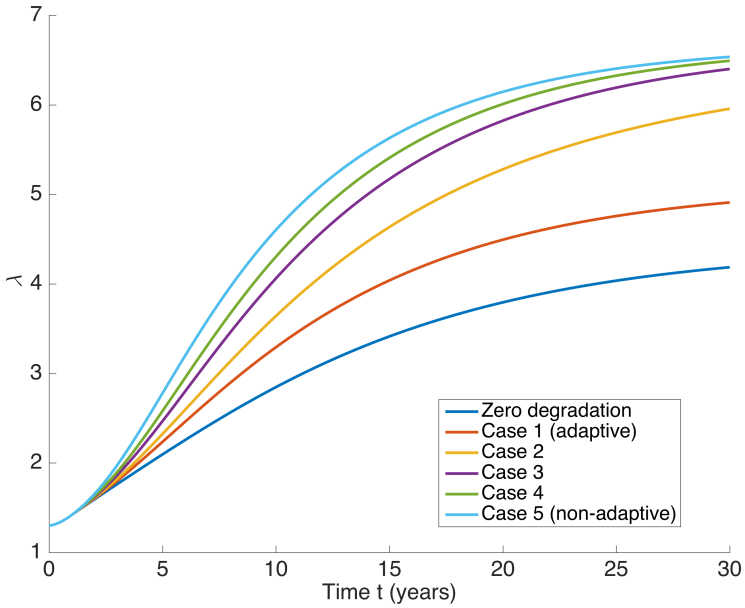

Figure 2.5: Evolution of circumferential stretch (λ) in a 1D conceptual model of aneurysm evolution (study of WSS homeostasis).

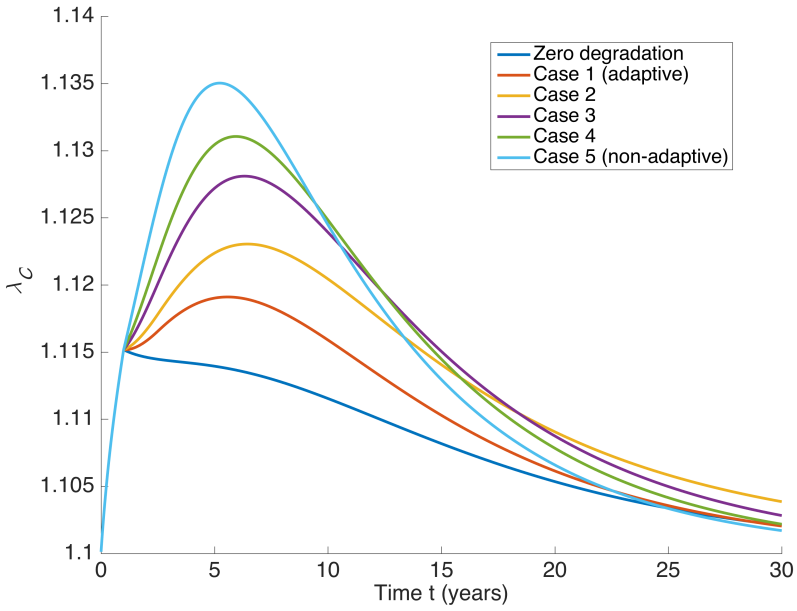

Figure 2.6: Evolution of collagen stretch (λ_C) in a 1D conceptual model of aneurysm evolution (study of WSS homeostasis).

takes place, λ_C for the first 5 to 6 years increases for all cases (within a range of 1.19 for Case 1 to 1.135 for Case 5), but then λ_C gradually decreases returning, for all cases, back towards the attachment value of 1.1.

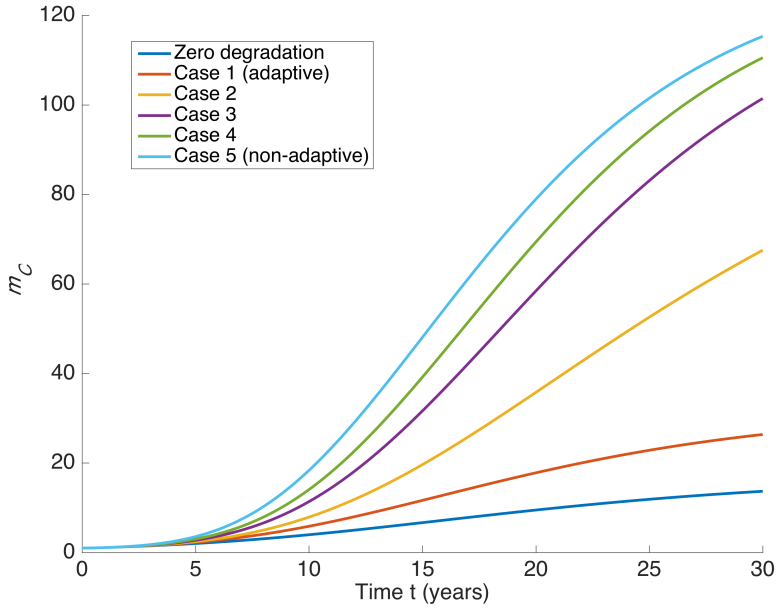

Figure 2.7: Evolution of normalised mass density of collagen fibres (m_C) in a 1D conceptual model of aneurysm evolution (study of WSS homeostasis).

Figure 2.7 also shows the growth in collagen fibre mass densities according to Eqn. (2.13), following the deviations of collagen stretches. There is a steady increase in the mass density of the collagen fibres for all cases. Case 1 reaches a steady final value of 26, while the other cases continue to increase reaching collagen mass densities within a range of 67 (Case 2) to 115 (Case 5) by the end of the simulation.

2.2 1D CYLINDRICAL MODEL OF CEREBRAL ANEURYSM EVOLUTION - STUDY ON SMOOTH MUSCLE CELL FUNCTION

Following the same 1D conceptual framework from §2.1, a novel conceptual 1D two-layer model for aneurysm evolution is also suggested that models the active response of smooth muscle cells (SMCs). SMCs, apart from contributing to the production of important fibres in the medial layer, also exert some of the forces

that balance the blood flow forces on the arterial wall, aiming to maintain vascular homeostasis. While elastin and collagen fibres have been observed to exert passive stresses (represented by current models as proportional to arterial stretches), SMCs are observed to exert active stresses, whereby different levels of smooth muscle tone (activity) are associated with certain ranges of stretches (Rachev and Hayashi, 1999). Those stresses help regulate the arterial diameter and they can change in response to altered arterial wall shear stress (WSS) via signalling from ECs (Hsiai, 2008). Moreover, it is hypothesised that the degradation of elastin, which represents the inception of aneurysm evolution in the models, is also followed by SMC apoptosis (Kondo et al. (1998), Zhang et al. (2003)).

The 1D model for the representation of SMC function presented in this chapter is implemented for two sets of simulations: the first case (case a) validates the expected SMC stress response by setting a step drop in elastin degradation as an initial disturbance to mechanical equilibrium; the second case (case b) investigates how the collagen fibres in the adventitial layer respond to the gradual decomposition of the medial layer (elastin and medial collagen degradation, SMC apoptosis), while examining whether or not the active SMC stress response has in this case an effect on the growth of the 1D aneurysm. Both case simulations were run without (cases a1, b1) and with (cases a2, b2) the active SMC stress response.

2.2.1 Update on methodology

For the purposes of this study, the 1D conceptual cylindrical model is updated to represent the artery as being comprised of two layers: the media and the adventitia. The mechanical equilibrium of Eqn. (2.1) is then updated as:

$$p = \frac{1}{R\lambda^2\lambda_z} \sum_{J=E,C,SMC} \sum_{L=M,A} H_L m_{J_L} \hat{\sigma}_{J_L}(\lambda_{J_L}), \tag{2.15}$$

where the subscript L refers to the arterial layer (either M for the media or A for adventitia) with the corresponding unloaded thickness H_L and SEF ψ_L. The subscript J refers to the arterial constituent; the media is modelled to consist of elastin (E) and collagen fibres (C), as well as smooth muscle cells (SMC), whereas the adventitia is modelled to be embedded with only collagen fibres. The introduction of SMC function in the constitutive model offers an update from the currently presented conceptual models of aneurysm evolution. The SEF for the medial elastin fibres fol-

lows Eqn. (2.4) and the SEFs for the medial and adventitial collagen fibres follow Eqn. (2.5).

Figure 2.1 applies for the reference configurations of the arterial constituents of this simulation set up. Equivalently, as SMCs are also not the main load-bearing constituent at the initial configuration, the same mathematical concept is used for the introduction of stretches by the SMCs and therefore Eqn. (2.3) is generalised as:

$$\lambda_{J_L} = \frac{\lambda}{\lambda^R_{J_L}}, \quad where \quad J = C, SMC \quad L = M, A \tag{2.16}$$

So far the arterial constituents (elastin and collagen fibres) have been modelled to exert passive stresses (stresses proportional to the arterial stretches). However, it has been observed that SMCs also exert active stresses; this implies that different levels of smooth muscle tone (activity) are employed for certain ranges of stretches. In order to represent this in the equilibrium equation, Eqn. (2.17) is adopted from Rachev and Hayashi (1999) and Baek et al. (2007):

$$\hat{\sigma}^{active}_{SMC_M}(\lambda_{SMC_M}) = T(C)\lambda_{SMC_M}(1 - (\frac{\lambda^{max}_{SMC_M} - \lambda_{SMC_M}}{\lambda^{zero}_{SMC_M} - \lambda_{SMC_M}})^2) \tag{2.17}$$

$\lambda^{max}_{SMC_M}$ determines the value of SMC stretch for which SMC active stress contribution is at its greatest, whereas $\lambda^{zero}_{SMC_M}$ defines the upper SMC stretch boundary at which active SMC stress contribution remains. This is illustrated in Figure 2.8. A value for attachment stretch $\lambda^{AT}_{SMC_M}$ is also set for SMCs (as was for collagen fibres) to represent a homeostatic state of stretch; the value is indicated in Figure 2.8, lying between the lower bound for the onset of SMC active force generation and the stretch where maximum active force occurs. The reason behind this is that, as stretch deviates from the initial homeostatic value and increases, SMCs instantaneously attempt to increase their active stress contribution in order to constrict the artery and return it to its initial condition. If the stretch continues to increase and passes the point of maximum force activation, then SMCs become decreasingly capable of responding to further stretch increases (an unstable state). Conversely, a reduction of the stretch from the homeostatic values leads to an instantaneous decrease of the active force generation, aiming to dilate the artery back to its initial state (Ji et al., 2002).

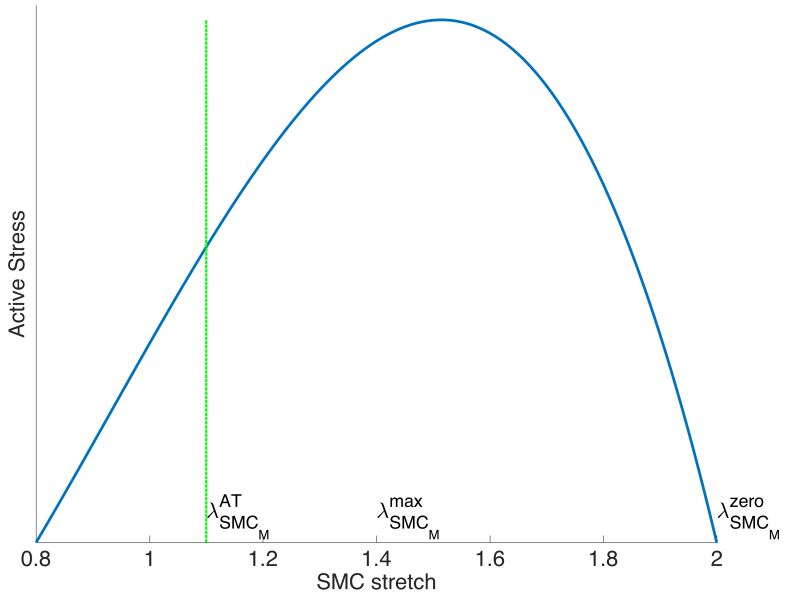

Figure 2.8: Illustration of the varying SMC active tone for a range of defined stretches. $\lambda^{max}_{SMC_M}$ and $\lambda^{zero}_{SMC_M}$ determine where active tone is at maximum and where the active contribution stops respectively. The assumed attachment stretch for SMCs is also indicated in the figure.

The term C in Eqn. (2.17) is defined as the concentration ratio of vasodilators (for example the molecule nitric oxide NO) and vasoconstrictors (for example the protein endothelin ET-1). Dilation or constriction of the SMCs in the blood vessels has been shown to take place as a response to the upregulation of vasodilators or vasoconstrictors respectively. This upregulation has been observed to react to deviations of the magnitudes of wall shear stresses (τ), from homeostatic levels, denoted here as τ_{hom}. More specifically, WSS values higher than homeostatic levels appear to upregulate vasodilator production, while WSS values lower than homeostatic magnitudes upregulate vasoconstrictor production (Malek et al., 1999). Eqn. (2.18) and Eqn. (2.19) describe this behaviour within the term $T(C)$ from Eqn. (2.17):

$$T(C) = K^{active}_{SMC}(1 - e^{-C^2}), \tag{2.18}$$

where:

$$C = \xi(C_B - C_S\frac{\tau - \tau_h}{\tau_h}) \tag{2.19}$$

When the artery is in equilibrium and shear stresses are in homeostasis, there is a basal magnitude for this ratio C_B and C_S is the shear-induced magnitude. Concentration C is then calculated as per Eqn. (2.19); values for C_B and C_S are taken from Rachev and Hayashi (1999) and Baek et al. (2007). ξ is defined as an endothelium damage term, to represent the fact that, since the endothelium is exposed to haemodynamic forces, there is a possibility of its damage from changes in its immediate mechanical environment (Reneman et al., 2006). ξ can take values between 0 (total damage) and 1 (no damage) in order to control the extent of shear-induced vasodilation. As a consequence, the term $T(C)$ represents the level of activation, influenced by the vasodilator ratio and possible endothelium damage; the term K_{SMC}^{active} represents a material parameter for the active response of the SMCs.

There is also an illustrative passive term to the SMC stress contribution for which a neo-Hookean expression (similar to the Cauchy stress for the elastin fibres, Eqn. (2.4)) is set defined with respect to a reference configuration in the direction of the cell. Due to lack of sufficient guidance from the literature, the accompanying material parameter is assumed to be a proportion of the elastin stress response (by setting the parameter K_{SMC}^{active} to a tenth of K_E). Consequently, the total mechanical response of SMCs, counting for both passive and active responses (contributing to the mechanical equilibrium) is:

$$\hat{\sigma}_{SMC_M} = \hat{\sigma}_{SMC_M}^{active} + \hat{\sigma}_{SMC_M}^{passive} \tag{2.20}$$

Remodelling of the collagen fibres for both the media and adventitia, in the case of degradation of medial constituents and a distortion of the geometry (as was presented in §2.1.1), follows the calculation in Eqn. (2.12). A similar behaviour for the remodelling of the reference configuration for SMCs can also be assumed, generalising the evolution equation as:

$$\frac{d\lambda_{J_L}^R}{dt} = \alpha_{J_L}\left(\frac{\lambda_{J_L} - \lambda_{J_L}^{AT}}{\lambda_{J_L}^{AT}}\right),\ where\ J = SMC, C\ and\ L = M, A \tag{2.21}$$

Growth of the density of the medial and adventitial collagen fibres follow Eqn. (2.13), for which the rate parameters β_{C_M} and β_{C_A} respectively will need to be determined.

Regarding the evolution of SMC mass density evolution as elastin degrades, a generalised growth function (adapted by Rachev and Hayashi (1999), Baek et al. (2007)) is adopted:

$$\frac{dm_{SMC_M}}{dt} = m_{SMC_M}(\beta^1_{SMC_M}(\frac{\lambda_{SMC_M} - \lambda^{AT}_{SMC_M}}{\lambda^{AT}_{SMC_M}}) + \beta^2_{SMC_M}(\frac{C - C_B}{C_B}) + \beta^{WSS}_{SMC_M}(\frac{\tau - \tau_{hom}}{\tau_{hom}})) \tag{2.22}$$

The first term, following from the growth function of the collagenous mass densities, illustrates that SMC mass density evolves in order for the stretch to return to attachment levels. The second term relates growth to the deviation of vasoconstrictor ratio from basal values. The third term shows that the SMC density can change also in order to return WSS levels to the homeostatic values. When elastin degrades and load is shifted to the other arterial constituents, a healthy artery's SMCs should increase their active tone to maintain arterial diameter (Fridez et al., 2002). This is the instantaneous response; however, the long-term healthy response is to relax or contract close to the homeostatic state. This will be achieved by SMCs shifting the load bearing to other constituents, while at the same time not disrupting the preferred geometry. A phenomenological way to achieve this is by the third term of the growth function, which aims to return WSS to homeostatic levels. The parameters in this newly introduced growth function (β^{WSS}_{SMC}, β^1_{SMC} and β^2_{SMC}) are set to take non-negative values.

In order to present the effect of the introduced smooth muscle cell function, two illustrative simulation cases are implemented:

- Case (a): SMC Load Bearing
- Case (b): Degeneration of the medial layer

For Case (a), the system is tested by imposing a step drop in elastin mass density to 80% at the beginning of Year 2 of the simulation:

$$m_{E_M}(t) = \begin{cases} 1, & for\ t \leq 2\ years, \\ 0.8, & for\ t > 2 years \end{cases} \tag{2.23}$$

For Case (b), a similar pattern of degradation to the one described §2.1.1 is chosen, informed by the observations on that study, but it is also updated to represent the degeneration of the whole of the medial layer (Kondo et al., 1997). Elastin and medial collagen degradation, as well as SMC apoptosis (Sakaki et al., 1997) are therefore modelled. At the beginning of the simulation, the elastin degradation is prescribed according to Eqn. (2.7); specifically, the elastin is set to degrade to 80% by the end of two years. Following the first period of prescribed degradation, further degradation is set to follow deviations of WSS from homeostatic values:

$$\frac{dm_{E_M}}{dt} = -b_E(1 - e^{\tau - \tau_{hom}}),\ for\ t > 2\ years, \tag{2.24}$$

where the definition of homeostasis follows τ_{hom_2} in Eqn. (2.11), i.e. the adaptive definition, averaging the values of WSS over the past 2 years. To illustrate SMC apoptosis and medial collagen degradation, the evolution of mass densities for SMC and medial collagen fibres is defined as:

$$m_{J_M} = m^1_{J_M} m^2_{J_M}, \quad where \quad J = C, SMC \tag{2.25}$$

where $m^1_{J_M}$ represents the number of cells and fibres for SMCs and collagen, respectively; for Case (b), this is set to exponentially drop to 1% within the first ten years (following Eqn. (2.7)). $m^2_{J_M}$ represents the size of SMCs and collagen fibres and is allowed to adapt, according to the growth function (Eqn. (2.22) and Eqn. (2.13) for SMC and medial collagen respectively).

For both cases the simulations are test run without and with the active SMC mechanical response; they are called Case a1 or b1 and Case a2 or b2 respectively. However, for that reason, a distinction point for both Case (a) and (b) needs to be made when run without the active SMC response. The role of the active stress response of SMCs presented here is that, when there is an increase in stretch that drives SMC stretch away from attachment levels, an instantaneous stress response occurs to initiate reduction in stretches. Further decrease in stretch is then attributed to SMC growth. In the absence of an active SMC stress contribution, the passive SMC stress element is not capable of instantaneously responding to the drop in elastin to the same extent. Therefore the decrease is solely dependent on SMC growth; however, this renders the system unstable. Therefore, for illustration purposes, it was decided to suspend SMC growth for the cases where the active response is excluded, in order

to draw conclusions about the role of introducing the active response to the existing 1D model.

Table 2.2: Overview for the geometrical data, physiological data and parameters for the media degradation in the 1D cylindrical conceptual model of aneurysm evolution (study of SMC function).

Modelling variables for 1D cylindrical model(Part 1)	
Geometry and pressure	
R	2mm
H_M	0.533mm (Holzapfel et al., 2000)
H_A	0.267mm (Holzapfel et al., 2000)
p	16kPa
Stretches	
$\lambda(0)$	1.3
$\lambda^{AT}_{C_M}$	1.1 (Watton and Hill, 2009)
$\lambda^{AT}_{C_A}$	1.05 (Watton and Hill, 2009)
$\lambda^{AT}_{SMC_M}$	1.1
λ_z	1.3
Degradation - Case (b)	
$m^{min}_{E_M}$	0.8
$t_{prescribe}$ (elastin)	2(years)
$m^{min}_{J_M}$	0.01
$t_{prescribe}$ (SMC and medial collagen)	10(years)
T	2(years)
b_E	0.3 ($years^{-1}$)

The parameters for both cases of simulations are summarised in Table 2.2 and Table 2.3. The geometrical, initial stretch and pressure data are consistent with the WSS homeostasis study earlier in the chapter; however, it is assumed that in physiological conditions, the medial layer is approximately $\frac{2}{3}$ of the total thickness (Holzapfel et al., 2000). The attachment stretch for the adventitial collagen is set lower than that of medial collagen (following Watton and Hill (2009)), to represent

Table 2.3: G&R parameters, SMC active stress variables and material parameters for the 1D study of SMC function).

Modelling variables for 1D cylindrical model(Part 2)	
Growth and Remodelling ($years^{-1}$)	
α_{C_M}	1
α_{C_A}	1
α_{SMC_M}	0.2
β_{C_M}	2
β_{C_A}	2
β^1_{SMC}	1
β^2_{SMC}	1
β^{WSS}_{SMC} (for Case (a))	500
β^{WSS}_{SMC} (for Case (b))	10
SMC active stress	
C_B	0.68 (Baek et al., 2007)
C_S	1.36 Baek et al. (2007)
$\lambda^{max}_{SMC_M}$	1.4
$\lambda^{zero}_{SMC_M}$	2
ψ	1
Material parameters	
F_{E_M}	0.6
F_{C_A}	0.1
F_{SMC_M} (with active response)	0.15
T (with active response)	0.12MPa
K_E	0.12MPa
K_{C_A}	0.48kPa
$K^{passive}_{SMC}$	11.8kPa
K^{active}_{SMC}	0.12MPa
K_{C_M} (with active response)	32.6kPa
K_{C_M} (without active response)	58.3kPa

the fact that adventitial collagen fibres are not acting as a major load-bearing constituent in physiological conditions (for further analysis on the attachment stretch, see Chapter 3 and Chapter 5). G&R rate parameters were calibrated, driven by previous work (Watton and Hill, 2009), to ensure resulting stretches within physiological ranges for the time frame of this illustration of aneurysm evolution. It is assumed here that SMC remodelling takes place at a slower speed than that of collagen to introduce a preliminary link to the degrading elastin network and the damaged endothelium, which gradually also damages the normal function of SMCs. For the calculation of the material parameters, the analytic calculations from Eqn. (2.14) are followed, whereby a certain ratio of stress distribution is assumed as the initial condition of the arterial environment. Elastin is the main load-bearing constituent, with SMCs (when the SMC active response is included) and medial collagen fibres having similar load bearing contributions. For the cases where active response is not counted for, the passive contribution of SMCs is a very small portion of the total arterial mechanical response (of around 3%). The calculations for each time increment (representing a period of 2 days) were implemented on MATLAB and the simulation for both cases ran for 20 years.

2.2.2 Simulation results

2.2.2.1 SMC Load Bearing

For both cases (without (a1) and with (a2) the active SMC mechanical response), elastin fibre mass density m_E is prescribed to drop to 0.8 with a step change after two years; following this, m_E is kept constant (Figure 2.9(i)).

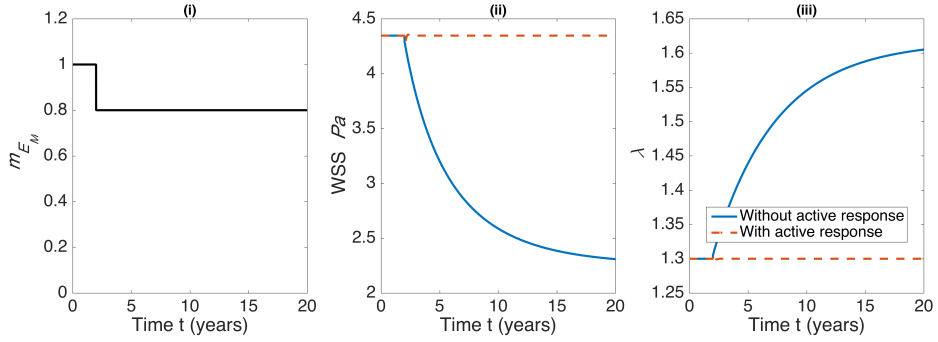

Figure 2.9: Evolution of elastin concentration m_E, WSS τ and circumferential stretch λ in a 1D conceptual model of aneurysm evolution without and with active SMC mechanical response for the study of SMC load bearing .

For case a1, the response follows similar observations to those in §2.1.2. When the elastin density drop takes place, λ starts to increase towards a value of 1.6 by the end of the twenty-year simulation (Figure 2.9(iii)) and consequently (under the constant flow rate assumption) a decrease in WSS is observed to a value of 2.3Pa (Figure 2.9(ii)). Following the elastin drop, it is noted that the immediate increase in the stretches of the constituents (Figure 2.10); for SMC λ_{SMC_M} increases to 1.12 (Figure 2.10(i)), for medial collagen, λ_{C_M} to 1.105 (Figure 2.10(ii)), and for adventitial collagen, λ_{C_A} to 1.054 (Figure 2.10(iii)), representing the shift of load bearing from the lost elastin fibres to the rest of the arterial constituents. The gradual return of the SMC and collagen stretches back to homeostatic levels are noted during the simulation's period, which allows the remodelling of the constituents' reference configurations. In Figure 2.11, the evolution of the normalised densities can be observed, based on the G&R assumptions; there is no SMC growth assumed for the case where only its passive mechanical response is accounted for (Figure 2.11(i)), medial collagen mass density m_{C_M} increases to a value of 1.7 and for adventitia, m_{C_A} increases to 1.8.

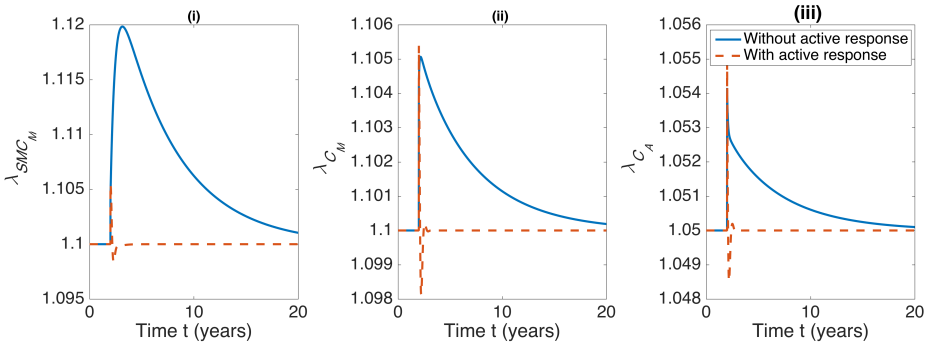

Figure 2.10: Evolution of stretches in a 1D conceptual model of aneurysm evolution without and with active SMC mechanical response for the study of SMC load bearing; (i) SMC stretches λ_{SMC_M}, (ii) medial collagen fibre stretches λ_{C_M} and (iii) adventitial collagen fibre stretches λ_{C_A} .

For case a2 (where the active response is included), the difference in mechanical response to step drop in m_E is noted. There is virtually no change in either WSS (Figure 2.9(ii)) or λ (Figure 2.9(iii)). λ_{SMC_M} (Figure 2.10(i)), λ_{C_M} (Figure 2.10(ii)) and λ_{C_A} (Figure 2.10(iii)), following an instantaneous fluctuation, return within a year to the attachment levels for the rest of the simulation. Based on Eqn. (2.22), the abrupt disturbance in λ_{SMC_M} causes the instantaneous increase in SMC mass density, seen in Figure 2.11(i), reaching a high of 2 and an immediate steady state of 1.8 until the

end of the simulation. On the contrary, neither m_{C_M} nor m_{C_A} show a remarkable change in their values.

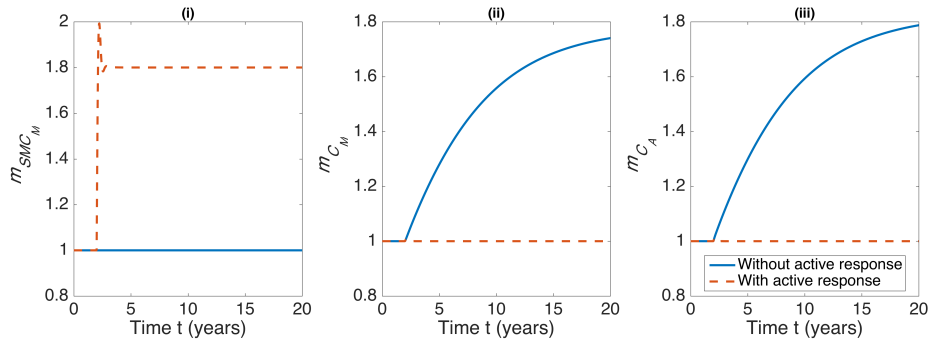

Figure 2.11: Evolution of normalised densities of arterial constituents in a 1D conceptual model of aneurysm evolution without and with active SMC mechanical response for the study of SMC load bearing; (i) SMC, (ii) medial collagen fibre and (iii) adventitial collagen normalised densities (m_{SMC_M}, m_{C_M} and m_{C_A} respectively).

Figure 2.11 illustrates the stress contributions by the active and the passive terms of the SMC stress response for case a2; the total SMC stress response is also indicated in the figure. It can be observed that for the active muscle tone (activity), stress increases instantaneously to a maximum value of 61.6kPa (and subsequently a steady state of 55.9kPa) as a response to the m_E drop and increase in λ, according to Eqn. (2.17). The passive stress contribution is significantly smaller, with a maximum of 16.8kPa and a steady state value of 15.3kPa.

2.2.2.2 Degeneration of the medial layer

For both Case b1 and b2, the simulations are instigated by an initially prescribed elastin degradation for the first two years of the simulation (Figure 2.13). Following this initial period, m_E WSS driven reductions for Case b1 (case without the SMC active stress contribution) lead a value of 0.07 by the end of the simulation, while for Case b2 m_E stabilises to a value of 0.17 by Year 10. For both cases, the degradation of the medial layer constituents is also prescribed, as illustrated in Figure 2.14, exponentially reducing to a value of 0.1 by Year 5; by the end of the simulation, medial SMCs and collagen fibres have virtually disappeared.

Figure 2.15 and Figure 2.16 show the relations for the evolution of WSS and λ respectively; for Case b1, WSS reduces gradually to an eventual value of 0.25Pa and λ increases to 3.5, whereas for Case b2 the steady state values from Year 10 onward

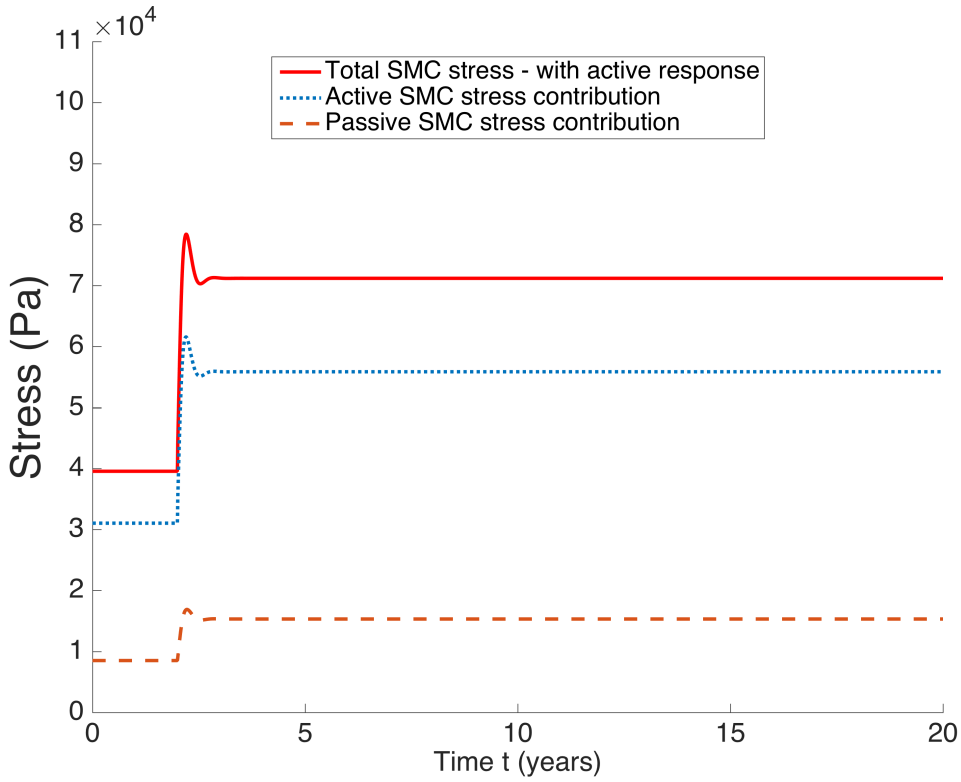

Figure 2.12: Passive and active stress SMC stress contributions and total SMC stress in a 1D conceptual model of aneurysm evolution for the study of SMC load bearing; (i) SMC.

are 1.36Pa for WSS and 1.9 for λ. Degradation of elastin follows the deviations of WSS from the homeostatic values that are averaged over the past two years of the simulation; degradation for Case b2 continues until the new homeostatic state is observed since Year 10.

The disturbance of the mechanical equilibrium, due to the degradation of the arterial constituents in the media, leads to an initial increase of stretches in the arterial constituents. Figure 2.17 shows the evolution of λ_{SMC_M} (Figure 2.17(i)) and λ_{C_M} (Figure 2.17(i)), to summarise the stretch response of the medial constituents prescribed to decrease in density. Case b1 for both stretches show the bell-shape function with maximum values of 1.2 and 1.19 respectively, returning to attachment levels by the end of the simulation. For Case b2 the stretches barely fluctuate around the attachment value and both stabilise to their corresponding attachment values by Year 10.

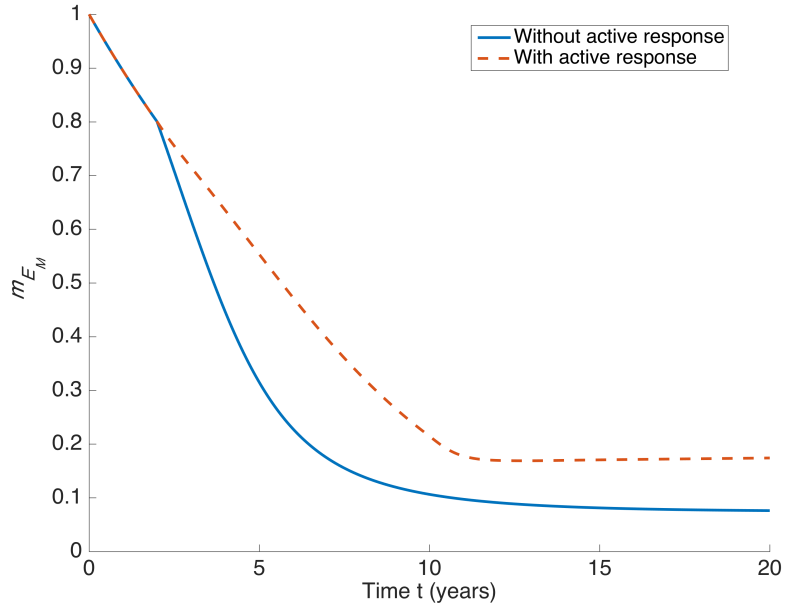

Figure 2.13: Evolution of normalised density of elastin m_E in a 1D conceptual model of aneurysm evolution without and with active SMC mechanical response for the study of the SMC mechanical role during media degradation.

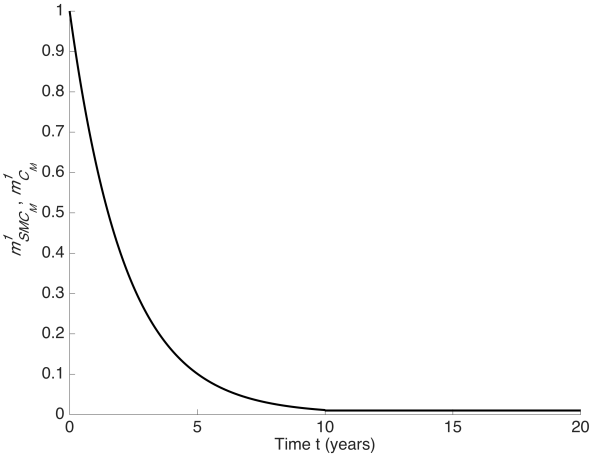

Figure 2.14: Evolution of normalised densities for SMCs $m^1_{SMC_M}$ and medial collagen fibres $m^1_{C_M}$ representing SMC apoptosis and collagen fibre degradation in a 1D conceptual model of aneurysm evolution without and with active SMC mechanical response for the study of the SMC mechanical role during media degradation.

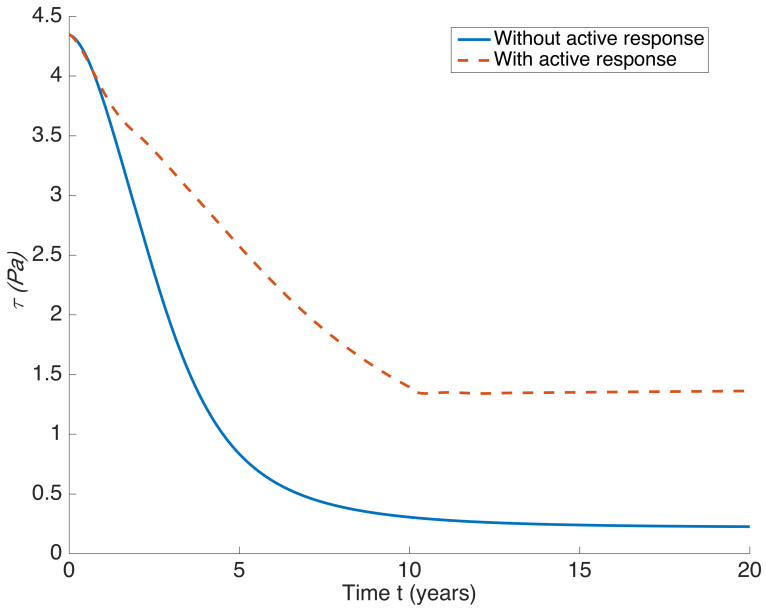

Figure 2.15: Evolution of WSS in a 1D conceptual model of aneurysm evolution without and with active SMC mechanical response for the study of the SMC mechanical role during media degradation.

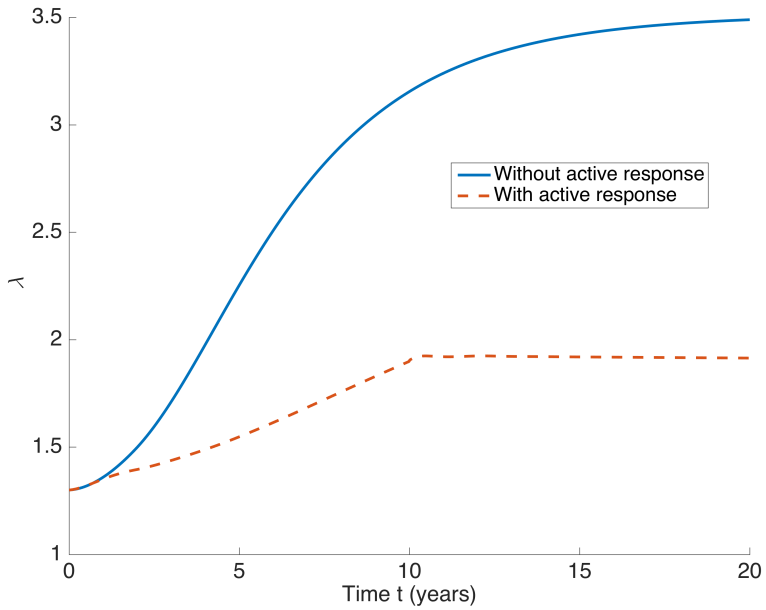

Figure 2.16: Evolution of circumferential stretch λ in a 1D conceptual model of aneurysm evolution without and with active SMC mechanical response for the study of the SMC mechanical role during media degradation.

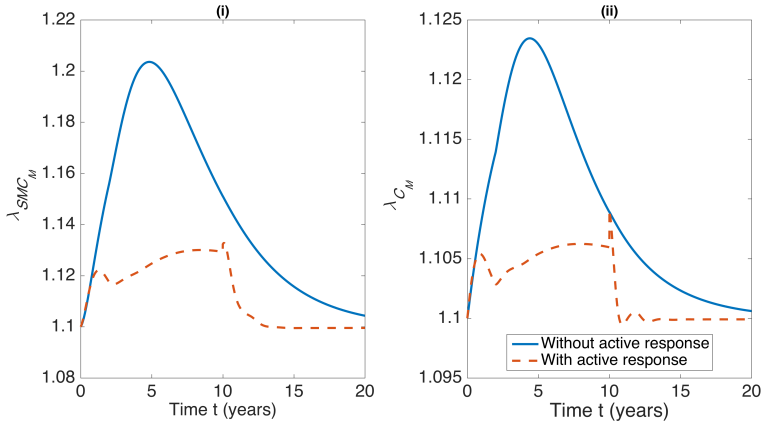

Figure 2.17: Evolution of SMC stretch λ_{SMC_M} (i) and medial collagen stretch λ_{C_M} (ii) in a 1D conceptual model of aneurysm evolution without and with active SMC mechanical response for the study of the SMC mechanical role during media degradation.

By Year 5, because of the decrease in m_E, $m^1_{SMC_M}$ and $m^1_{C_M}$, adventitia becomes essentially the main load bearing constituent of this arterial configuration. Figure 2.18 illustrates the evolution of λ_{C_A}; with a lower defined starting attachment value of 1.05, λ_{C_A} in Case b1 increases to a value of 1.062 and gradually returns to homeostasis, while λ_{C_A} shows a similar behaviour to the one seen for the medial constituents and only show a negligible fluctuation and eventual return to homeostasis by Year 10. Figure 2.19 assists in understanding the evolution of reference configurations for adventitial collagen $\lambda^R_{C_A}$. Based on Eqn. (2.21), $\lambda^R_{C_A}$ increases for both cases; in Case b1 the increase is larger (to a value of 3.3), whereas for Case b2 the fluctuations in Figure 2.18 result in a small increase in $\lambda^R_{C_A}$ to 1.8 by the end of the simulation.

Figure 2.20 also shows the evolution in m_{C_A}; in the absence of the SMC active stress response, Case b1 shows a large increase to 64 at the end of the twenty-year simulation, whereas Case b2 shows a much smaller steady state increase of 3.

2.3 DISCUSSION

Aneurysm evolution modelling is a multiscale problem, in terms of length and time scales, which requires the mathematical description of complex biological relations from a molecular to an organ level in order to investigate the inception, growth and

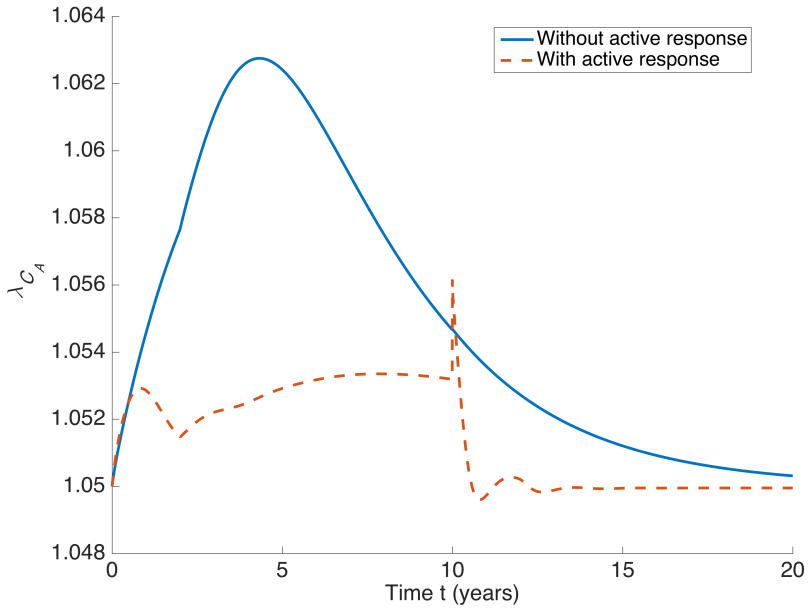

Figure 2.18: Evolution of adventitial collagen fibre stretch λ_{C_A} in a 1D conceptual model of aneurysm evolution without and with active SMC mechanical response for the study of the SMC mechanical role during media degradation.

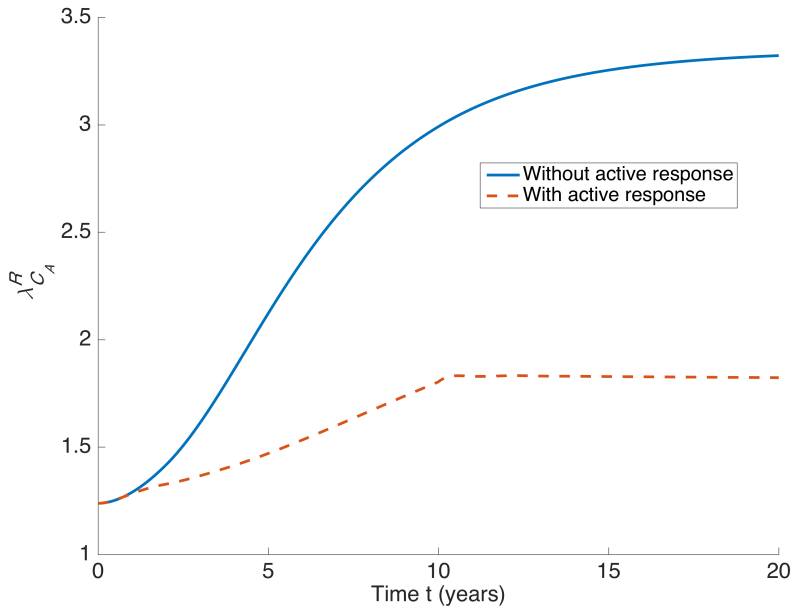

Figure 2.19: Evolution of adventitial collagen fibre recruitment stretch $\lambda^R_{C_A}$ in a 1D conceptual model of aneurysm evolution without and with active SMC mechanical response for the study of the SMC mechanical role during media degradation.

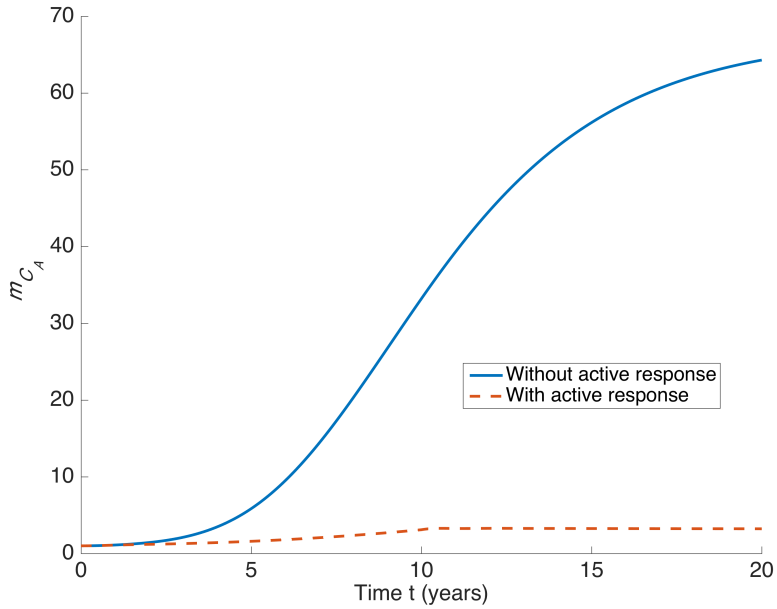

Figure 2.20: Evolution of normalised density of adventitial collagen fibres m_{C_A} in a 1D conceptual model of aneurysm evolution without and with active SMC mechanical response for the study of the SMC mechanical role during media degradation.

potential rupture of aneurysms (Ho et al., 2011). The conceptual 1D mathematical modelling framework for intracranial aneurysms introduced in this chapter allowed the preliminary investigation of two important mechanobiological concepts, not incorporated previously in models of aneurysm evolution.

The first study (§2.1) examined mechanical homeostasis by defining adaptive and non-adaptive definitions for homeostatic WSS. The mathematical investigation was biologically inspired by Regan and Aird (2012), who discussed the mechanisms of endothelial heterogeneity and the combined effects of nurture (temporally adaptive homeostasis) versus nature (temporally non-adaptive homeostasis) of the endothelium. This homeostasis definition was then linked to elastin degradation, as WSS induces changes in the endothelium (Davies, 2009) and the effect of WSS on the expression of elastase, an enzyme that breaks down elastin fibres, has been examined (Hennig et al., 2011). Combining the adaptive and non-adaptive cases with the help from the weighting factor w, the range of effect of the homeostatic definition on the degradation of elastin, the aneurysm growth and the growth and remodelling evolution of the collagen fibres were observed.

For all the presented cases, collagen remodelling manages to return the collagen fibre stretch towards its homeostatic value within the period of 30 years and therefore the circumferential stretch approached a new increased equilibrium. However, for the non-adaptive case, this is a slower process, leading to greater increases in collagen fibre density (more than 100 times the initial values) and in the cylinder's diameter (up to 6 times the initial value). This can be explained by the fact that in the non-adaptive case, there are virtually no elastin fibres left; consequently, the mechanical equilibrium is sustained only by the collagenous constituents. The final dimensions and collagen mass densities observed seem physiologically unrealistic. The role of G&R parameters is important here: the lack of validating data to guide the choice of such parameters is a known problem when modelling complex physiological processes. *In vitro* models of aneurysm evolution would help with phenomenologically calibrating mathematical models: Chapter 3 will introduce a research workflow that would assist in the interaction between experimental and mathematical modelling. Experimental work is further required in understanding the significance of mechanical homeostasis and the physiological mechanisms behind its definition. For the more explicit representation of the endothelium in the models, further work should model the biological mechanisms that link degradation of elastin to the WSS stimuli, for example, with the representation of ECs and associated signalling pathways leading to increased expression of matrix degrading enzymes. It should be noted that the intraluminal thrombus (ILT) that is present in fusiform intracranial aneurysms (Rayz et al., 2010) is not modelled. More specifically, it is assumed that no ILT is present and that the ECs remain functional, so as to continue to transduce a signal to the medial and adventitial layers.

Within the 1D context of the presented model, the heterogeneity of the endothelium was restricted to a temporal scale; however, a variable WSS environment, such as one in a 3D setting, introduces the aspect of spatial heterogeneity to the endothelium, as motivated by Aird (2005). The presented 1D study served as a research basis for the implementation of WSS homeostasis and elastin degradation, presented in Chapter 5 for intracranial aneurysm modelling and, furthermore, in Aparício et al. (2014) for abdominal aortic aneurysm modelling.

The conceptual 1D model of aneurysm evolution was further developed in §2.2 to account for the active response of vascular SMCs. This modelling step was driven by research indicating that vascular smooth muscle cells secrete connective tissue

and matrix degrading enzymes (Asanuma et al., 2003) and are subject to apoptosis during aneurysm evolution (Zhang et al., 2003); there is therefore the need to explicitly model the SMCs with a suitable constitutive model (Zulliger et al. (2004), Murtada et al. (2010)).

The active mechanical role of SMCs (Baek et al., 2007) was introduced, to distinguish it from the passive mechanical response of the elastin and collagen fibres. The purpose of Case a was to examine the evolution of important arterial variables (such as stretches and mass densities of arterial constituents), when SMCs are incorporated, demonstrating its role in two distinct cases, with and without the active SMC stress contribution. The differences in the results between active and no active response illustrate a limitation of previous models of aneurysm evolution to represent this mechanobiological aspect in aneurysm disease. The illustrated results show how the active response leads to a quick increase in the stress contribution following an increase of SMC stretch from homeostatic levels and the active response drives WSS to homeostatic levels over short time scales. An immediate response to disturbance of the haemodynamic environment occurs as a result of the varying SMC tone defined for certain range of stretch values. On the other hand, lack of active response allows the G&R mechanisms of the passive stress contributors to return the artery to the initial homeostatic state, or perhaps, to a new homeostatic state. However, this takes place within a longer time period based on my observations.

In case b, an important event in observed aneurysms was additionally represented, that of the eventual loss of the medial layer's structure. In my observations, the adventitial layer increasingly bears the majority of the load in the artery; the role of the adventitia as the initially protective sheath that becomes the main load-bearing constituent during aneurysm progression will be further investigated in the following chapters. Furthermore, in case b, the observations about mechanical homeostatic conditions from §2.1 were transferred and incorporated a temporally adaptive definition for WSS which drove elastin degradation by deviations of WSS from homeostatic values. The aim of this simulation set was to illustrate how SMCs aim to maintain WSS, while, simultaneously, SMC apoptosis takes place. The SMC active response acts quickly, similarly to case a, and the system does not deviate significantly from the initial condition. On the other hand, in case b1, in order for the system to return stretches to attachment levels, significant, and unrealis-

tic, increases in the mass density of the adventitial collagen were noted. The findings distinguish the short from the long-term mechanical response of the artery to a gradual increase in circumferential stretch with the combined modelling of the active response of SMCs with the SMC apoptosis.

Vascular SMC phenotype is complex and temporally changing (Warrell et al., 2003): SMCs can be found having a contractile or an ECM synthetic phenotype. The flexible switch between the two phenotypes (called phenotypic modulation) plays a significant role in the acquisition of characteristics that could be related to vascular disease (Owens et al., 2004). Additionally, there are different types of SMC contraction taking place within the arterial wall: phasic (rapid) and tonic (slower and sustained) contraction. Effective modelling of the mechanical behaviour of SMC should investigate the importance of phenotypic modulation and the underlying signalling pathways in the progression of vascular disease. Even though these biological mechanisms were not presented in detail here, we have identified the importance of incorporating the role of SMC in our modelling frameworks of aneurysm evolution, by representing the active stress response due to the contractile phenotype of SMCs as arterial stretch increases.

The difficulty in the parameterisation of biological systems were already mentioned. For the newly introduced SMC growth term, the difficulty in determining the extent of effect for a stretch-based, activity-based or WSS-based growth (Eqn. (2.22)) requires a series of experiments to investigate and distinguish those interactions. Controlled *in vitro* aneurysm experiments should also examine further explicit links for the SMC production of collagen and the interactions between the elastin fibre network and SMC production and tone. In order for models of aneurysm evolution to be ultimately utilised as aneurysm prediction tools, there is a need to define and distinguish well between a healthy state and the transition from a healthy state to a potentially diseased one. This encompasses difficulties in fully understanding the arterial biology and incorporating complex biological processes and interactions within the modelling frameworks. For example, the factor ξ, which was introduced by Baek et al. (2007) to represent endothelium damage and affects the effectiveness of the active SMC stress contribution (Eqn. (2.17)), should be more carefully examined and potentially linked to indicators of endothelium damage (such as intra-luminal thrombus formation).

2.4 CONCLUSIONS

In this chapter, we have described and investigated a conceptual mathematical model for the description of aneurysm evolution in a 1D cylinder, representing an artery. Existing models of aneurysm disease were formulated anew and extended in order to incorporate two important relationships between arterial constituents and their effect on aneurysm evolution rates and G&R, driven by biological knowledge and prior experimental work: a) endothelial heterogeneity and WSS homeostasis related to elastin degradation and (b) smooth muscle cell active mechanical response and apoptosis. We observe that a temporally adaptive definition of WSS homeostasis slows down the rate of degradation and can thus have an important effect on aneurysm enlargement rates. Additionally, introducing the effect of SMC active stress response results in significantly different aneurysm growth. Investigating the effect of biologically important events and interactions allows for further understanding about the biology itself and contributes to the creation of a strong modelling framework that can eventually be applied to more realistic models, such as those that use 3D geometries (Chapter 4). An aspect that I have not yet considered in this model formulation, but is the focus of the following chapter, has been the adaptive role of the adventitial collagen as a response to the degrading medial layer. Moreover, the calibration and validation of the models require further investigations into and suggestions on available *in vitro* and *in vivo* work. The following chapter also introduces the examination of a specific clinical case (with accompanying experimental data) that will assist in overcoming certain difficulties identified in this chapter, regarding the calculation of important modelling parameters.

CHAPTER 3

MATHEMATICAL STUDY OF CLINICAL IN VIVO AND VITRO DATA FOR IN SILICO MODELLING

This chapter introduces a methodology for the interaction between *in vivo* and *in vitro* data in *in silico* modelling for a clinical aneurysm case, specifically in order to tailor the material parameter for the adventitial collagen to the patient-specific case and use the knowledge on the geometry and the mechanical properties of the aneurysm for comparison with the simulations of aneurysm evolution, in 1D (in this chapter) and in 3D (in the following chapters). Comparisons between experimental and mathematical/computational data for aneurysms need to aim further than mere comparisons of predicted aneurysm geometries. In order for the theoretical models to incorporate a strong and realistic representation of the arterial mechanobiology of aneurysm disease, it is essential to validate the modelling hypotheses against *in vivo* and *in vitro* observations on the structure and biology of the arterial wall and relate the modelling variables and assumptions to experimental data.

A novel workflow for the parameterisation of the mathematical and computational modelling frameworks is proposed with the aid of available experimental data for a presented patient-specific clinical case. Figure 3.1 summarises the steps and inter-relations of the proposed workflow, which will be implemented in this

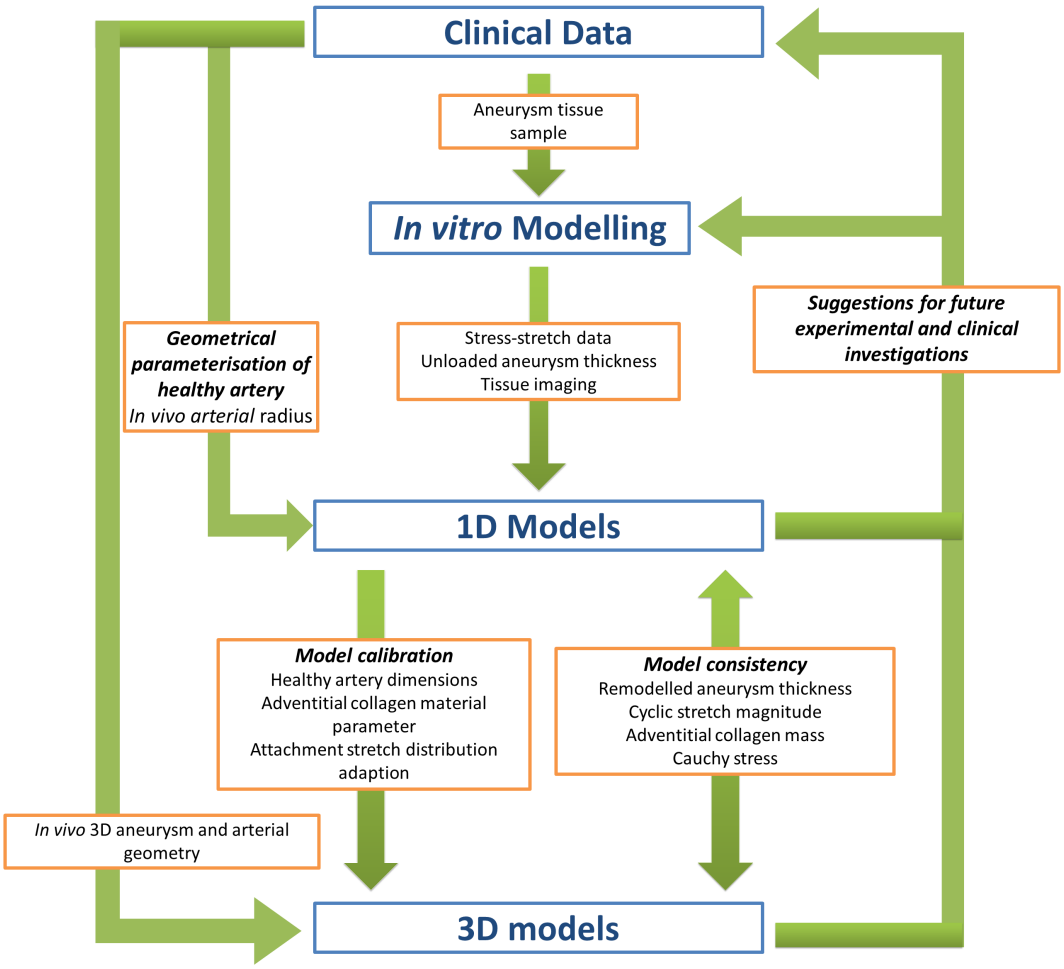

Figure 3.1: Illustration of workflow between *in vivo*, *in vitro* and *in silico* (1D and 3D) modelling. Clinical data from a patient-specific aneurysm case provide geometrical information to the 1D and 3D models. Estimations on the mechanical properties and unloaded thickness of the collagenous aneurysmal tissue are made from tissue samples of the clinical aneurysm. The 1D model analysis results in evaluations of the healthy artery dimensions, the adventitial collagen material parameter and suggestions on the attachment stretch distribution adaption, which help parameterise and calibrate the 3D models. Comparing estimations of remodelled aneurysm thickness, cyclic stretch magnitudes, adventitial collagen increased mass and Cauchy stresses between the 1D and 3D models allows for the consistency in the modelling hypotheses. Furthermore, the modelling analysis and conclusions help towards making suggestions for future experimental and clinical investigations.

and the following two chapters (Chapter 4 and Chapter 5). For this specific clinical aneurysm case, the *in vivo* imaged aneurysmal geometry has been acquired, which will aid in the geometrical parameterisation of the 1D models and will be utilised by the complex 3D models (Chapter 4 and Chapter 5). I have also been provided with an *in vitro* measurement of the aneurysm dome thickness and a representative stress-stretch curve of the aneurysmal tissue. This allows us, within a 1D cylindrical configuration that represents the arterial geometry, to evaluate the healthy artery dimensions, approximate a value for the adventitial collagen material parameter and propose the adaption of the adventitial collagen stretch distribution. These investigations inform and calibrate the complex 3D modelling framework. In turn, by implementing the calibrated and parameterised 3D models of aneurysm evolution, it is possible to compare predictions on remodelled thickness, cyclic stretch magnitude, adventitial collagen increased mass and cauchy stresses with those in the 1D models, allowing for consistency within the modelling analysis. Besides, these modelling steps further allow reflection on the potential of future experimental and clinical investigations that can further inform, calibrate and validate the conceptual and computational models.

The 1D model that was presented in Chapter 2 is extended to include the concepts of gradual recruitment of collagen fibres, fibre orientation, and a temporally adaptive distribution of attachment values. Combining such concepts on the mechanical behaviour of collagen fibres, it is possible to represent the adventitia of the aneurysmal tissue and inform the models of aneurysm evolution for the specific clinical case. The aim of the work presented in this chapter is to use rare combined clinical imaging and mechanical test data of human aneurysmal tissue to estimate material parameters and likely geometrical changes during aneurysm development.

The chapter starts by presenting the geometrical information acquired from the *in vivo* calculated aneurysmal geometry (§3.1). By approximating the aneurysm in a 1D configuration, the expected increase in adventitial collagen is estimated in the new mechanical aneurysmal equilibrium, as well as the dimensions of the healthy artery. The uniaxial mechanical testing data representing the mechanical behaviour of the aneurysmal tissue is fitted to a constitutive mathematical model and the material parameter for the adventitial collagen is therefore approximated (§3.3). Given this set of parameters, a range for the loaded thickness and the cyclic stretch magnitude of the aneurysmal tissue are approximated in a 1D cylindrical set up (§3.4).

The 1D cylindrical aneurysm evolution model (first introduced in Chapter 2) is informed with the adventitial collagen material parameter and indications on the final adventitial collagen attachment stretch distribution. The 1D evolution study looks to investigate the effect of the final adventitial collagen attachment stretch distribution on the G&R hypotheses.

3.1 PRESENTATION OF CLINICAL GEOMETRY

For the purposes of the mathematical investigation in this chapter, the case of a clinical intracranial saccular aneurysm is presented. The geometry of this aneurysm, as seen in Figure 3.2(a), can be described with respect to three key sections in the aneurysmal area: the cylinder (Figure 3.2(i)) along which the aneurysm has been found to have developed and where the *in silico* representation of the aneurysm mechanobiology focuses; the ostium area (Figure 3.2(ii)), representing the initially healthy arterial area from which the aneurysm has grown; and the aneurysm sac area (Figure 3.2(iii)), where the weakened arterial tissue has expanded into the pouch-like shape that is characteristic of intracranial aneurysms. The white arrow in Figure 3.2(a) indicates the direction of the blood flow in the geometry.

The 3D reconstructed image of the clinical intracranial aneurysm has been acquired *in vivo* from digital subtraction angiograms prior to surgical intervention. For further information on how those clinical images are acquired and how they have been utilised in parallel research, see Chapter 4, where the image is prepared to be incorporated in the FSG framework for 3D simulations (Chapter 5).

From an initial observation of the aneurysm geometry, it is possible to calculate changes in surface areas, as presented in Table 3.1; those are measurements in the loaded configuration, since the images were acquired *in vivo*. The aneurysm ostium area represents the arterial surface before the aneurysm growth ($t = 0$). It is assumed that the surface area of the aneurysm cylinder (as indicated in Figure 3.2(i)), not taking into account the ostium or the sac, remains the same between the initial healthy state and the new remodelled stabilised aneurysmal equilibrium ($t = rem$), of which the 3D image exists. These surface areas were calculated in ICEM CFD 4.0.

Two changes in surface area are therefore calculated. The first one is calculated by the following ratio:

$$\frac{sa(sac)}{sa(ostium)} \approx 9.7 \tag{3.1}$$

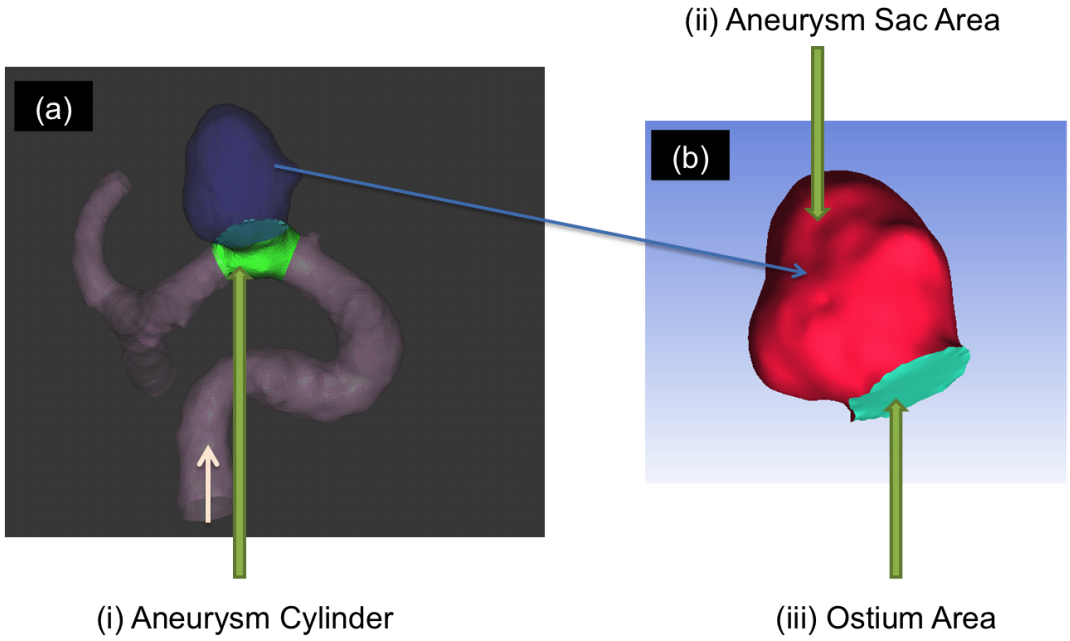

Figure 3.2: (a) *In vivo* image of clinical aneurysm geometry with a detail of the aneurysm cylinder (i); (b) Detail image of the aneurysm sac area (ii) and of the ostium area (iii).

Table 3.1: Calculations of surface areas in the loaded configuration of the clinical aneurysm geometry

Surface areas (in mm^2)		
Aneurysmal segment	Healthy state $t = 0$	Aneurysmal equilibrium $t = rem$
Aneurysm Ostium	22	-
Aneurysm Sac	-	21.4
Aneurysm Cylinder	54	54

where sa stands for surface area (lower case letters are used to indicate the loaded configuration). This ratio helps with the understanding of the Lagrangian deformation of the tissue with which the increase in tissue mass in the 3D growth model is quantified (Chapter 5).

The second change is calculated by the following ratio:

$$\frac{sa(cylinder + ostium)}{sa(cylinder + sac)} \approx 3.5 \tag{3.2}$$

In 1D modelling (as presented in Chapter 2), aneurysm evolution in a cylindrical membrane can be represented, with uniformly increasing radius; equivalently the aneurysm can be modelled as a spherical membrane with increasing radius. The clinical saccular aneurysm evidently has the peculiar geometry of a growing spherical dome on top of a cylindrical artery. For the purposes of the 1D analysis tailored to the clinical case in this chapter, the change in surface area is approximated in Eqn. (3.2) as a developing cylinder or sphere and in the following section a preliminary approximation is made for the expected increase in the adventitial collagen mass density as elastin degrades.

3.1.1 Approximating bounds for increase in collagen density

Following the analysis from Chapter 2 and Watton and Hill (2009), it is reminded that the deformation of a cylindrical membrane (with an unloaded thickness H and radius R) under constant axial stretch λ_z and pressure p, is governed by the following equation of mechanical equilibrium (for the simplicity of this calculation one layer is assumed that includes elastin and collagen and the collagen fibres are circumferentially oriented):

$$p = \frac{H}{R\lambda^2\lambda_z} \cdot (m_E\hat{\sigma}_E + m_C\hat{\sigma}_C) \tag{3.3}$$

where m refers to the normalised mass densities (as were defined in Eqn. (2.2)) and $\hat{\sigma}$ to the azimuthal Cauchy stress of the constituents.

Two distinct time points are then considered; firstly, $t = 0$ when elastin and collagen fibres act to achieve mechanical equilibrium, the constituents are in homeostasis (i.e. collagen stretches are at attachment levels, so $\hat{\sigma}_C^{AT}$), by definition $m_C(0) = 1$ and therefore the proportion of the load borne by the collagen fibres $P_{C:E}(0)$ is:

$$P_{C:E}(0) = \frac{H}{PR\lambda_0^2\lambda_z} \cdot \hat{\sigma}_C^{AT} \tag{3.4}$$

The second distinct time point is $t = rem$, where the elastin is gone and only collagen fibres remain to reach mechanical equilibrium. In this new remodelled

aneurysmal equilibrium, it is assumed that collagen stretches are at attachment levels again and the SEF of the collagen fibres have remained constant. It is therefore expected that $P_{C:E}(rem) = 1$ and:

$$p = \frac{H}{PR\lambda_{rem}^2\lambda_z} \cdot \left(m_{C_{rem}}\hat{\sigma}_C^{AT}\right) \tag{3.5}$$

Under those specific assumptions, an increase in the normalised mass density of the collagen fibres should be expected to be:

$$m_{C_{rem}} = (\frac{\lambda}{\lambda_0})^2 \tag{3.6}$$

Following the same process for the deformation of a spherical membrane, where the mechanical equilibrium is governed by:

$$p = \frac{2H}{R\lambda^3\lambda_z} \cdot (m_E\hat{\sigma}_E + m_C\hat{\sigma}_C) \tag{3.7}$$

It can be concluded that in the new collagenous load-bearing configuration an increase in the normalised mass density of collagen fibres is expected to be:

$$m_{C_{rem}} = (\frac{\lambda}{\lambda_0})^3 \tag{3.8}$$

The increase in stretch for the two cases can then be approximated by using the result of the increase in surface area (Eqn. (3.2)). Geometrically, for the cylindrical membrane, $\frac{\lambda}{\lambda_0} = 3.5$ and for the spherical membrane, $\frac{\lambda}{\lambda_0} = \sqrt{3.5}$. Consequently, for the two cases an increase in normalised collagen mass density is expected to be:

$$m_{C_{cylinder}} = 12.25, \qquad m_{C_{sphere}} \approx 6.55 \tag{3.9}$$

Even though this is a simplified case, it does help with the further understanding about the transition of the diseased artery to the new load-bearing configuration as the elastin degrades, for a complex aneurysmal geometry (a growing spherical dome on top of a cylindrical artery). In the following sections of this chapter, the 1D cylindrical model will be updated to describe the aneurysm evolution for the

clinical case and those updated calculations of collagen mass density increase can be discussed in relation to the ones presented here.

3.1.2 Thickness and Radius at $t = 0$ configuration

It is important at this stage to make a clear distinction about the unloaded and loaded 1D configurations at $t = 0$, for both cylindrical and spherical membranes. The notation is such that capital letters are used to represent the unloaded configuration and lower case letters the loaded configuration. This distinction becomes important for the modelling with relation to the available *in vivo* and *in vitro* data.

By assuming incompressibility of the tissue, the loaded thickness-to-radius ratio at $t = 0$ for a 1D cylindrical membrane is:

$$\frac{h_0}{r_0} = \frac{H_0}{R_0 \lambda_0^2 \lambda_z} \tag{3.10}$$

Equivalently the ratio for a spherical 1D membrane is:

$$\frac{h_0}{r_0} = \frac{H_0}{R_0 \lambda_0^3} \tag{3.11}$$

It is assumed, from the literature, that a healthy cerebral vessel has an unloaded thickness-to-radius ratio of around $\frac{1}{5}$ (Monson et al., 2005); axial stretch of 1.3 (Monson et al., 2003); and initial circumferential stretch of 1.3 (Kroon and Holzapfel, 2007). By definition, $\lambda_0 = \frac{r_0}{R(0)}$. A value for the loaded radius is estimated to be $r_0 \approx 2$mm, by averaging radii of the adjacent healthy parent vasculature on the *in vivo* clinical geometry. The calculation used coordinate files from cross-sections of the artery extracted from @neufuse, read by tecplot and averaged with MATLAB.

Consequently, the table summarises the resulting estimations for the loaded and unloaded thickness and radius of the 1D configuration; because the axial stretch and initial circumferential stretch are equal, the results are mathematically the same for the cylindrical and spherical case. These values will be useful in the 1D *in silico* modelling to follow.

Table 3.2: Loaded and unloaded thickness and radius for the 1D configuration of the clinical geometry at $t = 0$

Clinical geometry at $t = 0$		
Variable	Unloaded Configuration	Loaded Configuration
Thickness (in mm)	0.308	0.182
Radius (in mm)	1.5	2

3.2 MICROSCOPY AND MECHANICAL TESTING OF *ex-vivo* TISSUE FOR CLINICAL CASE

Apart from the acquired aneurysmal geometry (reconstructed from rotational angiography scans conducted at the Allegheny General Hospital, Pittsburgh, US), this clinical case, provided by the University of Pittsburgh Prof. Anne Robertson's research laboratory, was used to analyse the changes in the mechanobiology and the mechanical properties of the aneurysmal tissue with the aid of MPM. A cross-sectional MPM image from a tissue sample of the aneurysmal area (also acquired following surgical intervention at the US hospital) is seen in Figure 3.3. What can be observed is that the medial layer (which is the defining load-bearing layer in healthy arterial tissue) has virtually collapsed and the image illustrates the adventitial layer, where collagen fibres would then be expected to bear the majority of load of the growing aneurysm; this observation has been made before (Stehbens (1963), Gasparotti and Liserre (2005), Meng et al. (2011)). From this specific sample a cross-sectional *ex vivo* measurement of the arterial wall thickness took place, indicating an unloaded thickness seen in Table 3.3. This is an important measurement that will be used as a mathematical variable in the following 1D analysis and as a reference point in the results from the 3D FSG simulations. The combination of clinical imaging data and testing for the geometrical and mechanical properties of the aneurysmal tissue for a clinical case is unusual and rare in aneurysm modelling research and should therefore be fully utilised and closely investigated.

Results from the uniaxial mechanical testing of a tissue sample representing the aneurysmal area, i.e. essentially collagenous tissue, are seen in Figure 3.4. This sample was mechanically tested to failure and MPM images at various stretches were

Table 3.3: Values of experimentally calculated *ex vivo* thickness of aneurysmal tissue sample from clinical case.

Unloaded Aneurysmal Thickness
$H = 0.16$mm

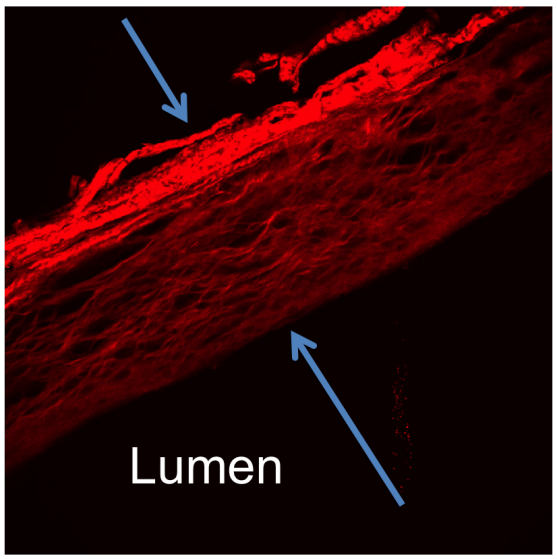

Figure 3.3: *Ex vivo* image of cut section of aneurysmal tissue from the clinical case, acquired with Multi-Photon-Microscopy. The media has essentially collapsed and the image shows the remaining adventitial layer, for which the unloaded thickness has been experimentally calculated.

captured. Observing the MPM images, where collagen fibres are indicated by red fluorescence, it is noted that there is a mix of straight and undulated collagen fibres at lower stretches and, at higher stretches, there is an increase in straight fibres oriented closer towards the axial direction. This illustrates the gradual recruitment of collagen fibres to load bearing, an observation which is known in prior experimental research (Schrauwen et al., 2012), where the quantification of collagen fibre waviness at increasing pressures showed the gradual straightening of fibres. This concept will be considered in the proposed mathematical descriptions in §3.3.

It is also interesting to mention that the stress-stretch curve shows a linear 'toe region' at small axial stretches of $\lambda_{axial} < 1.1$. The reasons for this initially linear mechanical response of the tissue are not fully clear. Elastin fibres, which are responsible for the linear mechanical response at low stretches of mixed elastinous-

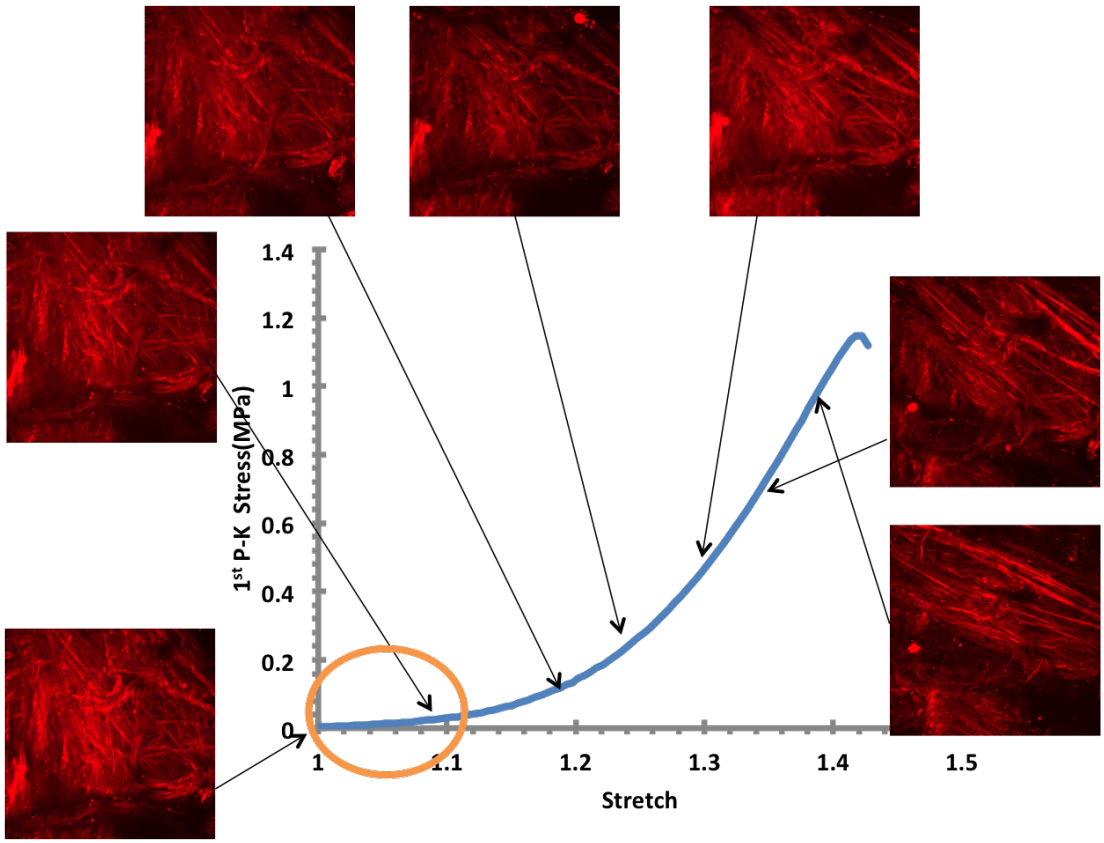

Figure 3.4: Stress-stretch curve representing the uniaxial mechanical testing of aneurysmal tissue. The sample was tested to failure and at several time steps, under increasing stretch, MPM images of the tissue have been captured. Attention is drawn to the linear toe region at lower stretches before non-linear mechanical behaviour is observed at higher stretches. Image provided by Prof. Anne Robertson's lab, Swanson School of Engineering, University of Pittsburgh.

collagenous healthy tissue (Chapter 2), are not present here. Possible explanations can relate to the gradual realignment and reorientation of the collagen fibres. Additionally, additional arterial ground substance, which has not been considered in the theoretical modelling, could be responsible for this linear response. It should be noted that, because this sample was only axially stretched, there is a limitation to the full understanding of the mechanical behaviour of the tissue; a biaxial test is recommended in order to provide a better understanding of this mechanical behaviour.

The following section presents the analysis in which those presented experimental data were fitted to a proposed 1D constitutive model, in order to approximate a value for the material parameter of the present adventitial collagen and further

mathematically test that aneurysmal tissue in a 1D model of a cylindrical collagenous membrane.

3.3 FIT OF CONSTITUTIVE MODEL TO EXPERIMENTAL DATA

Schriefl et al. (2012b) (also Schriefl et al. (2012a), Schriefl et al. (2012c)) proposed a fibre dispersion model, experimentally quantifying primary orientations of collagen fibres in the medial and adventitial layers with accompanying measurements of tissue thickness. Comparisons between constitutive relations and experimental observations with focus on fibre orientations have been presented before (Wagner and Humphrey, 2011) and further research has aimed to determine fibre material parameters from experimental data, considering the gradual recruitment of fibres to load bearing (Gasser et al. (2012), Lanir (1979), Hill et al. (2012a)).

Focusing on the mechanical behaviour of the aneurysmal tissue, I am proposing to find the best fit of the presented experimental data from the uniaxial mechanical test (Figure 3.3) to a constitutive mathematical model, with the aim of determining parameters for the material of the tissue. The tissue is modelled as a rectangular tissue sample, undergoing uniaxial stretch. From the observations in the previous section of this chapter, the aneurysmal tissue is represented so that is composed of primarily collagen fibres which are at an angle to the direction of the imposed stretch and are recruited to load bearing gradually; these collagen fibres represent the ones in the adventitial layer which are observed remaining in the clinical case. As a linear response is observed at lower stretches, an additive linear mechanical contribution is also mathematically modelled from other ground substance in the aneurysmal tissue.

Firstly, the mathematical description of the orientation and gradual recruitment of the collagen fibres is outlined. Chapter 2 presented the concept of the recruitment stretch, as the reference stretch of the tissue at which the collagen fibres are recruited to load bearing. This mathematical description is updated here to include the concept that the collagen fibres are at an angle to the direction of the tissue stretch. The new notation, that includes the subscript γ, is used to differentiate the stretches in the direction of the mechanical testing of the tissue from the ones that describe stretches in the direction of the collagen fibres. For the purposes of this

analysis, it is assumed that there is no reorientation of fibres from planes perpendicular to the 2D plane of the mechanical testing that are investigated here.

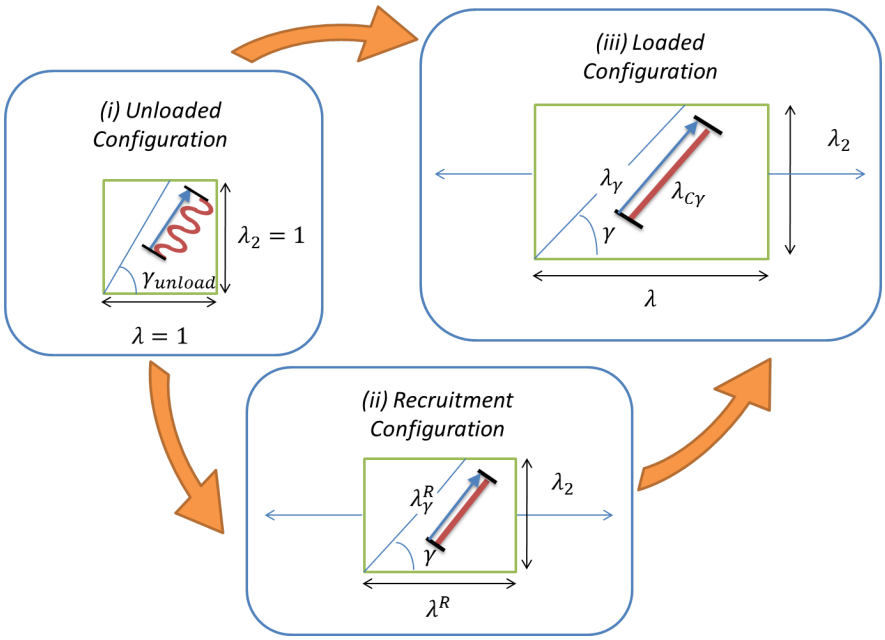

Figure 3.5: Definition of stretches during the uniaxial mechanical testing of a rectangular tissue sample, where collagen fibres are at an angle to the direction of the testing. The stretches, of both the fibres and of the tissue, are illustrated for the: (i) unloaded, (ii) recruitment and (iii) loaded configuration.

Figure 3.5 illustrates the updated stretch definitions (following the definitions from Figure 2.2 in Chapter 2). Figure 3.5(i) shows the unloaded configuration, where the stretches of the tissue in the 2D plane equal, by definition, one; λ is the stretch in the direction of the tissue's mechanical testing and λ_2 is the stretch in the direction perpendicular to the uniaxial stretch on the 2D plane shown. If it is said that λ_3 refers to the stretch out of the 2D plane and, because of the lack of biaxial mechanical testing data, it will be assumed for simplicity that the material being tested is isotropic, then:

$$\lambda_2 = \lambda_3 = \frac{1}{\sqrt{\lambda}} \tag{3.12}$$

Furthermore, the collagen fibre in the unloaded configuration is undulated and, therefore, not bearing load. The average direction of the fibre undulation is at an angle γ_{unload} to the direction of the λ testing stretch.

Figure 3.5(ii) represents the recruitment configuration of the collagen fibre depicted in the figure. This configuration can be described by either the stretch of the tissue in the direction of the testing λ_R or the stretch of the tissue resolved in the direction of the fibre λ_γ^R at that time. Mathematically λ_γ^R is calculated as (considering Eqn. (3.12)):

$$\lambda_\gamma^R = \sqrt{\frac{1}{\lambda^R}\sin^2\gamma + (\lambda^R)^2\cos^2\gamma} \tag{3.13}$$

By definition, the stretch of the collagen fibre, defined as $\lambda_{C\gamma}$ upon recruitment, equals to one.

At the loaded configuration (Figure 3.5(ii)) the definition for tissue stretch in the direction of the collagen fibre can then be generalised as:

$$\lambda_\gamma = \sqrt{\frac{1}{\lambda}\sin^2\gamma + (\lambda)^2\cos^2\gamma} \tag{3.14}$$

Moreover, following the mathematical expression in Chapter 2, the collagen stretch in the direction of the fibre can be defined as:

$$\lambda_{C\gamma} = \frac{\lambda_\gamma}{\lambda_\gamma^R} \tag{3.15}$$

The next step is to describe the gradual recruitment of collagen fibres to load bearing. For this, I follow the analysis presented in Chen (2014). In Chapter 2, a non-linear function for the mechanical response of the collagen fibres is assumed, which is based on the observation that healthy arterial tissue shows a non-linear mechanical response at higher stretches, dominated by the role of collagen. Accordingly, other models followed an implied sudden recruitment to load bearing at finite stretches (Watton et al. (2009b), Wulandana and Robertson (2005)). However, evidence indicates that individual collagen fibres show a linear mechanical response (Sopakayang et al., 2012) and the non-linear mechanical response of the tissue at higher stretches is the result of the gradual recruitment of collagen fibres to load bearing; similar approaches have been previously presented (Gleason and Humphrey (2005), Martufi and Gasser (2012)). For the purposes of fitting the experimental 1^{st} Piola-Kirchhoff (PK) stress to stretch data to the model, the strain energy

function (SEF) for the individual adventitial collagen fibre $\tilde{\psi}_C$ needs to be defined (where subscript C refers to the type of fibre (collagen in this case)):

$$\tilde{\psi}_C(\lambda_C) = \frac{K_C}{2} \cdot (\lambda_C - 1)^2 \tag{3.16}$$

This implies a linear mechanical response for each fibre, where K_C is a material parameter related to stiffness. This is exactly the parameter aimed to be approximated in the fit to the experimental data and will be specifically related to the adventitial collagen that has remained in the clinical tissue sample. In order to mathematically represent the mechanical response of the totality of the collagen fibres at a given stretch λ, the SEFs of all the fibres that have been recruited up to the current stretch λ need to be added:

$$\psi_C(\lambda) = \int_1^{\lambda} \tilde{\psi}_C(\lambda_C) \cdot \rho(\lambda^R) d\lambda^R \tag{3.17}$$

$\rho(\lambda^R)$ is the probability density function related to collagen fibres recruited at different stretches. For simplicity, a triangular function is used:

$$\rho\left(\lambda^R\right) = \begin{cases} 0 & \lambda^R < \lambda^{R,\min} \\ \frac{2\left(\lambda^R - \lambda^{R,\min}\right)}{\left(\lambda^{R,\max} - \lambda^{R,\min}\right)\left(\lambda^{R,mode} - \lambda^{R,\min}\right)} & \lambda^{R,\min} < \lambda^R < \lambda^{R,mode} \\ \frac{2\left(\lambda^{R,\max} - \lambda^R\right)}{\left(\lambda^{R,\max} - \lambda^{R,\min}\right)\left(\lambda^{R,\max} - \lambda^{R,mode}\right)} & \lambda^{R,mode} < \lambda^R < \lambda^{R,\max} \\ 0 & \lambda^R > \lambda^{R,\max} \end{cases}. \tag{3.18}$$

This triangular function can be characterised by only three values, $\lambda^{R,min}$, $\lambda^{R,max}$ and $\lambda^{R,mode}$. As a result, there are piecewise analytic continuous expressions (Hill et al., 2012b) for stress functions that allow for the description of gradual recruitment.

The 1^{st} PK stress for the collagen bundle (P_C) is then calculated by taking the derivative of the SEF. Finally, the concept of gradual recruitment is combined with fibre orientation, by assuming that there are two major families of fibre orientations in the tissue sample, one at an angle of γ and another at a mirrored angle with respect to the direction of the mechanical testing of $-\gamma$. This results in the stress function as:

$$P_C(\lambda) = \sum_{\gamma=+,-} \frac{\partial}{\partial \lambda} \left[\int_1^{\lambda_\gamma} m_{C\gamma} \cdot \tilde{\Psi}_{C\gamma} \left(\frac{\lambda_\gamma}{\lambda_\gamma^R} \right) \cdot \rho \left(\lambda_\gamma^R \right) d\lambda_\gamma^R \right] \tag{3.19}$$

Notice that the SEF is defined in terms of the stretch of the collagen in the direction of the fibres, as defined in Eqn. (3.15) and the triangular distribution for the recruitment of collagen fibres is defined with respect to the recruitment stretch in the direction of the fibre λ_γ^R, summed up to the value of the current stretch resolved in the direction of the fibres (λ_γ). $m_{C\gamma}$ refers to the normalised mass density of the collagen fibres. Appendix A shows in more detail the calculations of the piecewise stress function for the range of recruitment stretches. Figure 3.6 applies Eqn. (3.19) for varying values of γ between 0 and 90, normalised density of 1 and a prescribed isosceles triangular recruitment distribution (shown here in green) between 1.03 and 1.13. Here the decreasing stress contribution of the fibres is seen as the orientation is approaching the direction perpendicular to the direction of the tissue stretch.

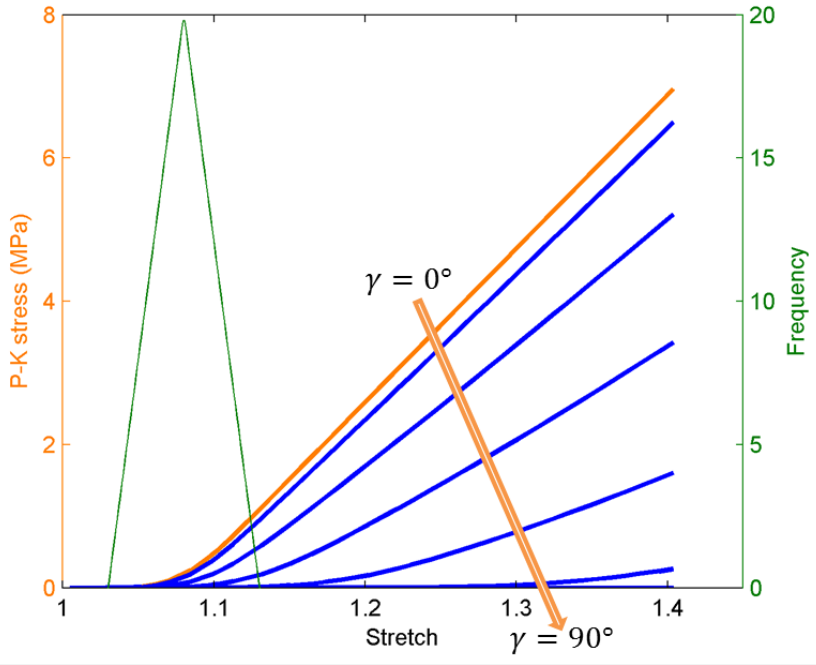

Figure 3.6: Stress-stretch plot for uniaxially stretched collagenous material. Collagen fibres are gradually recruited according to the prescribed recruitment stretch distribution. There are two families of collagen fibres, at γ and $-\gamma$ angle from the axial direction. Cases are here shown where γ takes a varying value between 0 and 90.

The stress function is now ready to be used for the fit of the constitutive model to the experimental uniaxial test data. As mentioned above, there is a linear response at lower stretches, which will be modelled as a neo-Hookean 'ground substance' material, resulting in a total stress function to represent the aneurysmal tissue as:

$$P_{fit}(\lambda) = \frac{\partial}{\partial \lambda}\left[\sum_{\gamma=+,-}\left[\int_1^{\lambda_\gamma} m_{C\gamma}\cdot\tilde{\Psi}_{C\gamma}\left(\frac{\lambda_\gamma}{\lambda_\gamma^R}\right)\cdot\rho\left(\lambda_\gamma^R\right)d\lambda_\gamma^R\right] + m_{GB}\cdot K_{GB}(\lambda-\frac{1}{\lambda^2})\right], \tag{3.20}$$

where m_{GB} refers to the normalised mass density of the ground substance and K_{GB} to the corresponding material parameter.

Given the functional form for the total tissue stress, the values for the variables are set as seen in Table 3.4. Since there is knowledge of the thickness of the tissue that will account for changes in mass densities it is assumed that $m_{C+} = m_{C-} = m_{KG} = 1$. The choice for the recruitment stretch distribution (defined in the direction of the fibres) was estimated on the basis of the observation that the transition from a linear to a non-linear mechanical behaviour takes place at a stretch in the direction of the mechanical testing of around 1.1. From the literature on adventitial collagen fibre orientation for a healthy artery (Kuhl and Holzapfel (2007), Holzapfel (2006)) and an observation of the MPM images of the aneurysmal tissue, a value of 45 degrees is decided for the angle of the fibres to the axial direction. Finally, tissue failure is not modelled at this stage, so the experimental points at the end of the test were not taken into consideration. A nonlinear regression function, using least squares estimation, was used and tested for a range of maximum and modal values of the recruitment stretch distribution. The final choice for the recruitment stretch distribution as it is observed in Figure 3.7 was based on the best fit (in terms of R^2 accuracy) of our constitutive model to the experimental data provided.

It is assumed that there is a symmetry between the two families of collagen fibres and therefore expect an equal material parameter value for both ($K_{C+} = K_{C-}$). The result of the curve fit is shown in Figure 3.7 and the estimation for the material parameters is shown in Table 3.5. The illustrated fit had an R^2 accuracy of 0.9986.

It must be noted that the recruitment stretch distribution depicted in Figure 3.7 is defined in the direction of the mechanical testing and clearly illustrates the transition between linear and non-linear mechanical response as the recruitment of collagen fibres sets in. This section allowed tailoring the material parameter for colla-

Table 3.4: List of values for variables in the constitutive model for the fit to clinical experimental uniaxial testing data.

Modelling variables	
$m_{C\gamma+}$	1
$m_{C\gamma-}$	1
m_{GB}	1
$\lambda_{\gamma}^{R,min}$	1.03
$\lambda_{\gamma}^{R,max}$	1.07
$\lambda_{\gamma}^{R,mode}$	1.11
γ	45

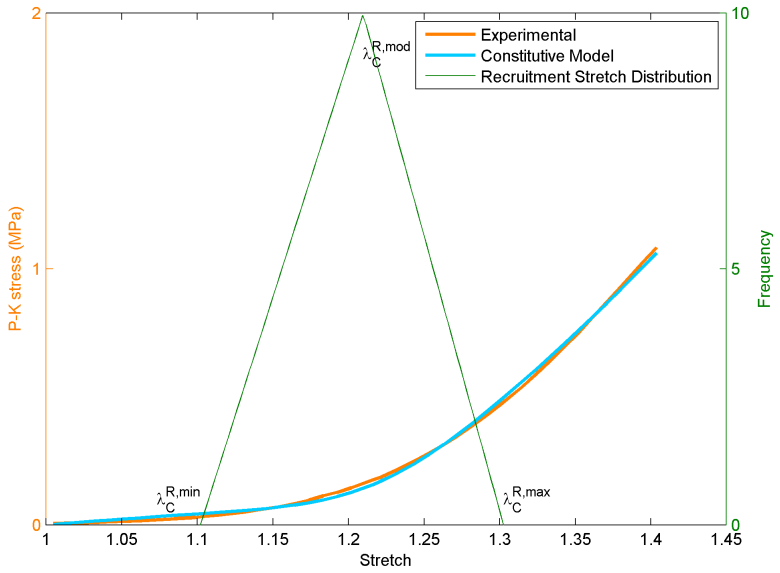

Figure 3.7: The triangular recruitment stretch distribution (determined by $\lambda_C^{R,min}$,$\lambda_C^{R,mod}$ and $\lambda_C^{R,max}$) prescribed and shown here is defined in the axial direction. The experimental curve is fitted with the constitutive model to represent the aneurysmal tissue from the experimental data. The SEF used includes collagen fibres' gradual recruitment to load bearing and reorientation, as well as a linear response from ground substance.

gen to the specific data. Considering this calculation, the following section proceeds to apply the presented stress functions to a cylindrical membrane composed of that aneurysmal collagenous tissue. Continuing to model fibre orientation and gradual

Table 3.5: Values of material parameters for the best fit of the constitutive model to the experimental data.

Material Parameters	
$K_{C+} = K_{C-} = 11.95MPa$	$K_{GB} = 0.1584MPa$

recruitment, a value for the loaded thickness of the aneurysm is estimated (based on the unloaded value provided by the experimental data) and systolic and diastolic stretches (and as a result cyclic stretches) of this tissue are investigated under the expected physiological pressures in a setting that more closely resembles the arterial geometry.

3.4 Collagenous cylindrical membrane investigation

In this section, a 1D cylindrical membrane of the collagenous tissue is modelled with the aim of predicting apparent thickness in the evolving loaded aneurysm, given the material parameter approximated in the previous section. The experimental data measured a value for the thickness of the aneurysmal tissue in the unloaded configuration (*ex vivo*). The 1D *in silico* model presented in this chapter allows the prediction of the apparent thickness for the evolving aneurysm in the loaded configuration. In order to have a value for loaded thickness from the experiment to compare the predictions with, the 1D cylindrical model for the collagenous tissue is used and inflated it to physiological pressures and consequently approximate the expected *in vivo* thickness.

For this purpose, the following equation is used to describe the pressure-stretch relationship in a cylindrical configuration, as was initially presented in Chapter 2:

$$p_{cylinder} = \frac{H_{an}}{R_{an}} \frac{1}{\lambda \lambda_{z_{an}}} \frac{\partial \psi_{C\gamma}}{\partial \lambda} \tag{3.21}$$

where ψ_C is the SEF, as defined in the previous section, keeping the same assumptions on recruitment stretch distribution and fibre orientation. The angle γ is defined with respect to the circumferential axis in the unloaded configuration and therefore $\psi_{C\gamma}$ defines the SEF with respect to the fibre stretch in the direction of

the fibres. The aneurysmal state is represented with this cylindrical configuration; therefore H_{an} (the subscript an refers to the geometric characteristics of the aneurysm) is the unloaded thickness of the tissue sample (for which there is an experimental value from Table 3.3). A value for the unloaded radius R_{an} of the 1D aneurysmal cylinder and values for the axial stretch $\lambda_{z_{an}}$ are also defined. Because of the complexity of the clinical aneurysmal geometry (a spherical aneurysm formation on a cylindrical artery), it is not straightforward to define the expected radius adjusted for the 1D set up. Moreover, the collagenous tissue modelled is expected to be stiff, so $\lambda_{z_{an}}$ cannot be set too high as that would render unhelpful results from the excessive axial stretching. For that reason, several cases are created to assess a range of values for R_{an} and $\lambda_{z_{an}}$. From the observations of the clinical geometry and considering the radius within the spherical aneurysm and the distance of the cylindrical parent artery from the dome of the aneurysm, three cases for R are chosen with respect to the unloaded radius of the healthy artery $R(0)$, as calculated in Table 3.2: (a)$R_{an} = 1.5 \cdot R(0)$, (b) $R_{an} = 2.5 \cdot R(0)$ and (c) $R_{an} = 3.5 \cdot R(0)$. Equivalently, keeping in mind *in vivo* measurements of healthy cerebral arteries are around 1.3, three different values for $\lambda_{z_{an}}$ are set as: (a) 1, (b) 1.05 and (c) 1.1. Consequently, there are nine cases in total, summarised in Table 3.6.

The pressure-stretch results for the nine cases presented are seen in Figure 3.8. As expected, for the higher thickness-to-radius ratios, higher pressures are observed for the same stretches. However, for the higher stretches, the mathematical description is not able to accurately describe what would be expected the mechanobiological behaviour of this collagenous tissue to be; it is not possible with the given stress functions to represent failure given that the pressures are unrealistically high under physiological conditions. I want to therefore focus my attention to the pressures expected to be present in the arterial environment (the green circle in Figure 3.8 indicates the area of interest). This is the purpose of the illustration in Figure 3.8. Here it is possible to clearly observe the range of the cases and identify the systolic and diastolic pressures *in vivo* in the artery. For those values, the pressures are set as $P_{systolic} = 16kPa$ and $P_{diastolic} = 10.667kPa$ (Hansen et al., 1995). The green lines in Figure 3.9 indicate the cross-over of the assumed physiological systolic and diastolic pressures with the range of cases.

With those values in mind the values for cyclic stretches are calculated as:

Table 3.6: Cases of varying unloaded thickness-to-radius ratio and axial stretch for modelling inflation of cylindrical membrane of aneurysmal collagenous tissue.

Cases for Collagenous Cylindrical Membrane Inflation		
Case	Unloaded Thickness to Radius Ratio H_{an}/R_{an}	Axial stretch $\lambda_{z_{an}}$
i (black solid line)	0.0711	1
ii (blue solid line)	0.0711	1.05
iii (red solid line)	0.0711	1.1
iv (black dashed line)	0.0427	1
v (blue dashed line)	0.0427	1.05
vi (red dashed line)	0.0427	1.1
vii (black dotted line)	0.0305	1
viii (blue dotted line)	0.0305	1.05
ix (red dotted line)	0.0305	1.1

$$\lambda_{cyc} = \frac{\lambda_{sys}}{\lambda_{dia}} \tag{3.22}$$

The summary of systolic and cyclic stretches for the range of cases are presented in Table 3.7. It should be noted that the systolic stretch expressed here is defined with respect to the unloaded configuration of the aneurysmal radius. In order to calculate the expected stretch with respect to the unloaded configuration of the healthy initial radius (this will become useful for comparison later on in the chapter), each factor from the cases in Table 3.6 needs to be multiplied with the corresponding systolic stretch from Table 3.7.

Cyclic stretches in healthy arteries are expected to be around 1.1. For this collagenous tissue lower values have been estimated in the $1.0181 - 1.0459$ range, known as a consequence of the shift from elastin-based to collagen-based load bearing. The range of resultant systolic stretches allows then the calculation of a range of values for the loaded thickness of the aneurysm, based on the calculated value for unloaded thickness. Calculating the thickness with respect to the systolic configuration and assuming incompressibility as with the calculations earlier in the

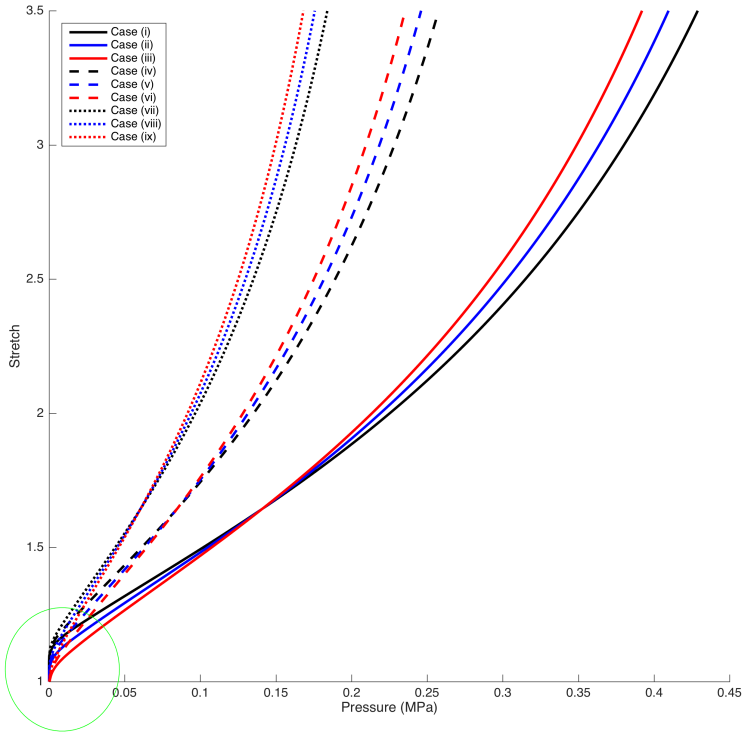

Figure 3.8: Stretch-pressure curves of 1D collagenous cylindrical membrane that includes fibre reorientation for cases of varying axial stretch and unloaded radius as defined in Table 3.6. Attention needs to be drawn to the range of physiological pressures, see Figure 3.9 for detail.

chapter for distinctions between loaded and unloaded configurations in the cylindrical membrane, it is expected that:

$$h_{an} = \frac{H_{an}}{\lambda_{z_{an}} \lambda_{sys}} \tag{3.23}$$

For the nine cases and the corresponding values for $\lambda_{z_{an}}$ and λ_{sys}, the resulting values for h_{an} are summarised in Table 3.8. The range of cases with the resulting range of values for loaded aneurysmal thickness following the knowledge on unloaded aneurysmal thickness allows a better understanding of the expected bounds in the mathematical predictions and several points of comparison depending on the choice of modelling approach and configuration.

There is one final calculation and observation that can be made in this sec-

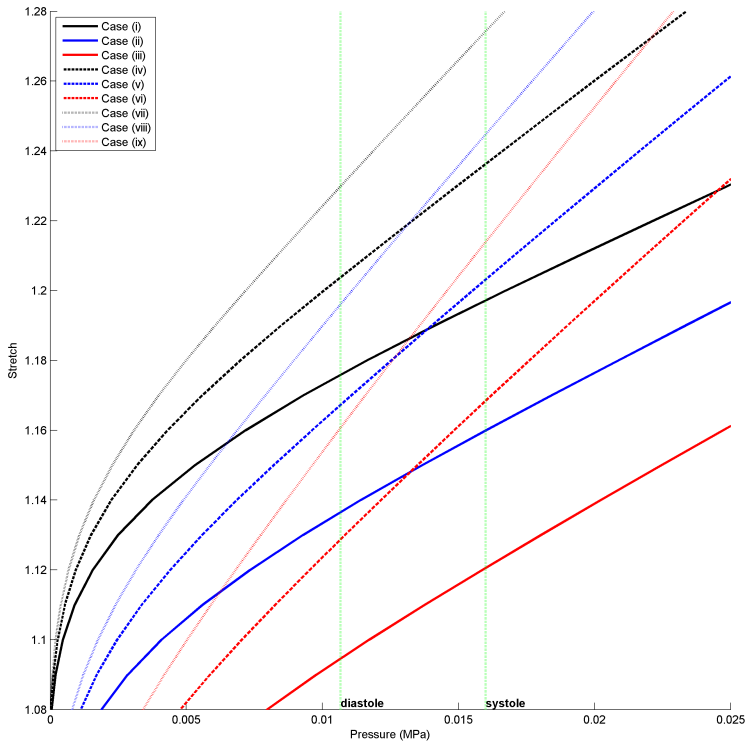

Figure 3.9: Stretch-pressure curves of 1D collagenous cylindrical membrane that includes fibre reorientation for cases of varying axial stretch and unloaded radius as defined in Table 3.6. Lines are drawn for representative values of diastolic and systolic pressures, to be matched with stretches for each presented case.

tion on the cylindrical configuration of the aneurysmal tissue. It is noted, from Eqn. (3.15), that a distribution of recruitment stretches will consequently imply a distribution of collagen stretches. Additionally, the concept of the attachment stretch was introduced in Chapter 2, as the stretch at which collagen fibres are laid down in the ECM and its definition implies a homeostatic, i.e. ideal, state of stretch. The importance of attachment stretch on the functional representation of collagen deposition has been expressed (Humphrey (1999), Gleason et al. (2004), Watton et al. (2009b)), with suggestions for ranges of such values (Gleason and Humphrey, 2005). Collagen fibres aim to sustain attachment stretches and remodelling is represented that drives those stretches back to homeostatic levels, when they deviate from those values. In the presented cylindrical set up, it can be assumed that the stretches of collagen fibres have reached attachment levels in a new

Table 3.7: Calculated systolic and cyclic stretches (from physiological values of systolic and diastolic pressures) for all cases of pressure inflation of cylindrical membrane of aneurysmal collagenous tissue.

Collagenous Cylindrical Membrane Inflation)		
Case	Systolic stretch λ_{sys}	Cyclic stretch λ_{cyc}
i	1.1972	1.0181
ii	1.1599	1.0206
iii	1.1206	1.0237
iv	1.2363	1.027
v	1.2032	1.0308
vi	1.1684	1.0352
vii	1.2743	1.0361
viii	1.2447	1.0407
ix	1.2139	1.0459

Table 3.8: Calculated loaded thickness for all cases of pressure inflation of cylindrical membrane of aneurysmal collagenous tissue

Collagenous Cylindrical Membrane Inflation	
Case	Loaded Thickness h_{an} (in mm)
i	0.13365
ii	0.13137
iii	0.1298
iv	0.12942
v	0.12665
vi	0.12449
vii	0.12556
viii	0.12242
ix	0.11983

stabilised aneurysmal equilibrium. This therefore implies a distribution of collagen fibre attachment stretches, which is supported by the experimental evidence of

a range of collagen fibre waviness in an unloaded configuration (Schrauwen et al., 2012). Moreover, Watton et al. (2004) states that we expect the maximum attachment stretch of the collagen fibre to take place during the peak of the cardiac cycle, i.e. the maximum attachment stretch is expected to be the maximum stretch of the fibres during systole. As a consequence, those collagen fibres at maximum attachment stretch are expected to be the first ones to be recruited to load bearing. In the formulation this follows because, remembering that the circumferential stretch λ in Eqn. (3.15) remains the same for the ranges of recruitment and attachment stretches in each configuration, it can be mathematically stated that:

$$\lambda_{C\gamma}^{AT,min} = \frac{\lambda_\gamma}{\lambda_\gamma^{R,max}} \tag{3.24a}$$

$$\lambda_{C\gamma}^{AT,max} = \frac{\lambda_\gamma}{\lambda_\gamma^{R,min}} \tag{3.24b}$$

$$\lambda_{C\gamma}^{AT,mode} = \frac{\lambda_\gamma}{\lambda_\gamma^{R,mode}} \tag{3.24c}$$

$$\tag{3.24d}$$

Note that here I am interested in the recruitment, attachment and circumferential stretches in the direction of the collagen (indicated by the subscript γ). Values for the recruitment stretch distribution are prescribed as seen in Table 3.4 for the fit of the constitutive model to the uniaxial experimental data and this is depicted in Figure 3.10(a). Based on the prescribed recruitment stretch distribution and Eqn. (3.24a) - Eqn. (3.24c) it is possible to estimate the attachment stretch distributions for each of the nine cases. Those distributions are shown in Figure 3.10.

The observed range of attachment stretch distributions for the presented cases is an important observation, as it follows from Watton et al. (2004) with regards to the maximum attachment stretch value in systole being around 1.1. Even though there is not exact agreement and clarity on how to define and calculate the range of attachment stretches (Valentín and Humphrey (2009a), Baek et al. (2006), Watton et al. (2004), Figueroa et al. (2009)), there seems to be an agreement for a value of around 1.1 for the choice of attachment stretch amongst different models. Figure 3.10 shows that for the majority of presented cases, the calculated maximum attachment stretch is below the threshold of 1.1 from the literature; and only for

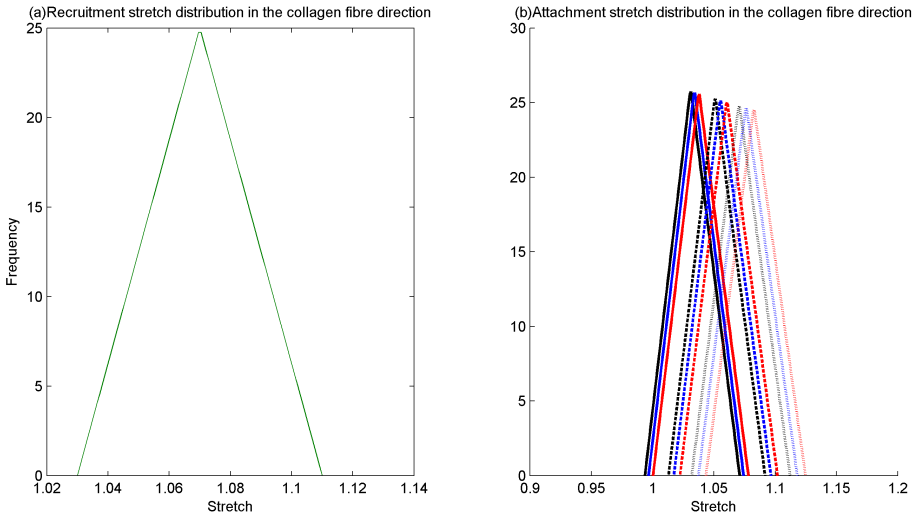

Figure 3.10: (a) Prescribed recruitment stretch distribution (defined in the direction of the collagen fibres); (b) Resulting attachment stretch distribution (for each case as presented in Table 3.6) from inflation of 1D collagenous cylindrical membrane to physiological systolic pressure.

cases vii-ix the maximum attachment stretch value exceeds this limit by less than 2%.

Even though the 1D cylindrical formulation of the aneurysmal tissue in this section is limited in that it does not represent the geometrical complexity of the clinical aneurysm, it allowed the implementation of the *in silico* mechanical set up and, through a range of cases for the geometry, formed a range of estimations for the loaded thickness and cyclic stretches of the aneurysm for comparisons (in 1D in §3.5 and in 3D in Chapter 5) as well as gave a better understanding of the mechanical behaviour of the collagenous aneurysmal tissue. Keeping this analysis in mind, the 1D model for aneurysm evolution is ready to be adapted to the specific clinical case in the following section, and the predictions on G&R of the collagen fibres as well as the projected geometrical properties of the developing aneurysm are analysed.

3.5 Model of aneurysm growth in 1D cylindrical membrane

The analysis from the previous sections of this chapter can be taken forward to implement a 1D model of aneurysm growth, as it was initially introduced in Chapter 2, for this specific clinical case. The aim of this study is to test the effect of the final adventitial collagen attachment stretch distribution on the G&R hypotheses during aneurysm progression.

3.5.1 1D cylindrical model update

I first note the differences and updates of this modelling framework following Chapter 2 and base the analysis on Chen (2014) in order to present the increasing role of the adventitia to load-bearing as the media is lost. I model a 1D 2-layer cylindrical membrane, which consists of elastin and collagen fibres, the deformation of which is characterised by increases in circumferential stretch λ, under constant pressure P and axial stretch λ_z. The governing equation (based on initial work from Watton et al. (2009b)) of pressure for the deformation of a 1D cylindrical membrane accounts for the additive contributions to strain energy from all arterial constituents (elastin and collagen fibres in this 1D model), and it is:

$$p = \frac{1}{R\lambda\lambda_z} \cdot [H_M \cdot P_M(\lambda) + H_A \cdot P_A(\lambda)], \tag{3.25}$$

where for the J constituent (E for elastin or C for collagen) of the L layer (media of adventitia) the stress function P_{J_L} (m refers to the mass density of the corresponding constituent) is:

$$P_{J_L}(\lambda) = m_{J_L} \cdot \frac{\partial \psi_{J_L}}{\partial \lambda} \tag{3.26}$$

It is assumed that the media (subscript M) consists of elastin and collagen fibres, whereas the adventitia (subscript A) consists of only collagen fibres. The neo-Hookean model for the elastin fibres is repeated, as presented in Eqn. (2.4). A recruitment stretch distribution for the collagen fibres of both the medial and the adventitial layer is assumed; this distribution will be determined for the beginning of the simulation according to Eqn. (3.24a)-Eqn. (3.24c) and prescribed attachment stretch distributions (defined for this simulation in §3.5.2). The piecewise stress

contributions of the collagen from the media and the adventitia are then described by Eqn. (3.19).

The clinical aneurysmal tissue shows a complete loss of the media; in the 1D simulation the degradation of the mass densities of the media and adventitia (m_{E_M} and m_{C_M}, respectively) is prescribed to represent this. As a result, there will be a disturbance in the equilibrium and an increase in circumferential stretch to account for the loss of the arterial constituents. As the geometry is distorted, it is expected that the collagen stretches, initially in homeostasis, deviate from their attachment values (as was presented in Chapter 2). The hypothesis for the resulting growth of the adventitital collagen fibre mass density is updated for the consideration of a distribution of stretches:

$$\frac{\mathrm{dm_{C_A}}}{\mathrm{d}t} = \beta \cdot \frac{\lambda_{C_{A\gamma}}^{mean} - \lambda_{C_{A\gamma}}^{AT,mean}}{\lambda_{C_{A\gamma}}^{AT,mean}} \tag{3.27}$$

The β rate parameter controls the speed of collagen fibre turnover and the 'mean' superscript for the collagen stretches and attachment values refer to a simple equal averaging of the minimum, maximum and modal values, to represent that growth is driven by the deviation of the stretch distribution from attachment levels. For the cases presented here, the stretch distribution is an isosceles triangle, so the averaging of the distribution corresponds to simply the modal value for collagen stretch and attachment stretch.

Continuing from Chapter 2, the remodelling evolution equations are updated for the recruitment stretches of both the medial and adventitial collagen to account for stretch distributions; keeping in mind Eqn. (3.24a) - Eqn. (3.24c), the equations for remodelling are:

$$\frac{\mathrm{d}\lambda_{\mathrm{L}}^{\mathrm{R,min}}}{\mathrm{d}t} = \alpha_L \cdot \frac{\lambda_{C_{A\gamma}}^{max} - \lambda_{C_{A\gamma}}^{AT,max}}{\lambda_{C_{A\gamma}}^{AT,max}} \tag{3.28a}$$

$$\frac{\mathrm{d}\lambda_{\mathrm{L}}^{\mathrm{R,max}}}{\mathrm{d}t} = \alpha_L \cdot \frac{\lambda_{C_{A\gamma}}^{min} - \lambda_{C_{A\gamma}}^{AT,min}}{\lambda_{C_{A\gamma}}^{AT,min}} \tag{3.28b}$$

Similarly to the growth evolution equation, values are only required for the minimum and maximum recruitment stretches, assuming a symmetry in the distribu-

tions. α_L is a remodelling rate parameter defined separately for each arterial layer in Table 3.9. All collagen stretches are defined relative to their respective orientation.

The assumption for the 1D configuration here is that the cylindrical membrane is thin and, assuming incompressibility, it is expected that the change in thickness follows Eqn. (3.10), so $h = \frac{H}{\lambda\lambda_z}$. However it is possible to account for changes in volumetric growth in the calculations of thickness, essentially following the change in normalised densities of the constituents in the media and adventitia. Based on Chen (2014) and updated to account for the two families of collagen fibre orientation in the adventitia (see Appendix B for details), the updated thickness, which is called 'remodelled thickness' represented with the subscript 'rem', is calculated by:

$$h_{rem} \approx \kappa_{rem} \cdot \frac{H}{\lambda\lambda_z}, \tag{3.29}$$

where κ is the remodelled parameter accounting for volumetric growth:

$$\kappa_{rem} \approx \frac{2\left[m_{E_M} + m_{C_M} + m_{C_A}\right]}{6} \tag{3.30}$$

The degradation of the media and the growth of the adventitia are therefore accounted to estimate the apparent loaded thickness in the model, which can then be compared with the experimental information. Following this calculation, it will be useful to examine the evolution of the Cauchy stress in the 1D model named σ_{rem}, that accounts for the changes in remodelled thickness. It is calculated as:

$$\sigma_{rem} = \frac{\lambda R}{h_{rem}} \cdot p \tag{3.31}$$

where p is from Eqn. (3.25).

3.5.2 Set up of 1D simulation and modelling variables

The 1D aneurysm evolution model here is parameterised for the specific presented clinical case and aims to investigate the G&R of the arterial constituents as the media degrades and the resulting geometry, especially in terms of the remodelled thickness, for which specific experimental evidence exists for validation purposes. The role of adventitia as a protective sheath in the initially healthy artery is represented, which increasingly contributes to load-bearing when the media has degraded. At

the start of the simulation I want to model that some medial collagen fibres are recruited to load bearing, whereas none of the adventitial collagen fibres are recruited. Mathematically it can be understood, from Eqn. (3.24a)-Eqn. (3.24c), that, for the $t = 0$ configuration where collagen stretches are expected to be at attachment levels, a maximum attachment stretch of less than 1 implies that none of the collagen fibres are recruited.

A symmetrical attachment stretch distribution is therfore assumed between 0.9 and 1.1 for the medial layer and a maximum attachment stretch for the adventitia of less than 1. Because there is no further experimental information about the initial attachment stretch distribution, a reasonable symmetrical range of $0.9-1$ is assumed. In order to simulate the gradually increasing mechanical role to load-bearing recruitment of the adventitial collagen fibres, the evolution of the adventitial attachment stretch distribution is also prescribed so that it temporally shifts to stretches greater than 1; as a result, when collagen fibres assume attachment levels after G&R, adventitial collagen fibres will still be recruited.

The choice for the final attachment stretch distribution in the evolution model is informed from the results on the adventitial collagen attachment distributions of the investigation on the collagenous cylindrical membrane (Figure 3.10). A set of six cases is initially set with a common final maximum attachment stretch $\lambda_A^{AT}|_{final}^{max}$ of 1.1 and a variable final width w_{final} of the distribution, as illustrated in Figure 3.11. The cases are differentiated as follows:

- Case 1: $w_{final} = w \cdot 1.0$
- Case 2: $w_{final} = w \cdot 0.8$
- Case 3: $w_{final} = w \cdot 0.6$
- Case 4: $w_{final} = w \cdot 0.4$
- Case 5: $w_{final} = w \cdot 0.2$
- Case 6: $w_{final} = 0.0001$

Case 6 is an extreme one, closely resembling a singular attachment stretch. The variable w is a reference width; $w = 0.1$ is set for the cases presented in Figure 3.11. The temporal evolution of the distribution follows a simplified Richard's growth

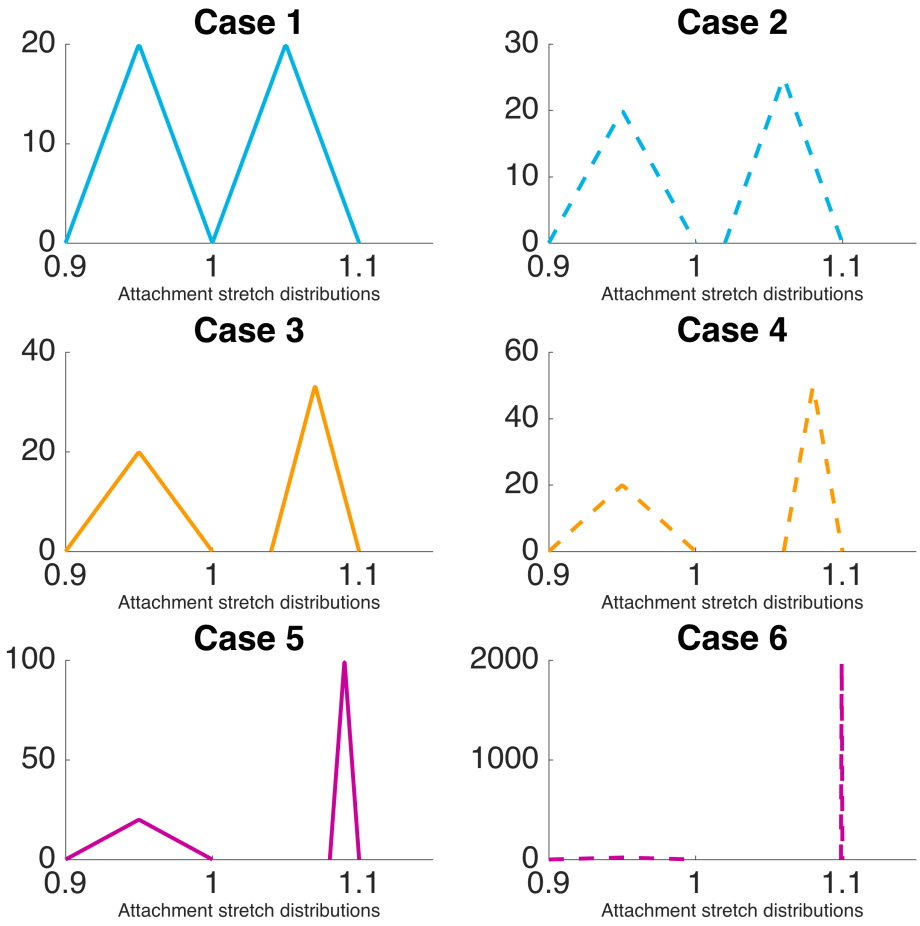

Figure 3.11: The initial and final prescribed attachment stretch distributions for the first six cases presented in the 1D cylindrical study. All cases present the same initial symmetric range of $0.9-1$ for the attachment stretch distribution and a final maximum attachment stretch of 1.1, but they vary on the basis of the final width in the final attachment stretch distribution: Case 1 ($w_{final} = 1.0$); Case 2 ($w_{final} = 0.8$); Case 3 ($w_{final} = 0.6$); Case 4 ($w_{final} = 0.4$); Case 5 ($w_{final} = 0.2$); Case 6 ($w_{final} = 0.0001$).

function (Chen, 2014). These six cases allow the examination of the effect of the width of the final attachment stretch distribution on the evolution hypotheses. Further to this, the effect of the choice for $\lambda_A^{AT}|_{final}^{max}$ is also investigated. Given the same variations to the width as presented above for Cases 1-6, the further results from three sets of six cases each will also be selectively outlined, characterised as follows:

- $\lambda_A^{AT}|_{final}^{max} = 1.05$ and $w = 0.05$
- $\lambda_A^{AT}|_{final}^{max} = 1.075$ and $w = 0.075$
- $\lambda_A^{AT}|_{final}^{max} = 1.12$ and $w = 0.12$

Having presented the governing equations for arterial mechanical equilibrium and the modelling hypotheses for G&R, the variables for a three-phase simulation are set: (1) inception; (2) evolution and remodelling; (3) growth, adaption and stabilisation. The first phase of inception is represented by the prescribed degradation of the medial elastin and collagen fibres, as seen in Figure 3.12. The normalised mass densities of the medial constituents (m_{E_M} and m_{C_M}) are equally exponentially degraded so that they reach a value of 0.1 within the first half of Year 1 and are virtually zero by the end of the first year.

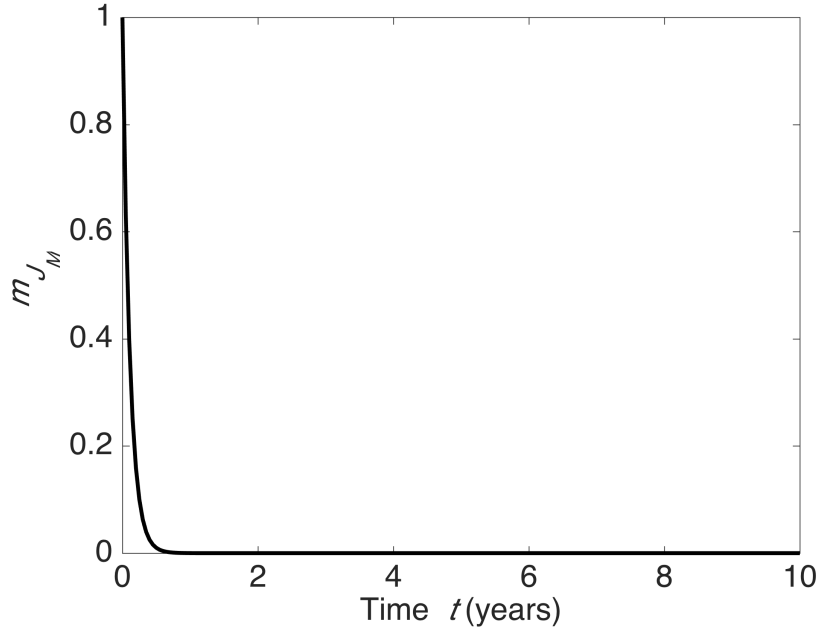

Figure 3.12: The degradation of the arterial constituents of the medial layer is prescribed, represented here as m_{J_M}. J stands for either E (elastin) or C (collagen). The normalised mass densities of the medial constituents are made to exponentially degrade to zero by the end of the first year of the simulation.

The second phase of evolution and remodelling refers to the disturbance of equilibrium caused by the media degradation, that results in the remodelling of recruitment stretches, following Eqn. (3.28a) -Eqn. (3.28b). For the third phase of growth

(expected increase in deposition of collagen fibres following the loss of media), the growth is set to start at the beginning of Year 3. Adaption refers to the temporal evolution of the adventitial attachment stretch distribution; as an instantaneous adjustment of the adventitia to being the main arterial load-bearer is not expected, the evolution of the attachment stretch distribution is set to start at the beginning of Year 4 and finish within half a year. As a result of growth and adaption, the stabilisation of the aneurysm geometry to a new homeostatic state is expected. The simulation was run for 10 years on MATLAB. The timeline and the distinct modelling phases might not be physiologically realistic, especially since there is limited experimental knowledge about the temporal evolution of clinical intracranial aneurysms (Kamitani et al. (1999), Juvela et al. (2001), Juvela et al. (2007)) and in fact there is literature hypothesising that growth rates can be irregular and discountinuous (Koffijberg et al., 2008). Nonetheless, our modelling approach helps with the understanding of the distinct role of the modelling hypotheses and focuses on the final simulated steady state that is to be compared with the initial healthy state, the *in silico* analysis from the previous sections of the chapter and the experimental knowledge on the case.

The values for important variables are summarised in Table 3.9. For the initial unloaded thicknesses of the arterial layers, bearing in mind Table 3.2, it is assumed that, in a healthy artery, the medial thickness is double the adventitial one (Holzapfel et al., 2000). The governing equation under systolic and diastolic pressures is solved (P_{sys} and P_{dia} respectively), as presented in §3.4. That way it is possible to evaluate cyclic stretches for the simulation. The rate parameters for G&R were tested to render physiological results in circumferential stretch for the cases, given that stabilisation, not rupture, is currently investigated. Initial circumferential, axial and cyclic stretches follow aforementioned analysis in this chapter. For the illustrative purposes of the evolution investigation and because the current models do not account for dispersion of fibre angles or the remodelling of fibre orientation, only circumferentially oriented collagen fibres are represented. The material parameters for the medial constituents (K_{E_M} and K_{C_M}) are mathematically calculated from solving the $t = 0$ governing equation for the systolic and diastolic configurations. The material parameter for the adventitial collagen fibres is obtained from experimental data from §3.3.

Table 3.9: Overview for the modelling variables in the constitutive model for the 1D cylindrical aneurysm evolution.

Modelling variables for 1D cylindrical model	
H_M	0.2 mm
H_A	0.1 mm
R	1.5 mm
P_{sys}	16 kPa
P_{dia}	10.667 kPa
β	20
α_M	3
α_A	3
$\lambda(0)$	1.3
λ_z	1.3
λ_{cyc}	1.1
γ	0
K_{E_M}	0.15 MPa
K_{C_M}	1 MPa
K_{C_A}	11.95 MPa

3.5.3 1D cylindrical simulation results

Following the degradation of the media, as seen in Figure 3.12, an increase in the circumferential stretch is expected for sustaining mechanical equilibrium, which is evident in Figure 3.13. During the remodelling phase, the increase in circumferential stretch λ continues and reaches a maximum of 3.5 for all cases by the third year. Following that point in time, entering the third phase of stabilisation, the circumferential stretch decreases and reaches a steady state value, for all cases, of approximately 3.2. It is noted that the evolution of λ is essentially identical for all six cases.

Figure 3.14 shows the growth of adventitial collagen, in terms of the value for normalised mass density of the fibres m_{C_A}. As it was defined in §3.5.2, the growth algorithm is not initiated until after the end of the third year, which is evident in the figure. During the fourth year, a steady increase in all cases is observed, reaching

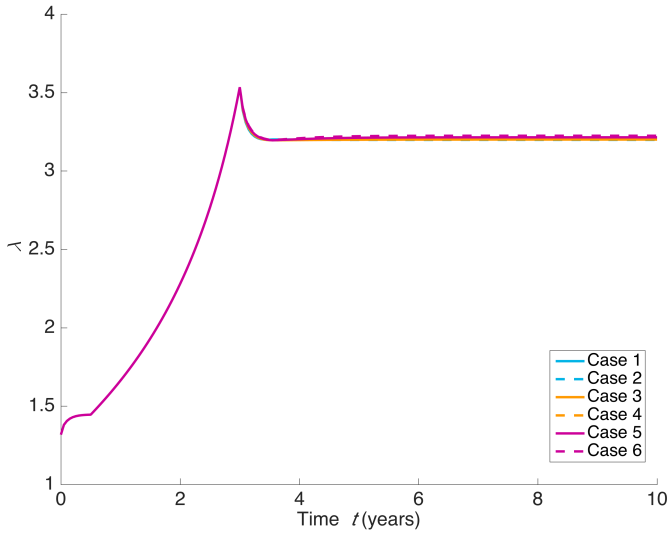

Figure 3.13: Circumferential stretch λ represents the distortion of the geometry. As the media degrades and the aneurysm grows, λ increases for all cases and, past the third year of the simulation, decreases and stabilises by the end of the simulation to a value of approximately 3.2 for all cases.

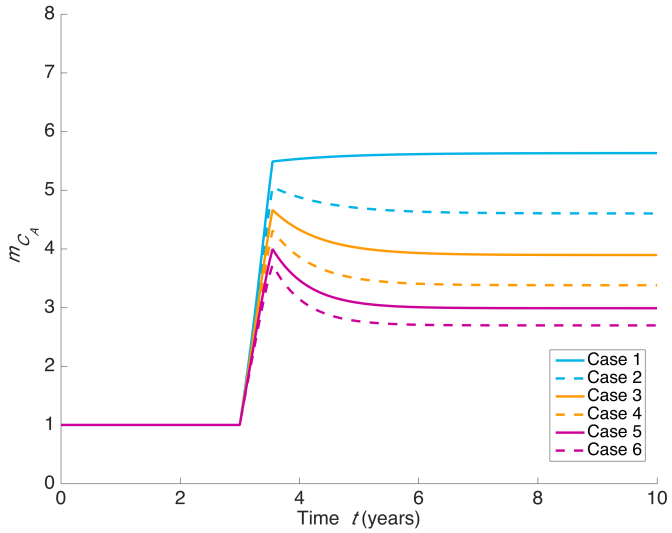

Figure 3.14: Adventitial collagen density is represented by m_{C_A}. Growth is suspended during the first three years of medial degradation and remodelling and it is subsequently determined by the deviation of the average collagen stretch from average attachment values. By the end of the simulation, m_{C_A} for Case 1 to 6 stabilises tos a range between 5.6 and 2.7.

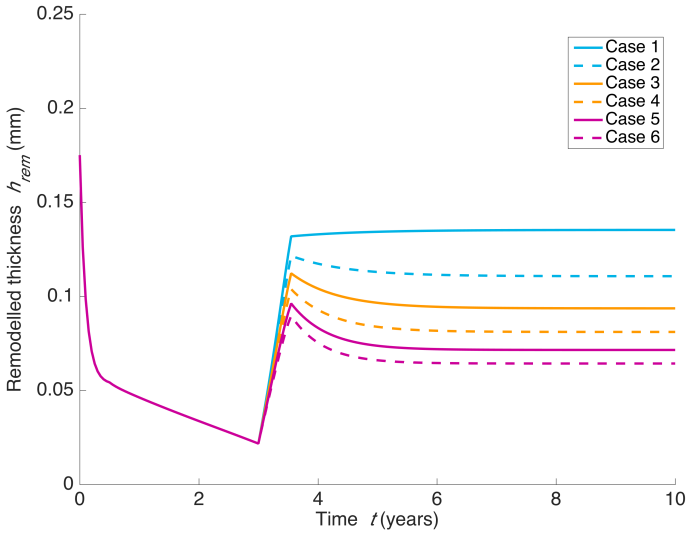

Figure 3.15: The remodelled thickness (h_{rem}), which accounts for changes in volumetric growth, initially decreases (from a value of 0.178mm) following the increase in stretch and media degradation and subsequently increases as adventitial collagen growth sets in. By the end of the simulation, remodelled thickness in Cases 3-6 are less than 0.1 mm; in Cases 2 it is approximately 0.11mm; and in Case 1 it is 0.135mm.

maxima just before the end of the fourth year, of a range between 5.5 and 3.7 (in a decreasing order from Cases 1 to 6). For Case 1, this is approximately the value at which m_{C_A} stabilises until the end of the simulation. For the rest of the cases, there is a small decrease towards steady state values of 4.6-2.7 range (for Cases 2 - 6, respectively).

Combining the conclusions from Figure 3.13, Figure 3.14 and Figure 3.12, I obtain the results in Figure 3.15, since the calculations for remodelled thickness h_{rem} take into account the change in circumferential stretch and volumetric growth via the change in the normalised mass densities of the constituents in the media and adventitia (as defined in Eqn. (3.29) and Eqn. (3.30)). Initially, there is an increase in circumferential stretch but no growth, therefore it is observed that h_{rem} decreases from the initial value of 0.178mm for all cases. With the increase in adventitial collagen fibres and the stabilisation of the circumferential stretch, h_{rem} increases back and eventually reaches a different value for each case; Cases 4, 5 and 6 show the lowest end values in the 0.06 – 0.08mm range; Case 3 stabilises at 0.09mm, Case 2 at 0.11mm and Case 1 at 0.135mm.

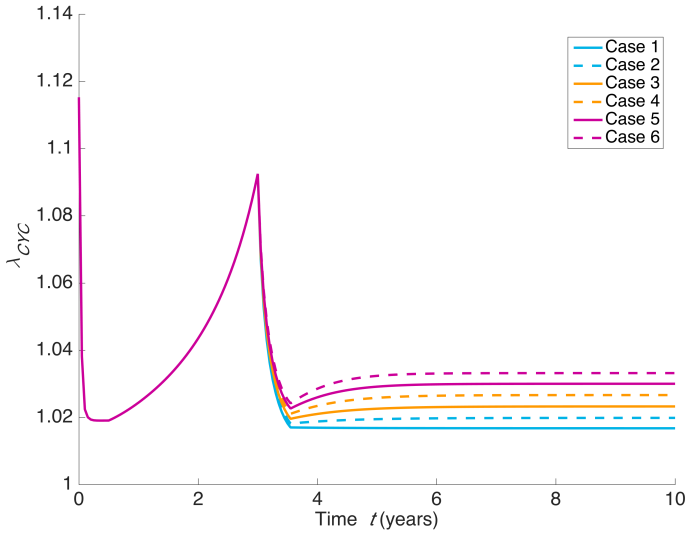

Figure 3.16: Cyclic stretch λ_{CYC} (representing the ratio of systolic to diastolic circumferential stretch) evolves to a low (of around 1.02 across the cases) followed by a high (of around 1.09 across the cases) during the first three years of the simulation and before the growth and adaption stage. Subsequently, λ_{CYC} reduces and by the end of the simulation stabilises; for Case 1 at 1.017, for Cases 2 and 3 at around 1.02 and Cases 4,5 and 6 at around 1.03.

In Figure 3.16 the evolution of cyclic stretches λ_{cyc} is observed, which indicates the differences in the evolution of systolic and diastolic stretches. There is a pattern between the cases, where an initial decrease (to a low of 1.02) during the first year of degradation follows an increase during the remodelling stage (to a value of 1.09) across the cases. This transitioning stage is probably the result of the distinct modelling stages that were defined to resemble the changing role of the adventitia as the media is quickly degraded, causing the abrupt increase in the circumferential stretch. After the start of the growth and adaption phase, cyclic stretches for all cases decrease to a stabilised range of values, as the stiff adventitial collagen becomes the main load-bearer and the stretches return to homeostatic levels. The end values are: for Case 1, 1.017; for Case 2, 1.02; for Case 3, 1.023; for Case 4, 1.027; for Cases 5 and 6, 1.03.

Figure 3.17 and Figure 3.18 illustrate the hypothesis on the remodelling of collagen fibres (for the media $\lambda_{C_M}^{max}$ and the adventitia $\lambda_{C_A\gamma}^{max}$ respectively) and follow the pattern seen in Chapter 2; it should be noted that the maximum values of the collagen stretch distributions are drawn here. The geometry is initially perturbed by the

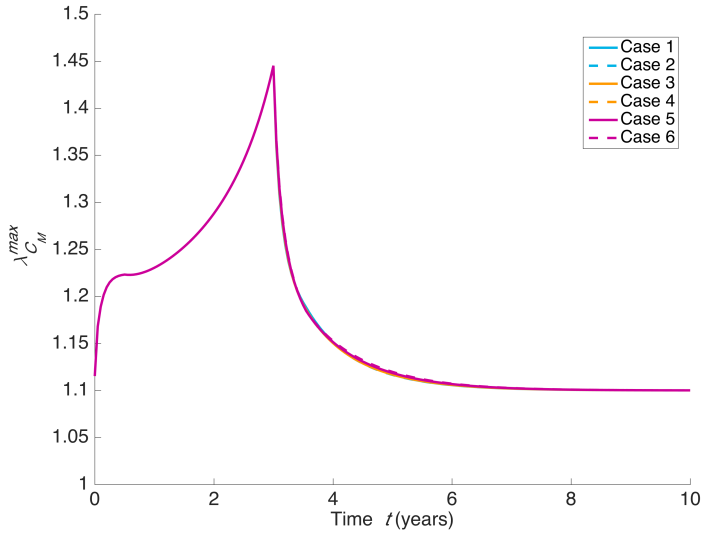

Figure 3.17: The maximum medial collagen stretch $\lambda_{C_M}^{max}$ initially increases from the value of maximum attachment stretch ($\lambda_{C_M}^{AT} = 1.1$), as the circumferential stretch increases during the first three years of degradation and remodelling. As growth and adaption takes place and the geometry stabilises, λ_{C_M} decreases and by the end of the simulation returns towards $\lambda_{C_M}^{AT}$.

degradation of the media and this results in an increase of circumferential stretch, which in turn results in an increase in the maximum values of collagen stretches. $\lambda_{C_M}^{max}$ reaches a maximum of around 1.45 and $\lambda_{C_A\gamma}^{max}$ of around 1.33. The peak for the media seems physiologically unrealistic; however, it can be explained due to the abrupt loss of its fibre mass density, and essentially its lost role to load bearing by the end of Year 1. As the remodelling takes place, i.e. the recruitment stretch distributions for both layers are updated and the evolution of the attachment stretch distribution is allowed for the adventitia, collagen stretches start decreasing and eventually they can be seen returning to attachment levels by the end of the simulation; for the media layer that corresponds to the initial maximum attachment stretch $\lambda_{C_M}^{AT}$ of 1.1 and for the adventitia that corresponds to the updated maximum attachment stretch $\lambda_A^{AT}|_{final}^{max}$ of 1.1, from the initial maximum attachment stretch value $\lambda_A^{AT}|_{initial}^{max}$ of 1. The evolution of these collagen stretches appears quantitatively almost identical for the entirety of the simulation for all cases.

Figure 3.19 illustrates the evolution of the Cauchy stress (see Eqn. (3.31)) that takes into account calculations on the remodelled thickness as seen in Figure 3.15. At the beginning of the simulation the contributions to stress are from both elastin

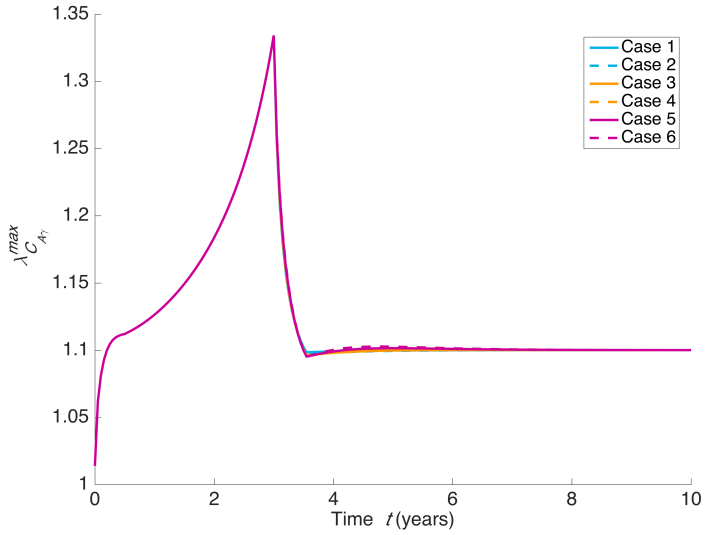

Figure 3.18: The maximum adventitial collagen stretch $\lambda_{C_{A\gamma}}^{max}$ initially increases from the value of maximum attachment stretch ($\lambda_A^{AT}|_{initial}^{max} = 1$), as the circumferential stretch increases during the first three years of degradation and remodelling. As growth and adaption take place and the geometry stabilises, $\lambda_{C_{A\gamma}}^{max}$ decreases and by the end of the simulation tends towards the updated value of $\lambda_A^{AT}|_{final}^{max}$ at 1.1.

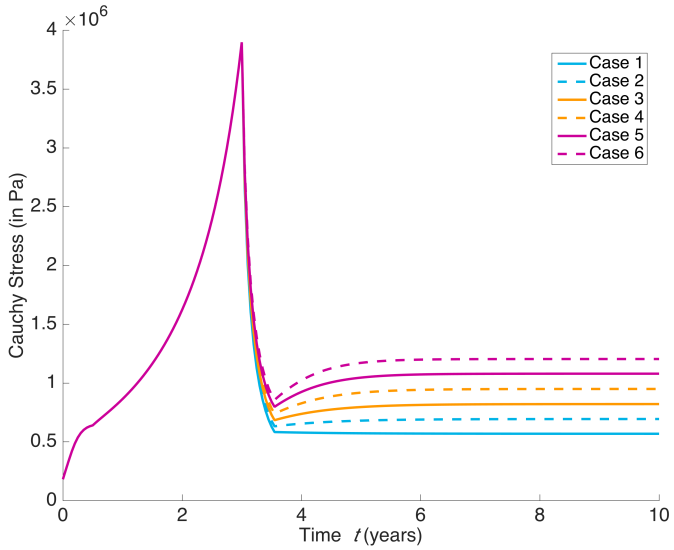

Figure 3.19: This calculation of the Cauchy stress takes into account the remodelled thickness h_{rem}. Cauchy for all cases increase during the first three years of media degradation and remodelling. After reaching a peak value before the end of the first three years, Cauchy stress reduces and stabilises in a range of 0.57-1.2MPa.

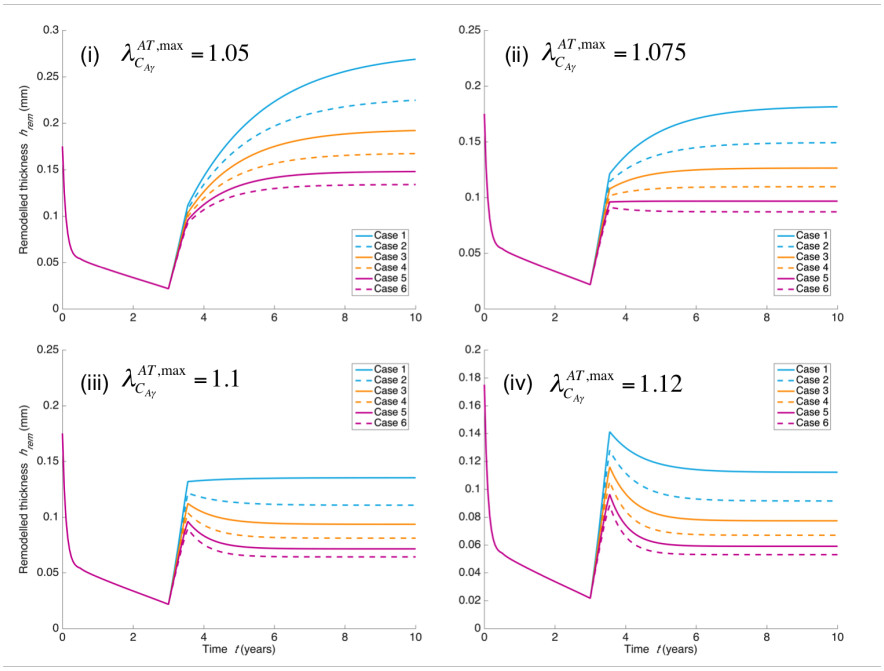

Figure 3.20: Comparison of the evolution of remodelled thickness h_{rem} for different result sets of maximum final attachment stretch values $\lambda_A^{AT}|_{final}^{max}$. For the sets with lower $\lambda_A^{AT}|_{final}^{max}$, the final range of h_{rem} is observed higher, with an overall range of $0.05-0.133$mm.

and collagen fibres (and the Cauchy stress equals 0.2MPa for all cases). As the media degrades, the circumferential stretch increases and the remodelled thickness decreases. Consequently, an increase in the Cauchy stress is observed during the first three years of the simulation (of around 3.8MPa for all cases). As the geometry stabilises, adventitial collagen is gradually the only stress contributor, and as the collagen stretches of the adventitia (seen in Figure 3.18) decrease and return to the updated attachment stretch distribution, while the normalised mass densities stabilise as seen in Figure 3.14, a variation in the end values of the Cauchy stress is observed amongst the cases, with a range between 0.57MPa for Case 1 and 1.2MPa for Case 6.

The simulation set presented so far investigated varying cases of width for the final attachment stretch distribution, assuming the same final maximum value of attachment stretch. I would also like to present and compare some of the results for a varying choice of $\lambda_A^{AT}|_{final}^{max}$, according to the description in §3.5.2, driven from the 1D investigations in §3.4. I focus on comparing the evolution of remodelled thickness h_{rem} in Figure 3.20 and cyclic stretches λ_{CYC} in Figure 3.21. It is noted that

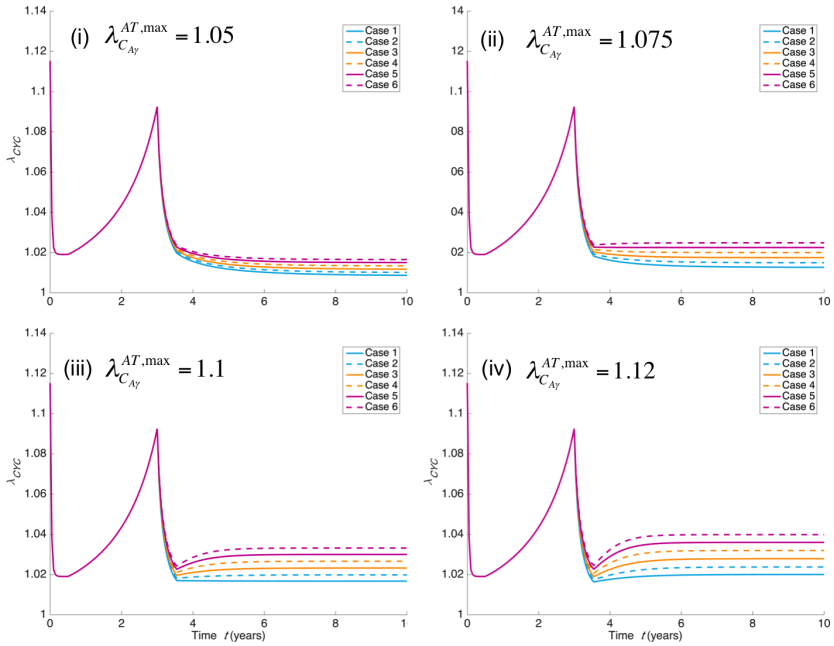

Figure 3.21: Comparison of the evolution of cyclic stretches λ_{CYC} for different result sets of maximum final attachment stretch values $\lambda_A^{AT}|_{final}^{max}$. For the sets with higher $\lambda_A^{AT}|_{final}^{max}$, the final range of λ_{CYC} is observed wider and higher, with an overall range of $1.01 - 1.04$.

the colour code corresponds to the variation in final attachment stretch distribution width within the specific result set and the figures characterise the result set by the chosen value of $\lambda_A^{AT}|_{final}^{max}$. In Figure 3.20 it is observed that, for lower value of $\lambda_A^{AT}|_{final}^{max}$, the range of final values of h_{rem} within the varying widths is higher, while, expectedly, the shape and variation within each result set follows the same pattern as described for the $\lambda_A^{AT}|_{final}^{max} = 1.1$ result set. Result set (i) shows a range of $0.133 - 0.26$mm; result set (ii) shows a range of $0.087 - 0.18$mm; and result set (iv) shows a range of $0.05 - 0.12$mm. Equivalently for cyclic stretches, in Figure 3.21, it is noted that for higher values of $\lambda_A^{AT}|_{final}^{max}$, there is a wider and marginally higher range of final stabilised cyclic stretches (while the behaviour within each case also remains the same as for the result presented in Figure 3.16). Specifically, result set (i) displays a range of $1.01 - 1.017$, result set (ii) of $1.013 - 1.025$ and result set (iv) of $1.02 - 1.04$.

3.6 DISCUSSION

The main motivation for this chapter has been to examine the experimental information available from a specific clinical aneurysmal case in order to inform the 1D analysis. There are several advantages in that respect for this clinical case as I have access to:

- the clinical aneurysmal geometry;
- evidence for the loss of the medial layers (which follows the modelling assumptions for representing aneurysm inception and initial progression);
- mechanical testing data for the behaviour of the remaining collagen fibres;
- a measure for the thickness of the aneurysm.

At the same time, there are several limitations with respect to experimental information that would certainly have contributed to a better validation of the modelling hypotheses and assumptions, such as the healthy arterial geometry, transition arterial wall data between the healthy and final aneurysmal state, *in vivo* measurements of thickness, *in vitro* measurements of recruitment stretch distribution or biaxial mechanical testing data. Some of these (the initial geometry or temporal data) are impossible to acquire for a clinical geometry; others (biaxial and recruitment data) have been applied to other cases (Pandit et al. (2005), Mohan and Melvin (1982)) but are unavailable for the specific case. These might limit the understanding of the observations; for example, the 'ground substance' response that was noted in §3.3 would have been better explained with the help from biaxial data.

Nonetheless, a modelling work flow and framework for the 1D investigation of experimental information has been suggested that creates several points of comparison and cross-validation. In the first part of this chapter, I looked into the two distinct time points and states of the artery; the healthy (from indications of the parent vasculature) against the aneurysmal state, in order to estimate changes in surface areas, projected increases in the mass densities of collagen fibres, values of loaded aneurysmal thickness, cyclic stretches and final attachment stretch distributions, under the simplifications of a 1D configuration.

In the second part, the 1D aneurysm evolution model was adapted to predict the evolution of the geometry and of the mechanical properties of the adventitial

collagen, making use of the estimated material parameter for the adventitial collagen and of the aneurysmal adventitial collagen attachment stretch distributions, from the analysis of the first part. The range of final remodelled thicknesses were also utilised from the first part as a modelling target for the evolution model of the second part, combining it with physiologically expected ranges for circumferential stretch, cyclic stretch and Cauchy stresses, as well as the modelling aim to return the system to a (new) homeostatic state of aneurysm stabilisation.

For the purposes of understanding the role of adventitia as the initially protective sheath that gradually becomes the primary load-bearing constituent within the model, the ranges of such role evolution were mathematically investigated, by varying the final maximum value of attachment stretch distribution, as well as the distribution's final width. It is noted that, regardless of the choice of width and maximum value, the evolution of the attachment stretch distribution achieves the return of collagen stretches to attachment levels and the increase of circumferential stretch to approximately the same final levels. However, there are differences observed with respect to the growth of adventitial collagen fibres and, consequently, the final Cauchy stresses and remodelled thicknesses, depending on the assumption of the final attachment stretch distribution. This variation is based on the fact that aneurysm stabilisation is the result of the combination from the G&R of the adventitial collagen fibres. A narrower final attachment stretch distribution or one with a larger final maximum attachment stretch implies that more fibres are recruited at higher stretches at the final new homeostatic state. That further implies that, for the system to stabilise, there is limited need for an increase in the quantities of fibres that are produced, and vice versa. It should be noted that a skew in the assumptions of the attachment stretch distributions have not been considered, since the investigated range of widths and maxima can adequately represent the investigation of the distribution of final attachment stretches.

From those two approaches, it is possible to compare the predicted increases in collagen mass densities and loaded thickness. The estimations of increased collagen density from §3.1.1 were 6.55 and 12.25. §3.5.3 predicts lower ranges, with the result case (i) (where $\lambda_A^{AT}|_{final}^{max}$ is at the lowest value of 1.05) being the closest to this predicted range $(5.6-11)$. I also have the range of predictions of loaded thickness from the inflation of the aneurysmal tissue to physiological pressures in §3.4 and from the 1D evolution model in §3.5.3. Across the result sets presented, there

are several cases that fall within the predicted range from §3.4 and those cases are summarised in Table 3.10.

Central to the investigation in this chapter was to approximate a value for the material parameter of the adventitial collagen. With the addition of the complexity in fibre orientation and gradual recruitment, I have attempted to make an informed decision on this value specific to the behaviour of collagen in the aneurysmal tissue (Table 3.11), even though biaxial mechanical testing data might have rendered a more accurate approximation. With that calculation it is possible to feed the evolution model and update it from previous versions, where the value choice was not based on specific data.

3.7 CONCLUSIONS

Table 3.10: Overview of final adventitial collagen attachment stretch distributions from the 1D evolution model that predict h_{rem} within the predicted ranges on the 1D configuration of the aneurysmal tissue (§3.4).

Summary of final attachment stretch distributions			
$\lambda_A^{AT}\|_{final}^{max}$	w_{final}	h_{rem} *(in mm)*	λ_{CYC}
1.12	0.12	0.1122	1.02
1.01	0.1	0.135	1.0167
1.01	0.8	0.1107	1.0198
1.075	0.045	0.1265	1.0175
1.05	0.0001	0.13397	1.0165

Table 3.11: Value of adventitial collagen material parameter, to be used in the following 3D modelling framework.

Adventitial Collagen Material Parameter
$K_{C+} = K_{C-} = 11.95 MPa$

This chapter developed the 1D modelling framework, introduced in Chapter 2, around a presented clinical intracranial aneurysm. The main aim was to determine the material parameter of the adventitial collagen by fitting experimental uniaxial

testing data of the aneurysmal tissue to a constitutive mechanical model of the arterial wall (Figure 3.11). *In vivo* information on the 3D geometry and *in vitro* measurements of tissue thickness created points of comparison for the theoretical modelling projections. The 1D evolution model was updated to take into account: (1) collagen fibre reorientation and alignment; (2) a gradual recruitment of fibres to load bearing; (3) a temporal evolution in the attachment stretch distribution of the adventitial collagen, in order to represent the transition in the mechanical role of the adventitia, from a protective sheath, in healthy conditions, to a primary load-bearer, which can be observed in this specific clinical case. These updates in the implementation of the 1D model of aneurysm evolution illustrated, amounting to the conclusions of Chapter 2, the importance of defining homeostasis for arterial mechanobiology and allowing its definition to adapt to changing arterial conditions. The findings in the 1D evolution simulation stress the effect of the attachment stretch distribution on cyclic stretch and collagen fibre growth. Later on in the thesis, I will focus further on proposed hypotheses for a link between cyclic stretch and growth (Chapter 5). Based on the projected values of remodelled thickness from the 1D evolution model result sets, possible final adventitial attachment stretch distributions are identified (Table 3.10), which result in final remodelled thickness comparable to the calculations from the aneurysmal tissue.

A central difficulty in the validation of mathematical models of aneurysm evolution is the lack of empirical knowledge both on the inception and the transitional stages of aneurysm development. In this chapter, I present a novel work flow that results in the full parameterisation of the modelling framework by utilising experimental findings for the mathematical hypotheses of aneurysm arterial mechanobiology, and particularly regarding the adaptive role of the adventitial collagen. The next chapter introduces further the clinical case, as well as an experimental animal model case, in order to build the FSG modelling framework required to test the G&R hypotheses (as have been presented in this chapter and in Chapter 2) for complex 3D geometries.

CHAPTER 4

METHODOLOGY FOR APPLICATION OF COMPUTATIONAL MODELLING IN 3D ANEURYSM GEOMETRIES

The interaction between experimental and computational work is required in order to accurately sophisticate the representation of mechanobiology of the vasculature. Even though qualitative data from experimental settings can help us draw certain conclusions about the evolution of parameters important for aneurysm growth, it is quantitative data that will directly inform the suggested computational models in order to test my hypotheses of tissue G&R in aneurysm disease. Chapter 3 illustrated the importance of such investigations. Following the analyses in 1D of the previous two chapters, this chapter introduces the implementation of an aneurysm evolution model in a 3D setting, where real complex geometries and tissue data can be utilised to test G&R hypotheses. For this purpose the previously developed Fluid-Solid-Growth (FSG) 3D framework (Watton et al. (2009a) and Watton et al. (2011)) was adapted. This chapter presents extensive modifications to FSG enabling a novel study of specific aneurysm cases and the mechanical representation of the arterial wall. The aim of the work in this chapter is therefore to investigate the influence of the following on aneurysm growth:

1. the gradual recruitment of collagen fibres to load bearing;

2. families of collagen fibre orientation in both the medial and the adventitial layer;

3. hypotheses on links between elastin degradation and flow;

4. the evolution of attachment stretch distribution for the adventitial collagen (following the degradation of the medial layer);

In addition, these adaptations enable us to test novel hypotheses on the links between cyclic deformation and collagen growth. A direct interaction between the FSG framework and two aneurysm cases, a rabbit model one and a clinical one (introduced in Chapter 3), present a unique opportunity to test the validity of the modelling hypotheses.

4.1 FSG OVERVIEW

The chapter starts by overviewing the modelling steps of the FSG framework, with the illustrative help of Figure 4.1. The cycle of the proposed computational modelling involves a quasi-static structural analysis that renders the equilibrium deformation fields for the systolic and diastolic configurations (Figure 4.1(i)). Stress, stretch and cyclic deformations under given pressure and boundary conditions are calculated. Computational fluid dynamic analysis follows; ANSYS ICEM is used to integrate the initial structural domain geometry (at systole and diastole) into a physiological geometrical domain and subsequently the volumetric domain is meshed; the flow is then solved in ANSYS CFX v14, provided that the flow rate and pressure boundary conditions are defined (Figure 4.1(ii)). Tecplot 360 is then used so that the resulting haemodynamic parameters (such as wall shear stress (WSS)) are interpolated for each node of the structural mesh (Figure 4.1(iii)). This is implemented so that the G&R algorithms (Figure 4.1(iv)) use the mechanical stimuli to adapt the tissue and update the systolic and diastolic deformation fields, leading back to step (i) of Figure 4.1. The previous steps are repeated; as a result, the aneurysm geometry develops.

This computational modelling framework aims to represent aneurysm evolution in 3D, taking into account complex geometries and realistic representations of the mechanical environment due to blood flow, while adapting the modelling hypotheses on G&R in a 3D representation of the arterial wall. §4.2 and §4.3 present

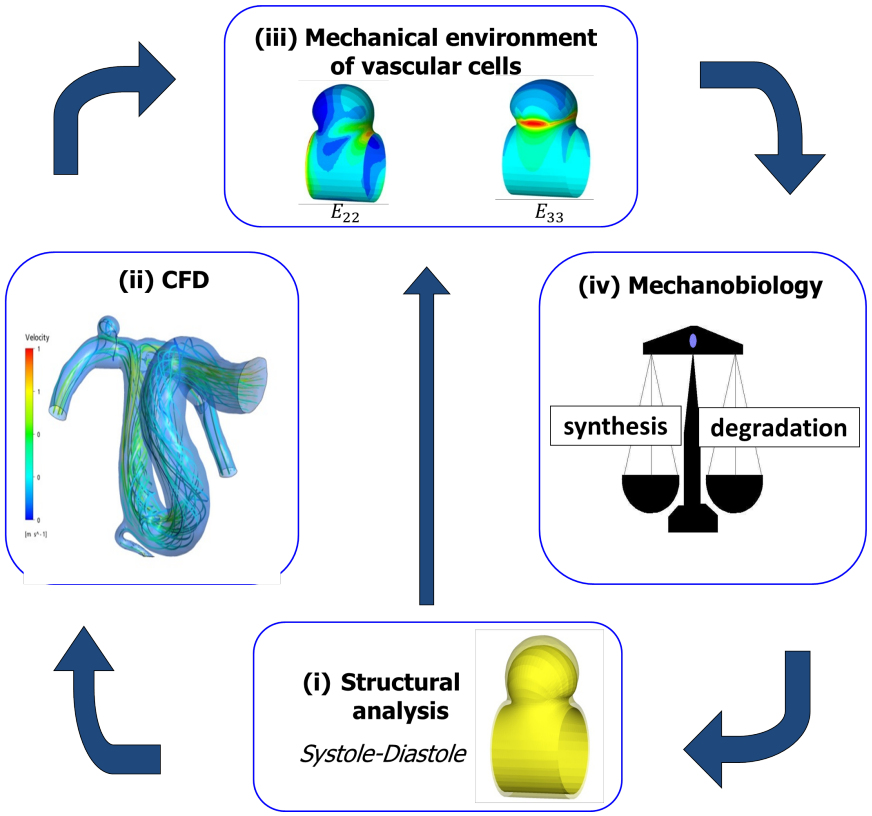

Figure 4.1: Illustrative overview of the Fluid-Solid-Growth framework consisting of: (i) structural analysis; (ii) CFD; (iii) local mechanical environment of vascular cells; (iv) growth and remodelling algorithms for the description of synthesis and degradation of arterial constituents.

the two aneurysm geometries that my 3D analysis will focus on; the clinical case, introduced in Chapter 3, and a rabbit aneurysm case, respectively. §4.4 describes a methodology for the vessel reconstruction of these two geometries, resulting in the creation of geometries that closely represent the initial healthy state of those two arterial environments; these are going to be used as the geometric starting points of the FSG framework. §4.5 introduces the structural analysis corresponding to step Figure 4.1(i). §4.6 summarises the computational fluid dynamics analysis (CFD) employed for the FSG framework and §4.7 outlines the updated 1D G&R hypotheses for the 3D setting.

4.2 CLINICAL ANEURYSM MODEL

The clinical aneurysm was first introduced in Chapter 3. This case was part of a study that aimed to investigate the collagen fibre architecture from tissue samples of a group of clinical aneurysms (Robertson et al., 2015). The 3D geometry of the internal carotid artery (Figure 3.2) was built from 3D rotational angiography images (3DRA images acquired from different angles around the patient at the Allegheny General Hospital, Pittsburgh, US). The aneurysm dome investigated here was retrieved after surgical intervention on the unruptured aneurysm in the hospital and the harvested tissue was stored and tested at the University of Pittsburgh. Specific clinical information (gender, age, family history, lifestyle and health information) was collected from the consenting patient. The patient was a 27 year old male, whose aneurysm discovery was incidental following a traumatic head injury. There were no signs of drug use, hypertension or diabetes; however, there was a family history of aneurysms, since both the patient's mother and grandmother had previous incidents of cerebral aneurysms.

4.3 RABBIT ANEURYSM MODEL

In vivo experimental aneurysm models are of crucial importance in the efforts to understand more about this vascular disease. They are not only used to gain insight into the mechanisms of initiation, progression and rupture of aneurysms, but also to test aneurysm treatment devices before they are used clinically, to train interventionists at using those endovascular devices and to observe the effects of those devices after application. For example, experimental aneurysm models are used to investigate the possibility of recurrences after endovascular occlusion (Bouzeghrane et al., 2010).

In order for an experimental aneurysm model to be clinically relevant, it should have low surgical and endovascular morbidity, show similarities to human aneurysms in terms of anatomy, physical dimensions, mechanical properties, environment in the area around the aneurysm, and tissue response to changes in the mechanical environment due to blood flow. Moreover, the study of aneurysm progression in experimental models can only be useful when spontaneous thrombosis does not take place following the initiation of an aneurysm and when sufficient time is taken for an experimental aneurysm to fully enlarge (Fujiwara et al., 2001).

Consequently, the choice of an experimental aneurysm model to provide useful information about the progression of aneurysm disease can be a very difficult task.

As aneurysms rarely occur naturally in laboratory animals used for experimentation, aneurysms need to be induced. Various animals can be used for such experiments, such as dogs, rabbits, rodents or swine and there are different methods to induce the aneurysm. One of those cases is the elastase-induced rabbit aneurysm model, originally deviced at the Mayo clinic (US) by Kallmes et al. (2002), Ding et al. (2006), and used in the research group at University of Pittsburgh led by Professor Anne Robertson (Zeng et al., 2011), illustrated in Figure 4.2. According to this protocol, saccular aneurysms are induced in New Zealand white rabbits by introducing porcine elastase in the lumen of the Right Common Carotid Artery (RCCA) via a balloon catheter. Elastase is supplied for approximately 20 minutes before the catheter is removed. The reason for the elastase supply is that it is an enzyme known to break down elastin fibres; an event observed during aneurysm formation. Following the catheter system application, the RCCA is occluded; as a result, bulges along the RCCA are formed which resemble aneurysms.

The advantages of using rabbits for the experiments are that they are easy to handle and there is long-term survival following the process of inducing the aneurysm. Moreover, thrombus formation is not often observed, although the arterial wall sometimes thickens during aneurysm growth. The similarities between aneurysm growth as observed in the elastase-induced experimental setting and human aneurysms are well documented. Morphological similarities to saccular aneurysms have been identified, regarding aneurysm dome height and width, neck diameter and parent artery diameter; it has been suggested that saccular aneurysms in this model are geometrically comparable to human intracranial aneurysms (Short et al., 2001). Furthermore, computational fluid dynamic studies have been carried out to examine the similarity of haemodynamic properties (Zeng et al., 2011), such as the distribution and range of pressures, WSS, oscillatory stress index and transient recirculation regions within the aneurysms, which were found to be comparable to human intracranial aneurysms. On the other hand, aneurysm size in elastase induced rabbit models can be unrealistically large in some cases and when angiograms are used, that requires the sacrifice of the animal for arterial access. Moreover, there is a chance of complications during the experimental process, such as risk of stroke, iatrogenic laryngeal hemiplegia (Villano et al., 2012). However,

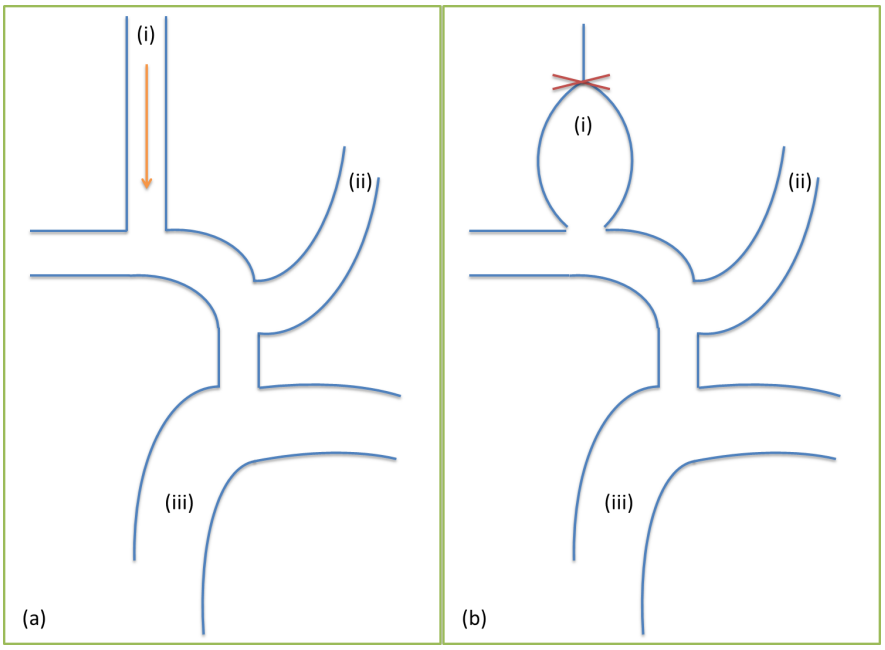

Figure 4.2: Illustration of elastase-induced rabbit aneurysm model protocol. The vasculature of interest is: (i) Right Common Carotid Artery, (ii) Left Common Carotid Artery and (iii) Aortic Arch. (a) At the beginning of the experiment, elastase is introduced via a catheter in the lumen of the Right Common Carotid Artery. Following the catheterisation (b), the Right Common Carotid Artery is occluded, elastin in the area is degraded and an aneurysmal bulge is developed.

in general, elastase-induced aneurysm rabbit model provides a good experimental case of investigating aneurysm growth.

The suggested experimental setting is unique because of the range of information that can be collected from the results. A 3D reconstruction of the aneurysmal geometry (as well as of the parent vasculature) may be obtained using 3DRA and a commercial package (MIMICS). These images can also provide more specific information about the physical dimensions of the animal's aneurysm (for example, aneurysm height and length). Following aneurysm formation, surgical intervention renders tissue samples from the aneurysmal RCCA. These samples are loaded onto a uniaxial test machine, with an actuator and a force cell that hooks onto the tissue sample. Stress-stretch curves can be obtained as the tissue undergoes increasing strain and it can be also tested to failure. The distinctive feature of this testing is that while loading occurs, it is possible to acquire images of the arterial wall's structure using multi-photon microscopy (MPM), in the same way that was introduced for the clinical case in Chapter 3. Such arterial geometric reconstruction and mechanical

testing are performed at the research laboratory of Prof. Anne Robertson (Swanson School of Engineering, University of Pittsburgh). This enables the observation on how the behaviour of the arterial constituents (elastin and collagen fibres) change as loading occurs. Using MPM has a great advantage of providing images of the arterial structure through the thickness of the wall, enabling comparisons between the different arterial layers (media versus adventitia). Because there is no need for manual slicing to be able to compare the arterial layers, this setup has an additional advantage as it leaves the tissue whole for further histological investigations, if they are required.

One of the most important reasons for conducting experimental aneurysm models, especially in order to be used in parallel with suggested theoretical models of aneurysm progression, is to collect temporal data. Previous research has focused on haemodynamic forces and biomarkers of vascular remodelling at various stages of the induced aneurysm development (Kadirvel et al., 2007). The way that this is done in the aforementioned experimental setting is by collecting strain-testing and imaging tissue samples from rabbit aneurysms at different time stages. There are, for example, tissue samples from a 'one-day aneurysm', 'seven-day aneurysm' and 'chronic aneurysm' (which implies the time duration of approximately a month after elastase supply and arterial occlusion). For the purposes of comparison, control tissue samples are also collected, most usually from the Left Common Carotid Artery (LCCA).

Tissue samples that undergo histological studies can also provide useful information about the composition of the wall during different stages of the aneurysms, that in turn would allow the categorisation of aneurysm types according to that composition, but also set hypotheses about the different stages of aneurysm evolution. For example in Frösen et al. (2004), four aneurysm wall types were identified, that differ in terms of the thickness, the presence of ECs, the organisation of SMCs and the existence of thrombus. Similarly with the histological study of the tissue samples from the elastase-induced animal model, and depending on the choice of staining, temporal data can be observed with regards to the presence of nuclei, the composition of cytoplasm and ECM, the presence and density of muscle fibres and even on a molecular level, the structures with higher proportions of certain carbohydrate macromolecules (such as glycogen and proteoglycans). This information can be helpful in order to draw conclusions about cell function (ECs, SMCs in the

medial layer and fibroblasts in the adventitial layer) during aneurysm evolution.

For the purposes of the analysis, I will be looking into a rabbit aneurysm model case, kindly provided by the research laboratory of Prof. Anne Robertson (Swanson School of Engineering, University of Pittsburgh). The geometry is seen in Figure 4.3, where the 3D *in vivo* reconstruction of the rabbit aneurysmal geometry allows the observation of the shape of the occluded RCCA post catheterisation from different perspectives. This is considered a 'chronic' aneurysm, given that the geometry is captured past the first month of catheterisation and arterial occlusion. LCCA (Figure 4.3(ii)), in the parent vasculature, is expected to have had similar dimensions to the healthy RCCA; therefore, it can be used as a control geometry against the occluded RCCA (Figure 4.3(i)). Consequently, it can be observed that the RCCA has, expectedly (Fujiwara et al., 2001) deformed and increased in size.

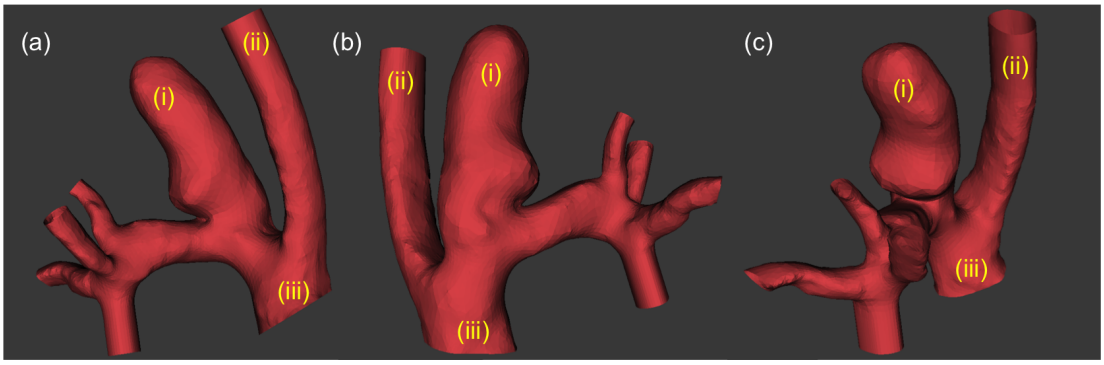

Figure 4.3: Presentation of rabbit aneurysm geometry (3D reconstruction image provided by Prof. Anne Robertson's laboratory, Swanson School of Engineering, University of Pittsburgh. (a), (b) and (c) are three different orientations of the same geometry, where the occluded RCCA (i), the healthy LCCA (ii) and the edge of the aortic arch (iii) can be identified.

An interesting observation, which creates a focus for the analysis in this thesis, is a secondary growth seen in the occluded arterial branch. As noted in Figure 4.4(a), the aortic arch is the inlet to the blood flow. RCCA has on the whole (compared to the LCCA) increased in radius; however, there is an additional 'bulge' on the downstream wall of the RCCA. It is not straightforward, and there is no precisely relevant literature, as to why this additional growth forms. Kadirvel et al. (2010) investigated the effect of aspect ratio. Aspect ratio for the rabbit model is defined as the height of the occluded arterial segment to neck width; it is considered high for values higher than 2.4 and low for values lower than 1.6. Histological tests of rabbit aneurysmal

tissue of both high and low aspect ratio showed that, for rabbit aneurysms of high aspect ratio, arterial walls are observed that have lost their layered structure, being primarily composed of fibrotic tissue and the distal walls of the occluded artery are seen to be thinner and largely collagenous compared to the proximal wall. Under these criteria, the presented case is one of high aspect ratio. The 3D investigations (introduced in this chapter and applied in Chapter 6) will focus on examining the effect of haemodynamics and hypotheses of G&R on the differential aneurysmal growth observed in this rabbit aneurysm model.

As part of this haemodynamics investigation, experimentally calculated flow boundary conditions will be taken into account. Figure 4.4(a) specifies the definition of inlet and outlets in the presented rabbit aneurysm geometry. Arterial rabbit-specific waveforms were captured *in vivo* from transthoracic duplex Doppler sonography, in the LCCA and the distal parent arteries, by Prof. Anne Robertson's laboratory for the case. Table 4.1 shows the average flow velocity for each outlet and Figure 4.4(b) shows the variations of this average velocity over 2 cardiac cycles (each cardiac cycle's time of 0.333s) in the form of a normalised magnitude, which is to be multiplied by the average velocity of the corresponding outlet from Table 4.1. For the inlet boundary condition, an average pressure of 3kPa is set, characteristic of the arterial location. This information will allow analysis of the haemodynamics of the occluded arterial branch, with a focus on the differences between steady and transient flow.

Table 4.1: Experimentally calculated average flow velocities for outlets of rabbit aneurysm model (provided by the lab of Prof. Anne Robertson, Swanson School of Engineering, University of Pittsburgh).

Average flow velocity for outlet boundaries	
Outlet number	Average velocity (in $\frac{m}{s}$)
1	0.49
2	0.277
3	0.184
4	0.23
5	0.168

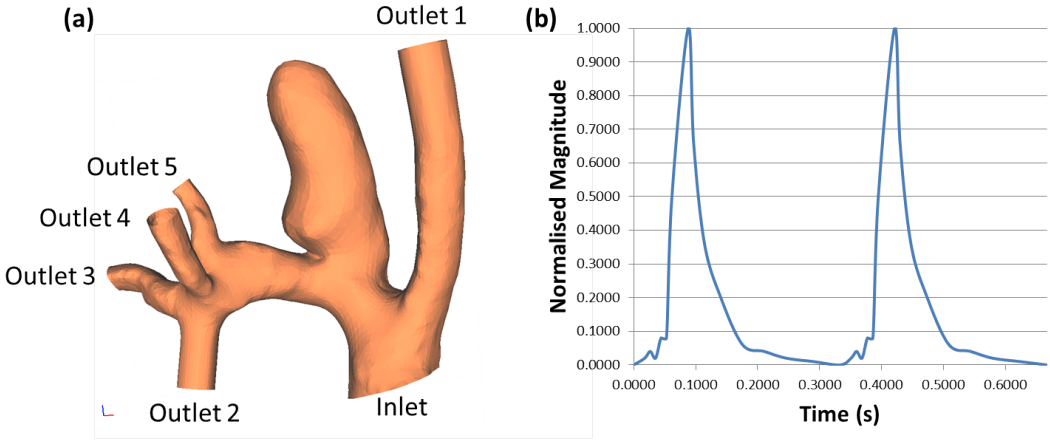

Figure 4.4: (a) specifies the inlet and outlets of the presented rabbit aneurysm geometry and (b) shows the variations of flow velocity over two heart cycles (with a total time of 0.666s), normalised for any of the outlets. Those variations were experimentally calculated *in vivo* with Doppler velocimetry (provided by the laboratory of Prof. Anne Robertson, Swanson School of Engineering, University of Pittsburgh).

4.4 GEOMETRICAL RECONSTRUCTION OF ANEURYSMAL GEOMETRIES

This section of the chapter overviews the steps taken in order to 'reconstruct' the $t = 0$ geometrical configuration of the clinical aneurysm case and the rabbit aneurysm case. The process follows the steps introduced by Chen (2014), Selimovic (2013) and presented in Chen et al. (2013) and Aparício et al. (2014), adapted for the specificity of the two aneurysm cases presented.

The aim of the process is to substitute the section of the 3D reconstructed image that includes the aneurysmal area with a smooth cylindrical region which will represent a healthy arterial segment for the beginning of the 3D simulations and along which the structural model of G&R will be applied, as presented in §4.5. This smooth cylindrical region, which will be called 'aneurysm cylinder', needs to be connected with the parent vasculature, which will be retained as initially provided so that there is a good representation of the neighbouring geometry of the aneurysm and it is possible to investigate the haemodynamics of the total area, as was captured *in vivo*. Consequently the following steps describe the creation and position of the aneurysm cylinder in the observed aneurysmal area and the connection of this cylinder with the rest of the geometry.

Figure 4.5 illustrates the steps for the vessel reconstruction process for the rabbit aneurysm case and Figure 4.6 illustrates the steps for the clinical case.

4.4.1 Choice of boundary planes

Firstly, the 3D reconstructed geometry is imported in @neufuse; this is an open source tool built within the context of the '@neurist' project (a European initiative to integrate biomedical informatics in the management of cerebral aneurysms, `http://www.aneurist.org//index.php`), for the purposes of segmentation, multimodel registration and advanced visualisation techniques. On @neufuse, a skeleton for the aneurysmal geometry is created (seen in Figure 4.5(a) for the rabbit case and in Figure 4.6(a) for the clinical case). The skeleton will help with choosing planes of separation between the aneurysmal area and the neighbouring vasculature, as well as to create the aneurysm cylinder and the connecting regions.

Figure 4.5(b) shows the choice of planes to separate those areas for the rabbit aneurysm model; this was achieved by clipping the rabbit aneurysm geometry on @neufuse. Figure 4.5(b-i) and (b-ii) indicate the boundaries chosen for the aneurysm cylinder. Considering the direction of the flow from the parent vessel, the plane shown in Figure 4.5(b-i) will be called the cylinder's outlet boundary and the one in Figure 4.5(b-ii) the cylinder's inlet boundary. Since the aneurysm cylinder is a straight cylindrical area, the cylinder's inlet boundary is chosen to determine the orientation of the aneurysm cylinder and the Figure 4.5(b-i) as an indicator for the expected length of the cylinder. This step was manually executed and improved to optimise the orientation and position of the aneurysm cylinder against the aneurysmal geometry. Additionally, another plane is chosen (illustrated in Figure 4.5(b-iii)), closer to the parent vessel; that will be called the connecting region boundary. This, and the cylinder's inlet boundary, will be the defining planes for creating a connecting region between the parent vessel and the aneurysm cylinder.

Figure 4.6(b) shows the similar procedure for the clinical case. In this case, there is both an upstream and a downstream connecting region, for which clipping planes were manually chosen. Figure 4.6(b-i) indicates the boundary for the upstream connecting region, Figure 4.6(b-ii) indicates the boundary for the cylinder's inlet, Figure 4.6(b-iii) indicates the boundary for the cylinder's outlet and Figure 4.6(b-iv) indicates the boundary for the downstream connecting region. The planes were carefully chosen so that the natural and complex tortuosity observed in the initial

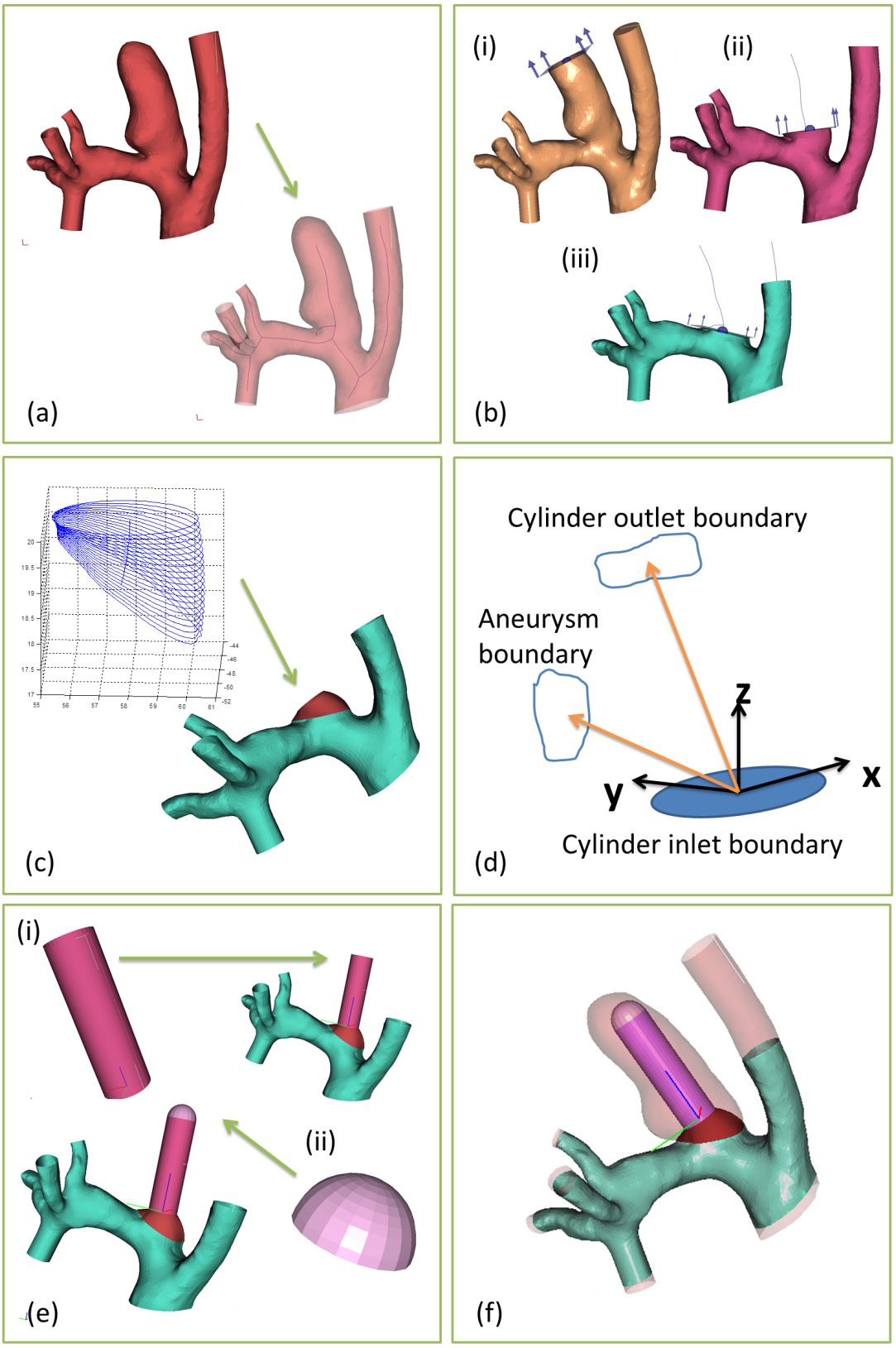

Figure 4.5: (Continued on the following page)

Figure 4.5: Illustration of the steps for the reconstruction of the rabbit aneurysm to a healthy initial state. (a) A skeleton of the aneurysmal geometry is created on @neufuse; (b) the geometry is clipped to define boundaries of the (i) aneurysm cylinder's outlet, (ii) aneurysm cylinder's inlet and (iii) connecting region; (c) propagating closed curves are created for a smooth surface to connect the parent vessel with the aneurysm cylinder; (d) a transformation of the Cartesian coordinate axes takes place, accounting for the downstream direction for the positive z-axis and the direction of the secondary aneurysm growth for the positive y axis; (e) (i) the aneurysm cylinder is constructed and positioned on the rabbit geometry and (ii) the geometrical reconstruction is completed by the position of a hemispherical surface to represent the arterial branch occlusion; (f) the completed arterial reconstruction is presented against the initial aneurysmal geometry.

geometry is sustained, while defining well the aneurysmal area with the position and orientation of the aneurysm cylinder.

4.4.2 Construction of connecting regions

The next step describes the creation of a connecting surface between the parent vasculature and the aneurysm cylinder. For those steps the segmented geometries from both cases were required; specifically, Figure 4.5(b-ii) and Figure 4.5(b-iii) for the rabbit case and Figure 4.6(b-i) and Figure 4.6(b-ii) for the clinical case. Those geometries were imported into Tecplot (a visual data analysis tool) and the boundary curves for the connecting region and the cylinder's inlet were extracted. The discrete points of the corresponding boundaries and the skeletons (as were created earlier on in @neufuse) are then imported in a MATLAB algorithm (presented in Chen (2014), Selimovic (2013) and summarised here), which will create the connecting region between the parent vessel and the aneurysm cylinder. The algorithm recreates the cylinder's inlet boundary into a circular one, with the same centre as the input one and a radius that was chosen as the healthy initial radius from measurements of the neighbouring vasculature.

- For the rabbit case, the systolic radius was chosen as $r = 1.5mm$
- For the clinical case that was chosen as $r = 2mm$ (as was reported in Chapter 3).

Using a cubic polynomial, a new skeleton is interpolated between the two

boundaries. Along this new skeleton, a Frenet frame is defined, namely a group of tangent, normal and bi-normal unit vectors in a local orthonormal coordinate plane. Closed curves are then created along the new skeleton between the two boundaries to create a smooth transition between the two of them, where a simple linear interpolation method between the discrete points of the two boundaries was applied to determine the radial vectors of the propagating closed curves. An example of the closed curves for the connecting region in the rabbit aneurysm case is seen in Figure 4.5(c). A smooth surface is created by those boundaries via triangulation.

- In Figure 4.5(c) it can be seen how the smooth surface is positioned to fit on the parent vessel for the rabbit case. Since most of the arterial branch in the rabbit aneurysm geometry appears aneurysmal, the connecting region had to be carefully chosen to be minimum in size, while allowing the algorithm to create a smooth connecting surface.
- In Figure 4.6(c) the smooth surface created for the upstream connecting region for the clinical case can be seen.

4.4.3 Transformation of the axes

For the purposes of the consistency in the application of the structural model along the aneurysm cylinder, the (0,0,0) point of the Cartesian coordinate system needs to be placed in the centre of the circular inlet to the aneurysm cylinder, with the positive y axis determining the direction of the aneurysm growth (for the rabbit model that would be the direction of the secondary growth) and the positive z axis in the downstream direction of the flow; those axes are schematically shown in Figure 4.5(d) for the rabbit case and in Figure 4.6(d) for the clinical case. In order to achieve this, the position vectors (they will be called $\mathbf{a}$) of the current geometries (of the parent vessel and of the connecting region) need to be rotated and translated, i.e. transformed. The transformation is governed by Eqn. (4.1).

$$\mathbf{a}_{transformed} = \mathbf{R}^{-1} \cdot (\mathbf{a} - \mathbf{t}), \tag{4.1}$$

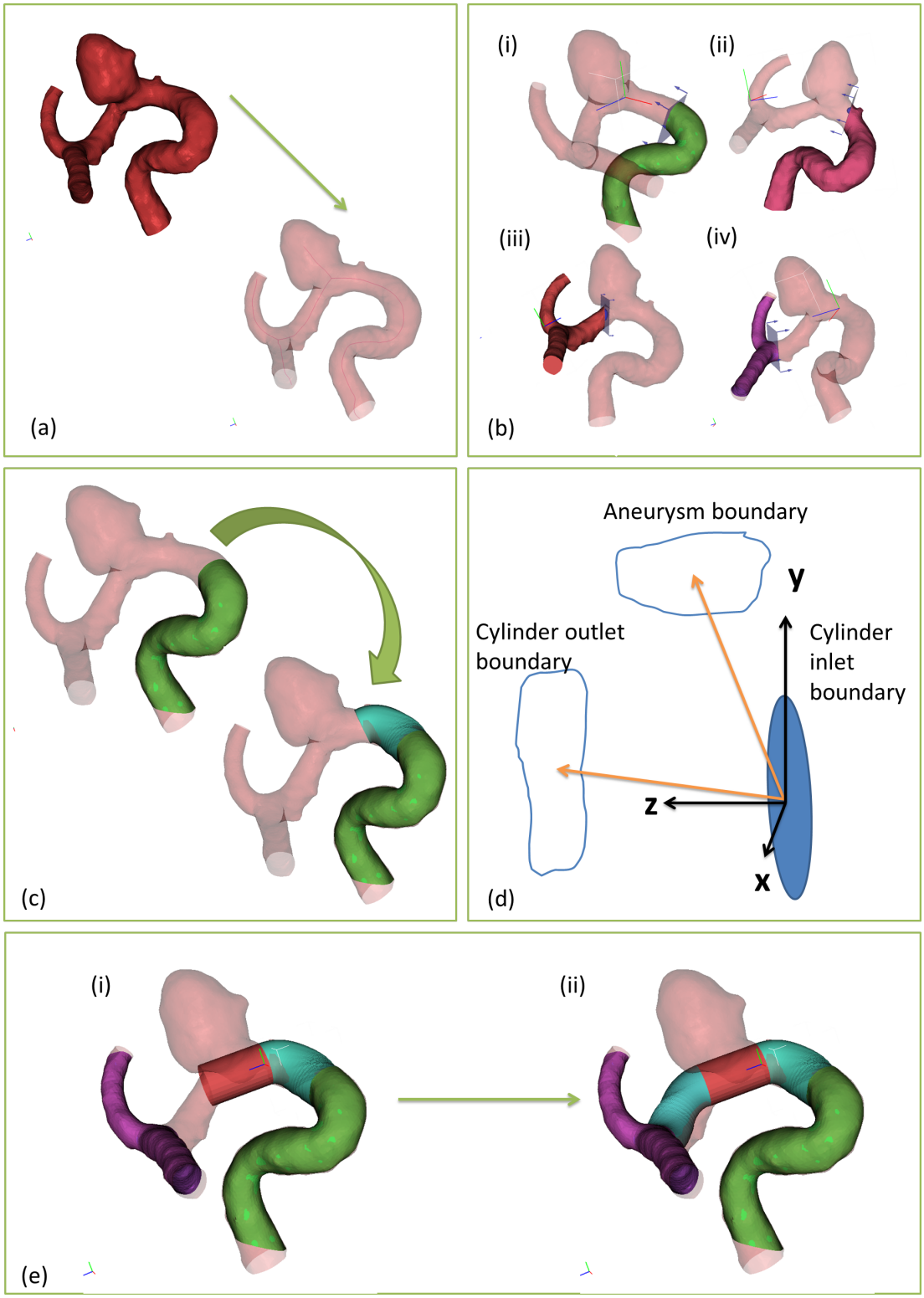

Figure 4.6: (Continued on the following page)

Figure 4.6: Illustration of the steps for the reconstruction of the rabbit aneurysm to a healthy initial state. (a) A skeleton of the aneurysmal geometry is created on @neufuse; (b) the geometry is clipped to define boundaries of the (i) upstream connecting region, (ii) aneurysm cylinder's inlet, (iii) aneurysm cylinder's outlet and (iv) downstream connecting region; (c) propagating closed curves are created for a smooth surface to connect the upstream parent vessel with the aneurysm cylinder; (d) a transformation of the Cartesian coordinate axes takes place, accounting for the downstream direction for the positive z-axis and the direction of the aneurysm growth for the positive y axis; (e) (i) the aneurysm cylinder is constructed and positioned on the rabbit geometry and (ii) an additional smooth surface is constructed to connect the aneurysm cylinder with the downstream parent vessel, where the completed arterial reconstruction can be observed against the initial aneurysmal geometry.

where $\mathbf{a}_{transformed}$ are the transformed position vectors (for each discrete point of the geometries), $\mathbf{R}^{-1}$ is the inverse of the rotation matrix and $\mathbf{t}$ is the translation vector. The rotation matrix is defined as:

$$\mathbf{R} = [\mathbf{X} \quad \mathbf{Y} \quad \mathbf{Z}] \tag{4.2}$$

Z needs to be a unit vector perpendicular to the plane of the cylinder's inlet boundary and with a downstream positive direction. In order to calculate this, the unit vector of the cross product from two vectors on the plane of the cylinder's inlet boundary was selected. In order to ensure the correct positive direction of the vector, a vector from the middle point of the cylinder's inlet boundary to the cylinder's outlet boundary was created (this vector is indicated in Figure 4.5(d) and Figure 4.6(d) for the two cases). The sign of the dot product of those two vectors ensures the accuracy of **Z**.

Y needs to be a unit vector on the plane of the cylinder's inlet boundary with a positive direction towards the aneurysm growth. In order to calculate this, a plane to represent a cross section of the aneurysms was required; a manual clipping of the geometries was therefore repeated (in @neufuse, as was done earlier on) to create a plane, a perpendicular vector of which will approximate the outward direction of the y axis sought. The corresponding boundaries were then extracted, schematically shown in Figure 4.5(d) and Figure 4.6(d) for the two cases. Following the procedure for **Z**, a vector perpendicular to the plane of the aneurysm boundary was calculated. The components of this vector were found in the direction of **Z** and its perpendicular

one and defined the unit vector of the latter as **Y**. **X** can then be calculated as the unit vector of the cross product of **Z** and **Y**. The position vectors of the discrete points were transformed on MATLAB and their triangulation remained the same as before. The new axis system for the two cases is seen in Figure 4.5(e) and Figure 4.6(e).

4.4.4 Construction of aneurysm cylinder

The next step is to create a cylindrical surface to represent the aneurysm cylinder. This is a simple triangulated cylindrical surface, the radius of which is defined to match the connecting region and the length is determined by calculating the distance between the centres of the cylinder's inlet and outlet boundaries. The results of the creation and position of the aneurysm cylinder are seen in Figure 4.5(e-i) and Figure 4.6(e-i).

- From Figure 4.5(b-ii) and (b-i), for the rabbit model case, a length of 9.3mm was calculated.
- From Figure 4.6(b-ii) and (b-iii), for the clinical case, a length of 5.9mm was calculated.

4.4.5 Connection with downstream geometrical segments

The next step of this reconstruction process is to compile the remaining downstream geometrical parts.

- For the rabbit model case, this requires closing the aneurysm cylinder to represent the occluded RCCA. A triangulated hemispherical surface (with the radius of the aneurysm cylinder) was created and positioned symmetrically centred with the cylinder's outlet boundary, as seen in Figure 4.5(e-ii).
- For the clinical case, this requires repeating the process in §4.4.3 for transformation of the downstream segment of Figure 4.6(b-iv) and the process in §4.4.2 to create a connecting region between the aneurysm cylinder and the downstream arterial segment, the result of which is seen in Figure 4.6(e-ii).

Figure 4.5(f) and Figure 4.6(e-ii) present the finalised vessel reconstruction for the rabbit and the clinical case respectively against the original aneurysmal geometries. The reconstruction process aimed to recreate the healthy arterial state before

the development of the aneurysms, informed by the natural tortuosity of the geometry and the neighbouring vasculature.

The resulting geometries from both cases were subsequently imported in Ansys ICEM, where the separate geometrical segments (upstream and downstream of the aneurysm cylinder), created on the previous sections, were connected, inlets and outlets were assigned and surfaces were put over all inlets and outlets. The healthy reconstruction of the geometries are therefore ready to be introduced to the FSG framework (Figure 4.1), where the haemodynamics environment is updated for the entire reconstructed geometry and the aneurysm cylinder determines the area where the structural model of aneurysm evolution and the G&R The following sections summarise the structural, haemodynamics and G&R analysis of the 3D FSG framework. They follow the fundamental hypotheses from 1D modelling as was presented in Chapter 2 and Chapter 3, adapted for a 3D framework, as was presented in Watton et al. (2011) and in Aparício et al. (2014) for abdominal aortic aneurysms and in Selimovic (2013) and Chen (2014) for cerebral aneurysms.

4.5 STRUCTURAL MODEL

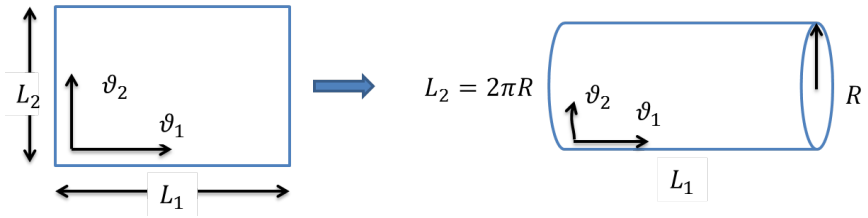

Figure 4.7: Specification of Lagrangian Coordinates ($\theta_1 \in [0, L_1], \theta_2 \in [0, 2\pi R)$) for the 3D computational domain.

A geometric nonlinear membrane theory is adopted to model the steady deformation of the arterial wall (Watton et al., 2004). The unloaded arterial wall is treated as a thin cylinder of undeformed radius R, length L_1, and thickness H. It is subject to a physiological pressure and physiological axial pre-stretch. A body fitted coordinate system is used to describe the cylindrical membrane with axial and azimuthal Lagrangian coordinates $\theta_1 \in [0, L_1]$ and $\theta_2 \in [0, 2\pi R)$, respectively (Figure 4.7). The initial displacement field for mechanical equilibrium can be analytically determined. An aneurysm evolves as the material constituents adapt (via G&R). The principle of stationary potential energy governs displacement field for

mechanical equilibrium, i.e.

$$\delta\Pi_{int} - \delta\Pi_{ext} = 0, \tag{4.3}$$

where $\delta\Pi_{int}$ represents the variation of the internal potential energy stored in the arterial wall and $\delta\Pi_{ext}$ represents the variation of the external potential energy due to the pressure. Strain-energy functions (SEFs) are specified so that $\delta\Pi_{int}$ can be computed.

To quantify the cyclic deformation the geometry of the aneurysm was determined at systolic and diastolic pressures. As the material constituents evolve, the systolic/diastolic deformation fields to satisfy Eqn. (4.3) are updated with a Newton-Raphson method using the systolic/diastolic deformation fields from the previous time-step as initial guesses; the positions of the boundaries of the domain ($\theta_1 = 0, L_1$) in the systolic/diastolic configuration are held fixed as the aneurysm evolves; the neighbouring vasculature is not deformed and the boundaries need not be updated.

Details of the theoretical formulation to describe the deformation of the arterial wall and the numerical formulation to solve (Eqn. (4.3)) can be found in Watton et al. (2004). For the structural simulations, a Lagrangian mesh was used (consisting of 36 x 54 bilinear elements for the clinical case, and 48 x 72 elements for the rabbit case); the Fortran subroutine MA38 (available from the Harwell software library `www.hsl.ac.uk`) was employed to solve the linear system that arises in the Newton iteration, which is required to update the deformation of the arterial wall at successive time steps.

The structural model presented here is the one utilised in Watton et al. (2004). The Holzapfel-Gasser-Ogden constitutive model (Holzapfel et al., 2000) was sophisticated to: (i) explicitly account for the distinct reference configurations of the constituents; (ii) incorporate normalised density variables so that the growth/atrophy of constituents can be simulated. The arterial wall is modelled as two layers.

The SEF for the elastinous contributions in the media is a neo-Hookean one (Watton and Ventikos, 2009) that is multiplied by a normalised spatially and temporally dependent concentration function, denoted $m^E(\theta_1, \theta_2, t)$. This is employed to prescribe the degradation of the elastinous constituents, where $m^E(\theta_1, \theta_2, t = 0) = 1$.

Fields of spatially and temporally dependent collagen fibre recruitment stretch $\lambda^R_{M_p}(\theta_1, \theta_2, t)$ and fibre concentration $m^C_{M_p}(\theta_1, \theta_2, t)$ variables are defined for the me-

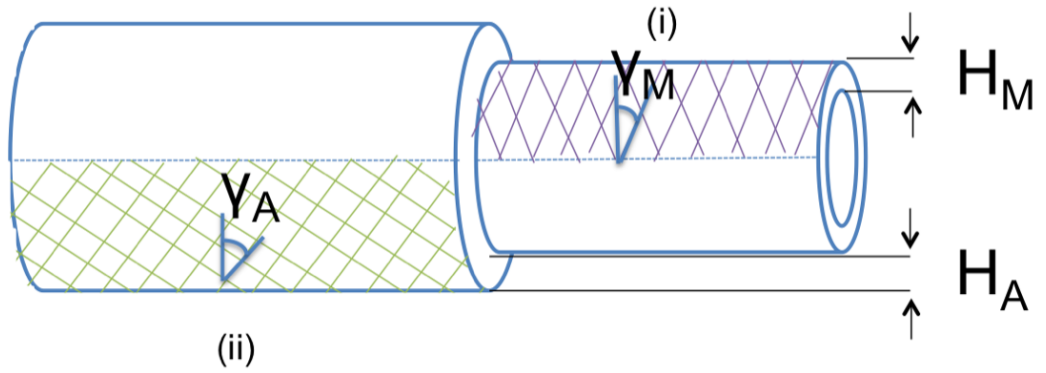

Figure 4.8: Illustration of collagen fibre orientations in the media and the adventitia in the 3D computational domain. (i) In the media (of thickness H_M) two families of fibre orientations are defined at an angle $\pm\gamma_M$ from the azimuthal axis (positively and negatively wound around the artery with respect to the azimuthal direction). (ii) In the adventitia (of thickness H_A), two families of fibres are defined at an angle $\pm\gamma_A$, which represent the protective sheath of the arterial wall.

dial layer (denoted by subindex M). The fibres are orientated at an angle of γ_{M_p} to the azimuthal axis, where p denotes the pitch $\pm\gamma_M$ relative to the azimuthal axis in the unloaded reference configuration. The fibres are thus positively and negatively wound around the artery (with respect to the azimuthal direction). For these groups of medial fibres, a highly non-linear SEF is employed (Holzapfel et al., 2000). As was introduced in Chapter 3, the reference configurations for those collagen fibres at an angle to the circumferential direction need to be solved in the direction of the fibres.

For the adventitial layer, I designate a set of collagen fibres that will represent the protective sheath, as was presented in Chapter 3. For those the set of angles γ_{A_p} (A denoting the adventitial layer) is defined. The families of collagen fibre orientations are illustratively summarised in Figure 4.8. I follow Chapter 3 to describe the SEF of a single collagen fibre in this group ($\Psi^{C\star}_{A_p}$) in a quadratic form (to represent the linear mechanical response of a single fibre):

$$\Psi^{C\star}_{A_p} = K^C_A (E^C_{A_p})^2 \tag{4.4}$$

where K^C_A is the collagen material parameter and $E^C_{A_p}$ the Green-Lagrangean (GL) strains (in the direction of the fibres, with respect to their reference configurations). The gradual recruitment of collagen fibres to load bearing is represented by defin-

ing a recruitment stretch distribution $Pr(\Lambda^R_{A_p})$ with a probability density function $f_{\Lambda^R_{A_p}}[\lambda^R_{A_p}(\theta_1,\theta_2,t)]$, to allow for spatial and temporal heterogeneity. Similarly to Chapter 3, the probability density function is defined as a triangular piecewise function. Consequently, the total SEF $\Psi^C_{A_p}$ per unit volume for this group of collagen fibres at an elastin stretch resolved in the direction of the fibres of λ_{A_p} is a piecewise function calculated by integrating the SEF of the individual collagen fibres which are recruited up to λ_{A_p} and multiplying them by the normalised concentration function $m^C_{A_p}(\theta_1,\theta_2,t)$, set to 1 for $t=0$:

$$\Psi^C_{A_p}(\lambda^C_{A_p}) = m^C_{A_p}\int_1^{\lambda_{A_p}} \Psi^{C*}_{A_p}(E^C_{A_p}) f_{\Lambda^R_{A_p}}(\lambda^R_{A_p})\mathrm{d}\lambda^R_{A_p} \tag{4.5}$$

where:

$$\lambda^C_{A_p} = \frac{\lambda_{A_p}}{\lambda^R_{A_p}} \tag{4.6}$$

The SEF of the media is then calculated (as the additive contributions from the elastin and the collagen fibres):

$$\Psi_M = m^E K^E_M(E_{11}+E_{22}+E_{33}) + \sum_{p=\pm,\ E^C_{M_p}>0} m^C_{M_p} K^C_M\{\exp[A^C(E^C_{M_p})^2]-1\} \tag{4.7}$$

The SEF of the adventitia (with the contribution from the protective sheath of collagen fibres) is:

$$\Psi_A = \sum_{p=\pm,\ E^C_{A_p}>0} \Psi^C_{A_p}(\lambda^C_{A_p}) \tag{4.8}$$

K is the material parameter for the corresponding arterial constituent, with A^C also representing a parameter related to the collagen fabric. The SEF to represent the total mechanical response of the arterial wall Ψ will then simply be the additive total of the SEFs of the medial Ψ_M and advential Ψ_A layers.

The GL strains of the elastin, i.e. E_{11}, E_{22} and E_{33}, are defined relative to the unloaded configuration; in the initial cylindrical configuration, these represent strains in the axial, azimuthal and radial directions, respectively. However, the GL strains in the collagen fibres are denoted by $E^C_{J_p}(\theta_1,\theta_2,t)$ (subindex J denotes the media M

or the adventitia A). They are defined relative to the configuration in which the collagen fibres are recruited to load bearing and resolved in the direction of the fibres. E_{J_p} can be computed from the components of the GL strain tensor:

$$E_{J_p} = E_{11}\sin^2\gamma_{J_p} + E_{22}\cos^2\gamma_{J_p} + 2E_{12}\sin\gamma_{J_p}\cos\gamma_{J_p} \tag{4.9}$$

They are related to the elastin stretches resolved in the directions of the collagen fibres λ_{J_p} by:

$$E_{J_p} = ((\lambda_{J_p})^2 - 1)/2 \tag{4.10}$$

The GL recruitment strains $E^R_{J_p}$ and the collagen strains $E^C_{J_p}$ can be equivalently calculated as in Eqn. (4.10) in terms of $\lambda^R_{J_p}$ and $\lambda^C_{J_p}$. Combining Eqn. (4.6) with the definitions of strains in terms of stretches, $E^C_{J_p}$ can then be calculated by:

$$E^C_{J_p} = \frac{E_{J_p} - E^R_{J_p}}{1 + 2E^R_{J_p}} \tag{4.11}$$

As was introduced in Chapter 2, Watton et al. (2004) hypothesised that fibroblasts configure the collagen fibres to achieve a maximum stretch during the cardiac cycle and introduced the terminology 'attachment stretch'. In Chapter 3 the concept of a distribution of attachment stretches was presented. For simplicity a constant value of attachment stretch is kept for the collagen fibre groups in the media, which is represented by λ^C_{AT}. To evaluate the state of stretches at the beginning of the simulation ($t = 0$), following the 1D analysis, it is assumed that the systolic stretch of the collagen fibres $\lambda^C_{M_p}|_{t=0}$ equals the attachment stretch λ^C_{AT}. Because of the symmetry of the collagen fibre orientations, it is expected that the values of attachment stretch, collagen stretch and recruitment stretch are the same for both pitches. Remembering Eqn. (4.6), the initial values for the recruitment stretches of those collagen fibres can then be evaluated:

$$\lambda^R_{M_p}|_{t=0} = (\sqrt{(\lambda_0)^2\cos^2\gamma_{M_p} + (\lambda_z)^2\sin^2\gamma_{M_p}})/\lambda^C_{AT} \tag{4.12}$$

where λ_0 is the systolic circumferential elastin stretch and λ_z is the axial elastin stretch, both of which are used to resolve the elastin stretch in the direction of the fibres.

For the adventitial collagen fibre group representing the protective sheath with a distribution of recruitment stretches, following the 1D analysis in Chapter 3, a distribution of attachment stretches is defined. The distribution is triangular; therefore, the initial recruitment stretch distribution needs to be determined by calculating the minimum, maximum and modal points following Eqn. (4.12), where it is implied that fibres with the highest attachment stretch will be the first ones to be recruited:

$$\lambda^R_{A_p}|^{min}_{t=0} = (\sqrt{(\lambda_0)^2\cos^2\gamma_{A_p} + (\lambda_z)^2\sin^2\gamma_{A_p}})/\lambda^{AT}_A|^{max}_{t=0} \tag{4.13a}$$

$$\lambda^R_{A_p}|^{max}_{t=0} = (\sqrt{(\lambda_0)^2\cos^2\gamma_{A_p} + (\lambda_z)^2\sin^2\gamma_{A_p}})/\lambda^{AT}_A|^{min}_{t=0} \tag{4.13b}$$

$$\lambda^R_{A_p}|^{mod}_{t=0} = (\sqrt{(\lambda_0)^2\cos^2\gamma_{A_p} + (\lambda_z)^2\sin^2\gamma_{A_p}})/\lambda^{AT}_A|^{mod}_{t=0} \tag{4.13c}$$

An index of interest associated the cyclic deformation that is calculated here is the Cyclic Areal Stretch A^{CS}. The cyclic areal stretch describes the ratio of the differential areal stretch at systole to the differential areal stretch at diastole. The areal stretches at systolic A_S and diastolic A_D pressures are calculated as follows:

$$A_S = \sqrt{(1+2E^S_{11})(1+2E^S_{22}) - 4E^S_{12}} \tag{4.14a}$$

$$A_D = \sqrt{(1+2E^D_{11})(1+2E^D_{22}) - 4E^D_{12}} \tag{4.14b}$$

Consequently, A^{CS} can be calculated as:

$$A_{CS} = \frac{A_S}{A_D} \tag{4.15}$$

The distribution of average Cauchy stresses is also evaluated that takes into account the remodelled thickness (as was introduced in Chapter 3). This Cauchy tensor σ is computed by:

$$\sigma_{ij} = J^{-1}F_{ik}S_{kl}F_{jl} \tag{4.16}$$

F is the deformation gradient tensor, $J = det(\mathbf{F})$ (which for an incompressible material is 1), and **S** is the 2nd PK stress tensor (where H_{rem} takes into account the

volumetric growth due to changes in the mass densities of the arterial constituents, following the analysis in Chapter 3):

$$S_{ij} = \frac{1}{H_{rem}} \frac{\partial (H_M \Psi_M + H_A \Psi_A)}{\partial E_{ij}} \tag{4.17}$$

For further details on the structural model, see Watton et al. (2004), Watton and Hill (2009).

4.6 COMPUTATIONAL FLUID DYNAMICS

The methodology to solve the haemodynamics as the aneurysm evolves starts with the geometry of the aneurysmal section being exported from the structural solver to the meshing suite ANSYS ICEM (refer back to Figure 4.1 for the FSG modelling steps). ANSYS ICEM automatically integrates the aneurysmal section into the physiological geometrical domain, i.e. attaches the upstream and downstream extensions, and then automatically generates an unstructured tetrahedral mesh with prism layers lining the boundary. Boundary conditions are generated and the flow is solved by ANSYS CFX which solves the incompressible Navier-Stokes equations using a finite volume formulation (Patankar, 1980). Blood is modelled as a Newtonian fluid and no slip, no-flux conditions are applied at the arterial wall boundaries.

There is the possibility to complete either a steady or a pulsatile flow analysis for each FSG modelling step. For the rabbit model case, there are specific experimentally calculated boundary conditions over the cardiac cycle, as were presented in §4.3; the application of those conditions is described in the analysis of Chapter 6. For the clinical case, for which there are no specific boundary conditions, the flow and pressure boundary conditions are taken from a 1D model of the arterial tree (Reymond et al., 2009) which has been integrated into the software suite @neufuse (Villa-Uriol et al., 2011). It solves the 1D form of the Navier-Stokes equation in a distributed model of the human systemic arteries, accounting for the ventricular-vascular interaction and wall viscoelasticity; it was recently validated through a comparison with *in vivo* flow measurements (Reymond et al., 2011). Further information for CFD is presented in Appendix C.

4.7 GROWTH AND REMODELLING

4.7.1 Media degradation

The dilation of an intracranial aneurysm is accompanied by loss of elastin because of increased elastolysis (Shimizu et al., 2006). As was introduced in Chapter 2, elastin degradation might also be affected by changes in the WSS in the aneurysms recirculation region, and thus, the spatial and temporal changes in the WSS distribution could influence the degradation of elastin and thus the rate at which an aneurysm enlarges. Aparício et al. (2014) explored this concept for an abdominal aortic aneurysm case and the following chapter will explore this for the clinical intracranial aneurysm case. For the purposes of that investigation, a phenomenological approach is proposed to model the link of elastin degradation to WSS that acts on the vascular wall.

Elastin degradation is modelled in two distinct stages. First, a degradation of elastin is prescribed to create a small aneurysmal area. This creates a perturbation in the geometry and the haemodynamic environment so that the WSS distribution is perturbed from its original distribution. Subsequently, elastin degradation is driven by deviations in WSS from homeostatic values (and those values need to be carefully defined). In order to simulate the saccular shape of the intracranial aneurysms, the elastin is only degraded within a prescribed circular area of the Lagrangian computational domain (i.e. of the defined aneurysm cylinder). Watton et al. (2011a) describes how the transition between the degrading domain and the rest of the computational domain is connected (by defining an inner and outer radius to the degradation circular area and linearly interpolating between the two). The functional form for the initial prescribed loss of elastin within the circular area is as follows:

$$m^E(\theta_1,\theta_2,t) = 1-(1-m^E_{MIN}(t)) \times \{\exp[-\omega_1(\frac{\theta_1-L_1/2}{L_1/2})^2] \cdot \exp[-\omega_2(\frac{\theta_2-L_2/2}{L_2/2})^2]\} \tag{4.18}$$

where m^E_{min} represents the minimum concentration of elastin, at time t (in years), which, by construction, is located at the centre of the circular area. The parameters ω_1 and ω_2 control the degree of localisation of the degradation function ($\omega_1 = \omega_2 = 20$ is adopted, see Watton and Hill (2009) for influence of this parameter). It is assumed that the minimum concentration decays exponentially for a period of time T:

$$m^E_{min}(t) = \exp\{\ln(m^E_T)(t/T)\} = (m^E_T)^{t/T}, \tag{4.19}$$

m^E_T determines the minimum value prescribed by time T and naturally, the value of m^E_{min} at $t = 0$ is 1. Following the simulations in 1D, where the degradation of the media, i.e. elastin as well as collagen fibres, was defined, Eqn. (4.18) and Eqn. (4.19) are used to determine $m^C_M(\theta_1, \theta_2, t)$ and $m^C_{min}(t)$, respectively, determining a corresponding m^C_T and T. It should be noted that, for the application of the FSG framework to the rabbit model case, and because of the different focus of that study, a prescribed degradation for the entirety of the simulation will be assumed - further details are provided on Chapter 6.

Following the initial prescribed degradation, the concentration of elastin m^E further evolves according to:

$$\frac{\partial m^E}{\partial t} = -F_D D_{max} m^E \tag{4.20}$$

where D_{max} specifies the maximum rate of degradation, and $F_D(\theta_1, \theta_2, t) : 0 \leq F_D \leq 1$ is a spatially-dependent function of the haemodynamic quantities to be linked to elastin degradation. Clearly, if $F_D = 1$, elastin degrades at the maximum rate D_{max}, whilst if $F_D = 0$, no degradation occurs. Deviations of WSS from homeostatic values then drive elastin degradation. Following Chapter 2, three definitions of WSS homeostasis are presented:

1. a spatially homogeneous and temporally non-adaptive;
2. a spatially heterogeneous and temporally non-adaptive;
3. a spatially heterogeneous and temporally adaptive.

For Case 1, elastin degradation is assigned to given intervals of WSS. Figure 4.9 illustrates this definition of WSS homeostasis (the function is not necessarily symmetric as illustrated in the figure, and the specific boundaries will be determined in Chapter 5). There is no elastin degradation ($F_D = 0$) for a given interval of WSS, $[\tau_{low-min}, \tau_{high-min}]$. Outside that interval, a quadratic function to maximum elastin degradation ($F_D = 1$) is used (illustrative monotonic function to represent the transition from zero to maximum degradation with a smooth increase in gradient).

Under those assumptions, both low and high values of WSS can drive elastin degradation. This definition does not take into account spatial or temporal variations of the mechanical arterial environment and is summarised in Eqn. (4.21):

$$F_D(\tau(\theta_1,\theta_2,t)) = \begin{cases} 1 & \tau \le \tau_{low-max} \\ (\frac{\tau_{low-min}-\tau(\mathbf{X},t)}{\tau_{low-min}-\tau_{low-max}})^2 & \tau_{low-max} < \tau < \tau_{low-min} \\ 0 & \tau_{low-min} \le \tau \le \tau_{high-min} \\ (\frac{\tau(\mathbf{X},t)-\tau_{high-min}}{\tau_{high-max}-\tau_{high-min}})^2 & \tau_{high-min} < \tau < \tau_{high-max} \\ 1 & \tau \ge \tau_{high-min} \end{cases} \tag{4.21}$$

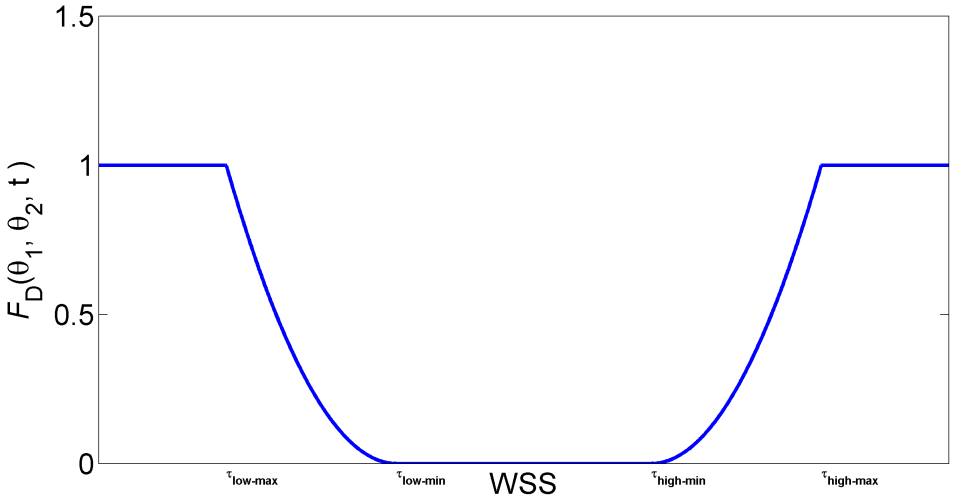

Figure 4.9: Illustration for spatially homogeneous and temporally non-adaptive WSS homeostasis.

For Cases 2 and 3, a simple quadratic functional form (similarly to Case 1, these are illustrative monotonic functions for the gradual transition from zero to maximum degradation) is used for the degradation function F_D that describes the relation between the local WSS ($\tau(\mathbf{X},t)$) and the degree of the degradation of elastin, i.e.

$$F_D(\tau(\theta_1,\theta_2,t)) = \begin{cases} 0, & \tau \ge \tau_h, \\ \left(\dfrac{\tau_h(\mathbf{X},t)-\tau(\mathbf{X},t)}{\tau_h(\mathbf{X},t)-\tau_X(\mathbf{X},t)}\right)^2, & \tau_X < \tau < \tau_h, \\ 1, & \tau \le \tau_X. \end{cases} \tag{4.22}$$

τ_X is set to 0Pa. The function implies that elastin degradation is only driven by low WSS values. The distinction between Case 2. and Case 3. lies in the definition of the homeostatic WSS threshold τ_h:

$$(2.) \qquad \tau_h(\mathbf{X}, t) = \tau(\mathbf{X}, t = 0) \tag{4.23}$$

$$(3.) \qquad \tau_h(\mathbf{X}, t) = \frac{1}{T_L} \int_{t-T_L}^{t} \tau(\mathbf{X}, t)\, dt \tag{4.24}$$

where for $t < 0$, $\tau_h(\mathbf{X}, t) = \tau_h(\mathbf{X}, t = 0) = \tau_0$, that is, the spatial distribution for the model of the healthy artery prior to aneurysm formation. In Case 2. WSS homeostasis is spatially heterogeneous with magnitudes defined by the initial WSS distribution at $t = 0$. Case 2. assumes that the τ_h is independent of time. However, as it was presented in Chapter 2, there is possibly the ability of the endothelium to adjust to changes in the arterial mechanical environment. Therefore, for Case 3. it is proposed that τ_h is assumed to be spatially heterogeneous and temporally adaptive, by averaging values of WSS over a past given number of years T_L.

As discussed in Chapter 2 and Chapter 3, the adaption of the collagen fabric during aneurysm evolution consists of two distinct mechanisms: G&R. The algorithms, adjusted for the 3D FSG framework, are presented in the next section.

4.7.2 Collagen remodelling

The concepts of recruitment and attachment stretches are here revisited. The concept of an attachment stretch implies that the collagen fibres have distinct natural reference configurations. A field of recruitment stretch variables is defined: these describe the stretch (relative to unloaded reference configuration) that the tissue must be stretched in the direction of a fibre for it to begin to bear load. The magnitude of the recruitment stretch variables $\lambda^R_{M_p}(\theta_1, \theta_2, t)$ (for the group of collagen fibres in the media with non-linear SEF) are defined such that at $t = 0$, the collagen stretches are equal to the attachment stretch throughout the domain. As the geometry evolves, the recruitment stretches evolve so that the maximum GL strain of the collagen during the cardiac cycle remodels towards the GL attachment strain, denoted E^C_{AT}. Initially, it was assumed that maximum strains are achieved in the systolic configuration and thus the remodelling scheme was implemented computationally by considering the steady deformation of the arterial at systolic pressure;

however, as the geometry becomes more complex this is not necessarily true (Watton et al., 2004). Consequently, the methodology is now updated to assume that the maximum strains occur in either the systolic or diastolic configuration, i.e.

$$\frac{\partial \lambda^R_{M_p}}{\partial t} = \alpha_{M_p}\left(\frac{E^C_{M_p}|_{max} - E^C_{AT}}{E^C_{AT}}\right), \tag{4.25}$$

where

$$E^C_{M_p}|_{max} = \max\left(E^C_{M_p}|_{sys}, E^C_{M_p}|_{dias}\right) \tag{4.26}$$

where $E^C_{M_p}|_{sys}$ and $E^C_{M_p}|_{dias}$ denote the magnitude of the collagen strains evaluated in the systolic and diastolic configurations, respectively, and α_{M_p} is a rate parameter controlling the speed of remodelling (and biologically implying an indication of the half-life of the collagen fibres).

For the adventitia collagen fibre group that was set as a protective sheath of the arterial wall, triangular distributions were defined for the recruitment and attachment stretches, in order to represent the range of fibre waviness in the unloaded configuration and the gradual recruitment to load bearing that has been experimentally observed (Rezakhaniha et al., 2012). Consequently, remodelling of the recruitment stretch distribution is expected for this group of collagen fibres. Mathematically, this is implemented by setting linear differential equations for the remodelling of the minimum, maximum and modal values of the distribution ($\lambda^R_{M_p}|^{min}$, $\lambda^R_{M_p}|^{max}$ and $\lambda^R_{M_p}|^{mod}$ respectively), initiated by deviations of the corresponding collagen fibre stretches ($\lambda^C_{M_p}$) from attachment levels (λ^{AT}_M):

$$\frac{\partial \lambda^R_{M_p}|^{min}}{\partial t} = \alpha_{M_p}\left(\frac{\lambda^C_{M_p}|^{max} - \lambda^{AT}_M|^{max}}{\lambda^{AT}_M|^{max}}\right) \tag{4.27a}$$

$$\frac{\partial \lambda^R_{M_p}|^{max}}{\partial t} = \alpha_{M_p}\left(\frac{\lambda^C_{M_p}|^{min} - \lambda^{AT}_M|^{min}}{\lambda^{AT}_M|^{min}}\right) \tag{4.27b}$$

$$\frac{\partial \lambda^R_{M_p}|^{mod}}{\partial t} = \alpha_{M_p}\left(\frac{\lambda^C_{M_p}|^{mod} - \lambda^{AT}_M|^{mod}}{\lambda^{AT}_M|^{mod}}\right) \tag{4.27c}$$

where α_{M_p} is the rate parameter controlling the speed of remodelling. As this group of collagen fibres acts as a protective sheath, in that they do not play initially a role in load bearing, the evolution of the attachment stretch distribution needs to be taken into consideration. As discussed in Chapter 3, this will represent the transition of

those collagen fibres to load bearing constituents. For simplicity in the 3D modelling and due to lack of further biological information, it is assumed that the shape (centre and width) of the distribution does not change in time; therefore, mathematically, the maximum value of the distribution ($\lambda_M^{AT}|^{max}$) needs to simply evolve in order to illustrate this evolution:

$$\lambda_M^{AT}|^{max}(t) = \begin{cases} \lambda_M^{AT}|_{t=0}^{max} & t \leq t_1 \\ \lambda_M^{AT}|_{t=0}^{max} + \frac{\lambda_M^{AT}|_{t_2}^{max} - \lambda_M^{AT}|_{t=0}^{max}}{1+e^{-B(t-t_1-t_2/2)}} & t_1 < t \leq t_2 \\ \lambda_M^{AT}|_{t_2}^{max} & t \geq t_2 \end{cases} \tag{4.28}$$

t_1 and t_2 determine the time during which the evolution of the attachment stretch distribution takes place, $\lambda_M^{AT}|_{t_2}^{max}$ determines the final value for the maximum attachment stretch of the distribution, and B determines the growth rate of the curve. For the purposes of these remodelling algorithms, it is assumed that there is no remodelling of the pitch for the collagen fibres and therefore only the initial ones (with respect to the unloaded configuration) need to be determined.

4.7.3 Collagen growth

In vascular homeostasis, the mass of the collagenous constituents is constant even though the collagen fibres are in a continual state of deposition and degradation. However, in response to perturbations to the mechanical environment, vascular cells can respond by upregulating synthesis and downregulating enzymes that degrade the matrix (Chiquet, 1999); this would lead to a net increase in mass. Conversely, a downregulation of synthesis coupled with an upregulation matrix-degrading enzymes would lead to a local decrease in mass. Note that if there is an upregulation of synthesis balanced by an upregulation of degrading enzymes (no net change in mass), this can be simulated by increasing the magnitude of the remodelling rate parameters from above, α_{J_p}. The algorithm proposed to simulate this is outlined, proposed by Watton and Ventikos (2009). The key assumptions are as follows:

- the reference configuration of the cells is equal to the reference configuration of the constituents that they are maintaining;

- the number of cells is proportional to the mass of constituents they are maintaining;
- in vascular homeostasis, the mass of the constituents is constant.

From these assumptions, a linear differential equation for adapting the concentration of the medial collagenous constituents can be derived to be:

$$\frac{\partial m^C_{M_p}}{\partial t} = \beta^C_{M_p} m^C_{M_p} \left(\frac{E^C_{M_p}|_{max} - E^C_{AT}}{E^C_{AT}} \right), \tag{4.29}$$

where β is a phenomenological rate parameter for the speed of increased deposition of collagen fibres (also related to the half life of the fibres). Similarly, for the collagen fibres of the protective sheath, Chapter 3 is followed so that the growth is dependent on the deviation of an average of the collagen stretch distribution from an average attachment stretch value. For the case investigated, where the distribution remains centred on the assigned modal value, the linear differential equation for growth is:

$$\frac{\partial m^C_{A_p}}{\partial t} = \beta_{A_p} m_{A_p} \left(\frac{\lambda^C_{A_p}|^{mod} - \lambda^{AT}_A|^{mod}}{\lambda^{AT}_A|^{mod}} \right) \tag{4.30}$$

In addition to the stretch-based growth, growth dependent on cyclic stretch is also suggested, which will be implemented in the investigations of Chapter 5. For these cases, the linear differential equations for the adaption of collagen fibre concentrations from Eqn. (4.29) and Eqn. (4.30) are updated by adding the following term:

$$\frac{\partial m^C_{J_p}}{\partial t}(cyclic \quad stretch) = m^C_{J_p} \beta(A^{CS}), \tag{4.31}$$

where:

$$\beta(A^{CS}) = \beta^{CS} \max\left(\frac{A^{CS}}{A^{CS}|_{t=0}} - 1, 0 \right) \tag{4.32}$$

$\beta(A^{CS})$ is then a phenomenological growth parameter that is a function of the magnitude of the (differential) cyclic areal stretch A^{CS}, that is, the ratio of the differential areal stretch at systole to the differential areal stretch at diastole (Schmid

et al., 2013). It is hypothesised that there exists a homeostatic range of magnitudes of cyclic strain for the vascular cells. Given that the magnitude of the cyclic strain decreases as an artery ages and stiffens, for example, from around 13% to 2% (Länne et al., 1992), it is postulated that the magnitude of the cyclic strain at $t = 0$ represents a suitable upper bound. It is assumed that this implies a similar upper bound for the magnitude of cyclic areal stretch. Consequently, a functional form for A^{CS} is selected that increases rates of production if the magnitude of the cyclic areal stretch increases from its initial values for the healthy artery at $t = 0$. The total growth equation, in this case, presents the additive effects of stretch based and cyclic stretch-based growth (a different approach to the multiplicative one presented in Aparício et al. (2014)). This is to explore the possibility of growth continuing even when the stretches of the constituents (and cells according to the assumptions) return to homeostatic levels.

The presented model is applied in a finite element method code on FORTRAN. Further details on the application of the finite element method for the FSG framework can be found in Watton (2002), Watton et al. (2004). The specific parameters used for the simulations in this thesis are presented in the following chapters (Chapter 5 and Chapter 6).

The structural, CFD, and G&R analyses, as described in this chapter, are coupled (although it should be noted that this is not a fluid-structure interaction simulation). The structural analysis uses a quasi-static approach to solve the systolic and diastolic deformation fields. The structural analysis is solved for 10 time steps and subsequently the CFD for the updated geometry is solved. The CFD simulation passes back haemodynamic indices of interest to be used in the G&R algorithms. Complete simulations involve approximately 200 to 500 timesteps, i.e. 20 to 50 CFD solutions. There are only small changes in the remodelled geometry every 10 steps, hence only small changes in CFD distributions. As we are interested in the qualitative behaviour of the interaction between spatial and temporal distributions of haemodynamic stimuli, and the enlargement of the aneurysm, this approach seems to be a reasonable trade-off to achieve computational efficiency. If the remodelling gives rise to more rapid changes in the geometry, the CFD analysis may need to executed more frequently.

4.8 DISCUSSION

This chapter outlined a 3D modelling framework for aneurysm evolution updated and sophisticated, for the first time, to include specific geometries (clinical and animal ones) and material properties with the aim of establishing a novel approach to informing and validating computational models from available experimental data.

The two geometries presented in this chapter can contribute to the models of aneurysm evolution in different ways. Since the aim of this research is to understand more about the physiology and mechanobiology of human aneurysms in order to eventually create supportive clinical tools for aneurysm diagnosis, *in vivo* and *in vitro* information on clinical aneurysms is vital and the focus of a wide range of research: *in vivo* 3D visualisation for endovascular treatment (Anxionnat et al., 2001), *in vivo* WSS measurements (Fillinger et al., 2002), *in vitro* tissue testing for MMP inhibition investigations (Thompson and Baxter, 1999), and *ex vivo* aneurysm tissue mechanical testing for the measurement of mechanical properties of the fibrous tissue (Raghavan et al., 1996). However, there is only limited clinical data on the inception and development of aneurysms. This difficulty is exactly the reason for experimental animal models. With animal models, such as the rabbit model that was presented here, the range of possibilities for analysis is wide; not only processes, such as histology, tissue mechanical testing and arterial wall imaging is possible, but it is particularly so for different stages of aneurysm development and against control samples. However, this field of study is not always closely and directly informed by and informing theoretical and computational models of aneurysm evolution.

The chapter introduced the FSG modelling framework in order to further discuss the need for this interaction between mathematical modelling and experimental work. The focus of the FSG simulation process is to enable the relation between the flow environment and the (changing) mechanical response of the arterial wall. Driven by literature and experiments (Humphrey et al. (2015), Humphrey and Holzapfel (2011), Humphrey (2009), McGloughlin (2011)), the importance of mechanotransduction has been clearly illustrated, even though biologically is not fully understood; several flow force metrics (such as WSS) have been related to aneurysm evolution, although the consensus on its relation to aneurysm evolution is unclear (Selimovic, 2013). The focus of the theoretical modelling framework (in 1D and 3D) here is to represent the structural constituents of the arterial wall, while characterising their ability to create new configurations and change the balance be-

tween their synthesis and degradation, in order to adapt to changing arterial conditions.

There are limitations to the structural and biological representation of the arterial wall in the 3D presentation: SMCs are not explicitly represented (as was introduced in Chapter 2)). More explicit biological links of mechanotransduction are required to more reliably describe pathways triggered by flow and affecting the layers of the arterial wall from the endothelium to the vascular cells and the fibres (for example growth factor $-\beta$ cytokine pathways ((Lindsay and Dietz, 2011), Jones et al. (2009)). The current modelling framework is chosen in part due to the incomplete biological data for such pathways that would inform the mathematical models. Modelling partially known pathways at this stage would simply increase the computational complexity, without adding useful mechanobiological knowledge. Despite certain modelling limitations, the suggested computational framework is still able to provide very useful insights into the suggested G&R hypotheses, driven by the initial investigations in 1D and taking into account specific complex geometries. The results of those investigations will be presented in the following chapters.

Part of the presented work in this chapter was also to describe the vessel reconstruction of the aneurysmal geometries, in order to recreate a healthy arterial environment prior to aneurysm formation, as the initial geometric configuration of the evolution simulations. This was a labour-intensive procedure which was dependent on manual estimations and observations of the neighbouring vasculature, since there was no *in vivo* information on the healthy geometries: for the clinical case, such information would have only been coincidental and for the rabbit model, it was seen as a costly and timely additional procedure. However, for the purposes of the simulation, it is an important aspect for a reliable representation of the healthy arterial state and one which should eventually be further automated as part of the FSG framework. This is one example where interaction between theoretical and experimental work can advance the reliability of the modelling framework.

4.9 CONCLUSIONS

This chapter presented two aneurysmal geometries (a clinical one and a rabbit model one) which are employed in the implementation of the suggested FSG framework for the computational representation of aneurysm evolution, stressing the rel-

evant clinical and experimental data which can inform the modelling hypotheses (the clinical geometry was already introduced in the analysis of Chapter 3). For the purposes of this framework, it was described how the aneurysmal segments and their neighbouring vasculature were reconstructed to a pre-aneurysmal 'healthy' state, by replacing the aneurysmal area with a computational domain where the 3D modelling framework of aneurysm development will be applied to represent the transition of the artery from a $t = 0$ healthy configuration to an aneurysmal one. Focussing on transferring the structural and G&R hypotheses for the mechanical behaviour of the arterial wall from 1D (Chapter 2 and Chapter 3) to 3D, the modelling steps for a cyclical stepwise simulation that relates the structural arterial wall analysis with the CFD of the blood flow environment and the G&R evolution of the collagen fabric were outlined. The following two chapters present the specific setup and results from the 3D computational simulations ran using the two presented geometries and framework. Chapter 5 examines the effect of the definition of WSS homeostasis on elastin degradation and of cyclic stretches on growth of collagen fibres for the clinical case. In Chapter 6 pulsatile flow conditions are applied on the framework and further links of pulsatile flow metrics with collagen growth and the functionality of endothelium are suggested.

CHAPTER 5

3D HUMAN ANEURYSM STUDY

In Chapter 3 a specific clinical aneurysm case was presented, accompanied by geometrical and aneurysmal tissue information. The 1D analysis for this case rendered an estimation for the material parameter and an indication for a final attachment stretch distribution of the adventitial collagen, since the medial layer is essentially lost. Those calibrating measures were incorporated in the FSG framework presented in Chapter 4 for the purposes of this chapter. Firstly, I focus on a simulation running the structural code of the FSG framework, following the concept of the gradual phases of degradation, remodelling and growth (with the evolution of attachment stretch distribution), implemented for the 1D growth model. The aim is to reflect on the estimations of aneurysm remodelled thickness in 3D, observing and critiquing the evolution of collagen stretches and densities.

The concluding point of this first study is the establishment and testing of links between stretch and collagen growth. Our hypothesis is that increased cyclic stretch enhances collagen synthesis. Even though current understanding of arterial mechanotransduction on a tissue, cellular and subcellular level is poor, there are many strong, published experiments that support this hypothesis (§5.3). Theoretical models have initiated relevant investigations, relating collagen growth to cyclic stretch (Kroon and Holzapfel (2009), Aparício et al. (2014), Watton et al. (2011)). Motivated by the literature and previous models, an advancement to the hypothesis is presented by investigating two separate homeostatic states for (a) collagen stretches

as well as (b) cyclic stretches.

This investigation (§5.2) on the 3D structural code, calibrated by the 1D analysis (Chapter 3) informs and calibrates the complete FSG framework, as it is implemented in §5.2, taking full advantage of the 3D clinical aneurysmal and surrounding arterial geometry. The principal question for this set of simulations thus revisits the concepts of endothelial heterogeneity and elastin degradation linked to flow, as was motivated in Chapter 2. The structural and FSG model results allow establishing the consistency between the 1D and 3D examinations and suggest future modelling directions.

5.1 3D Model of idealised saccular aneurysm growth

In this section, the setup is outlined and the results are presented for two 3D structural simulations on an idealised saccular aneurysm (with the geometrical characteristics of the healthy artery for the clinical case) that aim to investigate the effect of the hypothesis for collagen growth on the mechanical properties of the arterial constituents during aneurysm evolution. The parameters presented here follow the theoretical analysis from Chapter 4, with the additional guidance from the investigations in 1D (Chapter 2 and Chapter 3).

5.1.1 Simulation and parameter overview

Simulations were performed on a 64BIT desktop PC (Intel Xeon CPU E31245 @3.3 GHZ, 16 GB RAM) running Windows 7 Enterprise. A complete 3D structural simulation consisting of 250 solid steps (corresponding to five years), with structural data outputted every 10 steps, takes around 2 hours.

The geometrical characteristics of the computational domain for the application of the structural model can be seen in Table 5.1. The thin cylinder modelled has an unloaded radius of R, used as the reference configuration for the calculation of stretches, and a systolic radius of $r_s = \lambda_0 R$ at $t = 0$, given an assumed initial systolic circumferential stretch of λ_0. The *in vivo* loaded axial length is l (following the vessel reconstruction methodology in Chapter 4). An axial pre-stretch of λ_z is assumed for the duration of the simulation, resulting in an unloaded axial length of $L_1 = \frac{l}{\lambda_z}$ and

Table 5.1: Geometry and physiological data for the 3D structural and FSG simulations of the clinical case.

Geometry and Physiological Data		
Radii		
Unloaded (reference configuration)	R	1.5mm
Systolic ($t = 0$)	$r_s = \lambda_0 R$	2mm
Lengths		
Loaded axial ($t = 0$)	l	5.9mm
Unloaded axial (reference configuration)	$L_1 = \frac{L}{\lambda_z}$	4.539mm
Unloaded radial (reference configuration)	$L_2 = 2\pi R$	18.85mm
Stretches (Kroon and Holzapfel, 2009)		
Systolic ($t = 0$)	λ_0	1.25
Axial	λ_z	1.3
Cyclic ($t = 0$)	λ_D^S	1.1
Pressures (Watton and Hill, 2009)		
Systolic	P_{sys}	16kPa
Diastolic	P_{dia}	10.67kPa
Unloaded thicknesses ($t = 0$) (Holzapfel et al., 2000)		
Total	$H = \frac{1}{5}R$	0.4mm
Medial	$H_M = \frac{2}{3}H$	0.267mm
Adventitial	$H_A = \frac{1}{3}H$	0.133mm
Fibre orientation (unloaded configuration) (Schriefl et al., 2012b)		
Media	γ_M	30°
Protective sheath (adventitia)	γ_A	60°

an unloaded radial length of $L_2 = 2\pi R$. The cyclic stretch, defined as the ratio of systolic to diastolic stretches, is λ_D^S. This thin cylinder is subjected to a constant systolic pressure P_{sys} and diastolic pressure P_{dia}. The values for those stretches and pressures were guided by the literature previously used in the 1D modelling Chapter 3.

Table 5.2: Parameters to define prescribed media degradation for the 3D structural simulations of the clinical case.

Parameters for prescribed degradation		
Media degradation		
Time to minimum prescribed (elastin,collagen)	T	4(in years)
Minimum elastin density by time T	m_T^E	0.01
Minimum medial collagen density by time T	m_T^C	0.01

Table 5.3: Definition of recruitment and attachment stretches for the 3D structural simulations of the clinical case.

Recruitment and attachment stretches		
Recruitment stretches ($t = 0$)		
Media	$\lambda^R_{M_p}$	1.18
Protective sheath (adventitia, minimum)	$\lambda^R_{A_p}\|^{min}$	1.28
Protective sheath (adventitia, maximum)	$\lambda^R_{A_p}\|^{max}$	1.42
Protective sheath (adventitia, modal)	$\lambda^R_{A_p}\|^{mod}$	1.34
Attachment stretches ($t = 0$)		
Media	λ^{AT}_M	1.07 (Chen, 2014)
Protective sheath (adventitia, minimum)	$\lambda^{AT}_A\|^{min}$	0.9
Protective sheath (adventitia, maximum)	$\lambda^{AT}_A\|^{max}$	1
Protective sheath (adventitia, modal)	$\lambda^{AT}_A\|^{mod}$	0.95
Attachment stretch evolution (protective sheath)		
Start time for evolution	t_1	4(years)
Stop time for evolution	t_2	5(years)
Final minimum attachment stretch	$\lambda^{AT}_A\|^{min}_{t_2}$	0.95
Final maximum attachment stretch	$\lambda^{AT}_A\|^{max}_{t_2}$	1.05
Final modal attachment stretch	$\lambda^{AT}_A\|^{mod}_{t_2}$	1

The initial unloaded thickness H is calculated as $\frac{1}{5}R$, consistent with the use in Chapter 3. It is assumed that, at $t = 0$ medial thickness H_M is $\frac{2}{3}$ of the total thickness. Additionally, the initial unloaded fibre orientations $\pm\gamma_J$ (two symmetric families in

Table 5.4: Growth and remodelling and material parameters for the 3D structural simulations of the clinical case.

G&R and material parameters		
Recruitment rate parameters		
Media	α_{M_p}	0.1(years^{-1})
Protective sheath (adventitia)	α_{A_p}	0.1(years^{-1})
Growth rate parameters		
Media	β_{M_p}	0.5(years^{-1})
Protective sheath (adventitia)	β_{A_p}	0.5(years^{-1})
Cyclic-stretch based growth (media, adventitia)	β^{CS}	50(years^{-1})
Start time for increased growth	t_{gr1}	4(years)
Stop time for increased growth	t_{gr2}	5(years)
Material parameters		
Medial elastin	K^E	133.8kPa
Medial collagen	K^C_M	1.96kPa
Exponential constant (media)	A^C	60
Collagen (protective sheath, adventitia)	K^C_A	11.95MPa

each group need to be defined with respect to the circumferential direction) for the two groups of collagen fibres (in the media and the adventitia) presented in Chapter 4. Medial collagen fibres have been experimentally observed to be closer to the circumferential direction than the adventitial (Schriefl et al., 2012b) in the unloaded configuration and this accordingly informs our choice of collagen fibre angles to the azimuthal direction in our model.

For the purposes of this investigation and following the corresponding analysis in 1D for the clinical case in Chapter 3, the simulation phases involve: (a) prescribed degradation, (b) remodelling and (c) stabilisation through growth. The degradation of the media is prescribed to ensure that within the timeline of the simulation the medial layer almost completely disappears. Consequently for phase (a) of prescribed degradation, the normalised densities of the medial elastin m^E and collagen $m^C_{M_p}$ fibres are exponentially decreased to 0.01 by the end of Year 4 (Table 5.2); this density is sustained for the medial elastin during the final year of the simulation, but

medial collagen develops according to the growth hypothesis. Based on the vessel reconstruction method of Chapter 4, the aneurysm cylinder has been placed and the Cartesian coordinates have been defined so that the circular area of the degradation can be specified in the middle of the computational domain and towards the positive y-axis. Based on the observations of the ostium area in Chapter 3, inner and outer radii for the area of the medial degradation circle were evaluated (for the linear interpolation of the media degradation between the degrading circle and the rest of the computational domain) and defined as factors of the cylinder's radius in the unloaded configuration (with values of 0.5 and 0.75 respectively).

For phase (b) of remodelling, the deviations of collagen fibre stretches from attachment levels (due to the increase in the circumferential stretch following the medial degradation) are expected to allow for the remodelling of the collagen fibre reference configurations (recruitment stretches), following the analysis in §4.7. Table 5.3 summarises the parameters for the recruitment and attachment stretches for collagen fibres, at the beginning of the simulation. The same attachment value is set for the non-linear collagen fibres of the media (λ^{C}_{AT}) and the salient values (minimum, maximum, modal) for the attachment stretch distribution of the protective sheath in the adventitia (m^{AT}_{M}), so that no fibres in the group are recruited at the beginning of the simulation, i.e. maximum value of the distribution ($\lambda^{AT}_{M}|^{max}_{t=0}$) is less than 1; this establishes the media as the main load bearing arterial layer under physiological conditions and the adventitia's role as the protective sheath. The initial values for the recruitment stretches of the two groups of collagen fibres are then determined accordingly (Eqn. (4.12)-Eqn. (4.13c)), based on the initial attachment values, systolic and axial stretches. Table 5.4 also presents the rate parameters for the recruitment evolution equations of all collagen fibre groups; they are all equal to 0.1 years^{-1}.

The growth phase (c), following the prescribed medial degradation, is where the two simulations (the results of which are presented in §5.1.2) differ from one another.

- For Case (a) (results are shown in §5.1.2.1), collagen growth is dependent solely on the difference between current collagen stretch and the attachment stretch (according to Eqn. (4.29) and Eqn. (4.30)). Table 5.4 shows the rate parameters for the fibre growth differential equations (β_{J_p}), set to 0.5 (years^{-1}).

- For Case (b)(comparative results are shown in §5.1.2.2), collagen growth is additionally dependent on deviations of the areal cyclic stretch from the initial local values, as was described in §4.7.3 (according to Eqn. (4.31) and Eqn. (4.32)). The corresponding growth parameter β^{CS} is specified in Table 5.4.

In both cases, collagen growth (for the media and the adventitia) is specified to switch on between Year 4 and 5 of the simulation (t_{gr1} and t_{gr2} in Table 5.4). This will represent a period of growth that will aim to stabilise the geometry before further degradation.

The evolution of the attachment stretch distribution is also presented (determined in Table 5.3) in order to simulate the change in role of the adventitial collagen fibre group from acting as a protective sheath to principal load-bearing constituent. The evolution of the attachment stretch distribution (with a final range of $0.95-1.05$) takes place between Year 4 and 5, which will allow the observation of the specific changing role of the adventitia. It should be noted that the choice of rate parameters for the G&R of the collagen fibres was based on indications in literature (Langille, 1993), but also calibrated within the 3D structural model to allow for the development and stabilisation of an aneurysm geometry for the observation of the reactive behaviour of the collagen to the degrading of the media.

Table 5.4 additionally specifies the material parameters for the SEFs of the arterial constituents: neo-Hookean SEF for elastin fibres, highly non-linear SEF for medial collagen fibres, and quadratic functional form for the SEF of a single adventitial collagen fibre combined with a distribution of recruitment stretches. The material parameters for the medial elastin and collagen fibres were calculated so that the mechanical equilibrium at the beginning of the simulation is sustained in the systolic and diastolic configurations, with the elastin in the media bearing most of the load. The material parameter for the adventitial collagen of the protective sheath (which does not contribute to the mechanical equilibrium at the beginning of the simulation) is the value resulting from the analysis in Chapter 3. The values of the material parameters are equal for the two families of collagen fibres in the media and the adventitia and they do not change with remodelling.

5.1.2 Results

It must be noted that the downstream direction in the results presented is upwards in the depicted images.

5.1.2.1 Collagen growth only linked to stretch

This section of the results looks into the evolution of important metrics for the structural 3D simulation where growth depends solely on deviations of collagen stretches from homeostatic levels. It should be noted that all the results present data (both contour plots and geometric distortions) for the systolic configuration of the cylindrical artery.

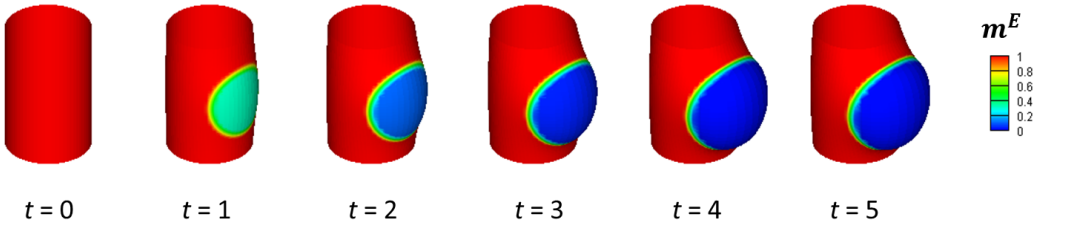

Figure 5.1: Spatial distribution of the evolution of prescribed normalised medial elastin m^E in the aneurysmal geometry, where $t = 0,1,2,3,4,5$ years, for the 3D structural model simulation, where growth is only linked to collagen stretches. m^E is prescribed to exponentially reach a value of 0.01 by the end of Year 4 and maintain it for the final year of the simulation.

Figure 5.1 confirms the definition for the prescribed degradation of the medial arterial constituents for the duration of the simulation. It depicts the normalised density of medial elastin m^E, which decreases to 1% by the end of Year 4 where no elastin turnover is biologically expected. The same prescribed degradation is applied for medial collagen $m^C_{M_p}$; however, parallel growth of medial collagen is also allowed, which will be observed in §5.1.2.2. This image allows the observation of the increase in the aneurysm geometry during the five-year period of the simulation, as media is prescribed to degrade in order to reproduce geometric features observed in the clinical aneurysmal tissue.

Figure 5.2 illustrates the axial (Figure 5.2(i)) and azimuthal (Figure 5.2(ii)) GL elastin strains; E_{11} and E_{22} respectively. These strains are calculated relative to the unloaded cylindrical configuration and represent the tissue strain. The elevated

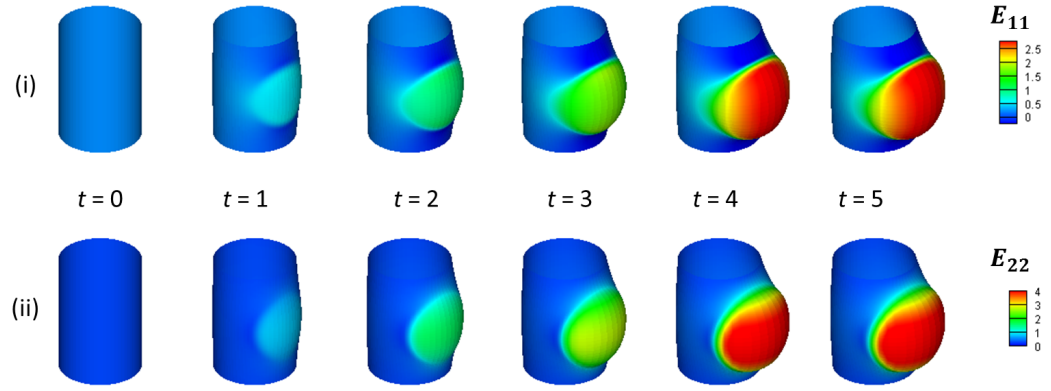

Figure 5.2: Spatial distribution of (i) axial and (ii) azimuthal GL elastin strains (E_{11} and E_{22} respectively), where $t = 0, 1, 2, 3, 4, 5$ years, for the 3D structural model simulation, where growth is only linked to collagen stretches. E_{11} reach a maximum of around 2.5 in the aneurysmal region and E_{22} a maximum of around 4 by the end of the simulation.

strains are observed in the aneurysmal region, consistent with the increased elastin stretches. Additionally, due to the axial contraction of the geometry during circumferential expansion, a small decrease in E_{11} is observed in the proximal and distal necks of the aneurysm.

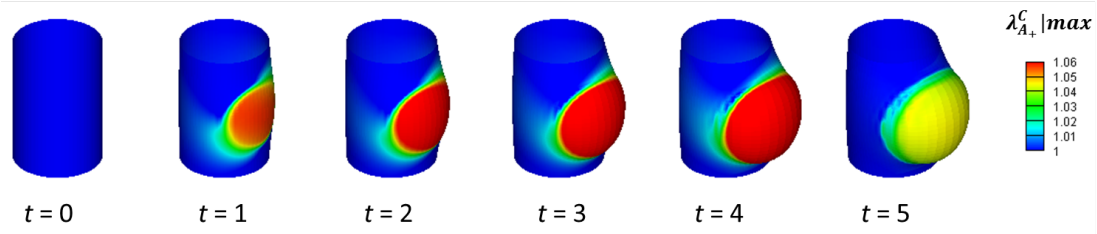

Figure 5.3: Spatial distribution of the evolution in the maximum stretch of positively wound adventitial collagen fibres $\lambda^C_{A_+}|^{max}$, where $t = 0, 1, 2, 3, 4, 5$ years, for the 3D structural model simulation, where growth is only linked to collagen stretches. $\lambda^C_{A_+}|^{max}$ steadily increases to a maximum of 1.06, as the media degrades and the geometry is distorted, reducing to an evolved homeostatic value of 1.05 by the end of the simulation.

Figure 5.3 and Figure 5.4 demonstrate the G&R behaviour of the adventitial collagen fibres. In Figure 5.3, the evolution of the maximum stretch of the positively

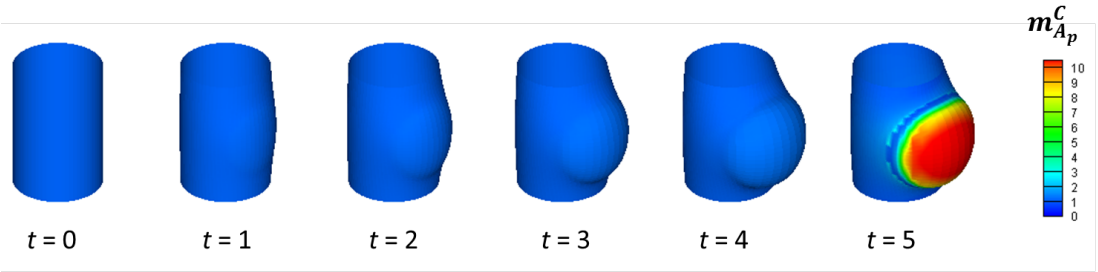

Figure 5.4: Spatial distribution of the evolution in the normalised density of adventitial collagen fibres $m^C_{A_p}$, where $t = 0,1,2,3,4,5$ years, for the 3D structural model simulation, where growth is only linked to collagen stretches. Growth is suspended until the final year of the simulation, when $m^C_{A_p}$ increases to a maximum of 10 by the end of Year 5, stabilising the geometry and establishing adventitial collagen as the primary load-bearer of the aneurysmal arterial tissue.

wound adventitial collagen fibres $\lambda^C_{A_+}|^{max}$ is observed. Even though the evolution of stretches between the positively and negatively wound collagen fibres is not symmetric (not a symmetric geometric distortion), the qualititative mechanical behaviour is the same and therefore, for the purposes of this study, the results for the positively wound collagen fibres are chosen to be presented here. Adventitial collagen strains, defined relative to their recruitment configurations in the direction of the fibres and calculated from the stretches depicted in the figure according to Eqn. (4.10), elevate during the media degradation stage and geometrical enlargement (to a maximum of around 1.06), albeit at a much lower magnitude than the elastin strains, which reach a maximum of 2.5 and 4 in the axial and circumferential directions respectively (from Figure 5.2). This difference in magnitudes of elevated strains relates to the difference in the definition of the reference configuration between the elastin and collagen fibres. For the collagen fibres, in particular, based on the remodelling algorithms, the evolution of their recruitment configurations is expected (according to Eqn. (4.27c)). During the final year of the simulation, the decrease of $\lambda^C_{A_+}|^{max}$ is noted to a final value of 1.05. This, of course, is the new maximum attachment stretch value, as determined by the definition of the evolution of the attachment stretch distribution (see Table 5.5). Collagen stretches are, by the end of the simulation, at homeostatic levels, while the stretch homeostasis has evolved to represent the changing load-bearing role of the adventitia. Since a distribution for the adventitial collagen stretches has been defined, the same behaviour is expected as seen in Figure 5.3 for the entirety of the distribution. In Figure 5.4,

the evolution of the adventitial collagen normalised density $m^C_{A_p}$ must be noted; for the purposes of this simulation, the growth phase for the collagen fibres during the final year of the simulation is represented. This growth phase contributes to the stabilisation of the geometry as the adventitial collagen becomes the major bear-loading constituent of the aneurysmal arterial wall; the value of $m^C_{A_p}$ has increased to a maximum of 10 by the end of Year 5.

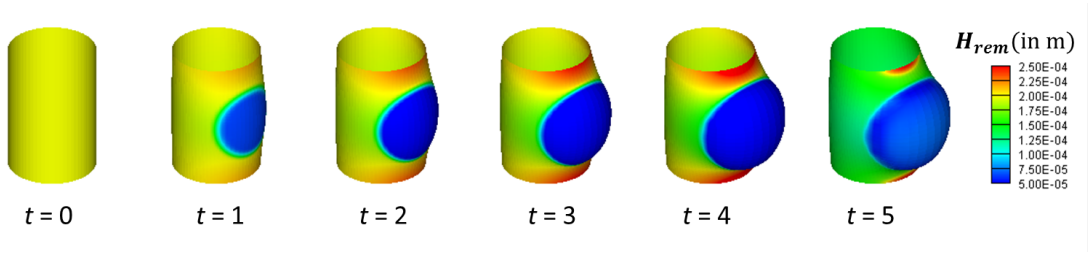

Figure 5.5: Spatial distribution of the evolution in the remodelled thickness H_{rem}, where $t = 0,1,2,3,4,5$ years, for the 3D structural model simulation, where growth is only linked to collagen stretches. H_{rem} in the aneurysmal area, initially at a value of 0.18mm, reduces to a minimum of 0.05mm during the first four years of media degradation and aneurysm development, and by the end of the Year 5, increases back to a minimum of approximately 0.11mm.

Figure 5.5 illustrates the evolution for the remodelled thickness of the computational domain H_{rem}, which takes into account changes in volumetric growth (with respect to the changes in the densities of the arterial constituents). The major changes in H_{rem} are anticipated in the circular aneurysmal region, where the media degradation, the geometrical distortion and collagen growth takes place. For the first four years of the simulation, the decrease in the medial constituents and the circumferential expansion result in a decrease of H_{rem} (minimum of about a fourth of the initial value, 0.18mm). During the final year of the simulation, however, due to the increased growth in adventitial collagen (as noted in Figure 5.4), H_{rem} increases to a minimum of approximately 0.11mm by the end of the simulation.

In Figure 5.6 the Cauchy stresses in the axial (σ_{11}) and the azimuthal (σ_{22}) direction are seen, as were calculated by Eqn. (4.16) to account for the evolution of the remodelled thickness H_{rem}. It is noted that there is a steady increase in both stresses (reaching maximum values of 0.5MPa and 0.9MPa respectively) for the first four years of media degradation and remodelling and a decrease to final values of 0.1MPa and 0.3MPa respectively, during the final year of growth and stabilisation.

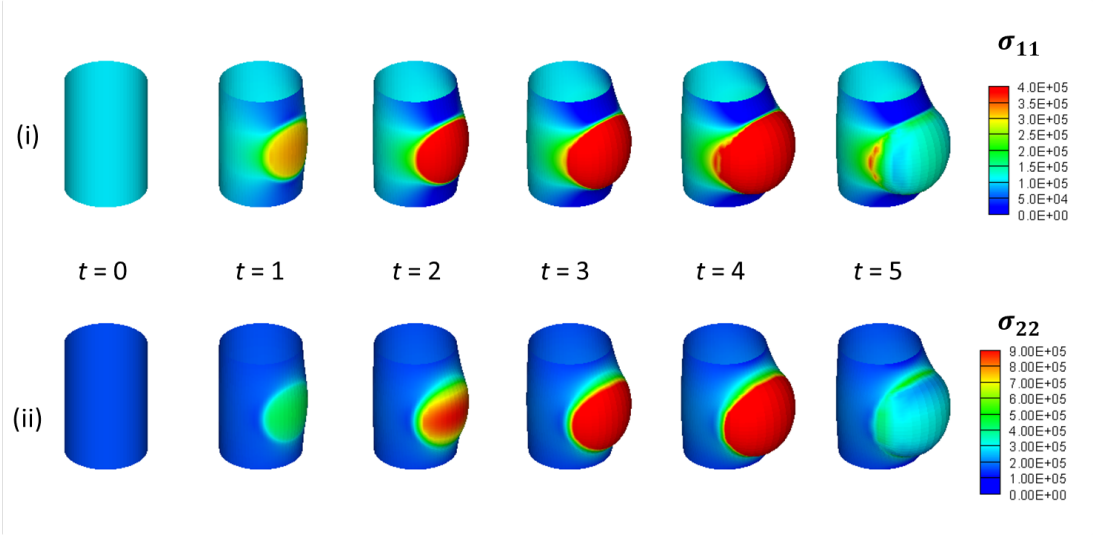

Figure 5.6: Spatial distribution of (i) axial and (ii) azimuthal Cauchy stresses calculating for the remodelled thickness (σ_{11} and σ_{22} respectively), where $t = 0,1,2,3,4,5$ years, for the 3D structural model simulation, where growth is only linked to collagen stretches. σ_{11} and σ_{22} within the aneurysmal circular region reach maxima of around 0.5MPa and 0.9MPa by Year 4 and decrease to values of 0.1MPa and 0.3MPa respectively by the end of the simulation.

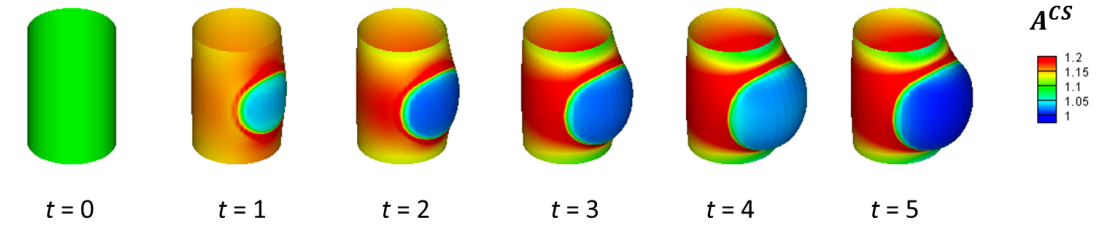

Figure 5.7: Spatial distribution of the evolution in the cyclic areal stretch A^{CS}, where $t = 0,1,2,3,4,5$ years, for the 3D structural model simulation, where growth is only linked to collagen stretches. A^{CS} decreases for the circular region of the aneurysm (minimum of 1.05) and increases for the surrounding computational domain (maximum of 1.4).

Figure 5.7 depicts the evolution of the areal cyclic stretch A^{CS}, illustrating the differences between systolic and diastolic stretches throughout the simulation and for the entirety of the computational domain. From the prescribed initial value of 1.1, A^{CS} gradually decreases within the circular defined aneurysmal region to a minimum of 1.05 (in the aneurysm dome) by the end of the simulation; however, A^{CS} increases rapidly for most of the surrounding computational domain, to a maximum of over 1.2, sustained to the end of the simulation and the stabilisation of the aneurysm. Given the indications for physiological cyclic stretches (Ando and Yamamoto, 2010), it is believed that the values of A^{CS} for the surrounding vasculature are unrealistic. Considering that the growth assumptions for this set of results only relate to deviations of collagen stretches from attachment values, the growth hypothesis, linked to cyclic deformation, is introduced for the following set of results.

5.1.2.2 Collagen growth linked to cyclic deformation

In this results sections, the final distributions of important metrics of interest between two cases of results are compared: Case (a) the five-year simulation outlined in §5.1.1, where collagen growth is solely dependent on deviations of collagen stretches from attachment levels (those results were investigated in §5.1.2.1) and (b) the same five-year simulation (degradation - remodelling - growth), with a term of growth that is dependent on the deviations of areal cyclic stretch from homeostatic values additive to the growth prescribed by deviation of collagen stretch from attachment levels, following Eqn. (4.31)-Eqn. (4.32) and the parameters in Table 5.4. Since growth is initiated for the final year of the simulations, the results and analysis up to Year 4 presented in §5.1.2.1 also apply for Case (b), the end results of which are presented here.

Figure 5.8 shows the distribution in the maximum stretch of positively wound adventitial collagen fibres $\lambda^{C}_{A_+}|^{max}$ for the two cases (a) and (b) at the end of the simulation (Year 5). It is noted that, in case (b), the majority of the aneurysmal area has reached the new prescribed attachment stretch value of 1.05 (a behaviour observed for Case (a) in §5.1.2.1 too). However, a difference is spotted in the geometry of the surrounding computational domain between the two cases. For Case (a), there is a slight expansion of the parent artery, which is not observed in Case (b). When the time sequences in §5.1.2.1 are examined, it can be seen that this expansion takes place during the first four years of the simulation. Therefore it can be said that, for Case (b), the parent artery eventually retracts from the expanded geometry during

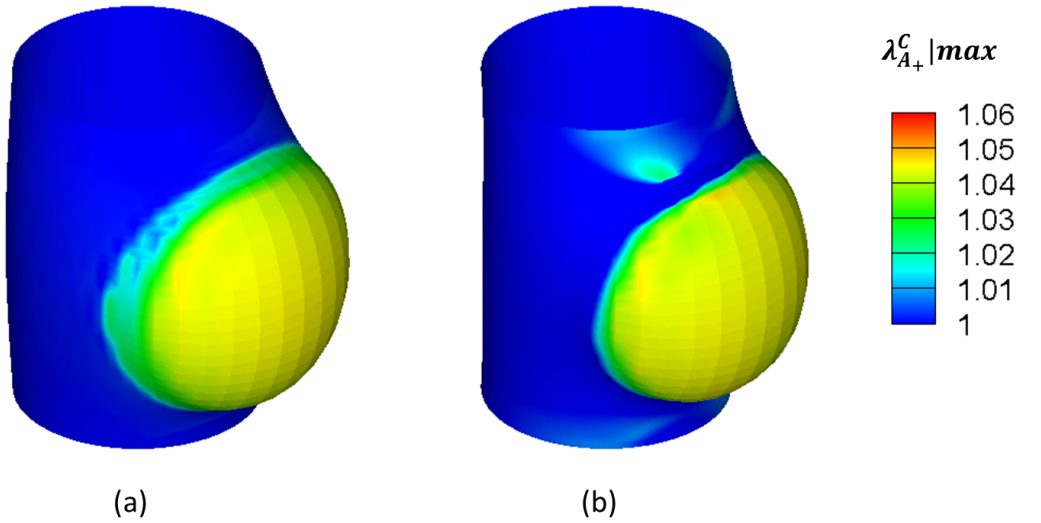

Figure 5.8: Comparison of the distribution in the maximum stretch of positively wound adventitial collagen fibres $\lambda^C_{A_+}|^{max}$ at the end of the simulation ($t = 5$ years) for growth linked (a) only to stretch and (b) also to cyclic deformation. $\lambda^C_{A_+}|^{max}$, for both cases, has reached the prescribed evolved attachment value of 1.05 for most of the aneurysmal region. There is an area of elevated $\lambda^C_{A_+}|^{max}$ in the downstream section of the aneurysm neck.

the final year of the simulations, i.e. during the differentiating growth phase. It can also be deduced from this observation that, due to the geometric retraction, a small area in the downstream neck of the aneurysm displays an isolated region of elevated collagen stretch.

In Figure 5.9, it is possible to compare the final distribution of cyclic areal stretch A^{CS} in the computational domain for the two cases. Contrary to Case (a), by the end of the simulation, A^{CS} for Case (b) has mostly returned to the physiological levels (in the range of $1.12 - 1.16$) for the computational domain neighbouring the circular aneurysmal region. The return of A^{CS} is therefore observed closer to the initial values for the majority of the neighbouring computational domain. Small regions on the side of the aneurysm show a slightly elevated A^{CS}, but those areas are significantly reduced compared to the results of Case (a).

Figure 5.10 depicts the final distribution for the normalised density of medial collagen $m^C_{M_p}$ for the two cases. This is in order to draw the attention to the differentiating collagen growth for the computational domain surrounding the aneurysm,

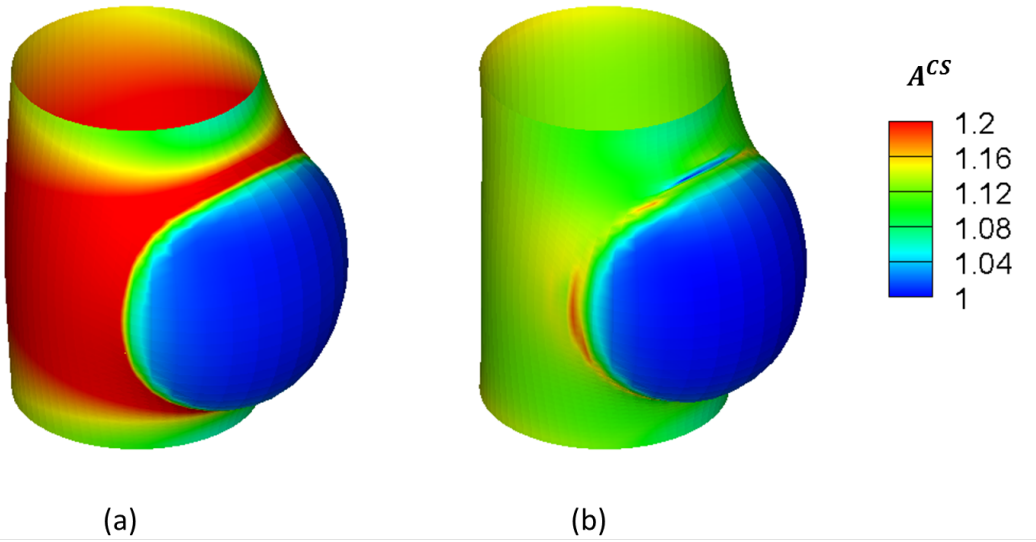

Figure 5.9: Comparison of the distribution in the cyclic areal stretch A^{CS} at the end of the simulation (t = 5 years) for growth linked (a) only to stretch and (b) also to cyclic deformation.

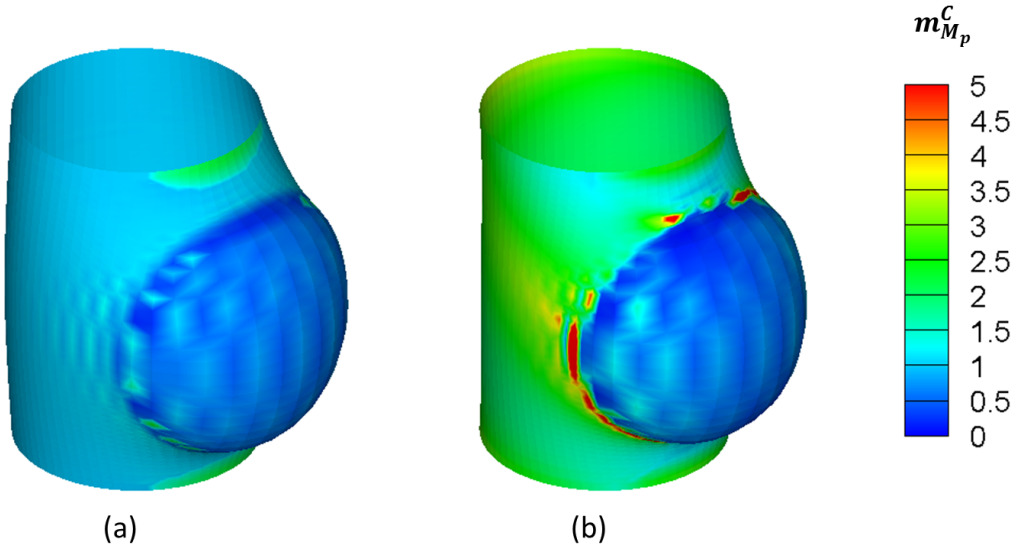

Figure 5.10: Comparison of the distribution in the normalised density of medial collagen fibres $m^C_{M_p}$ at the end of the simulation (t = 5 years) for growth linked (a) only to stretch and (b) also to cyclic deformation.

given the additional definition of A^{CS} homeostasis related to collagen growth. Since there is no media degradation and no evolution of the attachment stretch distribution for the adventitial collagen in the neighbouring vasculature, medial collagen remains a key load-bearing constituent, able to grow (elastin turnover is not possible). For Case (a), growth in that area is insignificant, since the collagen stretches do not deviate largely from the attachment values in that region. However, for Case (b), because a significant deviation of areal cyclic stretch A^{CS} from the initial values is seen by Year 4 (indicated in Figure 5.7 for $t = 4$ years), the increase in medial collagen is expected. For both cases, there is a small medial growth in the aneurysmal region; after it was prescribed to degrade until Year 4, $m^C_{M_p}$ reaches values of around 1.5 in the aneurysm dome.

5.2 IMPLEMENTATION OF FSG FRAMEWORK

Following the results in the structural code for an idealised saccular aneurysm on a cylindrical segment adjusted for the clinical case in the previous section, in this following section, the setup is described and the results are presented for the complete 3D FSG simulations using clinical imaging data that aim to investigate the effect of the definition for elastin degradation linked to flow on the structural model and G&R algorithms of aneurysm evolution.

5.2.1 Simulation and parameter overview

Simulations were performed on a 64BIT desktop PC (Intel Xeon CPU E31245 @3.3 GHZ, 16 GB RAM) running Windows 7 Enterprise. Flow was solved by ANSYS CFX using four cores. A complete FSG simulation consisting of 500 solid steps (corresponding to ten years) with the CFD performed every 10 steps takes around 6 hours. The geometrical and physiological data (radii, lengths, initial stretches, thicknesses, pressures and fibre orientations) for the computational domain of this set of simulations are kept the same as for the previous 3D structural simulations, described in §5.1 and summarised in Table 5.1.

Employing the form of the 1D simulations in Chapter 3, four phases are presented in the 3D FSG simulations in this section: (a) prescribed media degradation, (b) remodelling, (c) stabilisation through growth and (d) further elastin degradation linked to flow. For phase (a), the degradation of the medial constituents (elastin and

Table 5.5: Differentiating parameters for the simulation in §5.2 compared to the simulation presented in §5.1.

Differentiating simulation parameters		
Prescribed media degradation		
Time to minimum prescribed (elastin,collagen)	T	1(in years)
Minimum elastin density by time T	m_T^E	0.5
Minimum medial collagen density by time T	m_T^C	0.5
Attachment stretch evolution (protective sheath)		
Start time for evolution	t_1	8(years)
Stop time for evolution	t_2	10(years)
Final minimum attachment stretch	$\lambda_A^{AT}\|_{t_2}^{min}$	0.95
Final maximum attachment stretch	$\lambda_A^{AT}\|_{t_2}^{max}$	1.05
Final modal attachment stretch	$\lambda_A^{AT}\|_{t_2}^{mod}$	1
Elastin degradation linked to flow		
Maximum rate of degradation	D_{max}	0.5
Critical low WSS (maximum degradation)	$\tau_{low-max}$	0.5Pa
Critical low WSS	$\tau_{low-min}$	7Pa
Critical high WSS	$\tau_{high-min}$	10Pa
Critical high WSS (maximum degradation)	$\tau_{high-max}$	12Pa
Time period of WSS averaging	T_L	5(years)

collagen fibres) were prescribed, in a similar way to §5.1, with the different parameters presented in Table 5.5 (this table identifies the parameters in this section that are different from the ones in §5.1); by the end of Year 1 of the simulation, the normalised densities of medial elastin m^E and collagen fibres $m_{M_p}^C$ has been exponentially reduced to 0.5; this represents an initial small perturbation of the mechanical arterial equilibrium that, contrary to the previous simulation in this chapter, will be followed by further degradation linked specifically to flow. The same circular aneurysmal area that was defined for §5.1 was employed here.

For the remodelling phase (b) of the simulations, the setup of recruitment (single value) and attachment (distribution) stretches are as per Table 5.3. The evolution of

the attachment stretch distribution is also presented, as was implemented in §5.1, in order to simulate the change of the adventitial collagen fibre group from a protective sheath to principal load-bearing constituent. However, because of the different simulation time that is defined here and the fact that the focus lies in observing the differences in elastin degradation depending on the definition of WSS homeostasis, the evolution of the adventitial stretch distribution (to a $0.95-1.05$ range) is set to take place between Year 8 and 10 of the simulation, i.e. only at the final stage of the simulation (the difference from §5.1 is specified in Table 5.5).

At phase (c) of the simulation, increased growth of collagen fibres is set in the arterial wall (in the media and the adventitia) following the prescribed medial degradation, between Year 4 (t_{gr1}) and Year 5 (t_{gr2}), as was defined for the structural simulations in §5.1 and parameterised in Table 5.4.

For the purposes of this investigation, according to §4.7.1, three different simulations are run with the three different elastin degradation links to flow for phase (d) of further elastin degradation linked to flow, specified by parameters in Table 5.5. This further degradation of elastin is set to begin in Year 5. Up to Year 5, those three simulations have been identical.

- For Case 1. (spatially homogeneous and temporally non-adaptive WSS homeostasis), four boundaries are set (Figure 4.9); those were chosen on the basis of literature presented in Chapter 2 and observing the haemodynamics of the specific clinical case. These parameters imply that WSS homeostasis (and therefore no further elastin degradation) is achieved in a range between 7 and 10Pa.
- For Case 2. (spatially heterogeneous and temporally non-adaptive WSS homeostasis), a maximum rate of degradation D_{max} of 0.5 is set.
- For Case 3. (spatially heterogeneous and temporally adaptive WSS homeostasis), the same D_{max} is set. WSS homeostasis is then calculated by averaging the values of WSS at each node of the specified aneurysmal circle in the computational domain over the past period of $T_L = 5$ years.

Since this is the same clinical case and the initial conditions are the same, the material parameters are as presented in Table 5.4.

5.2.2 Results

The following FSG results, which research different hypotheses of WSS homeostasis, illustrate the changing geometry and the mechanical properties of the computational domain where the aneurysmal area is identified, while the entirety of the reconstructed artery as was indicated in Chapter 4 was used to simulate the blood flow; an indicative image (automatically outputted from ANSYS for every ten structural steps of an FSG simulation) is shown in Figure 5.11 to illustrate application of CFD in the suggested FSG framework for the complete arterial geometry, that includes both the computational domain where the algorithms of G&R are applied, and the neighbouring vasculature. It should be noted that, for all results, the downstream direction is upwards or leftwards in the depicted images. It should be mentioned here again that all the results present data (both contour plots and geometric distortions) for the systolic configuration of the cylindrical artery.

5.2.2.1 Initial prescribed media degradation

As was described in §5.2.1, the simulations for the investigation of links between elastin degradation and flow, with a total simulation time of ten years, are initiated by a five-year phase of prescribed degradation, remodelling and growth to illustrate a first perturbation of the arterial geometry, given the limited knowledge on exact reasons for the inception of aneurysms, but the evidence that the degradation of the medial layer takes place (Kim et al., 1992). Figure 5.12 illustrates the degradation of the media; the prescribed degradation is the same for the elastin and the collagen fibres of the media; however, past the first year of prescribed degradation, medial collagen is not further degraded, but is allowed to grow, according to the hypotheses (see Figure 5.15 below). Consequently, what is shown in the image (for the first two time points, $t = 0$ and $t = 1$ year) applies for the normalised density of either the medial elastin (m^E) or collagen ($m^C_{M_p}$) fibres. The prescribed degradation is applied symmetrically and reaches its minimum (0.5) by the end of the first year. The prescribed circular degradation area within the inner radius can be observed, where the minimum normalised density of the medial constituents is found and it gradually increases from the inner to the outer radius of the circular area, for the smooth transition within the computational domain. Following the first year of prescribed degradation and by the end of the first five years, a perturbation of the cylindrical geometry is in fact observed.

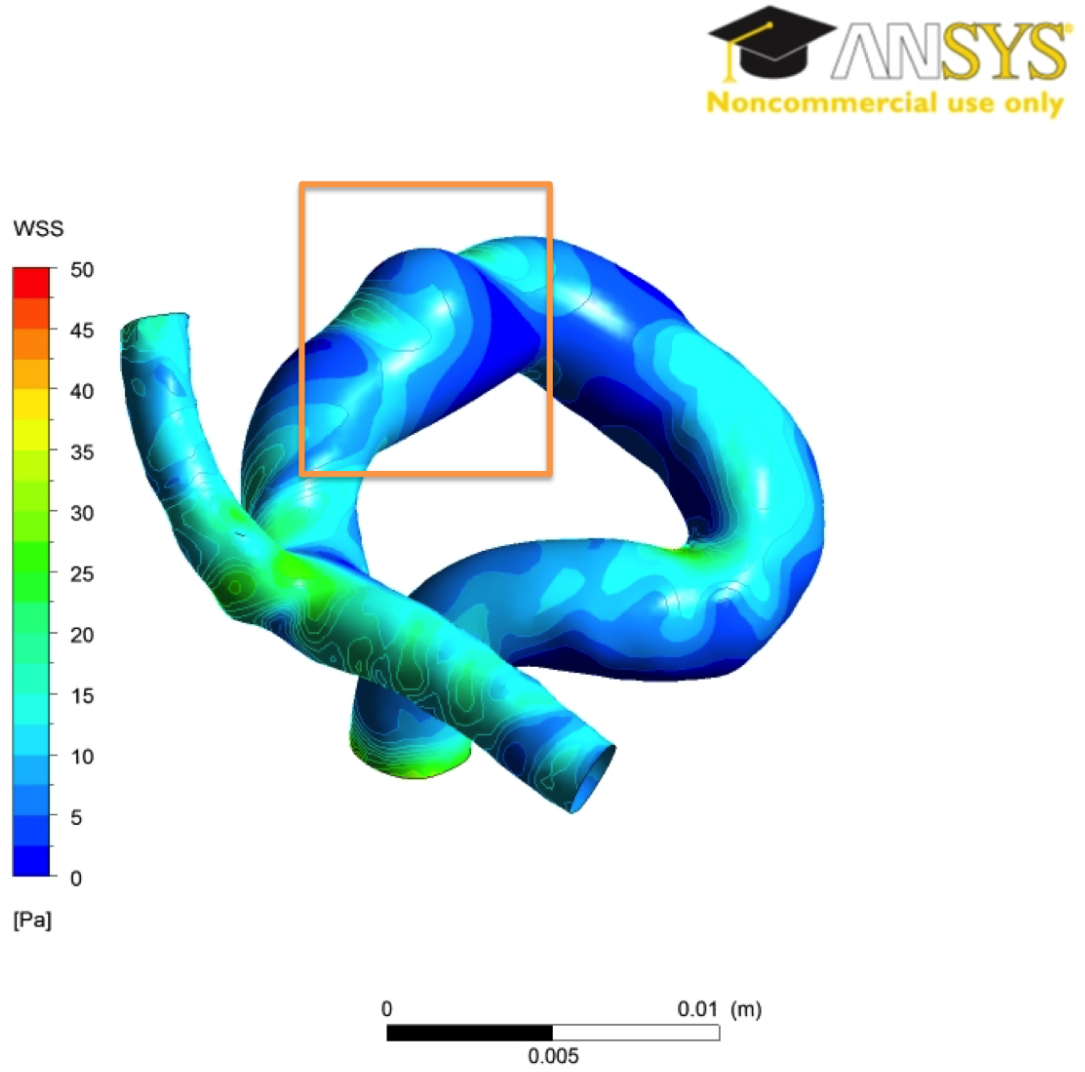

Figure 5.11: Automated output image from ANSYS depicting the distribution of WSS in the entirety of the clinical arterial geometry (computational domain of aneurysm indicated by the orange frame as well as neighbouring vasculature) for the purposes of the FSG framework of aneurysm evolution.

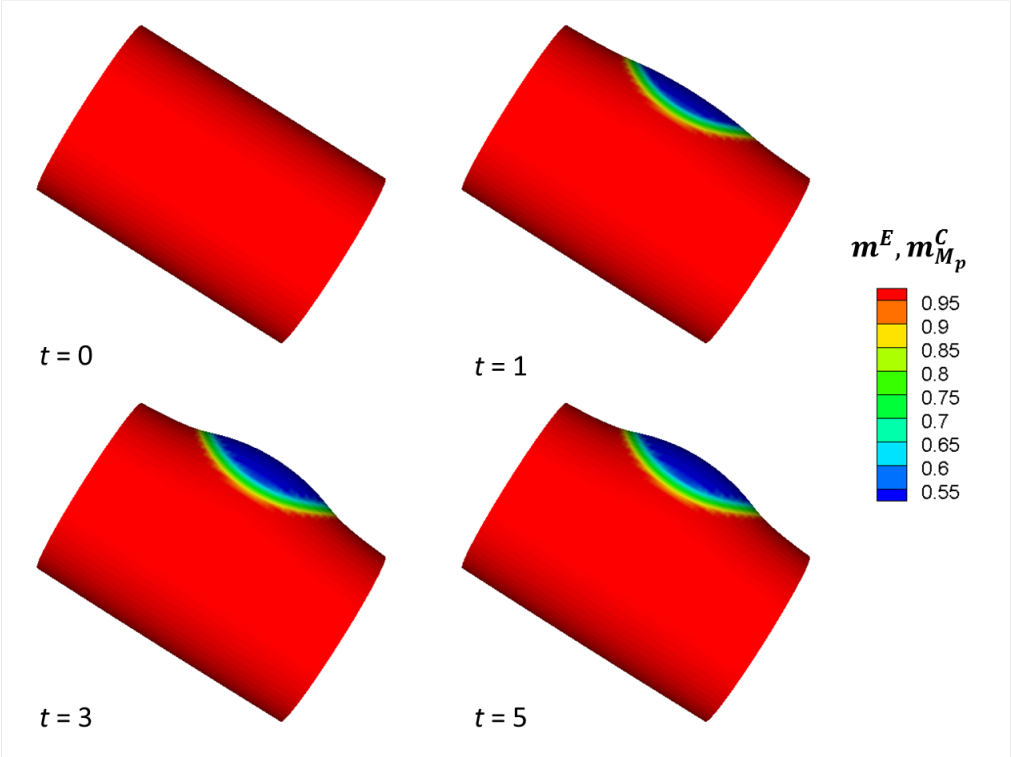

Figure 5.12: Spatial distribution of the evolution in the prescribed normalised medial elastin m^E and in the aneurysmal geometry, where $t = 0, 1, 3, 5$ years for the first stage of the clinical case FSG simulation (linked to flow). By the end of Year 1, the normalised densities of the medial constituents have reached a minimum of 0.5 and the geometry continues to increase by the end of five years.

Figure 5.13 depicts the evolution of the collagen stretches for the positively wound fibres in the media ($\lambda^C_{M_+}$), as a representation of the collagen stretches during the initial period of prescribed degradation. It can be observed that, at the beginning of the simulation, the value of the stretches in the computational domain is at the set attachment level (of 1.07), but as the media degrades and the elastin circumferential stretch increases, the collagen stretches expectedly increase as well over attachment levels. Due to the remodelling hypothesis, collagen fibres reconfigure themselves in order to return stretches at attachment levels and it can be observed that, by the end of the five years, stretches have essentially return to the 1.07 homeostatic value.

Similarly for the adventitial collagen fibres, in Figure 5.14, the evolution of pos-

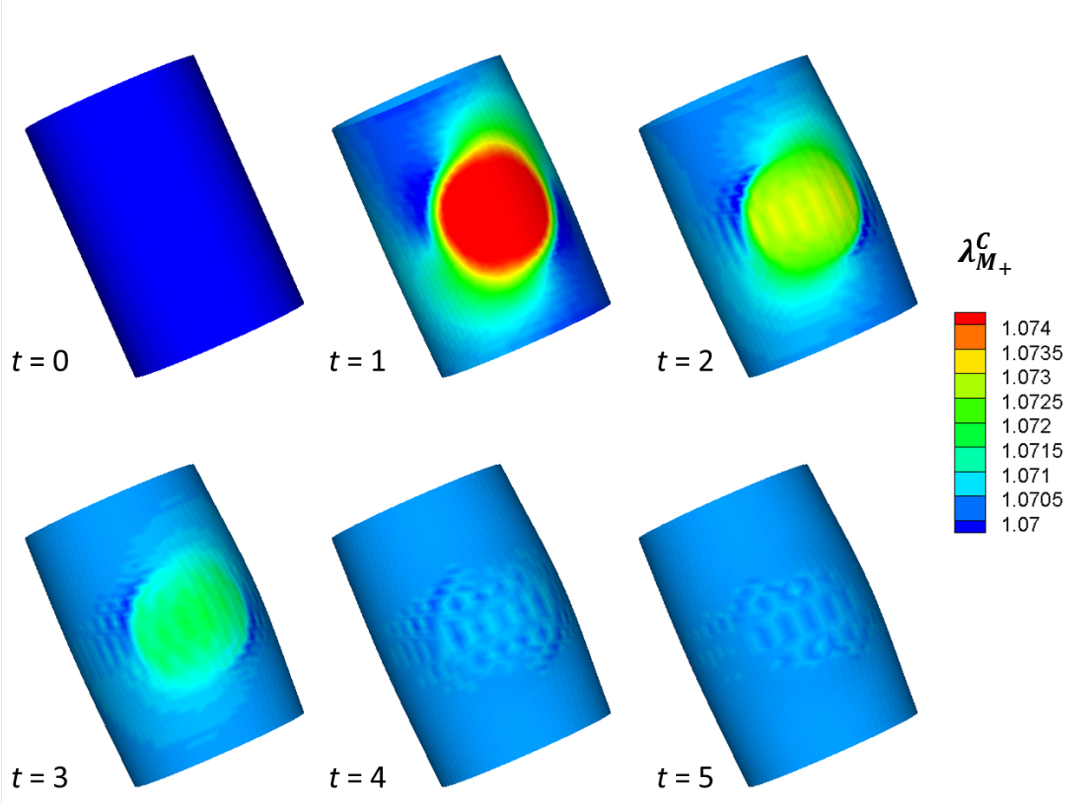

Figure 5.13: Spatial distribution of the evolution in the stretch of positively wound medial collagen fibres $\lambda^C_{M_+}$, where $t = 0,1,2,3,4,5$ years for the first stage of the clinical case FSG simulation (linked to flow). Those stretches initially increase from the homeostatic values as the media is prescribed to degrade, but towards the end of the five years, return towards the initial attachment stretch value of 1.07.

itively wound adventitial collagen fibre stretches is observed. Since a distribution for the recruitment and attachment stretches of the adventitial collagen have been defined, following the analysis Chapter 4, the evolution of the maximum $\lambda^C_{A_+}|^{max}$, minimum $\lambda^C_{A_+}|^{min}$ and modal $\lambda^C_{A_+}|^{mod}$ values for the adventitial collagen stretches are depicted. They initially increase and deviate from the the prescribed attachment stretch distribution (with a defined range between 0.9 and 1 and a modal value of 0.95), but eventually return to homeostatic levels through the remodelling of the recruitment stretches. For this stage of the simulation, the attachment stretch distribution has not evolved yet and, therefore, the final values of the stretches are the same as the initial ones.

Figure 5.15 depicts the evolution of the normalised densities for the medial $m^C_{M_p}$ (Figure 5.15(i)) and adventitial $m^C_{A_p}$ (Figure 5.15(ii)) collagen. For the medial col-

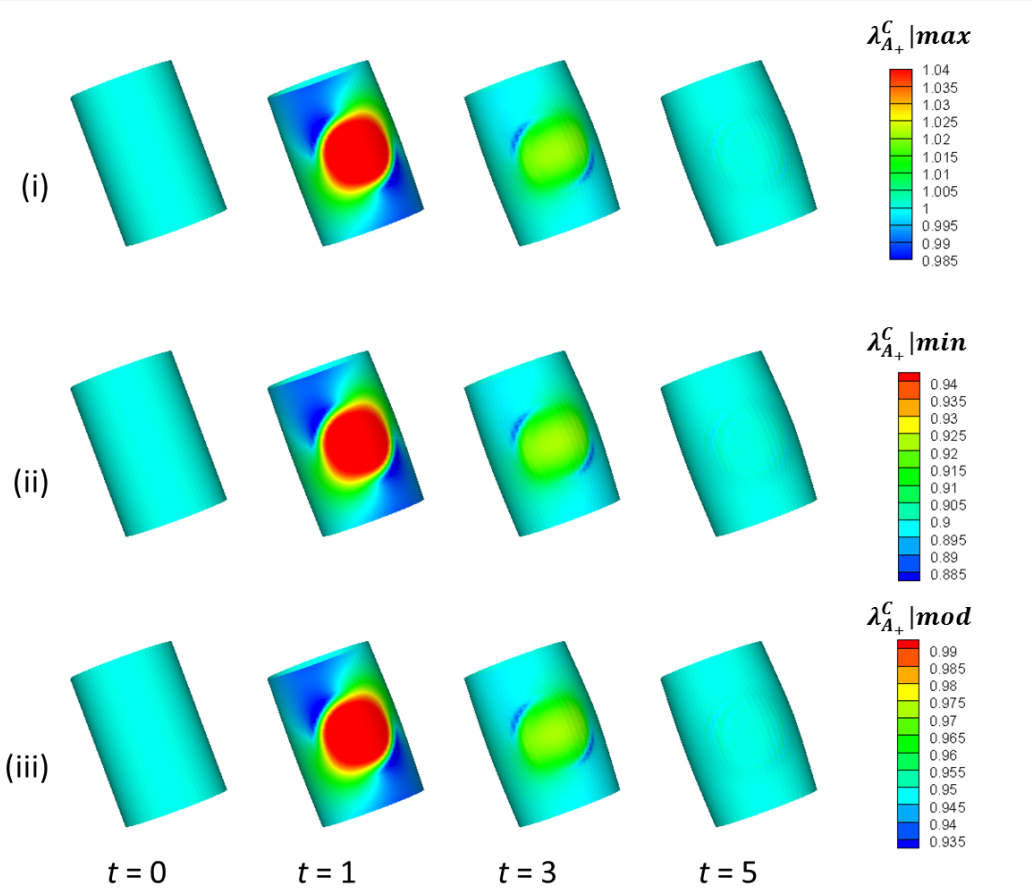

Figure 5.14: Spatial distribution of the evolution in the (i) maximum, (ii) minimum and (iii) modal stretch of positively wound adventitial collagen fibres, $\lambda^C_{A_+}|^{max}$, $\lambda^C_{A_+}|^{min}$ and $\lambda^C_{A_+}|^{mod}$ respectively, where $t = 0,1,3,5 years$ for the first stage of the clinical case FSG simulation (linked to flow). Stretches increase, initially deviating from attachment levels while the geometry is perturbed from the media degradation and return to the homeostatic range of the attachment distribution by the end of the five years.

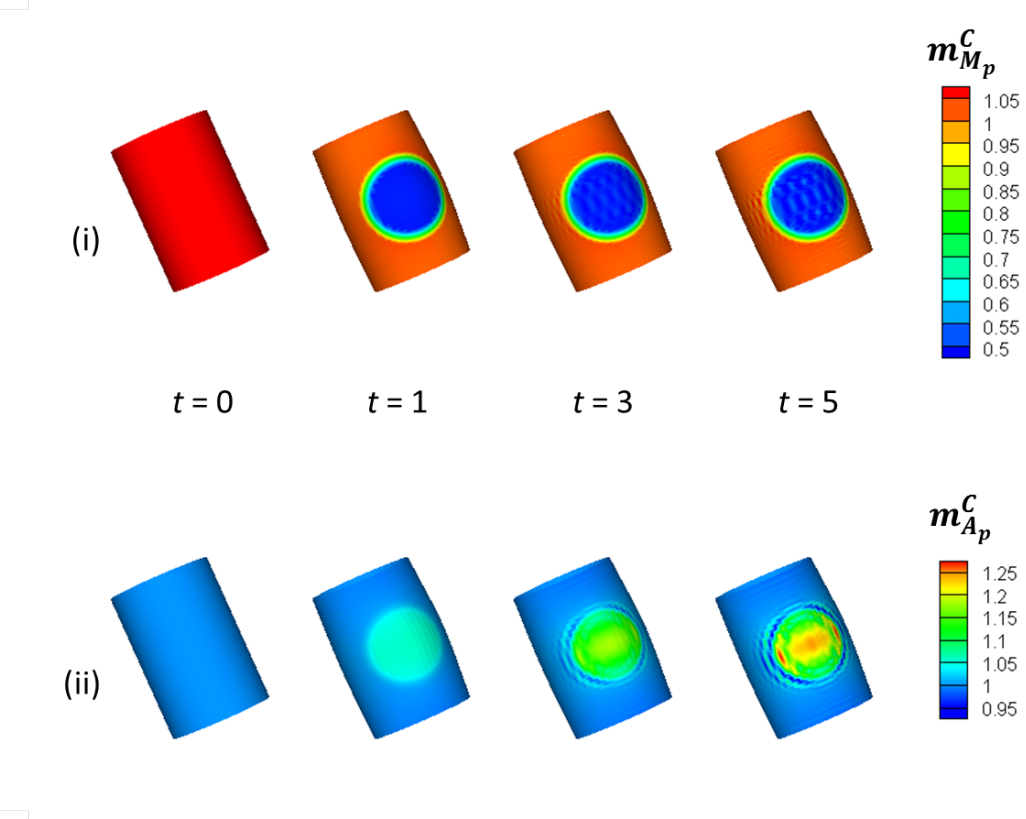

Figure 5.15: Spatial distribution of the evolution in the (i) medial and (ii) adventitial collagen normalised mass density, $m^C_{M_p}$ and $m^C_{A_p}$ respectively, where $t = 0, 1, 3, 5$ years for the first stage of the clinical case FSG simulation (linked to flow). Medial collagen degrades as part of the initial prescribed media degradation, but is allowed to subsequently grow; by the end of the five years, there is a small increase. For the adventitial collagen steady growth is observed, increasing during the fifth year.

lagen, an initial degradation is prescribed down to a minimum normalised density value of 0.5, but collagen is able to grow again and it is possible to see that, by the end of Year 5, there is a small increase in the circular area of prescribed degradation. For the adventitial collagen, it is observed that, as the medial constituents degrade and the collagen stretches increase, growth does take place. Especially between Year 4 and Year 5 a marginally bigger increase can be noticed, which is expected as an increased growth switch is set for that period (§5.2.1).

The next section shows the observations from linking further elastin degradation to flow and, specifically, deviations of WSS from homeostatic levels, as overviewed in §5.2.1. Therefore, it is important to observe changes in the WSS distribution during the first period of the simulation, before the onset of further degradation. Fig-

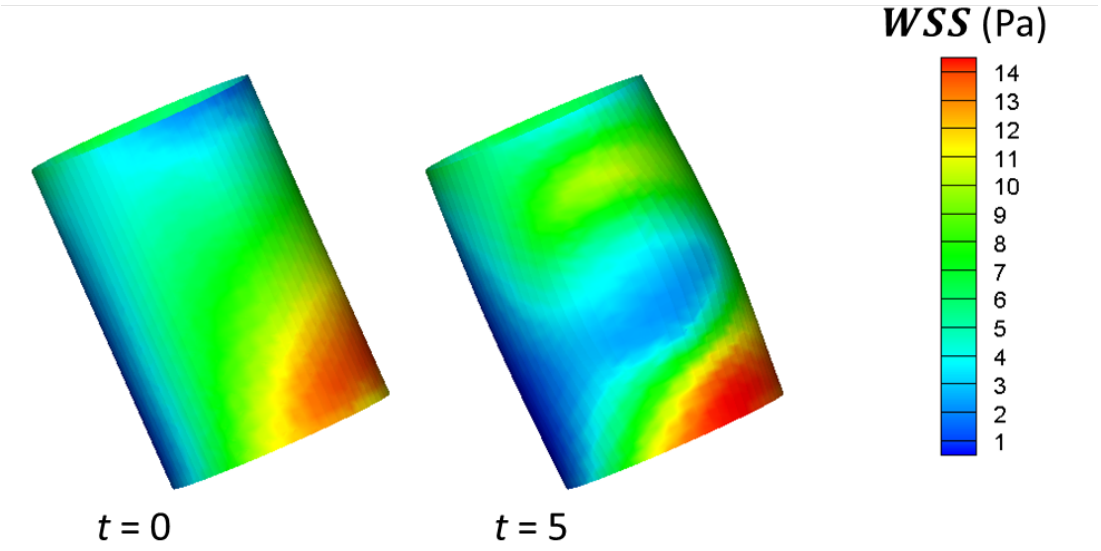

Figure 5.16: Spatial distribution of WSS, where $t = 0,5$ years for the first stage of the clinical case FSG simulation (linked to flow). At the end of Year 5, there is a WSS decrease in the upstream section a smaller increase in the downstream section of the aneurysmal area, where the prescribed degradation is applied.

ure 5.16 illustrates the WSS distribution at the beginning and the end of the first five-year period. It can be observed that, at the beginning of the simulation, the WSS in the area where the media degradation is prescribed, is relatively uniform and around 8Pa. By the end of the five-year period of prescribed medial degradation, remodelling and growth, the following observations can be noticed: (a) a decrease in the WSS on the upstream section of the aneurysmal area (of around $3-6$Pa) as well as (b)a smaller increase in a smaller part of the downstream section of the aneurysmal area (of around 2Pa).

5.2.2.2 Elastin degradation linked to flow

Following the initial five-year phase of prescribed elastin degradation, Figure 5.17 illustrates the differentiation in growth at the end of the ten-year simulation, for the three definitions of WSS homeostasis (spatially homogenous and temporally non-adaptive, spatially heterogeneous and temporally non-adaptive and spatially heterogeneous and temporally adaptive). A common characteristic among the three cases is the asymmetry in increased growth towards the upstream section. However, Case 1. also shows an increased growth in the downstream section. Case 2. appears

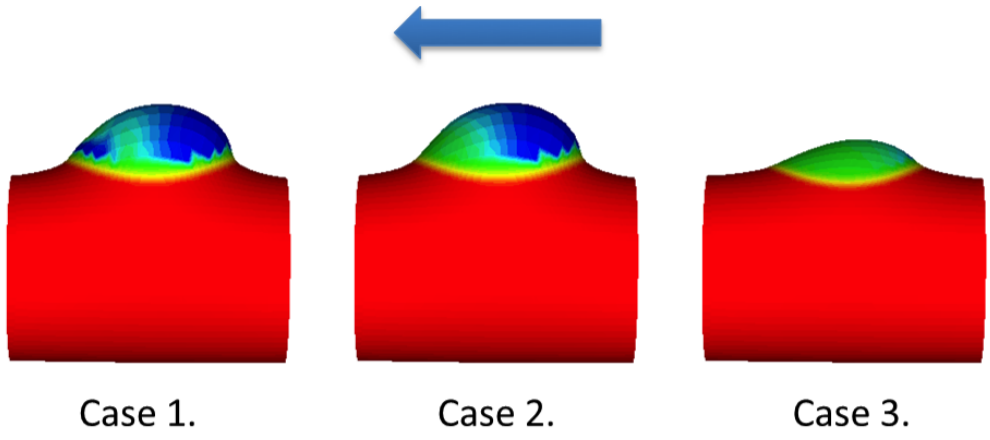

Figure 5.17: Aneurysm growth for three cases of elastin degradation linked to flow. WSS homeostatic threshold is for Case: 1. spatially homogeneous and temporally non-adaptive, 2. spatially heterogeneous and temporally non-adaptive and 3. spatially heterogeneous and temporally adaptive. The arrow indicates that the direction of the blood flow is leftwards. The images of aneurysm growth are depicting the end of the ten-year FSG simulation. Growth appears greatest for Case 1. and 2. with a similar increased growth upstream of the aneurysmal area. Case 1. also shows small growth on the downstream section. Case 3. shows very small asymmetric growth.

to have the largest general growth, with Case 1. marginally smaller, whereas Case 3. shows only a small growth past the growth which was the result of the prescribed degradation of the first simulation stage.

For the closer understanding of the differentiations between the defined cases, Figure 5.18 summarises the evolution of the medial elastin normalised density m^E for each case, from Year 6 to Year 10, i.e. the end of the simulation. As expected from observing growth in Figure 5.17, the density of medial elastin for Case 1. and 2. has dramatically decreased in most of the upstream section of the aneurysmal area, reaching a value of around 0.1 for most of the defined aneurysmal area. The same maximum elastin degradation is seen in Case 3. only for a small upstream strip. The general pattern of degradation, however, differs between Case 1. and 2., as it must be noted that for Case 1. there is an extra area of equal maximum degradation on the downstream boundary of the aneurysmal area.

Figure 5.19 exhibits elastin degradation for Case 1. by illustrating the WSS dis-

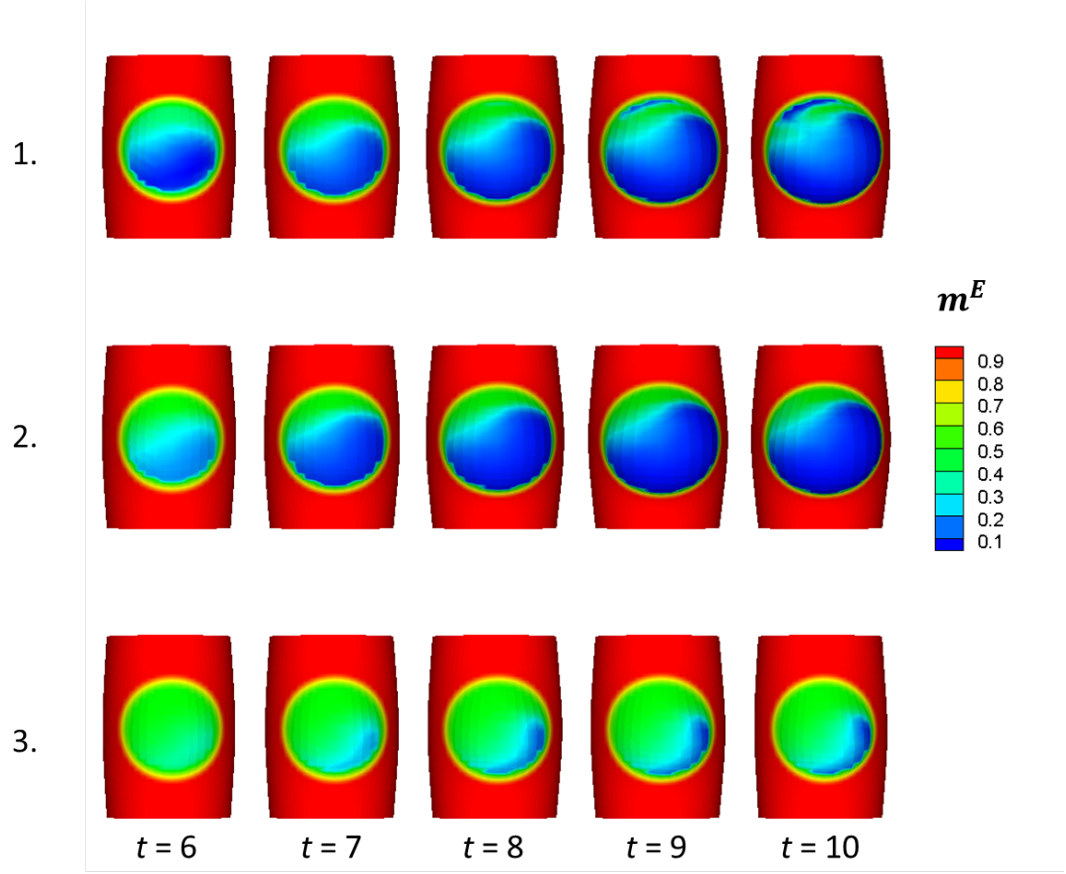

Figure 5.18: Spatial distribution of normalised elastin degradation for three cases of elastin degradation linked to flow. WSS homeostatic threshold is for Case: 1. spatially homogeneous and temporally non-adaptive, 2. spatially heterogeneous and temporally non-adaptive and 3. spatially heterogeneous and temporally adaptive. The FSG evolution of elastin degradation is illustrated here for $t = 6, 7, 8, 9, 10$ years. The pattern of degradation in the upstream section for Case 1. and 2. is very similar, with Case 1. also showing minimum degradation on a small upstream section. Further degradation in Case 1. appears in a small upstream section.

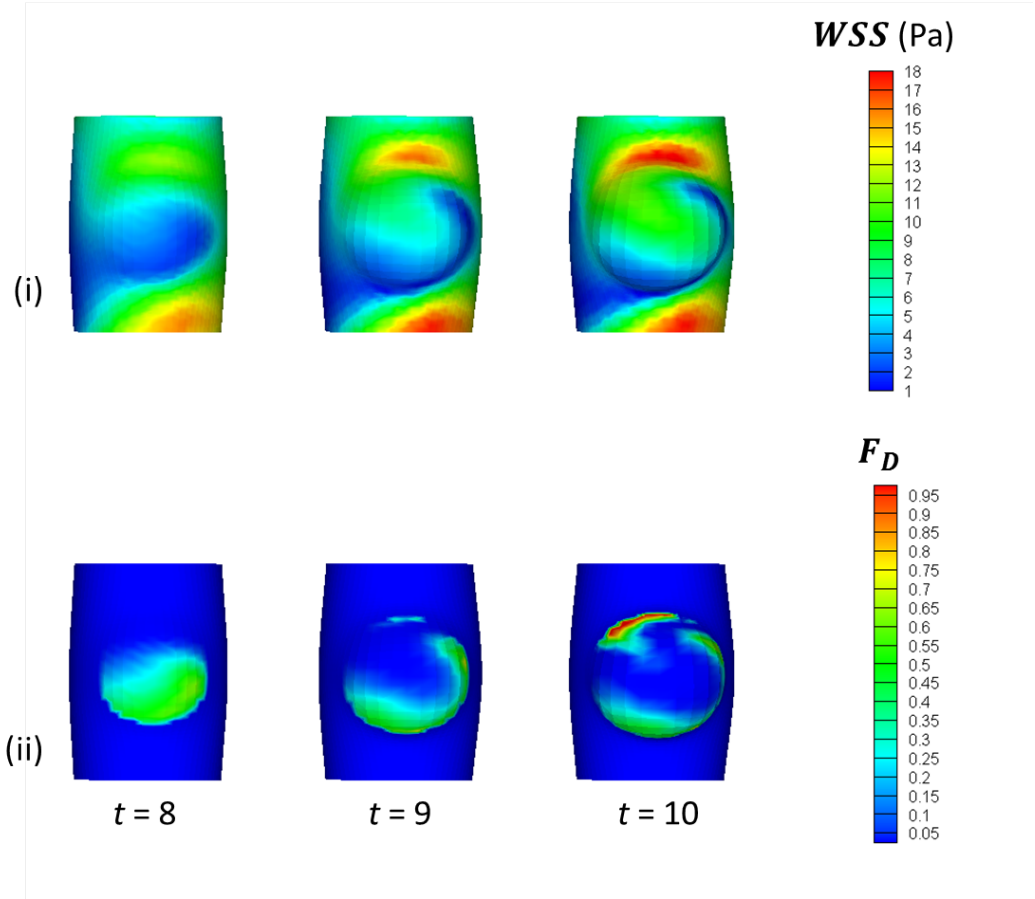

Figure 5.19: Investigation for Case 1.: spatially homogeneous and temporally non-adaptive WSS threshold for elastin degradation; (i) WSS distribution and (ii) WSS degradation factor F_D for $t = 8, 9, 10$ years. Deviations of WSS from the homeostatic range (both higher and lower stresses) for this case drive elastin degradation in the upstream and downstream sections.

tribution alongside the degradation factor F_D, introduced in Chapter 4, for the final two years of the simulation. For this case, degradation ($0 < F_D \leq 1$) was defined for WSS deviating from the homogeneous, non-adaptive range of $7 - 10$Pa. WSS can therefore be matched with the degradation. It should be noticed that in Year 8, the lower WSS in the upstream section drive the majority of the degradation; however, as the geometry further enlarges, WSS in that region tends towards the initial levels and, as a consequence, degradation reduces. On the other hand, it is only towards the end of the simulation that the increase in the downstream section and a much higher degradation (F_D close to 1) is seen.

Similarly for Case 2., Figure 5.20 illustrates WSS distribution and degradation

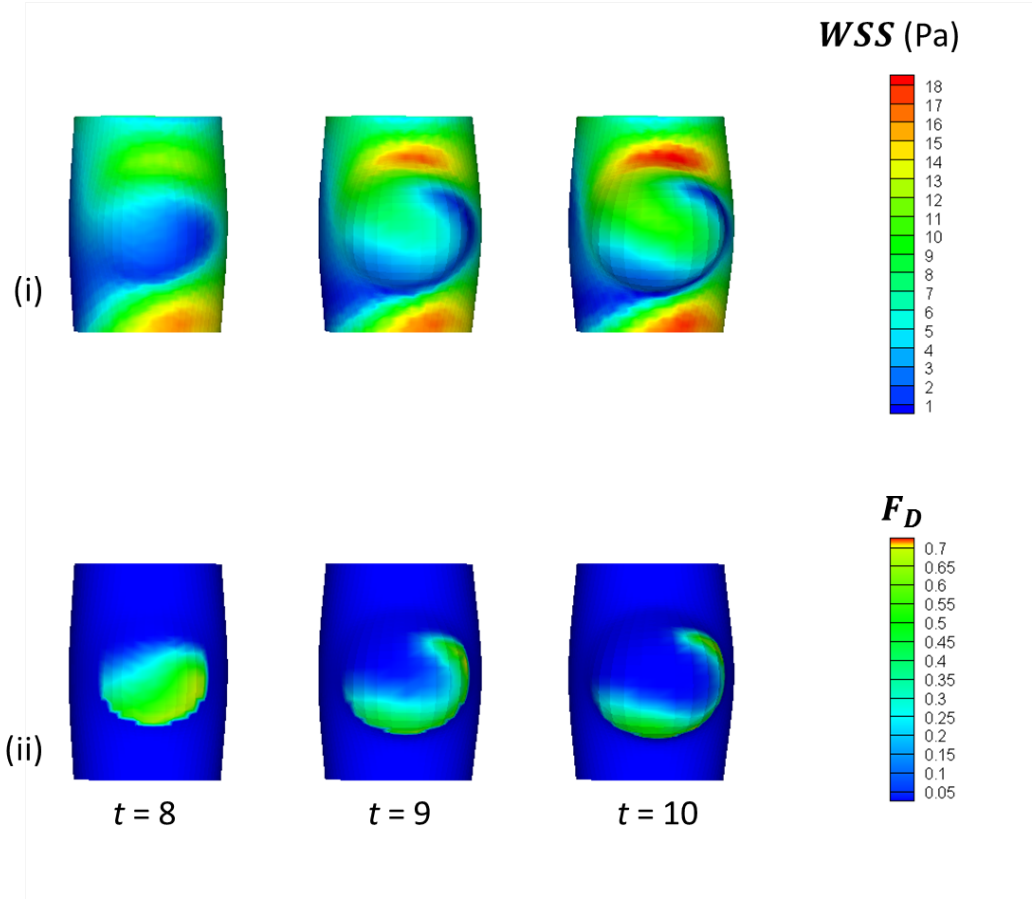

Figure 5.20: Investigation for case 2.: spatially heterogeneous and temporally non-adaptive WSS threshold for elastin degradation; (i) WSS distribution and (ii) WSS degradation factor F_D for $t = 8, 9, 10$ years. Deviations of WSS from homeostatic values (WSS distribution at $t = 0$) for this case drive elastin degradation in the upstream section.

factor, given the definition of WSS homeostasis is the initial $t = 0$ WSS configuration for each node, and so it is characterised as spatially heterogeneous, but temporally non-adaptive. The similarities with Case 1. in the downstream section are clarified by observing the initial decrease of WSS from homeostatic levels and eventual increase back towards the initial levels of WSS for most of the computational domain. Since it is only low WSS that drives degradation, F_D remains 0 in the downstream section.

Finally, for Case 3., WSS homeostasis was defined as the average of WSS at each node over the previous five years. In Figure 5.20, the evolution for the homeostatic WSS, alongside WSS distribution and the degradation factor F_D are observed. It can

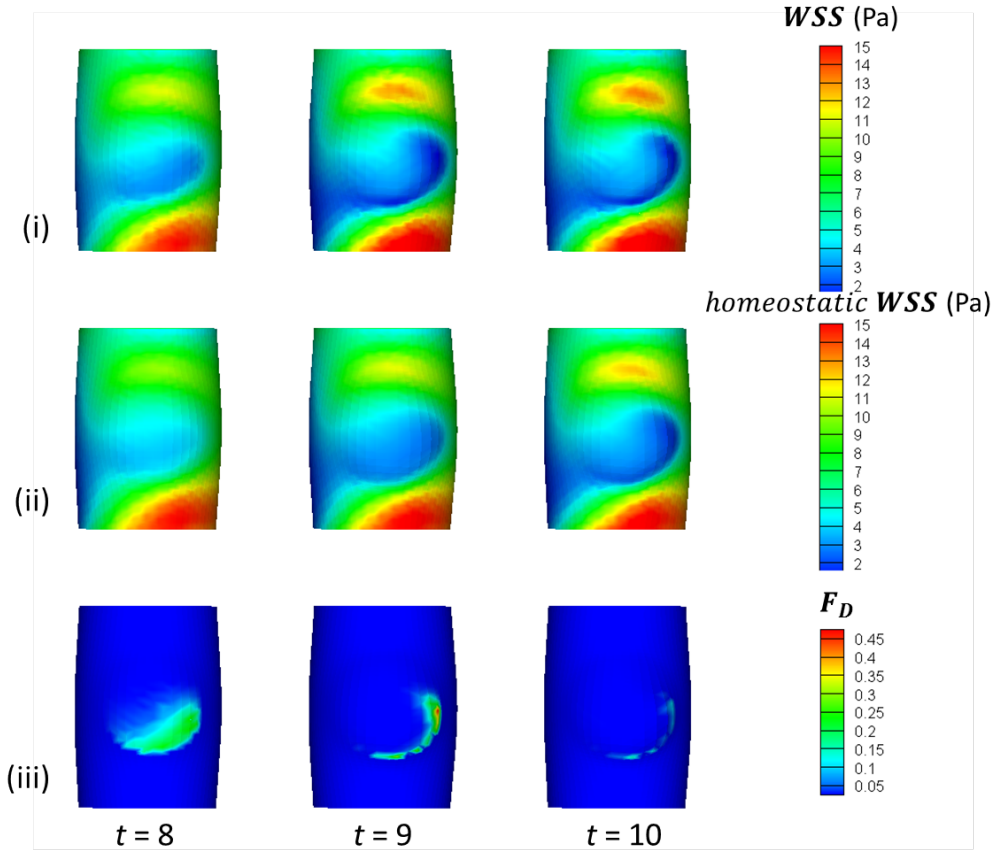

Figure 5.21: Investigation for case 3.: spatially heterogeneous and temporally adaptive WSS threshold for elastin degradation; (i) WSS distribution, (ii) homeostatic WSS and (iii) WSS degradation factor F_D for $t = 8, 9, 10$ years. Deviations from homeostatic values (average WSS over the past five years) for this case drive a small elastin degradation in the upstream section.

be observed that elastin degradation is greater around Year 8 of the simulation, as the deviations of WSS from homeostatic levels are greater. However, homeostatic WSS towards the end of the simulation is updated to follow the evolution in WSS and the smaller deviations from homeostasis lead to an insignificant current degradation by Year 10.

5.3 DISCUSSION

The investigations in this chapter aimed to improve our knowledge on the mechanobiological links in degradation and growth during arterial aneurysm growth. Cyclic stretch related collagen growth and flow linked elastin degrada-

tion enabled the possibilities of exploring more explicit representations of arterial mechanotransduction. Additionally, the fact that the simulations were informed and calibrated by the available experimental data allowed a unique comparison for examining these hypotheses. The structural simulations of §5.2 resulted in aneurysm thickness targets comparable to the aneurysmal tissue measurements under physiological levels of cyclic deformation in the domain, and the FSG simulations of §5.2, utilising the 3D clinical aneurysmal and surrounding arterial geometry, explored different definitions of WSS homeostasis to conclude that they can have an effect on the profile of geometric aneurysmal distortion and therefore on the question of the reasons behind a growing versus a stable aneurysm.

A crucial aspect of the 3D investigations looking into this specific clinical aneurysm case for this chapter has been the consistency between the 1D and 3D models (refer back to Figure 3.1). It can be seen from the results in Figure 5.5 that a target aneurysm remodelled thickness of approximately 0.11mm has been achieved that is comparable to the $0.11-0.13$ range predicted in Chapter 3. This range is the same within the aneurysmal area for the case of cyclic stretch based collagen growth, since the medial (Figure 5.10) and adventitial collagen growth for both cases are the same (growth in that area is dominated by deviations of collagen stretches from attachment levels). This consistency between the results strengthens the reliability of the model's assumption on the distribution of attachment stretch distribution and its evolution, which was informed by the 1D analysis. With respect to the estimated cyclic stretch magnitudes, the 3D model predicts an ultimate reduction from initial values of 1.1 to a lower range around 1.01 (Figure 5.9), following a similar path to that observed in the 1D growth model (Chapter 3). The increased adventitial collagen mass density is noted to have reached a normalised value of 10 at the end of the 3D structural simulations, which falls within the range of the approximations for spherical and cylindrical configurations in 1D (Eqn. (3.9)), as well as for some of the cases from the growth model in Chapter 3, which account for a final maximum attachment stretch closer to 1.05, which is the chosen assumption in the 3D model. Cauchy stresses σ, accounting for remodelled thickness, in 3D (Figure 5.6) can also be examined in parallel with the 1D calculations (Figure 3.19). 1D Cauchy stresses are slightly more elevated than in 3D estimations, although within a reasonable range and, in both cases, illustrating the changes in thickness and elastin strains as the media degrades, the geometry distorts and the adventitia comes into play.

Such observations of consistencies between the two investigations allowed the 3D studies in this chapter to develop new approaches to arterial homeostatic states. For the structural model simulations, the analysis presented an additional mechanobiologically significant definition of arterial homeostasis. The effect of cyclic deformation on the mechanobiology of healthy and diseased arterial tissue has been in the centre of a wide range of research. Leung et al. (1977) investigated the modulation of cellular response by mechanical load and specifically identified that increased collagen synthesis can be observed due to cyclic stretching, also proposed by Scapino et al. (1996). Cyclic physiological stretching is essential for the normal structure and function of vascular cells (Kanda and Matsuda, 1994) and relevant experimental backing has been conducted on rabbit abdominal aortic tissue (Courtman et al., 1998). Even though there has been a lot of research directed to understanding and testing hypotheses relating mechanical loading (including cyclic strains) and signalling pathways related to function, dysfunction, and remodelling within the arterial wall (Humphrey, 2002). However, the details of mechanotransduction on tissue, cellular or molecular level related to cellular growth, migration, and survival are still not clearly understood (Lee and Sumpio, 2004). Experimental studies in this area have often focused on the effects of cyclic strains on the regulation of MMPs (crucial matrix-degrading enzymes which are related to vascular remodelling) (Neidlinger-Wilke et al. (2002), von Offenberg Sweeney et al. (2004)). Relevant experiments examine the potential disruption in the interaction between ECs and ECM due to hypothesised changes in cyclic stretch induced changes in the expression of MMPs. The importance of the endothelium as the signalling link between the mechanical environment of the blood flow and the underlying effector vascular cells (fibroblasts, SMCs) becomes especially relevant in this research (Cummins et al., 2007), for the normal as well as the pathological functioning of the arterial wall. Cyclic pressure has been seen to affect EC proliferation and apoptosis (on the human umbilical vein endothelium, (Shin et al., 2002)). Further research (Gupta and Grande-Allen (2006),Matsumoto and Nagayama (2012)) looked into the ability of vascular cells to sense the change in mechanical strains and adapt the expression and synthesis of important ECM molecules as well as the effect of this ability on the cytoskeletal networks.

The incorporation of the cyclic deformation based collagen growth law helped with the illustration of the efficacy of introducing the impact of cyclic areal stretch to collagen growth in maintaining tissue homeostasis in the entirety of the geomet-

rical domain around the aneurysm. This appears as a particularly crucial point for the modelling of intracranial (saccular aneurysms), as opposed to abdominal aortic aneurysms, which are characterised by a fusiform enlargement and therefore the aneurysmal medial degradation would take place in the whole of the computational domain (as was modelled in Aparício et al. (2014)). The cyclic stretch based growth stipulation in that study, which was multiplicative to the total collagen growth equation, would not have captured the deviation of areal cyclic stretch from homeostasis, since collagen stretches in the immediately neighbouring area to the saccular intracranial aneurysms are at homeostatic levels for the duration of the simulation. The study therefore raises interesting questions and opens the possibility for further research into the G&R behaviour of the arterial tissue immediately surrounding saccular aneurysms, as the response to the changing mechanical environment in the progression of aneurysm disease.

With the guidance from the structural 3D simulations and taking advantage of the *in vivo* 3D aneurysm and arterial geometry, a link between the blood flow mechanical environment and the progression of aneurysm disease was investigated, by linking elastin degradation to deviations of local WSS from homeostatic values and exploring different definitions of WSS homeostasis.

Instead of assuming a constant homeostatic WSS throughout the arterial tree, mechanical homeostasis was examined by defining a spatially heterogeneous and temporally adaptive homeostatic WSS, and linked the degradation of elastin to deviations of WSS from the defined homeostatic values. An additional reason for focusing on the concept of mechanical homeostasis is the research interest in quantifying the effect of exercise in cardiovascular health (Bowker et al., 2010). Certain haemodynamic events (increased blood flow and heart rate, elimination of flow reversal and of areas of low WSS (Taylor et al., 1999) which alter during exercise may be linked to reducing the risk of vascular disease. This hypothesis can be translated to the context of homeostasis; the range of WSS values that the ECs are exposed to and the frequency with which they are exposed to certain WSS values may influence how homeostatic conditions are defined, and hence how the endothelium adaptive responses differ, temporally, spatially and between subjects.

Computational fluid dynamic analyses of the vasculature illustrate that the WSS is spatially heterogeneous within the vasculature tree. Hence, it is perhaps not so surprising (returning to the point initially examined in Chapter 2) that EC phe-

notypes display heterogeneity in both structure and function in the vascular tree (Davies (2009), Aird (2008)). Several recent articles by Aird (see Aird (2005) Aird (2006), Regan and Aird (2012)) suggest that this heterogeneity is the result of both nature and nurture, namely of both the epigenetics and the environment. It represents a balance between stability and plasticity in gene expression and phenotype and enables the ECs to adapt and function in different environments within the vasculature. Given the plasticity of ECs, it is believed that it may be beneficial to keep in mind that homeostatic values could potentially be both spatially heterogeneous and temporally adaptive. Mathematical models of arterial adaption in response to altered flow or pressure often utilise conceptual cylindrical geometries to represent the artery, and thus, it is not necessary for the definition of the homeostatic WSS to take into account spatial heterogeneity in the magnitude. For instance, a mean WSS of 1.5 Pa is typically taken to be representative for large arteries (Rachev and Hayashi (1999), Gleason et al. (2004), Gleason and Humphrey (2004), Gleason and Humphrey (2007), Figueroa et al. (2009)) whereas Valentín and Humphrey (2009b), Valentín and Humphrey (2009a) utilise 5.06 Pa for WSS homeostasis for a mature basilar artery. For more complex geometries, the WSS distribution is nonuniform. Until this investigation (and the equivalent one for abdominal aortic aneurysms in Aparício et al. (2014)), homeostatic WSS magnitudes utilised in FSG models have been constant, for example, the following thresholds were adopted for driving elastin degradation in recent FSG models of aneurysm evolution: WSS less than 2 Pa (Watton et al. (2009a), Watton et al. (2011a)); WSS less than 0.8 Pa (Zeinali-Davarani et al., 2011).

In the presented simulations, for cases (a), for a homogeneous and non-adaptive, and (b), for a heterogeneous and non-adaptive WSS homeostatic definition, elastin degradation and aneurysm growth appears very similar. This is largely due to the relatively homogeneous WSS field of this specific computational domain and the fact that the boundaries of WSS homeostasis of Case (a), even though homogeneous and non-adaptive, were chosen on the basis of observations from the specific geometry. This is an update from models so far which have mostly used spatially and temporally uniform WSS thresholds. A difference is noted for Case (a), where there is an initial predilection in the upstream direction, then an outpouching on the downstream surface, due to the links of elastin degradation with both high and low WSS thresholds. When compared to the clinical geometry which has a strong inclination towards the downstream face, this result simply illustrates

that the factor for aneurysmal growth might not be solely dependent on the commonly suggested WSS distributions and that it should be carefully considered what mechanical homeostasis might mean for healthy and diseased states and how to adapt the definition for each specific aneurysm case. This is further observed in Case (c), where employing a temporally and spatially adaptive WSS homeostasis does not result in significant elastin degradation and aneurysm growth. Those preliminary quantitative links between CFD and arterial structural modelling assist in incorporating in the computational model the known ability of the endothelium to adapt to changing conditions, and opens the discussion to investigate the difference between health and disease in terms of 'nature vs. nurture' for the endothelium. Of course, the link in this study is only tentative. The endothelium will need to be described and represented much more explicitly, in terms of its functionality under physiological and pathophysiological conditions.

For the specific clinical case investigated in this chapter, it is known that the patient's unruptured aneurysm was treated with surgical clipping. The tissue examined here was acquired during that procedure. Due to the decision on treatment at that stage, it is not possible to establish whether that specific aneurysm was indeed unstable or whether a more conservative clinical management for this young and generally healthy individual could have been recommended. Given that the ultimate aim of the research is to understand and predict *in silico* (and with the help from experimental data) whether an aneurysm would stabilise or not, it is difficult to state how closely our predicted aneurysms follow the specific case in that respect. However, introducing the mechanisms of aneurysm stabilisation through G&R can further help with identifying important mechanobiological characteristics of arterial homeostasis which could eventually distinguish between stable and unstable aneurysms.

There are certain limitations in the FSG framework presented in this chapter. The resulting simulated 3D images of developed aneurysms do not adequately represent the incredibly complex geometry of the clinical saccular aneurysm. A restriction for a close geometrical representation is the current inability of the computational domain's mesh to adapt under the large deformations required. Even though the choice of material parameters is based on biologically founded assumptions either on the physiological distribution of load between the media and the adventitia or direct approximations from *in vitro* data (as was the case for the ad-

ventitial collagen material parameter), the rate parameters for the G&R differential equations were not directly driven from biological knowledge. The 3D models in this chapter simulated aneurysm evolution by presenting distinct phases for degradation, remodelling and growth, which are not necessarily physiological; however, they contributed to the understanding of the G&R hypotheses and focused on the examination of the initial and final steady states.

5.4 CONCLUSIONS

In this chapter, a 3D analysis of aneurysm evolution has been completed for the specific clinical case, initially presented in Chapter 3 for the 1D analysis which provided estimations for the healthy arterial dimensions and the behaviour of the adventitia in the aneurysmal tissue, in terms of its material parameter and the final attachment stretch distribution. A full structural simulation incorporated the concept of a cyclic stretch homeostasis and linked it with the collagen growth, so it is possible to investigate the evolving behaviour of collagen in the aneurysmal and immediately surrounding area. An entire FSG simulation for the same clinical case was conducted to examine the hypothesis for WSS homeostasis and its link with elastin degradation. The evaluations of the remodelled aneurysm thickness and cyclic stretch magnitude created the basis for an interactive investigation between the 1D and 3D studies, reinforcing a strong modelling framework that takes full advantage of the available clinical and experimental data. Following the modelling methodology and framework presented so far, the next chapter investigates the effect of pulsatile flow in the FSG framework and suggests ways to introduce pulsatile metrics in the G&R hypotheses.

CHAPTER 6

PULSATILE FLOW IN FSG OF RABBIT ANEURYSM STUDY

Following the FSG simulations in the previous chapter for the clinical case, the FSG framework is applied to the rabbit aneurysm geometry, introduced in Chapter 4. As specific boundary pulsatile flow conditions are provided, experimentally calculated for the rabbit aneurysm case, there is a strong motivation to investigate the effect of pulsatile flow on the computational modelling. The distribution of the average WSS vectors and of a pulsatile flow index that determines the variation in the direction of the WSS vector over the cardiac cycle (oscillatory shear index, OSI) is investigated for the reconstructured rabbit RCCA ($t = 0$ configuration, immediately after ligation) and the parent vessel. This index has been used before for the investigation of correlations between pulsatile haemodynamics and atherogenesis (Cebral et al., 2002) as well as IA rupture (Omodaka et al., 2012). An illustrative FSG simulation is conducted on the occluded rabbit RCCA with a primary geometric distortion from the reconstructed configuration post-ligation, in order to focus on the growth of the observed secondary aneurysm at the distal lower part of the RCCA. An investigatory link between elastin degradation and OSI is proposed, and ways to further develop the integration of pulsatile flow modelling in the FSG computational framework are suggested.

6.1 SIMULATION SET UP

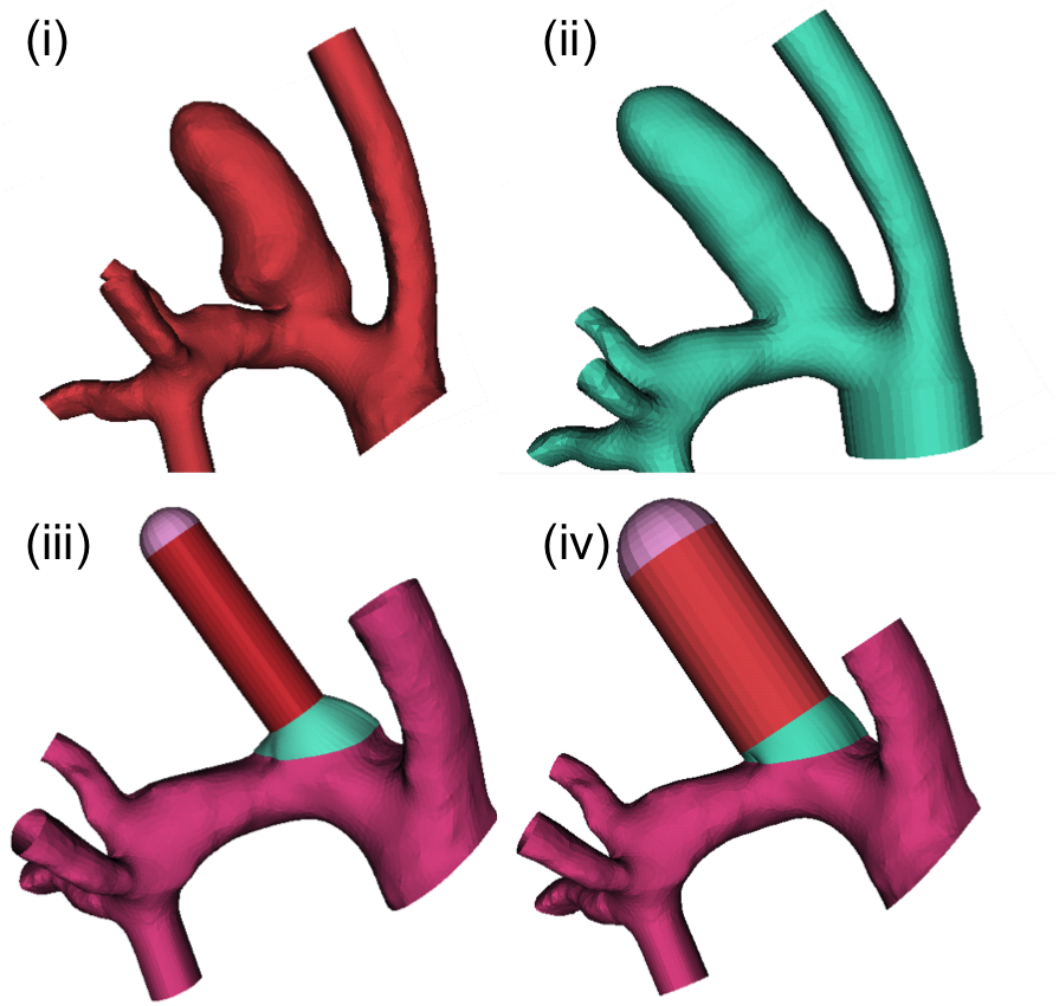

Figure 6.1: (i) Experimental rabbit aneurysm geometry, (ii) smoothed aneurysm geometry to represent rabbit RCCA without secondary growth (only primary branch geometric distortion), (iii) RCCA reconstruction immediately after ligation to represent the initial arterial geometry immediately after ligation, (iv) RCCA reconstruction to represent RCCA with primary distortion (and no secondary distal growth).

The rabbit aneurysm geometry is revisited in Figure 6.1(i). As observed in Chapter 4, apart from the general distortion of the arterial branch of RCCA, a secondary growth can also be noticed at the distal area close to the neck of the RCCA. The flow conditions are investigated in that specific area at the reconstructed vessel, as well as in a geometrical configuration that represents the aneurysmal arterial branch with a primary geometrical distortion but no secondary growth yet. This

is displayed in Figure 6.1(ii). The area around the secondary aneurysm growth was smoothed, using an automated tool on @neufuse, for illustration purposes. The geometry that is considered to represent the initial state (based on the dimensions of the neighbouring LCCA) was reconstructed in §4.4 and can be seen in Figure 6.1(iii). In addition the vessel reconstruction procedure is repeated to create an arterial branch with a cylindrical radius representing the elastase-induced aneurysm RCCA without secondary growth, the result of which is seen in Figure 6.1(iv). Approximated radii along the RCCA from the smoothed geometry in Figure 6.1(ii) assisted in the choice for the radius of the reconstructed vessel. The radii for the arterial branches (that define the computational domain) in the state immediately after ligation and the state of primary distortion are summarised in Table 6.1. The orientation of the computational domain (determined by the outlet boundary plane of the connecting region between the parent vessel and the arterial branch) was kept the same between the two reconstructed geometries, as was the length of the computational domain's cylinder.

Table 6.1: Choice of radii for reconstructed RCCA with and without primary geometric distortion.

Radii of reconstructed rabbit RCCA	
Post-ligation state (no distortion)	1.5mm
Primary distortion (no secondary growth)	2.5mm

For the specific rabbit aneurysm case, there are *in vivo* experimentally calculated velocities for the arterial outlets (§4.4). Calculating the cross-sectional areas of the outlets (on ANSYS ICEM), we set mass flow rates for the pulsatile outlet boundary conditions. These boundary conditions are utilised to run a pulsatile flow simulation on the reconstructed initial geometry (average boundary conditions render a steady simulation result that was used as an initial guess for the solution of pulsatile flow dynamics; for further information, see Appendix C. The pulsatile flow index of OSI (Ku et al., 1985) is chosen to investigate the variations of haemodynamics over the cardiac cycle in the whole of the rabbit geometry. OSI is defined as:

$$OSI = \frac{1}{2}\left\{1 - \frac{\left|\bar{\mathbf{t}_s}\right|}{\tau_{av}}\right\}, \tag{6.1}$$

where $\mathbf{t_s}$ is the WSS vector (defined by subtracting the normal component of the traction force vector from itself) and $\bar{\mathbf{t}_s}$ is then the average WSS vector, calculated

as:

$$\bar{\mathbf{t}_s} = \frac{1}{T}\int_0^T \mathbf{t_s} dt, \tag{6.2}$$

where T is the period of the cardiac cycle. Additionally, τ_{av} is the time averaged value for the magnitude of $\mathbf{t_s}$, denoted as τ and is simply calculated as follows:

$$\tau_{av} = \frac{1}{T}\int_0^T \tau dt, \tag{6.3}$$

According to those definitions, it can be concluded that a value of 0 for OSI implies unidirectional WSS, while 0.5 implies WSS with a time-average of zero, and values in between indicate that the direction of the WSS vector changes during the cardiac cycle.

Figure 6.2 shows the results of the pulsatile flow simulation for the reconstructed rabbit arterial geometry, illustrating the RCCA immediately after ligation. The WSS vectors are also displayed in Figure 6.2(i). It is noted that within the arterial branch the average WSS vectors follow a relatively uniform direction helically surrounding the cylindrical arterial branch (and their magnitude is relatively lower than in the downstream parent vessel). In Figure 6.2(ii) the distribution of OSI is examined, which helps to indicate the change in direction of the instantaneous WSS vector from its time averaged value, i.e. the variation of WSS vector direction over the cardiac cycle. Areas of higher OSI are observed towards the top of the RCCA (around 0.25) with the highest being at the very top of the dome (up to 0.4). Such high values of OSI have been associated with low WSS as potential simultaneous factors in aneurysm rupture (Tomohiro et al. (2012), Isoda et al. (2010), Xiang et al. (2010)). However, an additional area of high OSI is observed in the distal area close to the neck of the arterial branch (reaching values of around 0.3), where the secondary aneurysm 'bulge' in the rabbit geometry is noticed. This supports the idea of a direct correlation between high OSI and secondary aneurysm growth for which there is currently only limited experimental evidence; the pulsatile flow haemodynamics is now incorporated into our FSG computational modelling framework to further investigate this secondary aneurysmal growth.

The next step involved applying the FSG framework, as was presented in Chapter 4 (the geometrical and physiological data are summarised in Table 6.2), updated to run a pulsatile CFD solution for each step of the modelling framework cycle

Table 6.2: Geometry and physiological data for the 3D FSG simulation of the rabbit aneurysm case.

Geometry and Physiological Data		
Radii		
Unloaded (reference configuration)	R	2.5mm
Systolic ($t = 0$)	$r_s = \lambda_0 R$	3.125mm
Lengths		
Loaded axial ($t = 0$)	l	9.3mm
Unloaded axial (reference configuration)	$L_1 = \frac{L}{\lambda_z}$	7.15mm
Unloaded radial (reference configuration)	$L_2 = 2\pi R$	15.7mm
Stretches (Kroon and Holzapfel, 2009)		
Systolic ($t = 0$)	λ_0	1.25
Axial	λ_z	1.3
Cyclic ($t = 0$)	λ_D^S	1.1
Pressures (Watton and Hill, 2009)		
Systolic	P_{sys}	16kPa
Diastolic	P_{dia}	10.67kPa
Unloaded thicknesses ($t = 0$) (Holzapfel et al., 2000)		
Total	$H = \frac{1}{5}R$	0.5mm
Medial	$H_M = \frac{2}{3}H$	0.333mm
Adventitial	$H_A = \frac{1}{3}H$	0.167mm
Fibre orientation (unloaded configuration) (Schriefl et al., 2012b)		
Media	γ_M	30°
Protective sheath (adventitia)	γ_A	60°

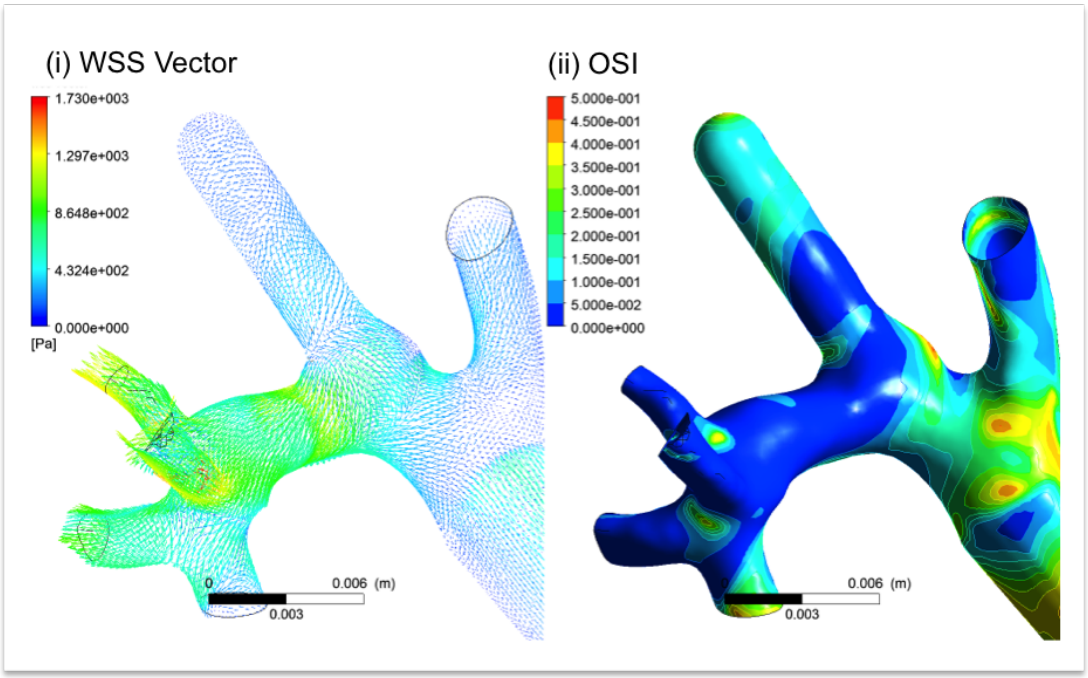

Figure 6.2: WSS vectors and OSI evolution for pulsatile simlation in rabbit aneurysm model (reconstructed geometry).

Table 6.3: Parameters to define prescribed media degradation and OSI drivern elastin degradation for the 3D FSG simulations of the rabbit aneurysm case.

Parameters for degradation		
Media prescribed degradation		
Time to minimum prescribed (elastin,collagen)	T	0.5(in years)
Minimum elastin density by time T	m_T^E	0.5
Minimum medial collagen density by time T	m_T^C	0.5
OSI driven elastin degradation		
Low threshold for degradation	OSI_{low}	0.1
Upper threshold for maximum degradation	OSI_{max}	0.2

Table 6.4: Growth and remodelling and material parameters for the 3D FSG simulation of the rabbit aneurysm case.

G&R and material parameters		
Recruitment rate parameters		
Media	α_{M_p}	$0.01(\text{years}^{-1})$
Protective sheath (adventitia)	α_{A_p}	$0.01(\text{years}^{-1})$
Growth rate parameters		
Media	β_{M_p}	$0.1(\text{years}^{-1})$
Protective sheath (adventitia)	β_{A_p}	$0.1(\text{years}^{-1})$
Material parameters		
Medial elastin	K^E	133.8kPa
Medial collagen	K^C_M	1.96kPa
Collagen (protective sheath, adventitia)	K^C_A	10MPa

(with an accompanying steady flow simulation solved and its result used as an initial guess for the pulsatile CFD simulation). For the purposes of the illustrative set up, elastin and medial collagen mass density are initially prescribed to 0.5 for the first half year of the simulation, defined within a circular area where the secondary aneurysm is located and indicated in Figure 6.1(i) (factors of the cylinder's radius in the unloaded configuration were defined with values of 0.7 and 0.8 in order to determine the inner and outer radius of the circular degradation area respectively): prescribed degradation is defined in Table 6.3. Following the first half year of the simulation, a link between elastin degradation and high OSI values is illustratively proposed for this specified area.

The definition of the degradation factor from Chapter 4 is used:

$$\frac{\partial m^E}{\partial t} = -F_D D_{max} m^E \tag{6.4}$$

The degradation factor is subsequently defined to linearly increase from 0 (no degradation) for low values of OSI to 1 (maximum degradation):

$$F_D(OSI(\theta_1,\theta_2,t)) = \begin{cases} 0 & OSI \leq OSI_{low} \\ \frac{OSI-OSI_{low}}{OSI_{max}-OSI_{low}} & OSI_{low} < OSI < OSI_{max} \\ 1 & OSI \geq OSI_{max} \end{cases} \tag{6.5}$$

The physiological threshold for OSI is taken to be 0.2, suggested in Glor et al. (2004), as an indicative value above which EC damage is thought to be initiated. The thresholds for the OSI driven elastin degradation are determined in Table 6.3. Since the focus of this simulation is to display the implementation of pulsatile flow in the proposed FSG framework and observe the evolution of OSI in the evolving secondary aneurysm geometry, the focus does not lie on the G&R algorithms, which were the subject of investigation in Chapter 5 (the initial recruitment and attachment stretches for medial and adventitial collagen fibres follow Table 5.3). G&R is set low with rate parameter values of 0.01 and 0.1 respectively and material parameters are calculated similarly to Chapter 5 (these parameters are outlined in Table 6.4). For the duration of the presented simulation, the adaption of the adventitial collagen attachment distribution is not represented. It should be noted that the t=0 reference configuration for this simulation refers to an already distorted geometry and following an initial dilation, the focus lies on a more local weakening of the arterial wall.

Simulations were performed on a 64BIT desktop PC (Intel Xeon CPU E31245 @3.3 GHZ, 16 GB RAM) running Windows 7 Enterprise. A complete 3D FSG simulation consisting of 200 solid steps (corresponding to five years), with structural and CFD data collected every 10 steps, takes approximately seven hours.

6.2 RESULTS

Figure 6.3 shows the evolution of the average WSS vectors (Figure 6.3(i)) and of OSI (Figure 6.3(ii), illustrated for every year of the simulation. The flow is low within the arterial branch compared to the parent vessel and there is a change in the pattern of the OSI, as the secondary aneurysm develops at the distal side of the arterial branch. OSI is high at the distal side of the whole RCCA (approximately 0.3) at the beginning of the simulation and subsequently there is a decrease around the area of the developing secondary aneurysm ($t = 1$ to $t = 4$). By the end of the simulation, it has again increased slightly, to a value of around 0.25 in the aneurysmal area. OSI at the dome

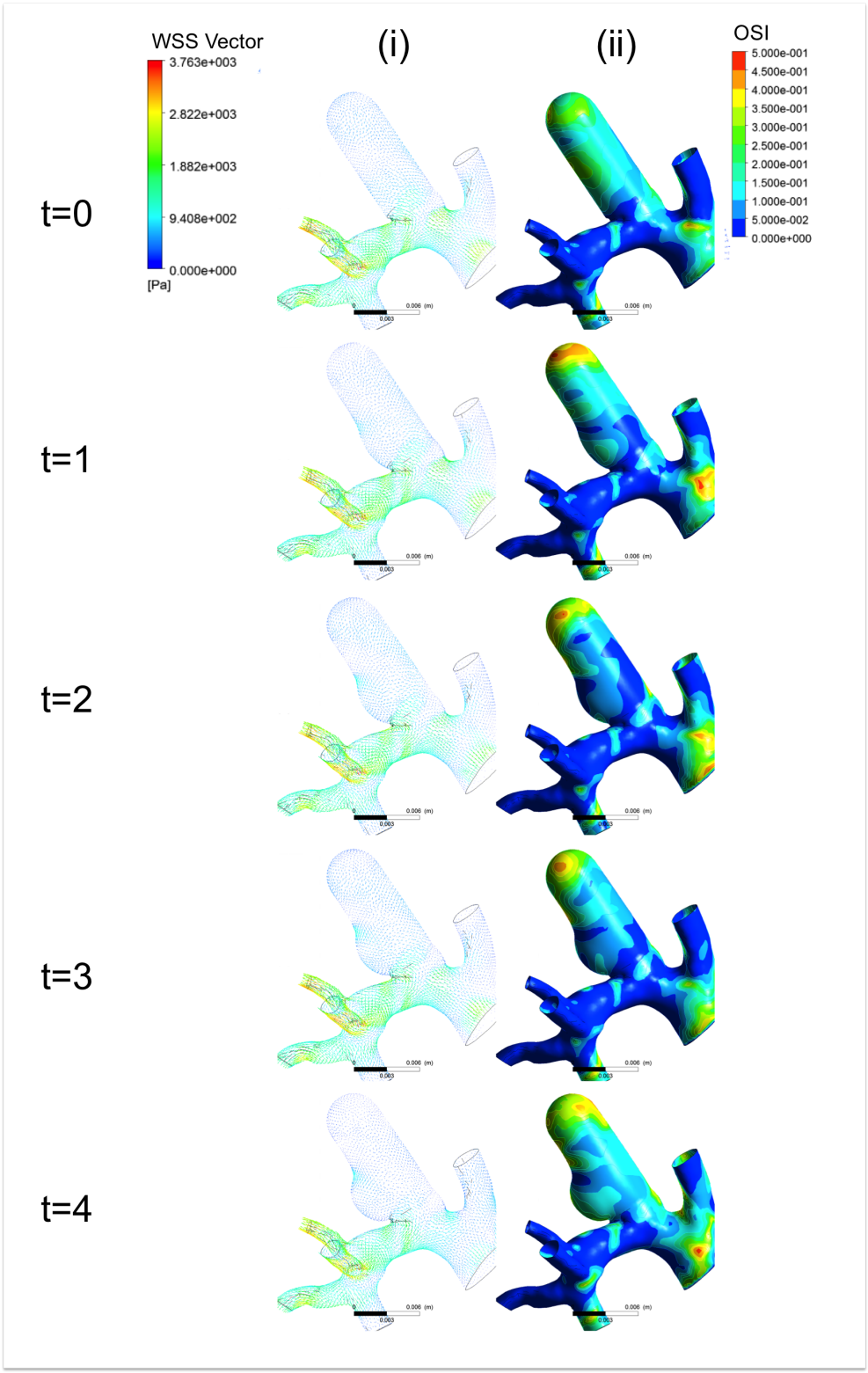

Figure 6.3: Spatial distribution of the evolution in WSS vectors and OSI for a pulsatile FSG simulation in a rabbit aneurysm model, where $t = 0, 1, 2, 3, 4$ years.

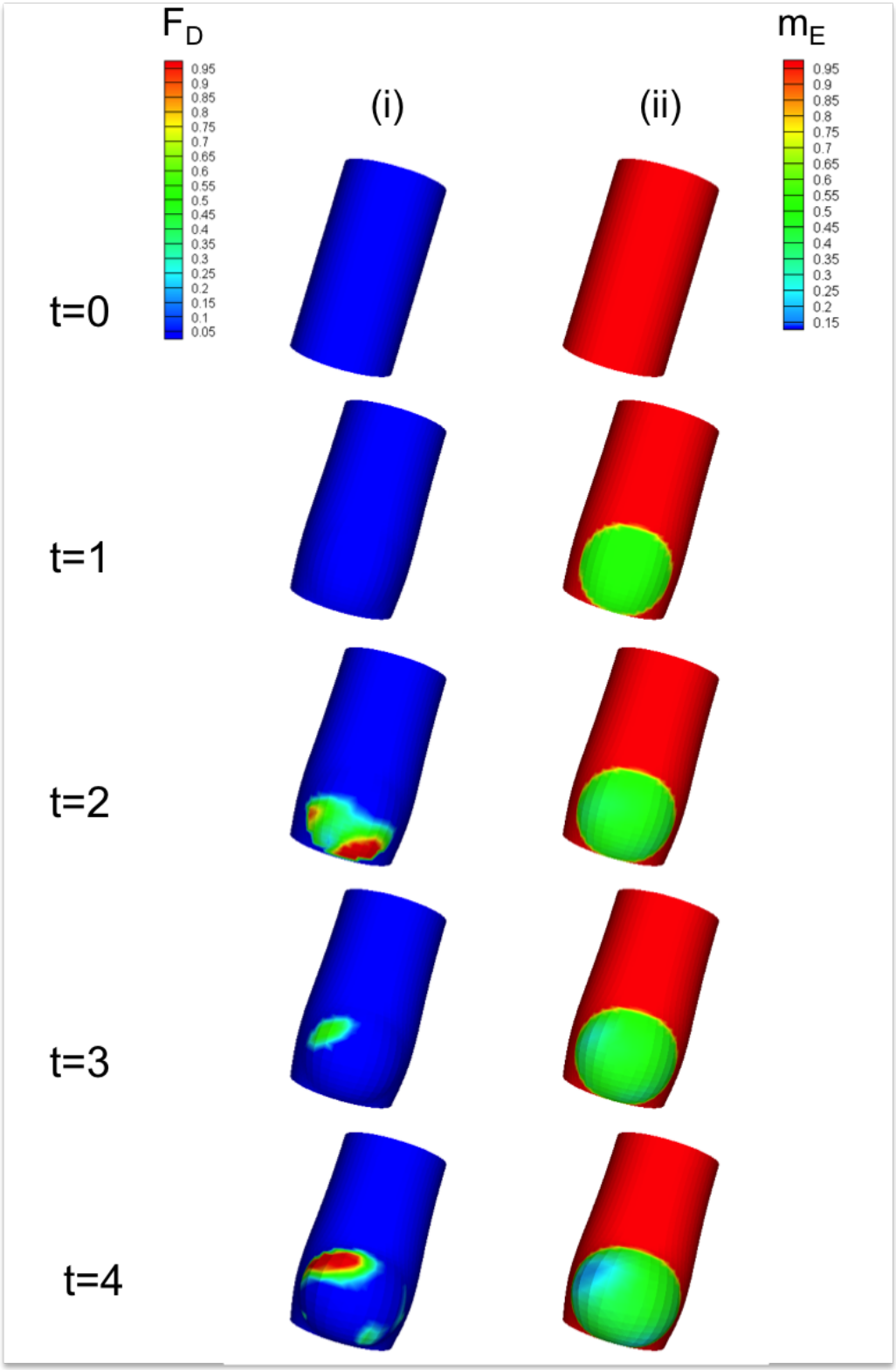

Figure 6.4: Spatial distribution in the degradation factor F_D and normalised mass density of elastin m^E for a pulsatile FSG simulation of a rabbit aneurysm model.

of the RCCA remains constantly high, in the range of 0.3 to 0.5, throughout the simulation. Additionally, observing the magnitude of WSS vectors in Figure 6.3(i), this is confirmed to be a region of low flow (WSS) along the arterial branch.

The direction of the flow is depicted upwards in the results of the computational domain presented. Figure 6.4 illustrates in parallel the evolution of the degradation factor F_D that is determined by current values of OSI (Eqn. (6.5)) and of the resulting normalised density of elastin fibres m^E around the area of defined secondary growth along the computational domain, for every year of the simulation. The pattern of degradation changes in the course of the years and a patch of high or maximum ($F_D = 1$) degradation is noticed at the bottom of the aneurysm (closest to the parent vessel) at $t = 2$ years migrating towards the upper part of the secondary aneurysm by the end of the simulation. Accordingly, the degradation of m^E can be observed: during the first year of the simulation, elastin degrades to 0.5 and from then onwards, there is gradual decrease in the density in the whole of the defined aneurysm area, reduced to approximately 0.35 by the end of the simulation (with an area at the top left of the the aneurysm of even lower density at a value of 0.15).

6.3 Discussion

The motivation behind this illustrative study is the incorporation of the experimentally calculated boundary pulsatile flow conditions in the proposed FSG computational framework. This more realistic and case-specific representation of arterial haemodynamics helps us think about the potential links between pulsatile flow and the biology of the arterial wall. Several CFD studies have inspected the role of WSS vectors and OSI: with relation to atherogenesis (Cebral et al. (2002), Birchall et al. (2006)) as well as aneurysms (IAs; Isoda et al. (2010), Omodaka et al. (2012), and AAAs; (Les et al., 2010)). It has been proposed that low WSS and high OSI can lead to an upregulation of the endothelial surface adhesion molecules, causing dysfunction to the flow-induced nitrous oxide, which results in increased permeability of the endothelium and can in turn promote atherogenesis, inflammatory cell infiltration and intimal dysplasia ((Nixon et al., 2010), (Malek et al., 1999)). This cascade of mechanobiological events results in the weakening of the wall which can also increase the risk of rupture. This study manages to reflect well on the actual progression of the disease in the rabbit, especially in terms of the geometric change of the observed secondary aneurysm growth. It should be noted that even though in

the presented aneurysm geometry there are other areas of high OSI (for example the dome of the occluded arterial branch), no further aneurysm growth is observed in those locations. Due to the illustration purposes of this simulation focusing on the secondary growth at the basis of the arterial branch and the fact that significant growth is not expected in the forced occluded dome, further growth is not prescribed in any other high OSI areas.

The rabbit aneurysm model provides the opportunity for a controlled experimental environment, where the introduced elastase guarantees the initial degradation of elastin fibres, but subsequent differential geometric distortion can help us to further understand about the mechanobiology of further arterial dysfunction and aneurysm growth. The current algorithms for the mechanobiology of the arterial wall within the FSG framework do not give an explicit representation of the functionality (permeability and proliferation) of the endothelium and the consequences that a pulsatile flow induced dysfunctional endothelium might have on the arterial wall (elastin degradation, SMC apoptosis or migration, thrombus formation, imbalance in the production of collagen). This introduction of pulsatile flow haemodynamics in the FSG framework and the constitutive models creates the basis for future modelling.

Finally, it should be noted that for future application of CFD in the FSG modelling framework to the elastase-induced rabbit aneurysm model, certain further modelling points will have to be considered. There have been investigations about the sensitivity of CFD to the proportion of the surrounding vasculature used for the simulations. The surrounding vasculature could include the LCCA, the aortic arch and further downstream vasculature of the parent vessel. There is a clear trade-off between a more realistic and accurate representation of the vasculature and computational time. Zeng et al. (2010) carried out several CFD studies to point out that the sensitivity of the results depends on the haemodynamic parameter on which you are focusing (bulk measurement of WSS magnitude, local sensitivity of WSS and OSI). Given that the WSS vector plays an important role in the G&R of physiology and pathophysiology, this concern needs to be taken into account. Another criterion that appears to influence CFD studies is the aspect ratio. The aspect ratio for the rabbit model (defined as the height of the occluded arterial segment to neck width) is considered high for values higher than 2.4 and low for values lower than 1.6 (the presented case is one of high aspect ratio). It appears to be an impor-

tant factor in influencing the haemodynamics within the aneurysm branch of the elastase-induced models (Kadirvel et al. (2010), Ding et al. (2007)). For example, differences are observed in the haemodynamics between the proximal and distal areas of the aneurysmal branch between the two experimental configurations. It is thus important to take this factor into account in any future computational cases of the rabbit aneurysm model.

6.4 CONCLUSIONS

This chapter concluded the simulations on the application of the FSG framework in realistic 3D geometries, by introducing pulsatile flow modelling and its potential importance in the progression of aneurysm disease. As has been mentioned throughout this thesis, in order for models of aneurysm evolution to become more sophisticated, they need to create more explicit descriptions of arterial mechanobiology. The presentation of a pulsatile FSG simulation motivates this, as the effects of varying WSS direction over the cardiac cycle, in combination with magnitudes of WSS, have been known to affect the proliferation of the endothelium and its function, which is crucial to the biology of the arterial wall and consequently to health and (aneurysm) disease. The following chapter presents the concluding remarks of the thesis, outlining the main themes of the research and suggesting future directions for improving mechanobiological representations in models of aneurysm evolution.

CHAPTER 7

SUMMARY AND FUTURE DIRECTIONS

7.1 THESIS SUMMARY

The main aim of the research presented in this thesis has been to determine, mathematically represent, and test important mechanobiological hypotheses in *in silico* models of aneurysm evolution, while proposing a framework of continuous interaction with *in vivo* and *in vitro* modelling. Novel sophistications to current mathematical models were introduced motivated from the important mechanobiological notions of:

1. spatial and temporal endothelial heterogeneity and mechanical WSS homeostasis;
2. SMC active mechanical stress response and apoptosis.

Chapter 2 modelled these two concepts within a conceptual mathematical 1D framework and concluded that incorporating these mechanobiological relations in my proposed mathematical models of aneurysm evolution can affect the rate of aneurysm enlargement (1.) or even result in significant differences in predicted aneurysm growth (2.). It is thus very important to continue the research for explicitly representing the function and form of the endothelium as well as the mechanical and biological role of SMCs in health and disease.

Vascular mechanical homeostasis is central to the function and dysfunction of the arterial wall and need to be explicitly linked to the G&R hypotheses. The arterial wall has a remarkable capacity of adapting to changing conditions and this capacity was represented by a fundamental hypothesis that the G&R mechanisms aim to drive the arterial mechanical system to (old and new) homeostatic states. Definitions of vascular mechanical homeostasis employed throughout this thesis are summarised as follows:

- WSS homeostasis;
- fibre stretch homeostasis;
- cyclic stretch homeostasis.

In Chapter 2 both temporally non-adaptive and adaptive definitions of WSS homeostasis were defined, in order to represent the 'nature versus nurture' argument of the endothelium's heterogeneity. It was hypothesised that elastin degradation can be driven by deviations of WSS from homeostatic levels and studied the effect of the definitions on the *in silico* 1D model. This hypothesis was also transferred to the 3D setting of the FSG framework in Chapter 5, which further allowed the inclusion of spatial heterogeneity in the WSS homeostatic definition. The 1D and 3D results emphasised that the definition of WSS homeostasis can has an effect on distinguishing between a healthy stabilising or a wall degrading response of the endothelium and is therefore crucial to be included in *in silico* models of aneurysm evolution. Fibre stretch homeostasis was represented by the attachment stretch, being the state of stretch fibres aim to retain or return to, driving G&R. The definition was utilised in the *in silico* models throughout the thesis: in Chapter 2 as a single value and in Chapter 3 updated to a distribution of stretches motivated from the variable fibre waviness of collagen fibres experimentally observed in the unloaded configuration of arterial tissue. Driven by the importance of the difference between the systolic and diastolic mechanical configurations of the arterial wall and experimental indications of physiological and pathophysiological levels of cyclic stretch, the evolution of cyclic stretches was observed in the 1D models (Chapter 3) and a link between collagen growth and cyclic areal stretch was investigated in Chapter 5. The study demonstrated the importance of incorporating the impact of cyclic areal stretch to collagen growth in maintaining tissue homeostasis for the entirety of the geometrical domain.

The main load-bearing constituents within the arterial wall retaining mechanical equilibrium in the mathematical models have been the elastin and collagen fibres. The proposed mechanisms of aneurysm inception (elastin degradation) disturb the load-bearing distribution among the fibres due to the degradation of the media (assumed to be a frequent event during IA progression), resulting in G&R of the remaining fibres. Specifically, there has been a focus on investigating the role of adventitial collagen as the initially protective sheath of the arterial wall, whose increased load-bearing role during aneurysm development can affect the remodelling process and eventual growth. The representation and study of important biology of the fibrous intramural network was central to in the models (both 1D and 3D) by incorporating mathematical representations of:

1. the gradual recruitment of collagen fibres to load bearing;
2. fibre orientation;
3. adaption of adventitial collagen fibres from a protective sheath to a primary load-bearing role.

Chapter 3 first applied (1.) by incorporating a distribution of recruitment stretches. Fibre orientation (2.) was taken into consideration for the mathematical fit of uniaxial mechanical testing data of aneurysmal tissue to the 1D constitutive model (Chapter 3). The adaption of the adventitial collagen fibres to the main load-bearing constituent (3.) was mathematically expressed by a distribution of attachment stretches that temporally evolves to a new distribution that represents a new arterial mechanical equilibrium. These expressions built a more realistic representation of the collagen fibrous network, which was crucial for the comparisons against *in vivo* and *in vitro* data.

These biological and mechanobiological concepts describing mechanisms of aneurysm inception and development, the arterial wall structure and its evolution in disease, and the G&R of collagen fibres driven by the arterial mechanical system's attempt to remain at homeostasis were all employed to a proposed modelling workflow that aimed to parameterise the mathematical and computational modelling frameworks with the aid of available experimental data for a specific patient aneurysm case. In Chapter 3 a value for the material parameter of the adventitial collagen was approximated by fitting experimental uniaxial data of aneurysmal tis-

sue to a constitutive mechanical model of the collagenous aneurysmal wall. Given provided information on the *in vivo* clinical 3D geometry and *ex vivo* measurements of the aneurysmal tissue thickness, a 1D conceptual configuration of the cylindrical arterial geometry was employed to approximate values for the loaded thickness of the tissue, a range of cyclic stretches and indications of the distribution of attachment stretches for the adventitial collagen. The approximations developed a description for the 'new' homeostasis of the aneurysmal tissue. This approach informed the 1D model of aneurysm evolution where a process of transitioning from a load-bearing media to a lost media with a load-bearing adventitia was illustrated. Given the calibration of the model (in terms of the dimensions of the healthy artery, the material parameter for the adventitial collagen and the evolution of the adventitial attachment stretch distribution), Chapter 5 implemented the FSG framework for aneurysm evolution on the *in vivo* 3D geometry of the clinical case (after it was reconstructed to a healthy geometrical state) and allowed comparisons between 1D and 3D investigations (in terms of the remodelled aneurysm thickness, cyclic stretch magnitudes, adventitial collagen increased mass and the distribution of cauchy stresses) for the proof of consistency within the models.

The proposed workflow suggests a strong modelling framework that takes full advantage of the available clinical and experimental data, promoting a comprehensive and self-reinforcing cycle of interaction between *in vitro*, *in vivo*, and *in silico* modelling. Within this context, applications in 3D are particularly important for the thorough representation of aneurysm evolution and understanding of the underlying biology. Utilising real geometries for the application of the FSG framework in both Chapter 5 and Chapter 6 allowed for a more realistic representation of the 3D wall structure, resulting in observations of spatial heterogeneities that can illustrate important differences in G&R. In Chapter 5, the links between WSS homeostasis and elastin degradation, and the G&R algorithms resulted in a heterogeneous pattern of degradation within the aneurysmal area, and a different distribution of cyclic areal stretches between the aneurysmal area and the immediately neighbouring arterial wall respectively. The haemodynamics of the complex 3D geometries are key to reliably determining important mechanics of the arterial wall that affect the mechanobiological algorithms. This was particularly important in Chapter 6, where specific knowledge of the pulsatile flow boundary conditions offered the opportunity to investigate the evolution of WSS vectors during the cardiac cycle, since they have been identified as potential mechanical triggers to biological sequences of ar-

terial cell and fibre degradation. These investigations motivate current and direct future work on the mechanobiology of IAs, which should aim to develop new cycles of *in silico* (1D and 3D) modelling interacting with *in vivo* and *in vitro* analyses.

The models presented in this work aimed to explore mechanobiological links that can help elucidate the differences between stability and instability of aneurysms: an adaptive (temporally and spatially) mechanical homeostasis can allow the artery to reach a new stabilised state (and a non-adaptive one could result in instability); SMC active stress response allows a short-term mechanical reaction to stretch changes that can help with long-term stabilisation (and the lack of this response could result in instability); the changing mechanical role of the adventitia from a protective sheath to a load-bearer can have a significant effect in attaining a new arterial state of stabilised equilibrium (and its inability to do so could lead to unstable aneurysm growth). For the clinical case, the evolving saccular aneurysm reached target wall thickness (consistent with the experimental data) with the contribution of the adaptive adventitial collagen. For the rabbit aneurysm case, the work focused on representing the secondary aneurysm growth, which morphologically resembled the one observed in the rabbit, while introducing the link between a pulsatile flow metric and G&R.

7.2 THESIS LIMITATIONS

There have been certain limitations to the availability of relevant biological information that could have better informed the models in this thesis. The importance of SMC apoptosis in the progress of aneurysm disease has been identified (Kondo et al. (1998), Geng (2000)) and illustrated in the 1D modelling framework of Chapter 2. However, more specific experimental information on this event, and on its relation to further wall degrading events (such as elastin degradation) prevented a more explicit representation of SMCs and their link to collagen production. Such information would have formed a more biologically relevant 3D representation of the arterial wall in Chapter 4. Moreover, combining processed MPM images of aneurysmal tissue to quantify the fibres recruited to load bearing at different stages of the tissue's mechanical testing would have rendered quantitative estimations of the recruitment stretches of the adventitial collagen in the aneurysmal tissue driven by specific experimental data. These estimations could have more accurately established the approximation on the material parameter of the adventitial collagen in

Chapter 3. Similarly, the vessel reconstruction process would have been more reliably validated if there was more information on the initial geometry (immediately post ligation) for the rabbit case. Such information for the clinical case could only have been circumstantial. This is experimental information that can be collected and is recommended for a future standardised work flow for the interaction of computational and experimental modelling (refer to §7.3 for further recommendations).

Further sophistication from the current representations of the arterial biology would certainly include more explicit expressions of signalling pathways on a cellular and molecular level. A system including the biochemical processes of the transforming growth factor (TGF)-β, for example, could represent the fibroblast-mediated collagen growth, describing a crucial signalling pathway of matrix deposition with specific mathematical expressions for collagen-producing enzymes and their inhibitors (Aparício et al., under review). Such modelling frameworks are important for exploring the more fundamental biological mechanisms represented at a larger scale within the arterial wall, but their increased parameter complexity requires specific experimental settings that would allow the model's calibration, following a similar workflow to the one suggested in this thesis.

The G&R hypotheses in the mathematical and computational models implicitly emphasise the significance of the endothelium's functionality (endothelial heterogeneity in WSS homeostasis and elastin degradation, effect of cyclic stretch on collagen growth). However, in order for the models to reliably represent the transmission of mechanics to chemical activity within the wall, the endothelium needs to be explicitly modelled. Figure 7.1 illustrates the type of intracellular processes of endothelial mechanotransduction due to the cell's cytoskeleton (via direct deformation of the luminal surface, junctional signaling, adhesion sites or lamin-induced nuclear deformation). Modelling the transmission of those forces and their effect on the form and function of the endothelial cell (EC), as well as on the neighbouring ECM is the natural next step in the *in silico* investigations.

The research in this thesis proposes the basis for a fully-integrative approach to IA evolution that requires a realistic, reliable and representative FSG framework. Within that context, an area of possible improvement regards the CFD meshing technique used. There are suggestions in the literature on anisotropic adaptive finite element methods for resolving complex 3D pulsatile flow dynamics in aneurysms (Prakash and Ethier (2001), Müller et al. (2005), Sahni et al. (2006)) and

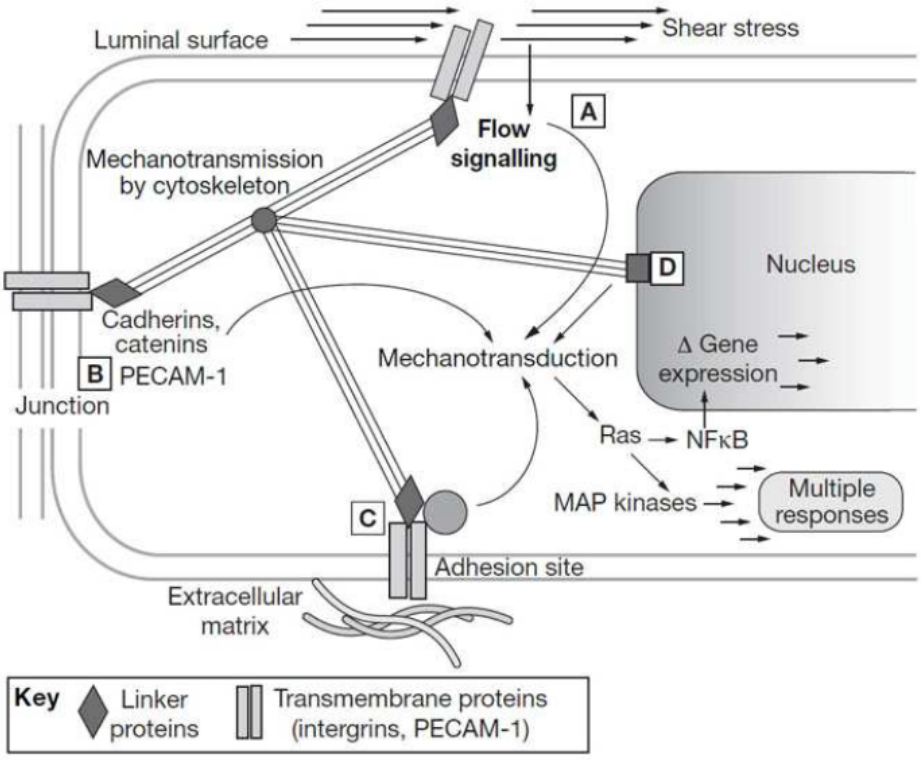

Figure 7.1: Mechanisms of endothelial cytoskeletal mechanotransduction: direct deformation of the luminal surface, junctional signalling, adhesion sites signalling, lamin-induced nuclear deformation (image adapted from Robertson and Watton (2013), David and Humphrey (2003)).

they should be considered in future computational studies. Improvements in meshing methods will allow a better representation of a range of complex and more realistic aneuyrsm types, in terms of their neck and dome size and shape. As was described in Chapter 4, the current FSG methodology involves the placement of a cylindrical segment along the area of aneurysm development. This allows the framework's automation and its quick application on a range of aneurysm cases. However, the strictly cylindrical shape for the computational domain currently limits the ability of the FSG methodology to be implemented for some aneurysm cases with a more complex arterial geometry, such as bifurcation aneurysms. An update for more options on the computational domain's shape will enable a wider application of the proposed 3D model. Furthermore, the current computational modelling assumption for a thin arterial wall needs to be upgraded to represent a thick-walled non-linearly elastic cylindrical tube (preliminary work within the FSG framework

has been introduced by Grytsan et al. (2015)). This would allow both the effect of transmurally nonuniform fibre strain that would render possibly tortuous (more realistic) geometries, and the modelling of transmural transport of, for example, oxygen and the representation of thrombus formation in the current models of G&R (Holland, 2012).

The investigations in this thesis suggest a parallel patient-specific study that could be of biological and clinical significance. The clinical case that was presented was that of a young patient and the experimental information indicated that the virtual loss of the aneurysm arterial wall's media has led to the increasing mechanical role of the adventitial collagen. A mechanobiological investigation (and its computational representation) on the different responses of the adventitia to a degrading media relative to age, based on a statistically big group of patients (such as the one in Robertson et al. (2015)), could shed some light on the mechanisms of aneurysm stabilisation and have an affect on clinical assessments of rupture risk.

7.3 OUTLOOK AND FUTURE DIRECTIONS OF *in vivo-in vitro-in silico* MODELLING OF IAS

This thesis introduced the work that will eventually lead to a fully integrative multidisciplinary approach that combines *in silico*, *in vitro* and *in vivo* modelling. In IAs this approach is essential, as clinical observations provide limited insight into the mechanobiology of the disease: once an IA is detected it is generally intervened, so follow-up imaging snapshots of evolving aneurysms are not available, nor are histologies. Whilst experimental models differ from the aetiology of human IA, the underlying biological mechanisms that control arterial mechanobiology are similar and thus they can provide fundamental insights into the remodelling processes driving enlargement and stabilisation. However, experimental models alone are insufficient to provide full insight given the strong role that mechanics has to play in the disease. *In silico* models can quantify the mechanical stimuli that act on arterial cells and other microstructural parameters that cannot be measured with current *in vivo* techniques, and so these are necessary in order to explore and understand IA mechanobiology. Moreover, *in silico* models assist in the interpretation of experimental data, the identification of questions that need to be addressed by experiments and the design of the experiments themselves. In return, *in vivo* and

in vitro models can be used to sophisticate, calibrate and validate *in silico* models. The framework proposed in this thesis can therefore be generalised as illustrated in Figure 7.2, and proposes a future modelling framework for the ideal integration between *in vivo, in vitro* and *in silico* modelling.

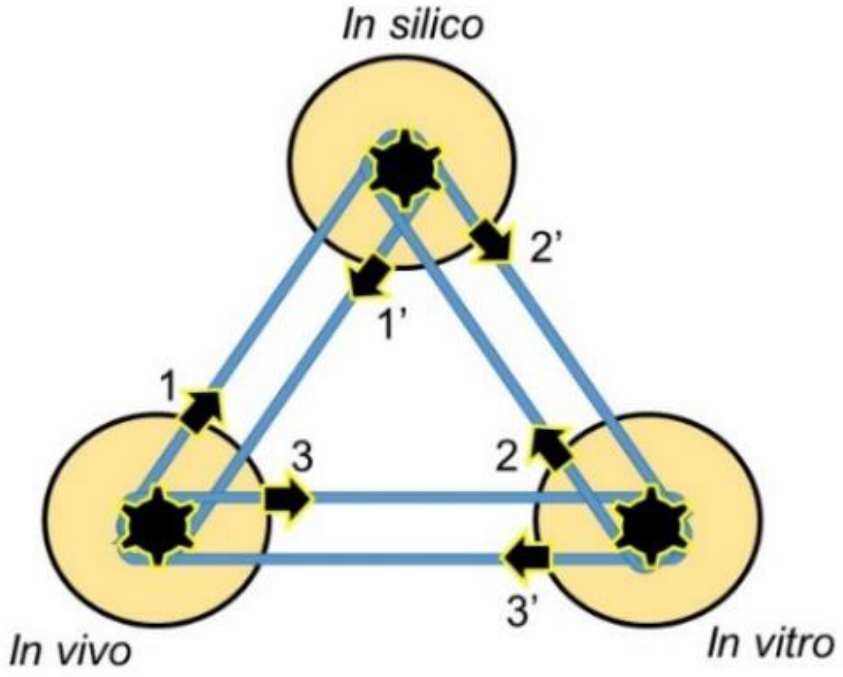

Figure 7.2: Interaction between *in silico, in vitro* and *in vivo* modelling. Feedback between the different research activities is as follows: 1,2: experimental models enable the formulation of *in silico* models and the definition of modelling hypotheses; 1',2': *in silico* models can be used to interpret experimental data, simulate experiments, test hypotheses, propose new hypotheses and experiments; 3: *in vivo* models guide the design of *in vitro* experiments to test hypotheses; 3': *in vitro* models help interpret *in vivo* observations.

7.3.1 Modelling developments

A comprehensive *in silico* modelling framework of IA evolution would rationally span subcellular, cellular, multicellular, tissue, and organ scales, and hence provide further insight into the underlying mechanisms that enable the majority of aneurysms to stabilise whilst others go on to rupture, with the help from reduced-

order models of arterial constituents. It should, for example, include a novel mathematical model of the EC representing the structural organisation, morphology, mechanics and permeability of ECs as functions of their local mechanical environment, i.e. WSS and cyclic deformation. Moreover, novel mathematical models of transmural cells (SMCs, fibroblasts) need to be developed and their interaction with the ECM need to be expressed.

Focusing on fibroblast functionality, in order to characterise the influence of mechanics on fibroblast functionality and the cellular mechanisms with which the cell controls the adaption of collagen microstructure, preliminary experimental investigations are crucial. *In vitro* experiments can provide guidance on linking fibroblast functionality to the local mechanical environment (cyclic deformation, substrate stiffness). More specifically, experiments can be built to characterise how the biaxial cyclic deformation environment on human arterial fibroblasts influences their morphology. Dynamic stretching experiments can be performed using a biaxial stretching bioreactor. Human fibroblasts can be transfected to enable the visualisation of actin cytoskeletal networks (Pierce et al., 2015). Fibroblasts can be subjected to variations in magnitude of cyclic deformation and in the degree of biaxial cyclic deformation (from uniaxial to equibiaxial). Resultant changes in cytoskeletal and nuclear morphologies under these stimuli can be compared against controls for the healthy artery. Additionally, experiments can examine the mechanisms with which the mechanical environment influences cellular expressions of collagen and elastin synthesis and degradation. This can be implemented by culturing cells and dynamically stretching them in order to investigate mRNA expression levels related to the balance between synthesis and degradation of ECM proteins, in response to uniaxial and biaxial dynamic stimuli.

A nonlinear elastic, mechanobiological model of fibroblast could then be developed based on experimental evidence to characterise the influence of matrix stiffness and biaxial cyclic deformation on fibroblast functionality, and in turn the effect of fibroblast mechanics on the collagen fibre network configuration to the ECM. Such novel cell models should then be integrated into the computational FSG frameworks for modelling aneurysm evolution (Watton et al. (2009a), Aparício et al. (2014), Grytsan et al. (2015)), extended to account for anatomic geometries (using a backward incremental approach (Kong et al., 2013)), as well as transport phenomena through arterial wall, by representing permeability of the arterial wall and

molecular transport (Butler et al., 2002). Tissue remodelling can then be linked to the heterogeneity of the endothelium and the heterogeneous flow field.

In parallel, specific experiments will also be required to investigate the complicated mechanobiological events to be included in *in silico* models of IAs. Elastase induced rabbit aneurysms, like the one presented in this thesis, can be extensively analysed. Both prior to intervention and prior to sacrifice, intra aneurysmal flow and pressure should be measured, and 3D rotational angiography should be performed. This will provide the data for 3D CFD simulations on the healthy and the aneurysmal arterial segment (and consequently allow for comparisons between healthy and aneurysmal states). Various aneurysmal tissue samples along the affected rabbit arterial branch should be collected and at various time points of the rabbit aneurysm development, for the collection of temporal data. These samples should be mechanically tested under an MPM compatible planar biaxial testing system, against control samples of the neighbouring vasculature. Histopathologic analysis can be performed using a semi-quantitative analysis. Immunohistochemical staining can be performed for identifying ECs, SMCs, cell proliferation, oxidative stress proteolysis and apoptosis, with the help from image analysis for the quantification of these constituents.

The collagen architecture should be quantified in MPM stacks to include measurements of: average fibre diameter, fibre tortuosity, fibre orientations, fraction of projected area with fibres. Additionally, cellular status (ECs, SMCs, fibroblasts) should be assessed with respect to cell content and distribution, using histology. Cell function should be examined using molecular biological techniques. For the experimental analysis of ECs, immuno-stained samples can be imaged en face for EC coverage using confocal microscopy. The morphology and number of ECs per unit area can be quantified: the existing ones should be characterised as isolated, dead or living. Correlations between flow, wall structure and mechanical properties need to be further examined for specific clinical aneurysms (both ruptured and unruptured), similarly to Pierce et al. (2015), Kong et al. (2013). Measurements of wall mechanics and biology can be similar to the aforementioned methodologies for the rabbit aneurysms.

The mechanobiological model developed can then be applied to specifically simulate *in silico* FSG models of rabbit and human aneurysm evolution (with an onset of elastin degradation). Suitable models of the healthy arterial wall can be

utilised based on vessel reconstruction methods presented in this thesis (in terms of geometry) and additional *in vitro* mechanical testing of healthy tissue samples (in terms of the healthy arterial mechanical equilibrium). Flow solutions can be directly parameterised by the *in vivo* experimental measurements. A huge database of experimental information, as the one described, can be invaluable both for the validation and the critique of the *in silico* model predictions of the evolving solid mechanics, as well as the structure and composition of the wall. Comparisons on flow solutions can take place between the CFD simulations within the FSG framework and the CFD simulations using the *in vivo* healthy and aneurysmal geometries. This way the reliability of both the reconstructed and the predicted aneurysm geometries can be examined. The predicted morphology of endothelium, the mapping of intramural cells and the evolved collagen microstructure (undulation, orientation, dispersion distributions) can be compared with experimental observations from both rabbit and human models. The additional advantage for the rabbit model is the comparison of the predicted *in silico* evolution against the temporal experimental data.

Limitations and criticisms of these comparisons will lead to updates of the *in silico* representations and to suggestions for more *in vitro* experiments that would further focus the mechanobiological insight for IA enlargement and stabilisation. The cycle of suggested workflow, presented in this thesis, can be thus continually developed and updated.

7.3.2 Need for standardisation

It is crucial that the developed computational framework, with the strong evidence from experimental and clinical data, is fully integrated into standardised engineering software. This will maximise its availability to academic communities, and assist its translation to healthcare technology industries and its future integration in the clinic. Especially due to the rapid advances in imaging technologies and computational techniques, an integrated imaging-computational modelling suite can now be envisaged that will assist with clinical management of the disease in real time, helping to stratify IAs by their stability, on the basis of the geometry (shape, thickness), properties (anisotropy, strength) and applied loads (haemodynamic, perivascular), much further from current criteria of the maximum aneurysm dimension. Such a tool could provide valuable decision support for those cases where interven-

tion is indicated.

Simulation workflows, such as finite element (FE) models, can be developed using both academic (FEAP) and commercial FE software (ANSYS). This will ensure that project outputs are available for translation by healthcare technology industries and thus provide the foundation to realise the longer term goals of the research: to revolutionise IA management and treatment. In the context of the presented framework in this thesis, the eventual full integration of the growth model into ANSYS Mechanical is recommended. This will require development of customised ANSYS subroutines to represent the novel nonlinear elastic constitutive models of the soft tissue (fibre reinforced constrained mixtures and possibly volumetric adaption) into ANSYS. Furthermore, benchmark ANSYS models of human and rabbit IA evolution should be integrated into VPH-Share (`https://portal.vph-share.eu/`). This is an online environment for the development, construction and storage of biomedical workflows to facilitate sharing with the academic and industrial community and it is exactly designed to help researchers, clinicians, and software developers share resources (data and tools) to build workflows quickly and easily. The models should link the flow environment to the heterogeneous functionality of the endothelium and heterogeneous remodelling of the aneurysm wall. This would additionally provide foundations for simulating the active remodelling response of the wall following device deployment. This proposed standardisation would also allow the input of important data from other platforms. For example, '7Tesla' imaging data, which depict permeability of the wall, would provide, within this framework, an input to the remodelling algorithms.

7.3.3 Towards the clinic

All fields of research around aneurysm evolution (physiology and pathophysiology, biochemistry, biology and mechanobiology), with experiments and *in silico* models, aim to understand more about the mechanisms of this disease and, naturally, to ultimately transfer and translate such knowledge to clinical tools for the diagnosis and treatment of the condition. From the simplest to the most complex models, research should always consider the ways with which the investigations in basic science could become clinically useful.

Assessment of rupture risk for intracranial aneurysms is a principal motivation for aneurysm research especially because, as it has been mentioned before, there is

a current lack of reliable and size independent clinical rupture risk criteria. Important contemporary research focuses on the mechanobiological analysis on several levels (tissue, cellular, molecular) given the range of available imaging and tissue testing techniques. However, the major difficulty in translating such knowledge is the need to use the maximum amount of possible information in the least invasive way. For instance, even though histological tissue testing can render indispendible information about the possibility of rupture, the use of such a technique as part of the diagnosis becomes too risky (comparable to intervening for treatment), thus potentially negating the value of the information it can provide. That is why groundbreaking translational research in this field needs to propose minimally invasive methods of diagnosis. An interesting example in this direction is work on using dynamic contrast-enhanced MR imaging to examine the permeability of a contrast agent as a measure of rupture risk (Vakil et al., 2015): this work uses a minimally invasive imaging method taking advantage of past comprehensive studies that have identified the change in permeability as a potential indicator of endothelial dysfunction leading to an increased risk of inflammation. Aneurysm research can also have important applications in clinical treatment: virtual stent deployments combined with reliable mechanobiological modelling of the arterial wall could revolutionise clinical intervention; models of biological changes in the arterial wall as a response to pharmacological drug therapy (for example, with a collagen-promoting drug) could significantly assist in choosing the most suitable patient specific treatment. In this area of translational research, the criteria for effectiveness set a trade off between reliability (in terms of imaging and mechanobiological representation) and computational speed as well as cost. This is therefore the challenge of translational aneurysm research: investigating biology and mechanobiology with the maximum amount of available information but apply it as clinical tools with the least risky and costly set of useful and relevant information.

7.4 CONCLUDING REMARKS

The work in this thesis builds on the aim to create a multi-scale computational model of intracranial aneurysm evolution which captures the relevant physics and biology, based on state-of-the-art experiments on clinical and animal aneurysms. Even though precise mechanisms by which IAs initiate, enlarge or rupture are not clear, it has been established that mechanobiology is key for the physiological and

pathophysiological arterial processes. The work has focused on representing such relations between the mechanics and the biology of the arterial constituents that are crucial to the weakening of the wall, as well as to its G&R capacity. The proposed workflow for interactive modelling creates the basis for the progressive sophistication of *in vivo*, *in vitro* and *in silico* modelling. The continual renewal and update of this modelling cycle will have a profound impact on the understanding of arterial biology in health and disease and, ultimately, on clinical methods for the diagnosis and treatment of detected IAs.

REFERENCES

ACEVEDO-BOLTON, G., JOU, L.-D., DISPENSA, B. P., LAWTON, M. T., HIGASHIDA, R. T., MARTIN, A. J., YOUNG, W. L., AND SALONER, D. Estimating the hemodynamic impact of interventional treatments of aneurysms: numerical simulation with experimental validation: technical case report. *Neurosurgery*, 59(2):E429–E430, 2006.

AIRD, W. C. Spatial and temporal dynamics of the endothelium. *Journal of thrombosis and haemostasis*, 3(7):1392–1406, 2005.

AIRD, W. C. Mechanisms of endothelial cell heterogeneity in health and disease. *Circulation Research*, 98(2):159–162, 2006.

AIRD, W. C. Phenotypic heterogeneity of the endothelium: I. Structure, function, and mechanisms. *Circulation research*, 100(2):158–73, February 2007. ISSN 1524-4571.

AIRD, W. C. Endothelium in health and disease. *Pharmacol Rep*, 60(1):139–143, 2008.

AKKAS, N. Aneurysms as a biomechanical instability problem. In MOSORA, F., editor, *Biomechanical Transport Processes*, pages 303–311. Plenum Press, 1990.

ALBERTS, B., JOHNSON, A., LEWIS, J., RAFF, M., ROBERTS, K., AND WALTER, P. *Molecular Biology of the Cell Fifth Edition*. Garland Science, 2008.

ALSHEKHLEE, A., MEHTA, S., EDGELL, R. C., VORA, N., FEEN, E., MOHAMMADI, A., KALE, S. P., AND CRUZ-FLORES, S. Hospital mortality and complications of electively clipped or coiled unruptured intracranial aneurysm. *Stroke*, 41(7):1471–1476, 2010.

ANDO, J. AND YAMAMOTO, K. Effects of shear stress and stretch on endothelial function. *Antioxidants & Redox Signaling*, 15(5):1389–1403, 2016/05/17 2010.

ANXIONNAT, R., BRACARD, S., DUCROCQ, X., TROUSSET, Y., LAUNAY, L., KERRIEN, E., BRAUN, M., VAILLANT, R., SCOMAZZONI, F., LEBEDINSKY, A., AND PICARD, L. Intracranial aneurysms: Clinical value of 3d digital subtraction angiography in the therapeutic decision and endovascular treatment. *Radiology*, 218(3):799–808, 2001. PMID: 11230659.

APARÍCIO, P., MANDALTSI, A., BOAMAH, J., CHEN, H., SELIMOVIC, A., BRATBY, M., UBEROI, R., VENTIKOS, Y., AND WATTON, P. Modelling the influence of endothelial heterogeneity on the progression of arterial disease: application to abdominal aortic aneurysm evolution. *International Journal for Numerical Methods in Biomedical Engineering*, 30(5):563–586, 2014. ISSN 2040-7947.

APARÍCIO, P., THOMPSON, M. S., AND WATTON, P. A novel chemoŰmechanoŰbiological model of arterial tissue growth and remodelling. *Journal of Biomechanics*, under review.

ARMENTANO, R., BARRA, J., LEVENSON, J., SIMON, A., AND PICHEL, R. Arterial wall mechanics in conscious dogs: Assessment of viscous, inertial and elastic moduli to characterize aortic wall behaviour. *Circulation Research*, 76:468–478, 1995.

ASANUMA, K., MAGID, R., JOHNSON, C., NEREM, R. M., AND GALIS, Z. S. Uniaxial strain upregulates matrix-degrading enzymes produced by human vascular smooth muscle cells. *American Journal of Physiology-Heart and Circulatory Physiology*, 284(5):H1778–H1784, 2003.

ASARI, S. AND OHMOTO, T. Growth and rupture of unruptured cerebral aneurysms based on the intraoperative appearance. *Acta medica Okayama*, 48(5): 257–262, 1994.

ATLAS, S. Magnetic resonance imaging of intracranial aneurysms. *Neuroimaging clinics of North America*, 7(4):709–720, 1997.

AVERY, N. C. AND BAILEY, A. J. The effects of the maillard reaction on the physical properties and cell interactions of collagen. *Pathol Biol (Paris)*, 54(7): 387–395, 2006.

BAEK, S., RAJAGOPAL, K. R., AND HUMPHREY, J. D. A theoretical model of enlarging intracranial fusiform aneurysms. *Journal of biomechanical engineering*, 128(1):142–149, 2006.

BAEK, S., VALENTÍN, A., AND HUMPHREY, J. D. Biochemomechanics of cerebral vasospasm and its resolution: II constitutive relations and model simulations. *Annals of Biomedical Engineering*, 35: 1498–1509, 2007.

BEDERSON, J. B., AWAD, I. A., WIEBERS, D. O., PIEPGRAS, D., HALEY, E. C., BROTT, T., HADEMENOS, G., CHYATTE, D., ROSENWASSER, R., AND CAROSELLI, C. Recommendations for the management of patients with unruptured intracranial aneurysms: A statement for healthcare professionals from the stroke council of the american heart association. *Stroke*, 31(11):2742–2750, 2000.

BENNDORF, G., IONESCU, M., VALDIVIA Y ALVARADO, M., BIONDI, A., HIPP, J., METCALFE, R., VALDIVIA, M., AND ALVARADO, Y. Anomalous hemodynamic effects of a self-expanding intracranial stent: Comparing in-vitro and ex-vivo models using ultra-high resolution microct based cfd. *Journal of Biomechanics*, 43(4):740–748, March 2010. ISSN 1873-2380.

BIRCHALL, D., ZAMAN, A., HACKER, J., DAVIES, G., AND MENDELOW, D. Analysis of haemodynamic disturbance in the atherosclerotic carotid artery using computational fluid dynamics. *European Radiology*, 16(5):1074–1083, 2006. ISSN 1432-1084.

BOUSSEL, L., RAYZ, V., MCCULLOCH, C., MARTIN, A., ACEVEDO-BOLTON, G., LAWTON, M., HIGASHIDA, R., SMITH, W. S., YOUNG, W. L., AND SALONER, D. Aneurysm growth occurs at region of low wall shear stress: Patient-specific correlation of hemodynamics and growth in a longitudinal study. *Stroke*, 39: 2997–3002, 2008.

BOUZEGHRANE, F., NAGGARA, O., KALLMES, D. F., BERENSTEIN, A., AND RAYMOND, J. In vivo experimental intracranial aneurysm models: a systematic review. *AJNR. American journal of neuroradiology*, 31(3):418–23, March 2010. ISSN 1936-959X.

BOWKER, T. J., WATTON, P. N., SUMMERS, P. E., BYRNE, J. V., AND VENTIKOS, Y. Rest versus exercise hemodynamics for middle cerebral artery aneurysms: a computational study. *AJNR. American journal of neuroradiology*, 31(2):317–23, February 2010. ISSN 1936-959X.

BRISMAN, J. L., SONG, J. K., AND NEWELL, D. W. Cerebral aneurysms. *The new England Journal of Medicine*, 355:928–939, 2006.

BRUNO, G., TODOR, R., LEWIS, I., AND CHYATTE, D. Vascular extracellular matrix remodeling in cerebral aneurysms. *Journal of Neurosurgery*, 89(3): 431–440, September 1998. ISSN 0022-3085.

BUECKER, A., SPUENTRUP, E., RUEBBEN, A., AND GÜNTHER, R. W. Artifact-free in-stent lumen visualization by standard magnetic resonance angiography using a new metallic magnetic resonance imaging stent. *Circulation*, 105(15):1772–1775, 2002.

BUTLER, J. P., TOLIĆ-NØRRELYKKE, I. M., FABRY, B., AND FREDBERG, J. J. Traction fields, moments, and strain energy that cells exert on their surroundings. *American Journal of Physiology - Cell Physiology*, 282(3):C595–C605, 2002.

CARANCI, F., BRIGANTI, F., CIRILLO, L., LEONARDI, M., AND MUTO, M. Epidemiology and genetics of intracranial aneurysms. *European journal of radiology*, 82(10):1598–1605, 2013.

CASIMIRO, M. V., MCEVOY, A. W., WATKINS, L. D., AND KITCHEN, N. D. A comparison of risk factors in the etiology of mirror and nonmirror multiple intracranial aneurysms. *Surgical neurology*, 61(6):541–545, 2004.

CEBRAL, J. R., CASTRO, M. A., SOTO, O., LÖHNER, R., AND ALPERIN, N. Blood-flow models of the circle of willis from magnetic resonance data. *Journal of Engineering Mathematics*, 47:369 – 386, 2003.

CEBRAL, J. R., MUT, F., WEIR, J., AND PUTMAN, C. Quantitative characterization of the hemodynamic environment in ruptured and unruptured brain aneurysms. *American Journal of Neuroradiology*, 32:145–151, 2011.

CEBRAL, J. R., CASTRO, M. A., BURGESS, J. E., PERGOLIZZI, R. S., SHERIDAN, M. J., AND PUTMAN, C. M. Characterization of cerebral aneurysms for assessing risk of rupture by using patient-specific computational hemodynamics models. *American Journal of Neuroradiology*, 26:2550–2559, 2005.

CEBRAL, J. R., HERNANDEZ, M., FRANGI, A., PUTMAN, C., PERGOLIZZI, R., AND BURGESS, J. Subject-specific modeling of intracranial aneurysms. In *Medical Imaging 2004*, pages 319–327. International Society for Optics and Photonics, 2004.

CEBRAL, J. R. AND MENG, H. Editorial — counterpoint: Realizing the clinical utility of computational fluid dynamics–closing the gap. *American Journal of Neuroradiology*, 2012.

CEBRAL, J. R., YIM, P. J., LÖHNER, R., SOTO, O., AND CHOYKE, P. L. Blood flow modeling in carotid arteries with computational fluid dynamics and {MR} imaging. *Academic Radiology*, 9(11):1286 – 1299, 2002. ISSN 1076-6332.

CHATZIPRODROMOU, I., POULIKAKOS, D., AND VENTIKOS, Y. On the influence of variation in haemodynamic conditions on the generation and growth of cerebral aneurysm and atherogenesis: A computational model. *Journal of Biomechanics*, 40:3626–3640, 2007a.

CHATZIPRODROMOU, I., TRICOLI, A., POULIKAKOS, D., AND VENTIKOS, Y. Haemodynamics and wall remodelling of a growing cerebral aneurysm: A computational model. *Journal of Biomechanics*, 40:415–426, 2007b.

CHEN, H. *Intracranial Aneurysm Disease: Novel Modelling of Inception and the Microstructural Adaption of Collagen Fabric*. Ph.d. thesis, Department of Engineering Science, University of Oxford, Oxford, 2014.

CHEN, H., SELIMOVIC, A., THOMPSON, H., CHIARINI, A., PENROSE, J., VENTIKOS, Y., AND WATTON, P. N. Investigating the influence of haemodynamic stimuli on intracranial aneurysm inception. *Annals of biomedical engineering*, 41(7):1492–1504, 2013.

CHENG, C. P., PARKER, D., AND TAYLOR, C. A. Quantification of wall shear stress in large blood vessels using lagrangian interpolation functions with cine phase-contrast magnetic resonance imaging. *Annals of Biomedical Engineering*, 30(8):1020–1032, 2002.

CHENG, J., ZHANG, J., MERCHED, A., ZHANG, L., ZHANG, P., TRUONG, L., BORIEK, A. M., AND DU, J. Mechanical stretch inhibits oxidized low density lipoprotein-induced apoptosis in vascular smooth muscle cells by up-regulating integrin $\alpha v\beta 3$ and stablization of pinch-1. *Journal of Biological Chemistry*, 282(47):34268–34275, 2007.

CHIEN, S. Effects of disturbed flow on endothelial cells. *Annals of Biomedical Engineering*, 36(4):554–562, 2007a.

CHIEN, S. Mechanotransduction and endothelial cell homeostasis: the wisdom of the cell. *American journal of physiology. Heart and circulatory physiology*, 292(3):H1209–H1224, 2007b.

CHIQUET, M. Regulation of extracellular matrix gene expression by mechanical stress. *Matrix Biology*, 18:417–426, 1999.

CHIQUET, M., GELMAN, L., LUTZ, R., AND MAIER, S. From mechanotransduction to extracellular matrix gene expression in fibroblasts. *Biochimica et Biophysica Acta - Molecular Cell Research*, 1793(5): 911–920, 2009.

CHIQUET, M., RENEDO, A. S., HUBER, F., AND FLÜCK, M. How do fibroblasts translate mechanical signals into changes in extracellular matrix production? *Matrix Biology*, 22:73–80, 2003.

CHIU, J. J. AND CHIEN, S. Effects of disturbed flow on vascular endothelium: pathophysiological basis and clinical perspectives. *Physiological Reviews*, 91 (1):327–387, 2011.

CLOFT, H. J., KALLMES, D. F., JENSEN, M. E., LANZINO, G., AND DION, J. E. Endovascular treatment of ruptured, peripheral cerebral aneurysms: parent artery occlusion with short guglielmi detachable coils. *American journal of neuroradiology*, 20(2): 308–310, 1999.

COTTIER, J.-P., PASCO, A., GALLAS, S., GABRILLARGUES, J., COGNARD, C., DROUINEAU, J., BRUNEREAU, L., AND HERBRETEAU, D. Utility of balloon-assisted guglielmi detachable coiling in the treatment of 49 cerebral aneurysms: A retrospective, multicenter study. *American Journal of Neuroradiology*, 22(2):345–351, 2001.

COURTMAN, D. W., SCHWARTZ, S. M., AND HART, C. E. Sequential injury of the rabbit abdominal aorta induces intramural coagulation and luminal narrowing independent of intimal mass: Extrinsic pathway inhibition eliminates luminal narrowing. *Circulation Research*, 82(9):996–1006, 1998.

CUMMINS, P. M., VON OFFENBERG SWEENEY, N., KILLEEN, M. T., BIRNEY, Y. A., REDMOND, E. M., AND CAHILL, P. A. Cyclic strain-mediated matrix metalloproteinase regulation within the vascular endothelium: a force to be reckoned with. *American Journal of Physiology - Heart and Circulatory Physiology*, 292(1):H28–H42, 2007. ISSN 0363-6135.

DALE, P. D., SHERRATT, J. A., MAINI, P. K., SHERRATT, A., AND MAINI, K. A mathematical model for collagen fibre formation during foetal and adult dermal wound healing. *Proceedings. Biological sciences / The Royal Society*, 263(1370):653–60, May 1996. ISSN 0962-8452.

DAVID, G. AND HUMPHREY, J. D. Further evidence for the dynamic stability of intracranial saccular aneurysms. *Journal of Biomechanics*, 36:1143–1150, 2003.

DAVIES, P. F. Hemodynamic shear stress and the endothelium in cardiovascular pathophysiology. *Nature clinical practice. Cardiovascular medicine*, 6 (1):16–26, 01 2009.

DE ROOIJ, N. K., LINN, F. H. H., VAN DER PLAS, J. A., ALGRA, A., AND RINKEL, G. J. E. Incidence of subarachnoid haemorrhage: a systematic review with emphasis on region, age, gender and time trends. *Journal of Neurology, Neurosurgery & Psychiatry*, 78 (12):1365–1372, 2007.

DEPAOLA, N., GIMBRONE, M. A., DAVIES, P. F., AND DEWEY, C. F. Vascular endothelium responds to fluid shear stress gradients. *Arteriosclerosis and thrombosis : a journal of vascular biology / American Heart Association*, 12(11):1254–1257, 1992.

DHAR, S., TREMMEL, M., MOCCO, J., KIM, M., YAMAMOTO, J., SIDDIQUI, A. H., HOPKINS, L. N., AND MENG, H. Morphology parameters for intracranial aneurysm rupture risk assessment. *Neurosurgery*, 63(2):185–187, 2008.

DING, Y., DAI, D., DANIELSON, M., KADIRVEL, R., LEWIS, D., CLOFT, H., AND KALLMES, D. Control of aneurysm volume by adjusting the position of ligation during creation of elastase-induced aneurysms: A prospective study. *American Journal of Neuroradiology*, 28(5):857–859, 2007.

DING, Y. H., DANIELSON, M. A., KADIRVEL, R., DAI, D., LEWIS, D. A., CLOFT, H. J., AND KALLMES, D. F. Modified technique to create morphologically reproducible elastase-induced aneurysms in rabbits. *Neuroradiology*, 48(8):528–532, 2006.

ERIKSSON, T., KROON, M., AND HOLZAPFEL, G. A. Influence of medial collagen organization and axial in situ stretch on saccular cerebral aneurysm growth. *Journal of biomechanical engineering*, 131 (10):101010, 2009.

ERIKSSON, T., WATTON, P., LUO, X., AND VENTIKOS, Y. Modelling volumetric growth in a thick walled fibre reinforced artery. *Journal of the Mechanics and Physics of Solids*, 2014.

FENG, Y., WADA, S., TSUBOTA, K.-I., AND YAMAGUCHI, T. The application of computer simulation in the genesis and development of intracranial aneurysms. *Technology and Health Care*, 13(4):281–291, 2005.

FIGUEROA, C. A., BAEK, S., TAYLOR, C. A., AND HUMPHREY, J. D. A computational framework for fluid-solid-growth modeling in cardiovascular simulations. *The British Journal of Radiology*, 82:55–61, 2009.

FILLINGER, M., RAGHAVAN, M., MARRA, S., CRONENWETT, J., AND KENNEDY, F. In vivo analysis of mechanical wall stress and abdominal aortic aneurysm rupture risk. *Journal of Vascular Surgery*, 36:589–597, 2002.

FINLAY, H. M., WHITTAKER, P., AND CANHAM, P. B. Collagen organization in the branching region of human brain arteries. *Stroke*, 29:1595–1601, 1998.

FOUTRAKIS, G. N., YONAS, H., AND SCLABASSI, R. J. Saccular aneurysm formation in curved and bifurcating arteries. *American journal of neuroradiology*, 20(7):1309–1317, August 1999. ISSN 0195-6108.

FRIDEZ, P., MAKINO, A., KAKOI, D., MIYAZAKI, H., MEISTER, J.-J., HAYASHI, K., AND STERGIOPULOS, N. Adaptation of conduit artery vascular smooth muscle tone to induced hypertension. *Annals of Biomedical Engineering*, 30(7):905–916, 2002. ISSN 1573-9686.

FRÖSEN, J., PIIPPO, A., PAETAU, A., KANGASNIEMI, M., NIEMELA, M., HERNESNIEMI, J., AND JAASKELELAINEN, J. Remodelling of saccular cerebral artery aneurysm wall is associated with rupture. histological analysis of 24 unruptured and 42 ruptured cases. *Stroke*, 35:2287–2293, 2004.

FRÖSEN, J., TULAMO, R., PAETAU, A., LAAKSAMO, E., KORJA, M., LAAKSO, A., NIEMELÄ, M., AND HERNESNIEMI, J. Saccular intracranial aneurysm: Pathology and mechanisms. *Acta Neuropathologica*, 123:773–786, 2012.

FRÖSEN, J., PIIPPO, A., PAETAU, A., KANGASNIEMI, M., NIEMELÄ, M., HERNESNIEMI, J., AND JÄÄSKELÄINEN, J. Growth factor receptor expression and remodeling of saccular cerebral artery aneurysm

walls: implications for biological therapy preventing rupture. *Neurosurgery*, 58(3):534–41; discussion 534–41, March 2006. ISSN 1524-4040.

FUJIWARA, N. H., CLOFT, H. J., MARX, W. F., SHORT, J. G., JENSEN, M. E., AND KALLMES, D. F. Serial angiography in an elastase-induced aneurysm model in rabbits: Evidence for progressive aneurysm enlargement after creation. *American Journal of Neuroradiology*, 22(4):698–703, 2001.

FUNG, Y. C. *Biomechanics. Mechanical Properties of Living Tissues.* Springer-Verlag, New York, 2nd edition, 1993.

GAETANI, P., TARTARA, F., GRAZIOLI, V., TANCIONI, F., INFUSO, L., AND BAENA, R. R. Y. Collagen crosslinkage, elastolytic and collagenolytic activities in cerebral aneurysms: A preliminary investigation. *Life Sciences*, 63:285–292, 1998.

GASPAROTTI, R. AND LISERRE, R. Intracranial aneurysms. *European radiology*, 15(3):441–447, 2005.

GASSER, T. C., OGDEN, R. W., AND HOLZAPFEL, G. A. Hyperelastic modelling of arterial layers with distributed collagen fibre orientations. *Journal of the Royal Society, Interface*, 3(6):15–35, 2006.

GASSER, T. C., GALLINETTI, S., XING, X., FORSELL, C., SWEDENBORG, J., AND ROY, J. Spatial orientation of collagen fibers in the abdominal aortic aneurysm's wall and its relation to wall mechanics. *Acta Biomaterialia*, 8:3091–3103, 2012.

GENG, Y. J. Molecular signal transduction in vascular cell apoptosis. *Cell Res*, 11(4):253–264, print 2000.

GLEASON, R. L. AND HUMPHREY, J. D. A mixture model of arterial growth and remodeling in hypertension: altered muscle tone and tissue turnover. *Journal of Vascular Research*, 41(4):352–363, 2004.

GLEASON, R. L. AND HUMPHREY, J. D. A 2d constrained mixture model for arterial adaptations to large changes in flow, pressure and axial stretch. *Mathematical medicine and biology*, 22(4):347–369, 2005.

GLEASON, R. L. AND HUMPHREY, J. D. Effects of a sustained extension on arterial growth and remodeling: a theoretical study. *J. Biomech. Eng.*, 38:1255–1261, 2007.

GLEASON, R. L., TABER, L. A., AND HUMPHREY, J. D. A 2-d model of flow-induced alterations in the geometry, structure, and properties of carotid arteries. *Journal of biomechanical engineering*, 126(3): 371–381, 2004.

GLOR, F. P., ARIFF, B., HUGHES, A. D., CROWE, L. A., VERDONCK, P. R., C, B. D., MCG THOM, S. A., FIRMIN, D. N., AND XU, X. Y. Image-based carotid flow reconstruction: a comparison between mri and ultrasound. *Physiological Measurement*, 25: 1495–1509, 2004.

GREVING, J. P., RINKEL, G. J. E., BUSKENS, E., AND ALGRA, A. Cost-effectiveness of preventive treatment of intracranial aneurysms: New data and uncertainties. *Neurology*, 73(4):258–265, July 2009. ISSN 1526-632X.

GRYTSAN, A., WATTON, P. N., AND HOLZAPFEL, G. A. A thick-walled fluid–solid-growth model of abdominal aortic aneurysm evolution: Application to a patient-specific geometry. *Journal of Biomechanical Engineering*, 137(3):031008–031008, 03 2015.

GUPTA, V. AND GRANDE-ALLEN, K. J. Effects of static and cyclic loading in regulating extracellular matrix synthesis by cardiovascular cells. *Cardiovascular Research*, 72(3):375–383, 2006. ISSN 0008-6363.

HANEIN, D. AND HORWITZ, A. R. The structure of cell-matrix adhesions: the new frontier. *Current opinion in cell biology*, 24(1):134–40, February 2012. ISSN 1879-0410.

HANSEN, F., MANGELL, P., SONESSON, B., AND LÄNNE, T. Diameter and compliance in the human common carotid artery–variations with age and sex. *Ultrasound in medicine & biology*, 21(1):1–9, 1995.

HASHIMOTO, N., HANDA, H., NAGATA, I., AND HAZAMA, F. Experimentally induced cerebral aneurysms in rats: Part v. relation of hemodynamics in the circle of willis to formulation of aneurysms. *Surg. Neurol.*, 13(1):41–45, 1980.

HASHIMOTO, N., KIM, C., KIKUCHI, H., KOJIMA, M., KANG, Y., AND HAZAMA, F. Experimental induction of cerebral aneurysms in monkeys. *Journal of Neurosurgery*, 67:903–905, 1987.

HASLACH, H. W. AND HUMPHREY, J. D. Dynamics of biological soft tissue and rubber: internally pressurized spherical membranes surrounded by a fluid. *International Journal of Non-Linear Mechanics*, 39(3):399–420, 2004.

HAZAMA, F., KATAOKA, H., YAMADA, E., KAYEMBE, K., HASHIMOTO, N., KOJIMA, M., AND KIM, C. Early changes of experimentally induced cerebral aneurysms in rats. light-microscopic study. *The American journal of pathology*, 124(3):399, 1986.

HENNIG, T., C, M., J, K., U, P., AND T, G. Shear stress induces the release of an endothelial elastase: role in integrin Îś(v)Îš(3)-mediated fgf-2 release. *CORD Conference Proceedings*, 48(6):453–464, January 2011. ISSN 0000-0000.

HIGASHIDA, R., LAHUE, B., TORBEY, M., HOPKINS, L., LEIP, E., AND HANLEY, D. Treatment of unruptured intracranial aneurysms: a nationwide assessment of effectiveness. *American Journal of Neuroradiology*, 28(1):146–151, 2007.

HILL, M. R., DUAN, X., GIBSON, G. A., WATKINS, S., AND ROBERTSON, A. M. A theoretical and non-destructive experimental approach for direct inclusion of measured collagen orientation and recruitment into mechanical models of the artery wall. *Journal of Biomechanics*, 45(5):762–771, 2012a.

HILL, M. R., DUAN, X., GIBSON, G. A., WATKINS, S., AND ROBERTSON, A. M. A theoretical and non-destructive experimental approach for direct inclusion of measured collagen orientation and recruitment into mechanical models of the artery wall. *Journal of Biomechanics*, 45(5):762 – 771, 2012b. ISSN 0021-9290. Special Issue on Cardiovascular Solid Mechanics.

HO, H., SURESH, V., KANG, W., COOLING, M. T. M., WATTON, P. N. P., AND HUNTER, P. P. J. Multiscale modeling of intracranial aneurysms: Cell signaling, hemodynamics, and remodelling. *IEEE Transactions on Biomedical Engineering*, 58(10):2974–2977, 2011. ISSN 15582531.

HOHLRIEDER, M., SPIEGEL, M., HINTERHOELZL, J., ENGELHARDT, K., PFAUSLER, B., KAMPFL, A., ULMER, H., WALDENBERGER, P., MOHSENIPOUR, I., AND SCHMUTZHARD, E. Cerebral vasospasm and ischaemic infarction in clipped and coiled intracranial aneurysm patients. *European Journal of Neurology*, 9(4):389–399, 2002.

HOI, Y., MENG, H., WOODWARD, S. H., BENDOK, B. R., HANEL, R. A., GUTERMAN, L. R., AND HOPKINS, L. N. Effects of arterial geometry on aneurysm growth: three-dimensional computational fluid dynamics study. *Journal of neurosurgery*, 101(4):676–81, 2004.

HOLLAND, E. *Computational momodelling transport phenomena in cerebral aneursyms*. PhD thesis, University of Oxford, 2012.

HOLZAPFEL, G. A. Determination of material models for arterial walls from uniaxial extension tests and histological structure. *Journal of Theoretical Biology*, 238:290–302, 2006.

HOLZAPFEL, G. A., GASSER, T. C., AND OGDEN, R. W. A new constitutive framework for arterial wall mechanics and a comparative study of material models. *Journal of elasticity*, 61(1–3):1–48, 2000.

HOLZAPFEL, G. A., GASSER, T. C., AND STADLER, M. A structural model for the viscoelastic behavior of arterial walls: \mbox{C}ontinuum formulation and finite element analysis. *European Journal of Mechanics A/Solids*, 21(3):441–463, January 2002. ISSN 09977538.

HSIAI, T. K. Mechanical transduction coupling between endothelial and smooth muscle cells: role of hemodynamic forces. *American Journal of Physiology: Cell Physiology*, 294:C695–C661, 2008.

HSU, F. P. K., LIU, A. M. C., DOWNS, J., RIGAMONTI, D., AND HUMPHREY, J. D. A triplane video-based experimental system for studying axisymmetrically inflated biomembranes. *IEEE Transactions on Biomedical Engineering*, 42:442–449, 1995.

HUMPHREY, J. D. Remodeling of a collagenous tissue at fixed lengths. *Journal of biomechanical engineering*, 121(6):591–597, 1999.

HUMPHREY, J. D. Vascular mechanics, mechanobiology and remodelling. *Journal of Mechanics in Medicine and Biology*, 9:243–257, 2009.

HUMPHREY, J. D. AND HOLZAPFEL, G. A. Mechanics, mechanobiology, and modeling of human abdominal aorta and aneurysms. *Journal of Biomechanics*, 2011. article in press doi:10.1016 / j.jbiomech.2011.11.021.

HUMPHREY, J. D. AND KYRIACOU, S. K. The use of laplace's equation in aneurysm mechanics. *Neurological Research*, 18:204–208, 1996.

HUMPHREY, J. D. AND RAJAGOPAL, K. R. A constrained maxiture model for growth and remodeling of soft tissues. *Mathematical Models and Methods in Applied Sciences*, 12(3):407–430, 2002.

HUMPHREY, J. D. AND TAYLOR, C. A. Intracranial and abdominal aortic aneurysms: Similarities, differences, and need for a new class of computational models. *Annual Review of Biomedical Engineering*, 10:221–246, 2008.

HUMPHREY, J. D. *Cardiovascular Solid Mechanics: Cells, Tissues, and Organs*. Springer-Verlag New York, 2002.

HUMPHREY, J. D., SCHWARTZ, M. A., TELLIDES, G., AND MILEWICZ, D. M. Role of mechanotransduction in vascular biology: Focus on thoracic aortic aneurysms and dissections. *Circulation Research*, 116(8):1448–1461, 2015.

HUMPHREY, J. Vascular adaptation and mechanical homeostasis at tissue, cellular, and sub-cellular levels. *Cell biochemistry and biophysics*, 50(2):53–78, 2008.

INAGAWA, T. AND HIRANO, A. Autopsy study of unruptured incidental intracranial aneurysms. *Surg Neurol*, 34:361–365, 1990.

INCI, S. AND SPETZLER, R. F. Intracranial aneurysms and arterial hypertension: a review and hypothesis. *Surgical neurology*, 53(6):530–542, 2000.

INTENGAN, H. D. AND SCHIFFRIN, E. L. Vascular remodeling in hypertension: Roles of apoptosis, inflammation, and fibrosis. *Hypertension*, 38(3):581–587, September 2001. ISSN 0194-911X.

ISODA, H., OHKURA, Y., KOSUGI, T., HIRANO, M., ALLEY, M. T., BAMMER, R., PELC, N. J., NAMBA, H., AND SAKAHARA, H. Comparison of hemodynamics of intracranial aneurysms between mr fluid dynamics using 3d cine phase-contrast mri and mr-based computational fluid dynamics. *Neuroradiology*, 52(10):913–920, 2010. ISSN 1432-1920.

JI, G., BARSOTTI, R. J., FELDMAN, M. E., AND KOTLIKOFF, M. I. Stretch-induced calcium release in smooth muscle. *The Journal of General Physiology*, 119(6):533–543, 06 2002.

JONES, A., DEB, R., TORSNEY, E., HOWE, F., DUNKLEY, M., GNANESWARAN, Y., GAZE, D., NASR, H., LOFTUS, I. M., THOMPSON, M. M., COCKERILL, G. W., AND DUNKELY, M. Rosiglitazone reduces the development and rupture of experimental aortic aneurysms. *Circulation*, 119(24):3125–3132, June 2009. ISSN 1524-4539.

JOU, L. D., WONG, G., DISPENSA, B., LAWTON, M. T., HIGASHIDA, R. T., YOUNG, W. L., AND SALONER, D. Correlation between lumenal geometry changes and hemodynamics in fusiform intracranial aneurysms. *American Journal of Neuroradiology*, 26(9):2357–2363, 2005.

JUVELA, S., PORRAS, M., AND POUSSA, K. Natural history of unruptured intracranial aneurysms: probability and risk factors for aneurysm rupture. *Journal of Neurosurgery*, 93:379–387, 2000.

JUVELA, S., POUSSA, K., AND PORRAS, M. Factors affecting formation and growth of intracranial aneurysms : A long-term follow-up study. *Stroke*, 32:485–291, 2007.

JUVELA, S., POUSSA, K., AND PORRAS, M. Factors affecting formation and growth of intracranial aneurysms: A long-term follow-up study. *Stroke*, 32 (2):485–491, 2001.

KADIRVEL, R., DING, Y.-H., DAI, D., LEWIS, D. A., AND KALLMES, D. F. Differential expression of genes in elastase-induced saccular aneurysms with high and low aspect ratios. *Neurosurgery*, 66(3):578, 2010.

KADIRVEL, R., DING, Y.-H., DAI, D., ZAKARIA, H., ROBERTSON, A. M., DANIELSON, M. A., LEWIS, D. A., CLOFT, H. J., AND KALLMES, D. F. The influence of hemodynamic forces on biomarkers in the walls of elastase-induced aneurysms in rabbits. *Neuroradiology*, 49(12):1041–1053, 2007.

KAKISIS, J. D., LIAPIS, C. D., AND SUMPIO, B. E. Effects of cyclic strain on vascular cells. *Endothelium*, 11: 17–28, 2004.

KALLMES, D. F., DING, Y. H., DAI, D., KADIRVEL, R., LEWIS, D. A., AND CLOFT, H. J. A new endoluminal, flow-disrupting device for treatment of saccular aneurysms. *Stroke*, 38(8):2346–2352, 2007.

KALLMES, D. F., FUJIWARA, N. H., BERR, S. S., HELM, G. A., AND CLOFT, H. J. Elastase-induced saccular aneurysms in rabbits: a dose-escalation study. *American journal of neuroradiology*, 23(2):295–298, 2002.

KALMES, D. F. Editorial — point: Cfd–computational fluid dynamics or confounding factor dissemination. *American Journal of Neuroradiology*, 2012.

KAMITANI, H., MASUZAWA, H., KANAZAWA, I., AND KUBO, T. Bleeding risk in unruptured and residual cerebral aneurysms – angiographic annual growth

rate in nineteen patients. *Acta Neurochirurgica*, 141 (2):153–159, 1999. ISSN 0942-0940.

KAMIYA, A. AND TOGAWA, T. Adaptive regulation of wall shear stress to flow change in the canine carotid artery. *Am. J. Physiol.*, 239(1):H14–H21, July 1980. ISSN 0002-9513.

KANDA, K. AND MATSUDA, T. Mechanical stress-induced orientation and ultrastructural change of smooth muscle cells cultured in three-dimensional collagen lattices. *Cell transplantation*, 3(6):481–492, 1994. ISSN 0963-6897.

KASSAM, A., HOROWITZ, M., CHANG, Y.-F., AND PETERS, D. Altered arterial homeostasis and cerebral aneurysms: A review of the literature and justification for a search of molecular biomarkers. *Neurosurgery*, 54(5):1199–1212, May 2004. ISSN 0148-396X.

KATAKOA, K., TANEDA, M., ASAI, T., KINOSHITA, A., ITO, M., KURODA, R., AND KATAOKA, K. Structural Fragility and inflammatory response of ruptured cerebral aneurysms : a comparative study between ruptured and unruptured cerebral aneurysms. *Stroke*, 30(7):1396–1401, July 1999. ISSN 0039-2499.

KEEDY, A. An overview of intracranial aneurysms. *McGill Journal of Medicine : MJM*, 9(2):141–146, 07 2006.

KILLER-OBERPFALZER, M., AICHHOLZER, M., WEIS, S., RICHLING, B., JONES, R., VIRMANI, R., AND CRUISE, G. M. Histological analysis of clipped human intracranial aneurysms and parent arteries with short-term follow-up. *Cardiovascular Pathology*, 21(4):299–306, 2012.

KIM, C., KIKUCHI, H., HASHIMOTO, N., AND HAZAMA, F. Histopathological study of induced cerebral aneurysms in primates. *Surgical Neurology*, 32:45–50, 1989a.

KIM, C., KIKUCHI, H., HASHIMOTO, N., HAZAMA, F., AND KATAOKA, H. Establishment of the experimental conditions for inducing saccular cerebral aneurysms in primates with special reference to hypertension. *Acta Neurochir (Wien)*, 96:132–136, 1989b.

KIM, C., CERVÓS-NAVARRO, J., KIKUCHI, H., HASHIMOTO, N., AND HAZAMA, F. Alterations in cerebral vessels in experimental animals and their possible relationship to the development of aneurysms. *Surgical Neurology*, 38(5):331 – 337, 1992. ISSN 0090-3019.

KOFFIJBERG, H., BUSKENS, E., ALGRA, A., WERMER, M. J. H., AND RINKEL, G. J. E. Growth rates of intracranial aneurysms: exploring constancy. *Journal of Neurosurgery*, 109(2):176–185, 2008. PMID: 18671627.

KOLAHI, K. AND MOFRAD, M. R. K. Mechanotransduction: A major regulator of homeostasis and development. *Wiley Interdisciplinary Reviews: Systems Biology and Medicine*, 2(6):625–639, 2010.

KONDO, S., HASHIMOTO, N., KIKUCHI, H., HAZAMA, F., NAGATA, I., AND KATAOKA, H. Cerebral aneurysms arising at nonbranching sites. an experimental study. *Stroke; a journal of cerebral circulation*, 28(2):398–403, 1997.

KONDO, S., HASHIMOTO, N., KIKUCHI, H., HAZAMA, F., NAGATA, I., AND KATAOKA, H. Apoptosis of medial smooth muscle cells in the development of saccular cerebral aneurysms in rats. *Stroke; a journal of cerebral circulation*, 29(1):181–189, 1998.

KONG, Y. P., CARRION, B., SINGH, R. K., AND PUTNAM, A. J. Matrix identity and tractional forces influence indirect cardiac reprogramming. *Scientific Reports*, 3:3474, 2013.

KOSIERKIEWICZ, T. A., FACTOR, S. M., AND DICKSON, D. W. Immunocytochemical studies of atherosclerotic lesions of cerebral berry aneurysms. *Journal of neuropathology and experimental neurology*, 53 (4):399–406, 1994.

KREX, D., SCHACKERT, H. K., AND SCHACKERT, G. Genesis of cerebral aneurysms – an update. *Acta Neurochirurgica (Wien)*, 143:429–448, 2001.

KRINGS, T., MANDELL, D. M., KIEHL, T.-R., GEIBPRASERT, S., TYMIANSKI, M., ALVAREZ, H., HANS, F.-J., ET AL. Intracranial aneurysms: from vessel wall pathology to therapeutic approach. *Nature Reviews Neurology*, 7(10):547–559, 2011.

KRISCHEK, B. AND INOUE, I. The genetics of intracranial aneurysms. *Journal of human genetics*, 51(7): 587–594, 2006.

KROON, M. AND HOLZAPFEL, G. A. A model for saccular cerebral aneurysm growth by collagen fibre remodelling. *Journal of Theoretical Biology*, 247(4): 775–787, 2007.

KROON, M. AND HOLZAPFEL, G. A. A theoretical model for fibroblast-controlled growth of saccular cerebral aneurysms. *Journal of Theoretical Biology*, 257(1):73–83, 2009.

KU, D. N., GIDDENS, D. P., ZARINS, C. K., AND GLAGOV, S. Pulsatile flow and atherosclerosis in the human carotid bifurcation. positive correlation between plaque location and low oscillating shear stress. *Arteriosclerosis, Thrombosis, and Vascular Biology*, 5(3):293–302, 1985.

KUHL, E. AND HOLZAPFEL, G. A. A continuum model for remodeling in living structures. *J. Mater. Sci. Mater. Med.*, 42(21):8811–8823, July 2007. ISSN 0022-2461.

KYRIACOU, S. K. AND HUMPHREY, J. D. Influence of size, shape and properties on the mechanics of axisymmetric saccular aneurysms. *J. Biomech.Biomechanics*, 29:1015–1022, 1996.

LACOLLEY, P., REGNAULT, V., NICOLETTI, A., LI, Z., AND MICHEL, J.-B. The vascular smooth muscle cell in arterial pathology: a cell that can take on multiple roles. *Cardiovascular research*, 95(2):194–204, July 2012. ISSN 1755-3245.

LANGILLE, B. L. Remodeling of developing and mature arteries: endothelium, smooth muscle, and matrix. *Journal of cardiovascular pharmacology*, 21:11 – 17, 1993.

LANIR, Y. A structural theory for the homogeneous biaxial stress-strain relationships in flat collagenous tissues. *Journal of biomechanics*, 12(6):423–436, January 1979. ISSN 0021-9290.

LÄNNE, T., SONESSON, B., BERGQVIST, D., BENGTSSON, H., AND GUSTAFSSON, D. Diameter and compliance in the male human abdominal aorta: Influence of age and aortic aneurysm. *European Journal of Vascular Surgery*, 6:178–184, 1992.

LASHERAS, J. C. The biomechanics of arterial aneurysms. *Annual Review of Fluid Mechanics*, 39 (1):293–319, 2007.

LEE, T. AND SUMPIO, B. E. Cell signalling in vascular cells exposed to cyclic strain: the emerging role of protein phosphatases. *Biotechnology and Applied Biochemistry*, 39(2):129–139, 2004. ISSN 1470-8744.

LES, A. S., SHADDEN, S. C., FIGUEROA, C. A., PARK, J. M., TEDESCO, M. M., HERFKENS, R. J., DALMAN, R. L., AND TAYLOR, C. A. Quantification of hemodynamics in abdominal aortic aneurysms during rest and exercise using magnetic resonance imaging and computational fluid dynamics. *Annals of Biomedical Engineering*, 38(4):1288–1313, 2010. ISSN 1573-9686.

LEUNG, D. Y., GLAGOV, S., AND MATHEWS, M. B. Elastin and collagen accumulation in rabbit ascending aorta and pulmonary trunk during postnatal growth. correlation of cellular synthetic response with medial tension. *Circulation Research*, 41(3):316–23, 1977.

LIEBER, B. B., STANCAMPIANO, A. P., AND WAKHLOO, A. K. Alteration of hemodynamics in aneurysm models by stenting: influence of stent porosity. *Annals of biomedical engineering*, 25(3):460–469, 1997.

LINDSAY, M. E. AND DIETZ, H. C. Lessons on the pathogenesis of aneurysm from heritable conditions. *Nature*, 473(7347):308–316, 05 2011.

LOW, M., PERKTOLD, K., AND RAUNIG, R. Hemodynamics in rigid and distensible saccular aneursyms: A numerical study of pulsatile flow characteristics. *Biorheology*, 30:287–298, 1993.

MA, B., LU, J., HARBAUGH, R. E., AND RAGHAVAN, M. L. Nonlinear anisotropic stress analysis of anatomically realistic cerebral aneurysms. *ASME Journal of Biomechanical Engineering*, 129:88–96, 2007.

MA, B., HARBAUGH, R. E., AND RAGHAVAN, M. L. Three-dimensional geometrical characterization of cerebral aneurysms. *Annals of Biomedical Engineering*, 32(2):264–273, February 2004. ISSN 0090-6964.

MA, J., YOU, Z., PEACH, T., BYRNE, J., AND RIZKALLAH, R. R. A new flow diverter stent for direct treatment of intracranial aneurysm. *Journal of Biomechanics*, 48(16):4206 – 4213, 2015. ISSN 0021-9290.

MALEK, A. M., ALPER, S. L., AND IZUMO, S. Hemodynamic shear stress and its role in atherosclerosis. *JAMA : the journal of the American Medical Association*, 282(21):2035–2042, 1999.

MANTHA, A., KARMONIK, C., BENNDORF, G., STROTHER, C., AND METCALFE, R. Hemodynamics in a cerebral artery before and after the formation of an aneurysm. *American Journal of Neuroradiology*, 27:1113 – 1118, 2006.

MARTUFI, G. AND GASSER, T. C. Turnover of fibrillar collagen in soft biological tissue with application to the expansion of abdominal aortic aneurysms. *Journal of The Royal Society Interface*, 9(77):3366 – 3377, 2012.

MATSUMOTO, T. AND NAGAYAMA, K. Tensile properties of vascular smooth muscle cells: Bridging vascular and cellular biomechanics. *Journal of Biomechanics*, 45(5):745 – 755, 2012. ISSN 0021-9290. Special Issue on Cardiovascular Solid Mechanics.

MCANULTY, R. J. Fibroblasts and myofibroblasts: Their source, function and role in disease. *The International Journal of Biochemistry & Cell Biology*, 39:666–671, 2007.

MCGLOUGHLIN, T. *Biomechanics and Mechanobiology of Aneurysms*. Studies in mechanobiology, Tissue Engineering and Biomaterials 7. Springer, 2011.

MCGLOUGHLIN, T. M. AND DOYLE, B. J. New approaches to abdominal aortic aneurysm rupture risk assessment. *Arteriosclerosis, Thrombosis and Vascular Biology*, 30:1687–1694, 2010.

MENG, H., METAXA, E., GAO, L., LIAW, N., NATARAJAN, S. K., SWARTZ, D. D., SIDDIQUI, A. H., KOLEGA, J., AND MOCCO, J. Progressive aneurysm development following hemodynamic insult. *Journal of Neurosurgery*, 114(4):1095–1103, 2011.

MENG, H., SWART, D. D., WANG, Z., HOI, Y., KOLEGA, J., METAXA, E., AND SZYMANSKI, M. P. A model system for mapping vascular responses to complex hemodynamics at arterial bifurcations in vivo. *Neurosurgery*, 59(5):1094 – 1100, 2006.

MENG, H., WANG, Z., HOI, Y., GAO, L., METAXA, E., SWART, D. D., AND KOLEGA, J. Complex hemodynamics at the apex of an arterial bifurcation induces vascular remodelling resembling cerebral aneurysm initiation. *Stroke*, 38:1924–1931, 2007.

MERAN, S. AND STEADMAN, R. Fibroblasts and myofibroblasts in renal fibrosis. *International journal of experimental pathology*, 92(3):158–67, June 2011. ISSN 1365-2613.

METAXA, E., MENG, H., KALUVALA, S. R., SZYMANSKI, M. P., PALUCH, R. A., AND KOLEGA, J. Nitric oxide-dependent stimulation of endothelial cell proliferation by sustained high flow. *American journal of physiology. Heart and circulatory physiology*, 295 (2):736–742, 2008.

METAXA, E., TREMMEL, M., NATARAJAN, S. K., XIANG, J., PALUCH, R. A., MANDELBAUM, M., AND SIDDIQUI, A. H. Characterization of critical hemodynamics contributing to aneurysmal remodeling at the basilar terminus in a rabbit model. *Stroke*, 41 (8):1774–1782, 2010.

MIMATA, C., KITAOKA, M., NAGAHIRO, S., IYAMA, K., HORI, H., YOSHIOKA, H., AND USHIO, Y. Differential distribution and expressions of collagens in the cerebral aneurysmal wall. *Acta neuropathologica*, 94(3):197–206, September 1997. ISSN 0001-6322.

MITCHELL, P. AND JAKUBOWSKI, J. Estimate of the maximum time interval between formation of cerebral aneurysm and rupture. *Journal of Neurology, Neurosurgery & Psychiatry*, 69(6):760–767, 2000.

MOHAN, D. AND MELVIN, J. W. Failure properties of passive human aortic tissue. ii- biaxial tension tests. *Journal of Biomechanics*, 16:31–44, 1982.

MOLYNEUX, A. J., KERR, R. S., BIRKS, J., RAMZI, N., YARNOLD, J., SNEADE, M., AND RISCHMILLER, J. Risk of recurrent subarachnoid haemorrhage, death, or dependence and standardised mortality ratios after clipping or coiling of an intracranial aneurysm in the international subarachnoid aneurysm trial (isat): long-term follow-up. *The Lancet Neurology*, 8(5):427 – 433, 2009. ISSN 1474-4422.

MONSON, K. L., GOLDSMITH, W., BARBARO, N. M., AND MANLEY, G. T. Axial mechanical properties of fresh human cerebral blood vessels. *Journal of biomechanical engineering*, 125(2):288–294, 2003.

MONSON, K. L., GOLDSMITH, W., BARBARO, N. M., AND MANLEY, G. T. Significance of source and size in the mechanical response of human cerebral blood vessels. *Journal of Biomechanics*, 38:737–744, 2005.

MOORE, J. A., RUTT, B. K., KARLIK, S. J., YIN, K., AND ETHIER, C. R. Computational blood flow modeling based in vivo measurements. *Ann. Biomed. Eng.*, 27:627–640, 1999.

MÜLLER, J., SAHNI, O., LI, X., JANSEN, K., SHEPHARD, M., AND TAYLOR, C. Anisotropic adaptive finite element method for modelling blood flow. *Computer methods in biomechanics and biomedical engineering*, 8(5):295–305, 2005.

MURTADA, S. I., KROON, M., AND HOLZAPFEL, G. A. A calcium-driven mechanochemical model for prediction of force generation in smooth muscle. *Biomechanics and Modeling in Mechanobiology*, 9 (6):749–762, 2010.

NEIDLINGER-WILKE, C., GROOD, E., CLAES, L., AND BRAND, R. Fibroblast orientation to stretch begins within three hours. *Journal of Orthopaedic Research*, 20(5):953–956, 2002. ISSN 1554-527X.

NEREM, R. M. Hemodynamics and the vascular endothelium. *J. Biomech. Engrg.*, 115(4B):510–514, November 1993. ISSN 0148-0731.

NHS. Nhs commissioning board clinical commisioning policy statement: Flow diverting devices for intracranial aneurysms. Technical report, NHS, 2012.

NISSEN, R., CARDINALE, G. J., AND UDENFRIEND, S. Increased turnover of arterial collagen in hypertensive rats. *Proceedings of the National Academy of Sciences of the United States of America*, 75(1):451–453, 1978.

NIXON, A. M., GUNEL, M., AND SUMPIO, B. E. The critical role of hemodynamics in the development of cerebral vascular disease. *Journal of neurosurgery*, 112(6):1240–1253, 2010.

OKAMOTO, E.-I., COUSE, T., DE LEON, H., VINTEN-JOHANSEN, J., GOODMAN, R. B., SCOTT, N. A., AND WILCOX, J. N. Perivascular inflammation after balloon angioplasty of porcine coronary arteries. *Circulation*, 104(18):2228–2235, 2001.

OMODAKA, S., SUGIYAMA, S., INOUE, T., FUNAMOTO, K., FUJIMURA, M., SHIMIZU, H., HAYASE, T., TAKAHASHI, A., AND TOMINAGA, T. Local hemodynamics at the rupture point of cerebral aneurysms determined by computational fluid dynamics analysis. *Cerebrovascular Diseases*, 34(2):121–129, 2012.

OPITZ, F., SCHENKE-LAYLAND, K., COHNERT, T. U., AND STOCK, U. A. Phenotypical plasticity of vascular smooth muscle cells-effect of in vitro and in vivo shear stress for tissue engineering of blood vessels. *Tissue engineering*, 13(10):2505–2514, 2007.

OWENS, G. K., KUMAR, M. S., AND WAMHOFF, B. R. Molecular regulation of vascular smooth muscle cell differentiation in development and disease. *Physiological Reviews*, 84(3):767–801, 2004. ISSN 0031-9333.

PANDIT, A., LU, X., WANG, C., AND KASSAB, G. S. Biaxial elastic material properties of porcine coronary media and adventitia. *American Journal of Physiology - Heart and Circulatory Physiology*, 288(6): H2581–H2587, 2005.

PANG, Y., WANG, X., LEE, D., AND GREISLER, H. P. Dynamic quantitative visualization of single cell alignment and migration and matrix remodeling in 3-d collagen hydrogels under mechanical force. *Biomaterials*, 32(15):3776–3783, 2011.

PARK, H.-K., HOROWITZ, M., JUNGREIS, C., GENEVRO, J., KOEBBE, C., LEVY, E., AND KASSAM, A. Periprocedural morbidity and mortality associated with endovascular treatment of intracranial aneurysms. *American Journal of Neuroradiology*, 26(3):506–514, 2005.

PATANKAR, S. V. *Numerical Heat Transfer and Fluid Flow (Hemisphere Series on Computational Methods in Mechanics and Thermal Science)*. Washington : Hemisphere Pub. Corp. ; New York : McGraw-Hill, 1980.

PIERCE, D. M., FASTL, T. E., RODRIGUEZ-VILA, B., VERBRUGGHE, P., FOURNEAU, I., MALEUX, G., HERIJGERS, P., GOMEZ, E. J., AND HOLZAPFEL, G. A. A method for incorporating three-dimensional residual stretches/stresses into patient-specific finite element simulations of arteries. *Journal of the Mechanical Behavior of Biomedical Materials*, 47:147 – 164, 2015. ISSN 1751-6161.

PIEROT, L. Flow diverter stents in the treatment of intracranial aneurysms: Where are we? *Journal of Neuroradiology*, 38(1):40 – 46, 2011. ISSN 0150-9861.

PLANK, M. J., WALL, D. J. N., AND DAVID, T. Atherosclerosis and calcium signalling in endothelial cells. *Progress in biophysics and molecular biology*, 91(3):287–313, July 2006. ISSN 0079-6107.

POELMA, C., WATTON, P. N., AND VENTIKOS, Y. Transitional flow in aneurysms and the computation of haemodynamic parameters. *Journal of The Royal Society Interface*, 12(105):20141394, 2015.

PRAKASH, S. AND ETHIER, C. R. Requirements for mesh resolution in 3d computational hemodynamics. *Journal of Biomechanical Engineering*, 123(2): 134, 2001. ISSN 01480731.

QIU, J., ZHENG, Y., HU, J., LIAO, D., GREGERSEN, H., DENG, X., FAN, Y., AND WANG, G. Biomechanical regulation of vascular smooth muscle cell functions: from in vitro to in vivo understanding. *Journal of the Royal Society, Interface*, 11(90):20130852, 2014.

RACHEV, A. A model of arterial adaptation to alterations in blood flow. *Journal of elasticity and the physical science of solids*, 61(1-3):83–111, 2000. ISSN 0374-3535.

RACHEV, A. AND HAYASHI, K. Theoretical study of the effects of vascular smooth muscle contraction on

strain and stress distributions in arteries. *Annals of Biomedical Engineering*, 27:459–468, 1999. ISSN 0090-6964.

RADAELLI, A. G., AUGSBURGER, L., CEBRAL, J. R., OHTA, M., RÜFENACHT, D. A., BALOSSINO, R., BENDORF, G., HOSE, D. R., MARZO, A., METCALFE, R., MORTIER, P., MUT, F., REYMOND, P., SOCCI, L., VERHEGGHE, B., AND FRANGI, A. F. Reproducibility of haemodynamical simulations in a subject-specific stented aneurysm model. a report on the virtual intracranial stenting challenge 2007. *Journal of biomechanics*, 41(10):2069–81, July 2008. ISSN 0021-9290.

RAGHAVAN, M., WEBSTER, M. W., AND VORP, D. A. Ex vivo biomechanical behavior of abdominal aortic aneurysm: assessment using a new mathematical model. *Annals of biomedical engineering*, 24(5): 573–582, 1996.

RAJESH, B., SANDHYAMANI, S., AND BHATTACHARYA, R. Clinico-pathological study of cerebral aneurysms. *Neurology India*, 52(1):82, 2004.

RAYZ, V. L., BOUSSEL, L., GE, L., LEACH, J. R., MARTIN, A. J., LAWTON, M. T., MCCULLOCH, C., AND SALONER, D. Flow residence time and regions of intraluminal thrombus deposition in intracranial aneurysms. *Annals of Biomedical Engineering*, 38 (10):3058–3069, 2010.

REGAN, E. R. AND AIRD, W. C. Dynamical systems approach to endothelial heterogeneity. *Circulation research*, 111(1):110–130, 2012.

RENEMAN, R. S., ARTS, T., AND HOEKS, A. Wall shear stress–an important determinant of endothelial cell function and structure–in the arterial system in vivo. discrepancies with theory. *Journal of Vascular Research*, 43(3):251–269, 2006.

RESNICK, N., YAHAV, H., SHAY-SALIT, A., SHUSHY, M., SCHUBERT, S., ZILBERMAN, L. C. M., AND WOFOVITZ, E. Fluid shear stress and the vascular endothelium: For better and for worse. *Progress in Biophysics and Molecular Biology*, 81(3):177–199, 2003.

REYMOND, P., BOHRAUS, Y., PERREN, F., LAZEYRAS, F., AND STERGIOPULOS, N. Validation of a patient-specific one-dimensional model of the systemic arterial tree. *AJP: Heart and Circulatory Physiology*, 301:1173–1182, 2011.

REYMOND, P., MERENDA, F., PERREN, F., RÜFENACHT, D., AND STERGIOPULOS, N. Validation of a one-dimensional model of the systemic arterial tree. *AJP: Heart and Circulatory Physiology*, 297:208 – 222, 2009.

REZAKHANIHA, R., AGIANNIOTIS, A., SCHRAUWEN, J. T. C., GRIFFA, A., SAGE, D., BOUTEN, C. V. C., AND VOSSE, F. N. V. D. Experimental investigation of collagen waviness and orientation in the arterial adventitia using confocal laser scanning microscopy. *Biomechanics and Modeling in Mechanobiology*, 11(3–4):461–473, 2012.

RINKEL, G. J., DJIBUTI, M., ALGRA, A., AND VAN. GIJN, J. Prevalence and risk of rupture of intracranial aneurysms: a systematic review. *Stroke; a journal of cerebral circulation*, 29(1):251–256, 1998.

RINKEL, G. Natural history, epidemiology and screening of unruptured intracranial aneurysms. *Revue neurologique*, 164(10):781–786, 2008.

RIVERO-ARIAS, O., GRAY, A., AND WOLSTENHOLME, J. Burden of disease and costs of aneurysmal subarachnoid haemorrhage (asah) in the united kingdom. *Cost Effectiveness and Resource Allocation*, 8 (1):1, 2010.

ROBERTSON, A. M. AND WATTON, P. Mechanobiology of the arterial wall. In M., B. S. AND KUZNETZOV, editors, *Transport in Biomedical Media*, chapter 8, pages 276–348. Elsevier Inc., 2013.

ROBERTSON, A. M. AND WATTON, P. N. Computational fluid dynamics in aneurysm research: critical reflections, future directions. *American journal of neuroradiology*, 33(6):992–995, 2012.

ROBERTSON, A. M., DUAN, X., AZIZ, K. M., HILL, M. R., WATKINS, S. C., AND CEBRAL, J. R. Diversity in the strength and structure of unruptured cerebral aneurysms. *Annals of Biomedical Engineering*, 43(7):1502–1515, 2015. ISSN 1573-9686.

RODRIGUEZ-FEO, J., SLUIJTER, J., DE KLEIJN, D., AND PASTERKAMP, G. Modulation of collagen turnover in cardiovascular disease. *Current pharmaceutical design*, 11(19):2501–2514, 2005.

RUIGROK, Y. M., RINKEL, G. J., AND WIJMENGA, C. Genetics of intracranial aneurysms. *The Lancet Neurology*, 4(3):179–189, 2005.

RYAN, J. M. AND HUMPHREY, J. D. Finite element based predictions of preferred material symmetries in saccular aneurysms. *Ann. Biomed. Eng.*, 27:641–647, 1999.

SAHNI, O., MÜLLER, J., JANSEN, K., SHEPHARD, M., AND TAYLOR, C. Efficient anisotropic adaptive discretization of the cardiovascular system. *Computer Methods in Applied Mechanics and Engineering*, 195(41Ű43):5634 – 5655, 2006. ISSN 0045-7825. John H. Argyris Memorial Issue. Part {II}.

SAKAKI, T., KOHMURA, E., KISHIGUCHI, T., YUGUCHI, T., YAMASHITA, T., AND HAYAKAWA, T. Loss and apoptosis of smooth muscle cells in intracranial aneurysms-studies with in situ DNA end labeling and antibody against single-stranded DNA. *Acta Neurochirurgica*, 139:469–474, 1997.

SCAPINO, R. P., CANHAM, P. B., FINLAY, H. M., AND MILLS, D. K. The behaviour of collagen fibres in stress relaxation and stress distribution in the jawjoint disc of rabbits. *Archives of Oral Biology*, 41 (11):1039 – 1052, 1996. ISSN 0003-9969.

SCHIEVINK, W. Intracranial aneurysms. *The New England Journal of Medicine*, pages 28–40, 1997.

SCHMID, H., GRYTSAN, A., POSHTAN, E., WATTON, P. N., AND ITSKOV, M. Influence of differing material properties in media and adventitia on arterial adaptation Ů application to aneurysm formation and rupture. *Computer Methods in Biomechanics and Biomedical Engineering*, 16(1):33–53, 2013. PMID: 22149119.

SCHRAUWEN, J. T. C., VILANOYA, A., REZAKHANIHA, R., STERGIOPULOS, N., VAN DE VOSSE, F. N., AND BOVENDEERD, P. H. M. A method for the quantification of the pressure dependent 3d collagen configuration in the arterial adventitia. *Journal of Structural Biology*, 180:335–342, 2012.

SCHRIEFL, A. J., COLLINS, M. J., PIERCE, D. M., HOLZAPFEL, G. A., NIKLASON, L. E., AND HUMPHREY, J. D. Remodeling of Intramural Thrombus and Collagen in an Ang-II Infusion ApoE-/- Model of Dissecting Aortic Aneurysms. *Thrombosis research*, May 2012a. ISSN 1879-2472.

SCHRIEFL, A. J., ZEINDLINGER, G., PIERCE, D. M., REGITNIG, P., AND HOLZAPFEL, G. A. Determination of the layer-specific distributed collagen fibre orientations in human thoracic and abdominal aortas and common iliac arteries. *Journal of The Royal Society Interface*, 9(71):1275–1286, 2012b.

SCHRIEFL, A. J., REINISCH, A. J., SANKARAN, S., PIERCE, D. M., AND HOLZAPFEL, G. A. Quantitative assessment of collagen fibre orientations from two-dimensional images of soft biological tissues. *Journal of The Royal Society Interface*, 9(76):3081–3093, 2012c.

SCOTT, S., FERGUSON, G. G., AND ROACH, M. R. Comparison of the elastic properties of human intracranial arteries and aneurysms. *Canadian Journal of Physiology and Pharmacology*, 50:328–332, 1972.

SELIMOVIC, A. *Patient-specific models of cerebral aneurysm evolution*. Ph.d. thesis, Department of Engineering Science, University of Oxford, Oxford, 2013.

SELIMOVIC, A., VENTIKOS, Y., AND WATTON, P. N. Modelling the evolution of cerebral aneurysms: Biomechanics, mechanobiology and multiscale modelling. *Procedia {IUTAM}*, 10:396 – 409, 2014. ISSN 2210-9838. Mechanics for the World: Proceedings of the 23rd International Congress of Theoretical and Applied Mechanics, {ICTAM2012}.

SESHAIYER, P., HSU, F. P. K., SHAH, A. D., KYRIACOU, S. K., AND HUMPHREYÂĹŮ, J. D. Multiaxial Mechanical Behavior of Human Saccular Aneurysms. *Computer Methods in Biomechanics and Biomedical Engineering*, 4(3):281–289, January 2001. ISSN 1025-5842.

SHADWICK, R. E. Mechanical design in arteries. *The Journal of experimental biology*, 202(23):3305–3313, 1999.

SHAH, A. D., HARRIS, J. L., KYRIACOU, S. K., AND HUMPHREY, J. D. Further roles of geometry and properties in the mechanics of saccular aneurysms. *Computer Methods in Biomechanics and Biomedical Engineering*, 1:109–121, 1997.

SHAH, A. D. AND HUMPHREY, J. D. Finite strain elastodynamics of intracranial saccular aneurysms. *Journal of Biomechanics*, 32:593–599, 1999.

SHEARD, G. J. Flow dynamics and wall shear-stress variation in a fusiform aneurysm. *Journal of Engineering Mathematics*, 64:379–390, 2009.

SHI, C., AWAD, I. A., JAFARI, N., LIN, S., DU, P., HAGE, Z. A., SHENKAR, R., GETCH, C. C., BREDEL, M., BATJER, H. H., AND BENDOK, B. R. Genomics of human intracranial aneurysm wall. *Stroke*, 40(4): 1252–1261, April 2009. ISSN 1524-4628.

SHIMIZU, K., MITCHELL, R. N., AND LIBBY, P. Inflammation and cellular immune responses in abdominal aortic aneurysms. *Arteriosclerosis, Thrombosis and Vascular Biology*, 26:987–994, 2006.

SHIMOGONYA, Y., ISHIKAWA, T., IMAI, Y., MATSUKI, N., AND YAMAGUCHI, T. Can temporal fluctuation in spatial wall shear stress gradient initiate

a cerebral aneurysm? A proposed novel hemodynamic index, the gradient oscillatory number (GON). *Journal of Biomechanics*, 42:550–554, 2009.

SHIMOGONYA, Y., KUMAMARU, H., AND ITOH, K. Sensitivity of the gradient oscillatory number to flow input waveform shapes. *Journal of Biomechanics*, 45(6):985–989, 2012.

SHIN, H. Y., GERRITSEN, M. E., AND BIZIOS, R. Regulation of endothelial cell proliferation and apoptosis by cyclic pressure. *Annals of Biomedical Engineering*, 30(3):297–304, 2002.

SHOJIMA, M., OSHIMA, M., TAKAGI, K., TORII, R., HAYAKAWA, M., KATADA, K., MORITA, A., AND KIRINO, T. Magnitude and role of wall shear stress on cerebral aneurysm: computational fluid dynamic study of 20 middle cerebral artery aneurysms. *Stroke; a journal of cerebral circulation*, 35:2500–2505, 2004.

SHORT, J. G., FUJIWARA, N. H., MARX, W. F., HELM, G. A., CLOFT, H. J., AND KALLMES, D. F. Elastase-induced saccular aneurysms in rabbits: comparison of geometric features with those of human aneurysms. *American journal of neuroradiology*, 22 (10):1833–1837, 2001.

SNUSTAD, D. P. AND SIMMONS, M. J. *Principles of Genetics*. John Wiley & Sons, 2006.

SOPAKAYANG, R., DE VITA, R., KWANSA, A., AND FREEMAN, J. W. Elastic and viscoelastic properties of a type i collagen fiber. *Journal of theoretical biology*, 293:197–205, 2012.

SPRANGER, K. AND VENTIKOS, Y. Which spring is the best? comparison of methods for virtual stenting. *IEEE Transactions on Biomedical Engineering*, 61 (7):1998–2010, July 2014. ISSN 0018-9294.

SPRING, S., VAN DER LOO, B., KRIEGER, E., AMANN-VESTI, B. R., ROUSSON, V., AND KOPPENSTEINER, R. Decreased wall shear stress in the common carotid artery of patients with peripheral arterial disease or abdominal aortic aneurysm: Relation to blood rheology, vascular risk factors, and intima-media thickness,. *Journal of Vascular Surgery*, 43: 56–63, 2006.

STEHBENS, W. E. Histopathology of cerebral aneurysms. *Arch. Neurol.*, 8:272–285, 1963.

STEHBENS, W. E. Etiology of Intracranial Berry Aneurysms. *J. Neurosurger.*, 70:823–831, 1989.

TABER, L. A. A model for aortic growth based on fluid shear and fiber stresses. *Journal of biomechanical engineering*, 120(3):348–54, June 1998. ISSN 0148-0731.

TAKAGI, Y., ISHIKAWA, M., NOZAKI, K., YOSHIMURA, S., HASHIMOTO, N., ELLIOTT, J., AWAD, I., STEINBERG, G., MACDONALD, R., LESNIAK, M., AND RIGAMONTI, D. Increased expression of phosphorylated c-jun amino-terminal kinase and phosphorylated c-jun in human cerebral aneurysms: Role of the c-jun amino-terminal kinase/c-jun pathway in apoptosis of vascular walls. *Neurosurgery*, 51(4): 997–1004, 10 2002. ISSN 0148-396X.

TATESHIMA, S. In vitro measurement of fluid-induced wall shear stress in unruptured cerebral aneurysms harboring blebs. *Stroke*, 34(1):187–192, December 2002. ISSN 00392499.

TATESHIMA, S., MURAYAMA, Y., VILLABLANCA, J., MORINO, T., TAKAHASHI, H., YAMAUCHI, T., TANISHITA, K., AND VIÑUELA, F. Intraaneurysmal flow dynamics study featuring an acrylic aneurysm model manufactured using a computerized tomography angiogram as a mold. *Journal of Neurosurgery*, 2001.

TATESHIMA, S., TANISHIMA, K., OMURA, H., VILLABLANCA, J. P., AND VIÑUELA, F. Intra-aneurysmal hemodynamics during the growth of an unruptured aneurysm: In vitro study using longitudinal ct angiogram database. *AJNR. American journal of neuroradiology*, 28(4):622–627, 2007.

TATESHIMA, S., VIÑUELA, F., VILLABLANCA, J. P., MURAYAMA, Y., MORINO, T., NOMURA, K., AND TANISHITA, K. Three-dimensional blood flow analysis in a wide-necked internal carotid artery-ophthalmic artery aneurysm. *Journal of neurosurgery*, 99(3):526–33, September 2003. ISSN 0022-3085.

TAYLOR, C. A., HUGHES, T. J., AND ZARINS, C. K. Effect of exercise on hemodynamic conditions in the abdominal aorta. *Journal of vascular surgery : official publication, the Society for Vascular Surgery [and] International Society for Cardiovascular Surgery, North American Chapter*, 29(6):1077–89, June 1999. ISSN 0741-5214.

THOMPSON, B. G., BROWN, R. D., AMIN-HANJANI, S., BRODERICK, J. P., COCKROFT, K. M., CONNOLLY, E. S., DUCKWILER, G. R., HARRIS, C. C., HOWARD, V. J., JOHNSTON, S. C. C., MEYERS, P. M., MOLYNEUX, A., OGILVY, C. S., RINGER, A. J., AND TORNER, J. Guidelines for the management of

patients with unruptured intracranial aneurysms: A guideline for healthcare professionals from the american heart association/american stroke association. *Stroke*, 46(8):2368–2400, 2015.

THOMPSON, R. W. AND BAXTER, B. T. Mmp inhibition in abdominal aortic aneurysms: rationale for a prospective randomized clinical trial. *Annals of the New York Academy of Sciences*, 878(1):159–178, 1999.

TODOR, D. R., LEWIS, I., BRUNO, G., AND CHYATTE, D. Identification of a serum gelatinase associated with the occurrence of cerebral aneurysms as promatrix metalloproteinase-2. *Stroke*, 29(8):1580–1583, 1998.

TOMOHIRO, K., SHINJITSU, N., MASAYUKI, K., HIROKI, T., SHUNSUKE, O., KENYA, S., NORIKO, M., YOKO, Y., HIROSHI, M., TATSUYA, S., AND MICHIHARU, N. Distinctive flow pattern of wall shear stress and oscillatory shear index: similarity and dissimilarity in ruptured and unruptured cerebral aneurysm blebs. *Journal of Neurosurgery*, 117(4): 774–780, 2012. PMID: 22920960.

TOTH, M., NADASY, G., NVARY, I., KERENYI, T., OROSZ, M., MOLNARKA, G., MONOS, E., TÓTH, M., NÁDASY, G. L., NYÁRY, I., KERÉNYI, T., AND MOLNÁRKA, G. Sterically inhomogeneous viscoelastic behavior of human saccular cerebral aneurysms. *Journal of vascular research*, 35:345–355, 1998.

TRAUB, O. AND BERK, B. C. Laminar shear stress : Mechanisms by which endothelial cells transduce an atheroprotective force. *Arterioscler. Thromb. Vasc. Biol.*, 18:677–685, 1998.

TREMMEL, M., XIANG, J., HOI, Y., KOLEGA, J., SIDDIQUI, A. H., MOCCO, J., AND MENG, H. Mapping vascular response to in vivo hemodynamics: application to increased flow at the basilar terminus. *Biomechanics and Modeling in Mechanobiology*, 9: 421–434, 2010.

UJIIE, H., SATO, K., ONDA, H., OIKAWA, A., KAGAWA, M., TAKAKURA, K., AND KOBAYASHI, N. Clinical analysis of incidentally discovered unruptured aneurysms. *Stroke*, 24(12):1850–6, 1993.

VAKIL, P., ANSARI, S., CANTRELL, C., EDDLEMAN, C., DEHKORDI, F., VRANIC, J., HURLEY, M., BATJER, H., BENDOK, B., AND CARROLL, T. Quantifying intracranial aneurysm wall permeability for risk assessment using dynamic contrast-enhanced mri: A pilot study. *American Journal of Neuroradiology*, 2015.

VALENTÍN, A. AND HUMPHREY, J. D. Evaluation of fundamental hypotheses underlying constrained mixture models of arterial growth and remodelling. *Philosophical transactions. Series A, Mathematical, physical, and engineering sciences*, 367(1902):3585–3606, 2009a.

VALENTÍN, A. AND HUMPHREY, J. D. Parameter sensitivity study of a constrained mixture model of arterial growth and remodeling. *Journal of biomechanical engineering*, 131(10):101006–1, 2009b.

VAN ROOIJ, W. AND SLUZEWSKI, M. Procedural morbidity and mortality of elective coil treatment of unruptured intracranial aneurysms. *American journal of neuroradiology*, 27(8):1678–1680, 2006.

VILLA-URIOL, M. C., BERTI, G., HOSE, D. R., MARZO, A., CHIARINI, A., PENROSE, J., POZO, J., SCHMIDT, J. G., SINGH, P., LYCETT, R., LARRABIDE, I., AND FRANGI, A. F. @neurist complex information processing toolchain for the integrated management of cerebral aneurysms. *Interface Focus*, 1:308 – 319, 2011.

VILLANO, J. S., BOEHM, C. A., CARNEY, E. L., AND COOPER, T. K. Complications of elastase-induced arterial saccular aneurysm in rabbits: Case reports and literature review. *Comparative Medicine*, 62(6): 480–486, 2012.

VON OFFENBERG SWEENEY, N., CUMMINS, P. M., BIRNEY, Y. A., CULLEN, J. P., REDMOND, E. M., AND CAHILL, P. A. Cyclic strain-mediated regulation of endothelial matrix metalloproteinase-2 expression and activity. *Cardiovascular Research*, 63(4):625–634, 2004. ISSN 0008-6363.

WAGENSEIL, J. E. AND MECHAM, R. P. New insights into elastic fiber assembly. *Birth Defects Res C Embryo Today*, 81(4):229–240, 2007.

WAGNER, H. AND HUMPHREY, J. Differential passive and active biaxial mechanical behaviors of muscular and elastic arteries: basilar versus common carotid. *Journal of biomechanical engineering*, 133 (5):051009, 2011.

WANG, J. H. C., GOLDSCHMIDT-CLERMONT, P., AND YIN, F. C. P. Contractility affects stress fiber remodeling and reorientation of endothelial cells subjected to cyclic mechanical stretching. *Annals of Biomedical Engineering*, 28:1165–1171, 2000.

WANG, S. AND TARBELL, J. M. Effect of fluid flow on smooth muscle cells in a 3-dimensional collagen gel model. *Arteriosclerosis, Thrombosis, and Vascular Biology*, 20(10):2220–2225, 2000.

WARRELL, D. A., COX, T. M., FIRTH, J. D., AND BENZ, E. J. *Oxford textbook of medicine. Vol. 1.* Oxford University Press, 2003.

WATTON, P. N. *Mathematical modelling of the abdominal aortic aneurysm.* Ph.d. thesis, Department of Applied Mathematics, University of Leeds, Leeds, 2002.

WATTON, P. N. AND HILL, N. A. Evolving mechanical properties of a model of abdominal aortic aneurysm. *Biomechanics and modeling in mechanobiology*, 8(1):25 – 42, 2009.

WATTON, P. N., HILL, N. A., AND HEIL, M. A mathematical model for the growth of the abdominal aortic aneurysm. *Biomechanics and modeling in mechanobiology*, 3(2):98 – 113, 2004.

WATTON, P. N., HOLZAPFEL, N. B., HOLZAPFEL, G. A., AND VENTIKOS, Y. Coupling the hemodynamic environment to the evolution of cerebral aneurysms: computational framework and numerical examples. *Journal of biomechanical engineering*, 131 (10):101003, 2009a.

WATTON, P. N., SELIMOVIC, A., RABERGER, N. B., HAUNG, P., HOLZAPFEL, G. A., AND VENTIKOUS, Y. Modelling evolution and the evolving mechanical environment of saccular cerebral aneurysms. *Biomechanics and Modeling in Mechanobiology*, 10 (1):109–132, 2011a.

WATTON, P. N. AND VENTIKOS, Y. Modelling evolution of saccular cerebral aneurysms. *The Journal of Strain Analysis for Engineering Design*, 44(5):375–389, 2009.

WATTON, P. N., VENTIKOS, Y., AND HOLZAPFEL, G. A. Modelling the growth and stabilization of cerebral aneurysms. *Mathematical medicine and biology*, 26 (2):133 – 164, 2009b.

WATTON, P. N., VENTIKOS, Y., AND HOLZAPFEL, G. A. Modelling cerebral aneurysm evolution. In MCGLOUGHLIN, T., editor, *Biomechanics and Mechanobiology of Aneurysms*, volume 7 of *Studies in Mechanobiology, Tissue Engineering and Biomaterials*, chapter 12, pages 307–322. Springer-Verlag, Heidelberg, 2011.

WEIR, B. Unruptured intracranial aneurysms: a review. *Journal of Neurosurgery*, 96(1):3–42, 2002.

WIEBERS, D. O., WHISNANT, J., AND ET. AL., J. H. Unruptured intracranial aneurysms: natural history, clinical outcome, and risks of surgical and endovascular treatment. *Lancet*, 362(9378):103–110, 2003.

WINN, H. R., RICHARDSON, A. E., AND JANE, J. A. The long-term prognosis in untreated cerebral aneurysms. {I}. {T}he incidence of late hemorrhage in cerebral aneurysm: a 10-year evaluation of 364 patients. *Ann Neurol*, 1:358–370, 1977.

WINN, H. *Endovascular Stenting of Intracranial Aneurysms*, chapter 376, pages 3929–3948. Saunders, 2011.

WOLFE, S. Q., BASKAYA, M. K., HEROS, R. C., AND TUMMALA, R. P. Cerebral aneurysms: learning from the past and looking toward the future. *Clinical neurosurgery*, 53:157–178, 2006.

WONG, G. K., KWAN, M. C., NG, R. Y., YU, S. C., AND POON, W. Flow diverters for treatment of intracranial aneurysms: Current status and ongoing clinical trials. *Journal of Clinical Neuroscience*, 18(6): 737 – 740, 2011. ISSN 0967-5868.

WULANDANA, R. AND ROBERTSON, A. M. An inelastic multi-mechanism constitutive equation for cerebral arterial tissue. *Biomechanics and Modeling in Mechanobiology*, 4:235–248, 2005.

WUYTS, F. L., VANHUYSE, V. J., LANGEWOUTERS, G. J., DAECRAEMER, W. F., RAMAN, E. R., AND BUYLE, S. Elastic properties of human aortas in relation to age and atherosclerosis: a structural model. *Physics in Medicine and Biology*, 40:1577–1597, 1995.

XIANG, J., NATARAJAN, S. K., TREMMEL, M., MA, D., MOCCO, J., HOPKINS, L. N., SIDDIQUI, A. H., LEVY, E. I., AND MENG, H. Hemodynamic–morphologic discriminants for intracranial aneurysm rupture. *Stroke*, 42:144–152, 2010.

ZEINALI-DAVARANI, S., SHEIDAEI, A., AND BAEK, S. A finite element model of stress-mediated vascular adaptation: application to abdominal aortic aneurysms. *Computer methods in biomechanics and biomedical engineering*, 14(9):803–817, 2011.

ZENG, Z., KALLMES, D. F., DURKA, M. J., DING, Y., LEWIS, D. A., KADIRVEL, R., AND ROBERTSON, A. M. Hemodynamics and anatomy of elastase-induced rabbit aneurysm models: Similarity to human cerebral aneurysms? *American journal of neuroradiology*, 32:595–601, 2011.

ZENG, Z., KALLMES, D. F., DURKA, M. J., DING, Y., LEWIS, D., KADIRVEL, R., AND ROBERTSON, A. M. Sensitivity of cfd based hemodynamic results in rabbit aneurysm models to idealizations in surrounding vasculature. *Journal of biomechanical engineering*, 132(9):091009, 2010.

ZHANG, J., SCHMIDT, J., RYSCHICH, E., SCHUMACHER, H., AND ALLENBERG, J. R. Increased apoptosis and decreased density of medial smooth muscle cells in human abdominal aortic aneurysms. *Chinese Medical Journal*, 116:1549–1552, 2003.

ZULLIGER, M. A., RACHEV, A., AND STERGIOPULOS, N. A constitutive formulation of arterial mechanics including vascular smooth muscle tone. *American journal of physiology. Heart and circulatory physiology*, 287(3):H1335–H1343, 2004.

APPENDIX A

DERIVATION OF STRAIN ENERGY FUNCTION OF COLLAGEN FIBRES INCLUDING A RECRUITMENT STRETCH DISTRIBUTION AND FIBRE ORIENTATION

The general form for the 1^{st} Piola-Kirchohoff stress for adventitial collagen (to account for gradual recruitment of the fibres to load bearing, and two symmetric families of fibres at an angle to the circumferential direction), used in the analysis of Chapter 3, is as follows:

$$P_{C_A}(\lambda) = \sum_{\gamma=+,-} \frac{\partial}{\partial \lambda} \left[\int_1^{\lambda_\gamma} m_{C_{A\gamma}} \cdot \tilde{\Psi}_{C_{A\gamma}} \left(\frac{\lambda_\gamma}{\lambda^R_{A\gamma}} \right) \cdot \rho \left(\lambda^R_{A\gamma} \right) d\lambda^R_{A\gamma} \right], \tag{A.1}$$

where the definition of the stretch in the direction of the fibres is:

$$\lambda_\gamma(\lambda) = \sqrt{\frac{1}{\lambda} \sin^2 \gamma + \lambda^2 \cos^2 \gamma} \tag{A.2}$$

We assume symmetry for the families of collagen fibres (where the angle is symmetric with respect to the circumferential direction) in terms of normalised densities and material parameters: $m_{C_{A+}} = m_{C_{A-}} = m_{C_A}$ and $K_{C_{A+}} = K_{C_{A-}} = K_{C_A}$

Given those assumptions on the simplifications for the collagen fibre families, the general form of Eqn. (A.1) can be written as:

$$P_{C_A}(\lambda) = 2m_{C_A}\frac{\partial}{\partial\lambda}\left[\int_1^{\lambda_\gamma}\tilde{\Psi}_{C_{A\gamma}}\left(\frac{\lambda_\gamma}{\lambda^R_{A\gamma}}\right)\cdot\rho\left(\lambda^R_{A\gamma}\right)d\lambda^R_{A\gamma}\right] \tag{A.3}$$

The density of fibres recruited at a stretch λ (given a triangular distribution for the recruitment stretches) can be expressed by a piecewise function as follows:

$$\rho\left(\lambda^R_{A\gamma}\right) = \begin{cases} 0 & \lambda^R_{A\gamma} < \lambda^{R,min}_{A\gamma} \\ \frac{2\left(\lambda^R_{A\gamma}-\lambda^{R,min}_{A\gamma}\right)}{\left(\lambda^{R,max}_{A\gamma}-\lambda^{R,min}_{A\gamma}\right)\left(\lambda^{R,mode}_{A\gamma}-\lambda^{R,min}_{A\gamma}\right)} & \lambda^{R,min}_{A\gamma} < \lambda^R_{A\gamma} < \lambda^{R,mode}_{A\gamma} \\ \frac{2\left(\lambda^{R,max}_{A\gamma}-\lambda^R_{A\gamma}\right)}{\left(\lambda^{R,max}_{A\gamma}-\lambda^{R,min}_{A\gamma}\right)\left(\lambda^{R,max}_{A\gamma}-\lambda^{R,mode}_{A\gamma}\right)} & \lambda^{R,mode}_{A\gamma} < \lambda^R_{A\gamma} < \lambda^{R,max}_{A\gamma} \\ 0 & \lambda^R_{A\gamma} > \lambda^{R,max}_{A\gamma} \end{cases} \tag{A.4}$$

For simplification we set, $a = \lambda^{R,min}_{A\gamma}$, $c = \lambda^{R,mode}_{A\gamma}$ and $b = \lambda^{R,max}_{A\gamma}$. We can therefore express the general stress form as a piecewise function:

$$P_{C_A}(\lambda) = \begin{cases} f(\lambda) & \lambda_\gamma < a \\ g(\lambda) & a \le \lambda_\gamma < c \\ h(\lambda) & c \le \lambda_\gamma < b \\ i(\lambda) & \lambda_\gamma \ge b \end{cases} \tag{A.5}$$

For the simplification of each part of the piecewise function, we set some convenient variables:

$$\epsilon = \frac{K_{C_A}}{(b-a)(c-a)} \qquad \delta = \frac{K_{C_A}}{(b-a)(b-c)} \tag{A.6}$$

We can therefore calculate the stress for each function in Eqn. (A.5). For $\lambda_\gamma < a$, $P_{C_A}(\lambda) = f(\lambda)$ where

$$\begin{aligned} f(\lambda) &= 2m_{C_A}\cdot\frac{\partial}{\partial\lambda}\left[\int_1^{\lambda_\gamma}\frac{K_{C_A}}{2}\left(\frac{\lambda_\gamma}{\lambda^R_{A\gamma}}-1\right)^2\cdot 0\, d\lambda^R_{A\gamma}\right] = \\ &= 0 \end{aligned} \tag{A.7}$$

For $a \leq \lambda_\gamma < c$, $P_{C_A}(\lambda) = g(\lambda)$, where:

$$\begin{aligned} g(\lambda) &= 2m_{C_A} \cdot \frac{\partial}{\partial \lambda} \left[\int_a^{\lambda_\gamma} \frac{K_{C_A}}{2} \left(\frac{\lambda_\gamma}{\lambda_{A\gamma}^R} - 1 \right)^2 \cdot \frac{2\left(\lambda_{A\gamma}^R - a\right)}{(b-a)(c-a)} d\lambda_{A\gamma}^R \right] \\ &= 2m_{C_A} \cdot \epsilon \cdot \frac{\partial}{\partial \lambda} \left[\left(ln(\lambda_\gamma) - \ln(a) \right) \left((\lambda_\gamma)^2 + 2a\lambda_\gamma \right) - \frac{5}{2}(\lambda_\gamma)^2 + 2a\lambda_\gamma + \frac{3}{2}a^2 \right] \\ &= \zeta \cdot \epsilon \cdot \frac{\left((c\ln(c) + (-\ln(a) - 1)c + a)\lambda_\gamma + ac\ln(c) - c^2 + (a - a\ln(a))c \right)}{c\lambda^2 \lambda_\gamma}, \end{aligned} \tag{A.8}$$

where $\zeta = 2m_{C_A} \cdot \left(2\cos^2(\gamma)\lambda^3 - \sin^2(\gamma) \right)$

For $b \leq \lambda_\gamma < c$, $P_{C_A}(\lambda) = h(\lambda)$, where:

$$\begin{aligned} h(\lambda) &= 2m_{C_A} \cdot \frac{\partial}{\partial \lambda} \left[\int_a^{c} \frac{K_{C_A}}{2} \left(\frac{\lambda_\gamma}{\lambda_{A\gamma}^R} - 1 \right)^2 \cdot \frac{2\left(\lambda_{A\gamma}^R - a\right)}{(b-a)(c-a)} d\lambda_{A\gamma}^R \right. \\ &\quad \left. + \int_c^{\lambda_\gamma} \frac{K_{C_A}}{2} \left(\frac{\lambda_\gamma}{\lambda_{A\gamma}^R} - 1 \right)^2 \cdot \frac{2\left(b - \lambda_{A\gamma}^R\right)}{(b-a)(b-c)} d\lambda_{A\gamma}^R \right] \\ &= 2m_{C_A} \cdot \frac{\partial}{\partial \lambda} \left[\epsilon \cdot \left[(\ln(c) - \ln(a)) \left((\lambda_\gamma)^2 + 2a\lambda_\gamma \right) + (\lambda_\gamma)^2 \left(\frac{a}{c} - 1 \right) - 2\lambda_\gamma (c-a) + \frac{c^2}{2} - ac + \frac{3}{2}a^2 \right] \right. \\ &\quad \left. + \delta \cdot \left[\lambda_\gamma (\lambda_\gamma + 2b) \left(\ln(c) - \ln(\lambda_\gamma) \right) + (\lambda_\gamma)^2 \left(\frac{3}{2} + \frac{b}{c} \right) - 2c\lambda_\gamma - bc + \frac{c^2}{2} \right] \right] \\ &= \zeta \cdot \left[\epsilon \cdot \frac{(c\ln(c) + (-\ln(a) - 1)c + a)\lambda_\gamma + ac\ln(c) - c^2 + (a - a\ln(a))c}{c\lambda^2 \lambda_\gamma} \right. \\ &\quad \left. - \delta \cdot \frac{2\left(c\lambda_\gamma + bc\right)\ln(\lambda_\gamma) + (-2c\ln(c) - 2c - 2b)\lambda_\gamma - 2bc\ln(c) + 2c^2 + 2bc}{2c\lambda^2 \lambda_\gamma} \right] \end{aligned} \tag{A.9}$$

Lastly, for $\lambda_\gamma \geq b$, $P_{C_A}(\lambda) = i(\lambda)$, where:

$$
\begin{aligned}
i(\lambda) &= 2m_{C_A} \cdot \frac{\partial}{\partial \lambda} \left[\int_a^c \frac{K_{C_A}}{2} \left(\frac{\lambda_\gamma}{\lambda_{A\gamma}^R} - 1 \right)^2 \cdot \frac{2\left(\lambda_{A\gamma}^R - a\right)}{(b-a)(c-a)} d\lambda_{A\gamma}^R \right. \\
&\quad + \int_c^b \frac{K_{C_A}}{2} \left(\frac{\lambda_\gamma}{\lambda_{A\gamma}^R} - 1 \right)^2 \cdot \frac{2\left(b - \lambda_{A\gamma}^R\right)}{(b-a)(b-c)} d\lambda_{A\gamma}^R \\
&\quad \left. + \int_b^{\lambda_\gamma} \frac{K_{C_A}}{2} \left(\frac{\lambda_\gamma}{\lambda_{A\gamma}^R} - 1 \right)^2 \cdot 0 \, d\lambda_{A\gamma}^R \right] \\
&= 2m_{C_A} \cdot \frac{\partial}{\partial \lambda} \left[\epsilon \cdot \left[(\ln(c) - \ln(a)) \left((\lambda_\gamma)^2 + 2a\lambda_\gamma \right) + (\lambda_\gamma)^2 \left(\frac{a}{c} - 1 \right) - 2\lambda_\gamma (c-a) + \frac{c^2}{2} - ac + \frac{3}{2}a^2 \right] \right. \\
&\quad \left. + \delta \cdot \left[-(\ln(b) - \ln(c)) \left(2b\lambda_\gamma + (\lambda_\gamma)^2 \right) - (\lambda_\gamma)^2 \left(1 - \frac{b}{c} \right) + 2\lambda_\gamma (b-c) + \frac{3}{2}b^2 - bc + \frac{c^2}{2} \right] \right] \\
&= \zeta \cdot \left[\epsilon \cdot \frac{(c\ln(c) + (-\ln(a) - 1)c + a)\lambda_\gamma + ac\ln(c) - c^2 + (a - a\ln(a))c}{c\lambda^2\lambda_\gamma} \right. \\
&\quad \left. - \delta \cdot \frac{(c\ln(c) + (-\ln(b) - 1)c + b)\lambda_\gamma + bc\ln(c) - c^2 + (b - b\ln(b))c}{c\lambda^2\lambda_\gamma} \right]
\end{aligned}
\tag{A.10}
$$

APPENDIX B

CALCULATION OF REMODELLED THICKNESS CONSIDERING TWO COLLAGEN FIBRE GROUPS IN THE ADVENTITIA

We follow the analysis for volumetric growth from Chen (2014) and update it to include two collagen fibre groups in the adventitia for the purposes of the mathematical investigations in Chapter 3.

A generalised equation for the volumetric growth of a thin cylindrical surface can be expressed as:

$$h_{rem}(t) \approx \kappa_{rem}(t) \cdot \frac{H}{\lambda(t)\lambda_z}, \tag{B.1}$$

where the $\frac{H}{\lambda(t)\lambda_z}$ term refers to changes in thickness due to an incompressibility assumption, while $\kappa_{rem}(t)$ is the term representing the changes in the mass of the constituents leading to volumetric changes. We define $\kappa_{rem}(t)$ as:

$$\kappa_{rem}(t) = \frac{M_{rem}(t)}{M(0)} = \frac{M_{rem|E_M(t)} + M_{rem|C_M(t)} + M_{rem|C_{A+}(t)} + M_{rem|C_{A-}(t)} + M_{rem|GS_A(t)}}{M_{E_M}(0) + M_{C_M}(0) + M_{C_{A+}}(0) + M_{C_{A-}}(0) + M_{GS_A}(0)}, \tag{B.2}$$

where $M_{rem}(t)$ is the total mass of the arterial wall containing elastin, collagen fibres (in the media and the adventitia) and ground substance (GS) and therefore the vol-

umetric growth ratio is the ratio of the total mass growth at time t to the total mass growth at $t = 0$. Expressing masses for each constituent in terms of normalised mass densities m, initial mass densities ρ and initial volumes V(0), we can express $\kappa_{rem}(t)$ as:

$$\kappa_{rem}(t) = \frac{(m_{E_M}(t)\rho_{E_M} + m_{C_M}(t)\rho_{C_M})V_M(0) + (m_{C_{A+}}(t)\rho_{C_{A+}} + m_{C_{A-}}(t)\rho_{C_{A-}})V_A(0) + G}{(m_{E_M}(0)\rho_{E_M} + m_{C_M}(0)\rho_{C_M})V_M(0) + (m_{C_{A+}}(0)\rho_{C_{A+}} + m_{C_{A-}}(0)\rho_{C_{A-}})V_A(0) + G}, \tag{B.3}$$

where G represents the mass of ground substance. Due to lack of relevant experimental knowledge, we assume that initial densities of the two families of adventitial collagen are equal, i.e. $\rho_{C_{A+}} = \rho_{C_{A-}} = \rho_{C_A}$, as are the normalised densities at time t, i.e. $m_{C_{A+}} = m_{C_{A-}} = m_{C_A}$.

For convenience, we set ratios of densities as follows:

$$\omega_1 = \frac{\rho_{E_M}}{\rho_{C_A}} \tag{B.4}$$

$$\omega_2 = \frac{\rho_{C_M}}{\rho_{C_A}} \tag{B.5}$$

Consequently, we can re-write the volumetric growth parameter as:

$$\kappa_{rem}(t) = \frac{[\omega_1 m_{E_M}(t) + \omega_2 m_{C_M}(t)]V_M(0) + 2m_{C_A}(t)V_A(0) + \frac{G}{\rho_{C_A}}}{(\omega_1 + \omega_2)V_M(0) + 2V_A(0) + \frac{G}{\rho_{C_A}}} \tag{B.6}$$

In a generalised form, we assume that the volume of the media is a proportion z of the adventitia's volume, i.e.:

$$V_M(0) = zV_A(0) \tag{B.7}$$

This in turn results in the calculation of κ_{rem}:

$$\kappa_{rem}(t) = \frac{z[\omega_1 m_{E_M}(t) + \omega_2 m_{C_M}(t)] + 2m_{C_A}(t) + \frac{G}{\rho_{C_A}V_A(0)}}{z(\omega_1 + \omega_2)V_M(0) + 2 + \frac{G}{\rho_{C_A}V_A(0)}} \tag{B.8}$$

Due to lack of further knowledge on the density of , but an indication that the ratio term of $\frac{G}{\rho_{C_A}V_A(0)}$ is very small, we can assume it can be taken out of the equation. Therefore, the expression of the volumetric remodelling parameter is updated as:

$$\kappa_{rem}(t) \approx \frac{z[\omega_1 m_{E_M}(t) + \omega_2 m_{C_M}(t)] + 2m_{C_A}(t)}{z(\omega_1 + \omega_2) + 2} \tag{B.9}$$

Finally, if we assume, for convenience, that the mass densities of the elastins and collagens are the same ($\omega_1 = \omega_2 = 1$), we can conclude that our volumetric growth remodelling parameter κ_{rem} can be calculated as follows:

$$\kappa_{rem}(t) \approx \frac{z[m_{E_M}(t) + m_{C_M}(t) + m_{C_A}(t)]}{6} \tag{B.10}$$

APPENDIX C

FURTHER INFORMATION ON COMPUTATIONAL FLUID DYNAMICS

In order to solve the fluid flow at each step of the FSG framework, ANSYS CFX solves the incompressible Navier Stokes equations (a group of partial differential equations) (Eqn. (C.1)) for the conservation of momentum, heat and mass transfer, considered as Newton's second law of motion for fluids for the attainment of equilibrium:

$$\underbrace{\rho(\frac{\partial \mathbf{u}}{\partial t} + \mathbf{u}\cdot\nabla\mathbf{u})}_{1} = \underbrace{-\nabla p}_{2} + \underbrace{\nabla\cdot(\mu(\nabla\mathbf{u} + (\nabla\mathbf{u})^{T}))}_{3} + \underbrace{\mathbf{F}}_{4} \tag{C.1}$$

where ρ is the fluid density, $\mathbf{u}$ is the fluid velocity, p is the fluid pressure, and μ is the fluid dynamic viscosity. Term (1) refers to the inertial forces, (2) to pressure forces, (3) to viscous forces, and (4) to external forces applied to the fluid. These equations represent the momentum conservation. The Navier Stokes equations are solved in combination with the continuity equation (Eqn. (C.2)) for the conservation of mass of incompressible fluids:

$$\nabla\cdot(\rho\mathbf{u}) = 0 \tag{C.2}$$

The solution of the equations result in predicting the fluid velocity and pressure

in a given geometry. Because of the complexity of the geometry, the equations are discretised and solved numerically (implicit finite volume method). Discretisation is implemented by meshing the geometries (in tetrahedral elements) and the fluid-flow equations that satisfy the conservation of mass and energy are then solved for each control volume. The solutions of interest regard the spatial distribution and relative magnitudes of specific indices, such as WSS vectors.

The blood flow is modelled as a Newtonian fluid of constant density ($\rho = 1066 kg m^{-3}$) and constant viscosity ($\mu = 0.0035 Pa \cdot s$). The arterial wall is assumed to be rigid (no remeshing required to account for wall pulsatility).

For each CFD case, the boundary flow conditions need to also be set. For the clinical case in Chapter 5, where a steady state flow solution is implemented, the boundary conditions are set for the internal carotid artery based on an experimentally calibrated 1D model of the arterial tree (Reymond et al., 2009) aimed for its integration into the software suite @neufuse (Villa-Uriol et al., 2011). The steady-state boundary flow conditions are illustrated in Figure C.1. The fluid mesh in this case comprises of approximately two million elements with three prism layers lining the boundary. A file (with the .ccl extension) containing the boundary conditions and blood flow properties, combined with a file (with the .msh extension) for the geometry's fluid mesh automatically create a definition file that is sent to ANSYS CFX solver that solves the flow for each cycle of the FSG framework.

Nearly all flows in nature, including blood flow, are transient. Steady state methods in *in silico* modelling are preferred due to their lower computational cost and the relative simplicity of post-processing and analysing. For the rabbit aneurysm case of Chapter 6, outlet transient boundary flow conditions (mass flow rate) have been experimentally calculated, as illustrated in Figure C.2.

Transient simulations are solved by computing a solution for many discrete points in time and for each point the solution must be iterated. The ANSYS .ccl file is updated to a transient flow analysis and the profiles for the oulet conditions are expressed as temporal functions by manually inputting points from the experimentally calculated flow conditions. It is important, in order to resolve transient changes, to have equally spaced solution points, with a time step small enough to maintain solver stability. For that reason, a large set of equally spaced points are interpolated from the experimental outlet boundary conditions points (as seen in

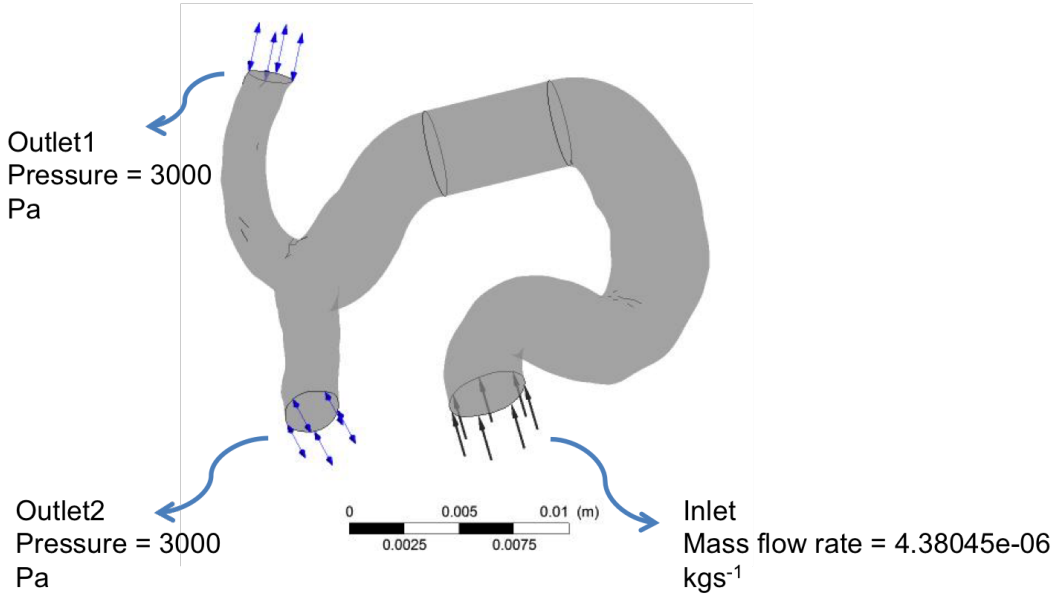

Figure C.1: Illustration of steady flow boundary conditions for the clinical case, based on a 1D model of the arterial tree (Reymond et al., 2009) which has been integrated into the software suite @neufuse (Villa-Uriol et al., 2011).

Figure C.2). Solution points are set during three cardiac cycles (in order to avoid artefacts introduced at initialisation): the results are investigated from the final cycle. The total set time duration (for three heart cycles) is 0.999s and the size for each time step is 0.0066s. It is crucial that the initial conditions are physically realistic. In this case a converged steady state solution is used as a starting point for the transient CFD solution of each cycle of the FSG framework (utilising the average outlet boundary conditions from the experimental data for the solution of a steady state simulation). A default first-order backward Euler scheme is used as the ANSYS recommended method in order to solve the transient terms. For each time step there are also initialisation controls: the automatic option is used in this case, which implies switching between just using the last solution as it is and extrapolating the previous solution to attempt a better starting point, depending on the chosen time step. Additionally, ANSYS CFX-pre allows to set the number of iterations used within each timestep. Primarily adjusting the time step size rather than the number of loops to achieve convergence, limits between a minimum of one loop and a maximum of ten loops were set. Finally, it was possible to export transient statistics (running statistics for solution variables) for variables of interest, such as the distribution of WSS vectors, of the WSS gradient or of the OSI.

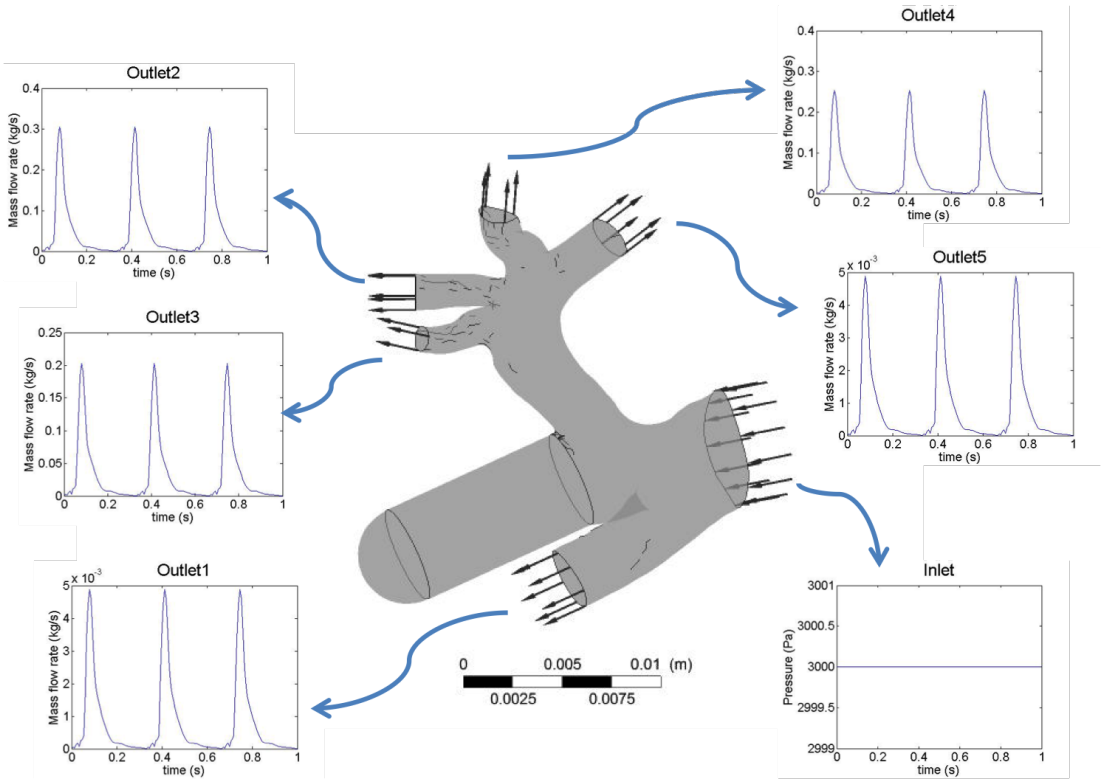

Figure C.2: Illustration of pulsatile boundary conditions for the rabbit aneurysm model, based on experimentally calculated mass flow rates at the outlets and an assumed value for the inlet pressure.